UNIVERSITY OF SOUTHAMPTON
FACULTY OF ENGINEERING AND THE ENVIRONMENT
INSTITUTE OF SOUND AND VIBRATION RESEARCH

ACOUSTICS OF HIGH PERFORMANCE TRANSMISSION-LINE LOUDSPEAKERS

by

Hessam Alavi

A thesis submitted in partial fulfillment for the
degree of Doctor of Philosophy

January 2016

Declaration of Authorship

I, Hessam Alavi, declare that this thesis titled, 'Acoustics of High Performance Transmission-line Loudspeakers' and the work presented in it are my own. I confirm that:

- This work was done wholly or mainly while in candidature for a research degree at this University.
- Where any part of this thesis has previously been submitted for a degree or any other qualification at this University or any other institution, this has been clearly stated.
- Where I have consulted the published work of others, this is always clearly attributed.
- Where I have quoted from the work of others, the source is always given. With the exception of such quotations, this thesis is entirely my own work.
- I have acknowledged all main sources of help.
- Where the thesis is based on work done by myself jointly with others, I have made clear exactly what was done by others and what I have contributed myself.

Signed:

Date: January 2016

"When I let go of what I am, I become what I might be."

Tao Te Ching
Lao Tzu 6^{th} century BC philosopher

UNIVERSITY OF SOUTHAMPTON
Faculty of Engineering and the Environment
Institute of Sound and Vibration Research

Abstract

Doctor of Philosophy

ACOUSTICS OF HIGH PERFORMANCE TRANSMISSION-LINE LOUDSPEAKERS

by Hessam Alavi

Acoustically treated, lined ducts are used in a wide range of applications, one of which is a transmission-line loudspeaker (*TLL*), which consists of a long, acoustically-lined, folded duct attached to the rear of the loudspeaker driver. Consequently, knowledge and understanding of sound propagation within acoustically treated ducts is essential in order to be able to create and analyse designs for the intended applications. The low-frequency driver of a loudspeaker creates pressure fluctuations on both sides of the diaphragm. Therefore, a loudspeaker cabinet of some sort is required to control the sound radiation from the rear of the driver and to prevent the unwanted interference of those sounds with that radiated from the front of the loudspeaker.

The transmission-line loudspeakers are however, designed and optimized to control this rear driver radiations by redirecting the pressure at the back of the driver and use them to extend the overall low-frequency response of the loudspeaker system. Transmission-line loudspeakers rely on the use of sound absorbing materials and, although attempts at modelling the performance of these have been reported in the literature, most transmission-line loudspeakers are designed empirically, using a combination of experience and trial-and-error. This project is concerned with creating and evaluating an engineering method of accurately modelling the sound propagating inside the transmission-line loudspeaker waveguides.

Loudspeaker systems inherently suffer from an insufficient low-frequency response, due to their inefficiency at low-frequencies. Therefore, *TLL* rely on the use of sound absorbing materials added on their internal boundaries to extend their overall response of the loudspeaker at the low-frequency region. The acoustic load on the driver and the sound radiated from the open end of the *TLL* duct both depend upon the propagation of sound through the duct; and the physical length of the duct determines the frequencies that can propagate within it. The addition of sound absorbing materials along the interior boundaries of the *TLL* reduces the speed of propagating sound within it, causing the *TLL* to respond such as having a much longer internal waveguide, consequently accommodating far lower frequencies within the *TLL* duct, extending the overall response of the loudspeaker system.

The characteristics of sound propagation through a variety of two-dimensional and three-dimensional acoustically lined ducts at low-frequencies have been analyzed. Analytical models of straight ducts have been compared with the developed numerical models. In this research dissipative mufflers, that consist of ducts lined on the inside with an acoustically absorptive material, have been considered. Starting with the propagation of sound within hard-walled boundary condition ducts, this investigation moves to the modelling of waveguides treated with locally-reacting acoustic liners and next into the analysis of ducts treated with bulk-reacting acoustic absorbent materials; two kinds of excitations have been considered, namely pistonic and non-uniform excitation. The impedance mismatch and acoustic dissipation between the sound absorbing layer and the free propagation within the duct has been modelled numerically, and the results have been compared with the in-situ measurements conducted on a range of acoustically treated and purpose built transmission-line loudspeakers. A wide range of sound absorbing materials, namely fibrous and porous absorbers, have been characterized using their flow-resistivity and acoustic impedance. Based on their individual characteristics, acoustical optimization was applied on a simple geometry U-shaped *TLL* duct.

Acknowledgements

"If you want to awaken all of humanity, then awaken all of yourself. If you want to eliminate the suffering in the world, then eliminate all that is dark and negative in yourself. Truly, the greatest gift you have to give is that of your own self-transformation."

Hua Hu Ching
Lao Tzu 6^{th} century BC philosopher

My PhD journey provided me with an opportunity to get to know myself a bit better and learn a little bit more about the subject that I have always been fascinated by. I would like to express my sincere gratitude to the following who have helped me throughout my research and supported me through my journey of self-transformation. I would like to begin by thanking Mrs Maureen Mew and Dr Cristóbal González Díaz, for their support during my entire time at the *ISVR*, and for the early reading of the manuscript of this thesis; Dr Daniel Fernández Comesaña, for his help with the measurements and analysis of the data, and for creating a connection between *Microflown Technologies* and this project; Dr Paul Murray, for his practical advice and for connecting this project with *Alenia Aermacchi*; Dr Mahdi Azarpeyvand, for his help with analytical and numerical tasks; Dr Chris Powles, for his help with analytical modelings; Dr Rami Saba, for his help with the *3D* drawings and numerical modeling; Mr Symeon Mattes, for his help with modelings; Ms Sarah Brooks, for her help and support during my studies at the *ISVR*.

In particular I would like to express my utmost gratitude and thanks to my teacher, mentor and friend Mr Xuelong Li, for guiding me straight and true through the many obstacles in my path and for keeping me resolute when all else have lost interest on me. I would also like to thank him for teaching me, and I am deeply proud that he found it worth his while to get to know me and has taught me many lessons in life, for which I am eternally grateful and forever in his debt.

To my family and friends here and all around the world: Armin, Afshin, Nooshin, Ahmadreza, Amirreza, Bijan, Moujan, Rojien, Morteza, PJ,

Paúl, Martina, Sifu Prath, Feargus, Bleddyn, Jess, Samuel, Margaret, Michy, Simon, Yanis, Timooos, Elena, Alex, Mariachi, Olga, Pili, Viki, Albert, Alice, Sensei Lorenzo, Ferdinando, Vince, Vincent, Salvatore, Nikitas, Giorgio, Vassili, Shura, Zsolt, Thanos, Aliki, Juan, Susana, Benoît, Becca, Persefoni, Mengyang, Prateek, Ajit, Diego, Amoo Farhad, Hessam, Leili, Khem, Sifu Gim bow, James, Phil, Eugene, Saeid, Carlos, Fabricio, who have all helped me through some of the most difficult and exhausting times of my life and academic work, for that I would like to thank them all.

The following companies have supported this project and I would like to show my gratitude for their support:

- *Microflown Technologies*, for providing measurement equipment.
- *Alenia Aermacchi*, Centre of Acoustic-Liner Technology, for help with measurements of a range of fibrous and porous materials.
- *Carpenter Co.*, for providing a range of porous materials.
- *Solent Premier Foams*, for providing a range of foams.
- *JA Milton Upholstery Supplies Ltd*, for providing a range of fibrous materials.

Finally, I would like to thank my dearest, my Mother and Father, for their continuous support and patience, for all the sacrifices they have made for me, for their belief in me and my ability to reach where I am today.

Contents

List of Figures

List of Tables

Abbreviations

2D	**T**wo **D**imensional
3D	**T**hree **D**imensional
AVS	**A**coustic **V**ector **S**ensor
BC	**B**oundary-**C**ondition
BR	**B**ulk-**R**eacting
Hi-Fi	**H**igh-**F**idelity
HW	**H**ard-**W**all **D**uct
NUE	**N**on-**U**niform **E**xcitation
LR	**L**ocally-**R**eacting
PE	**P**istonic **E**xcitation
PU	**P**ressure **V**elocity **P**robe
SDOF	**S**ingle-**D**egree-**O**f-**F**reedom
TDOF	**T**wo-**D**egree-**O**f-**F**reedom
TLL	**T**ransmission-**L**ine **L**oudspeaker
USP	**U**ltimate **S**ound **P**robe

Physical Constants

c	$=$	343.21 [m s^{-1}]	Speed of sound at free air at 20°C
$\mathbf{I}$			Identity matrix
j	$=$	$\sqrt{-1}$	Imaginary unit
x			Transverse direction *x-axis*
y			Transverse direction *y-axis*
z			Transverse direction *z-axis*
$\hat{i}$	$=$	1	Unit vector codirectional with x axis
$\hat{j}$	$=$	1	Unit vector codirectional with y axis
$\hat{k}$	$=$	1	Unit vector codirectional with z axis
μ	$=$	$185e^{-7}$ [kg m^{-1} s^{-1}]	Air viscosity
π	$\approx$	3.141 592 6535	Ratio of circumference to diameter of circle
ρ	$=$	1.2041 [kg m^{-3}]	Density of air medium at 20°C

Symbols

A	Complex amplitude of incident wave	[-]
A_i	Acoustic admittance	[m^3 s^{-1} Pa^{-1}]
B	Complex amplitude of reflecting wave	[-]
B_v	Magnetic flux density	[T]
c	Speed of sound in free-air	[m s^{-1}]
$\tilde{c}$	Complex speed of sound	[m s^{-1}]
C_i	Empirical constant	[-]
D	Drag parameter	[N]
E	Stiffness modulus of fibrous tangle	[N m^{-1}]
f	Frequency	[Hz]
f_b	Baffle-step frequency	[Hz]
f_c	Cabinet resonance frequency	[Hz]
f_s	Driver resonance frequency in free-air	[Hz]
F	Net force on driver diaphragm	[N]
F_n	Pressure function	[Pa]
h	Thickness of sound absorbing material	[m]
H	Ratio of transfer functions H_1 and H_2	[-]
H_1	Transfer functions at position x_1	[-]
H_2	Transfer functions at position x_2	[-]
I	Driving current	[A]
I_A	Active acoustic intensity	[W m^{-2}]
J_p	Acoustic cost function	[-]
J_R	Reactive acoustic intensity	[W m^{-2}]

k	Acoustic wavenumber	[rad m^{-1}]
$\tilde{k}$	Complex acoustic wavenumber	[rad m^{-1}]
k_{ms}	Stiffness of driver suspension	[N m^{-1}]
k_{xn}	Axial wavenumbers in *2D x-axis*	[rad m^{-1}]
k_{xnm}	Axial wavenumbers in *3D x-axis*	[rad m^{-1}]
k_{yn}	Axial wavenumbers in *2D y-axis*	[rad m^{-1}]
l_v	Length of voice coil wire in the gap	[m]
L_e	Voice coil electrical inductance	[H]
L_x	Length of *TLL* duct	[m]
L_y	Width of *TLL* duct	[m]
L_z	Height of *TLL* duct	[m]
m	Mode index	[-]
M_f	Mass of fiber per unit volume	[kg]
M_{ms}	Effective mass of driver diaphragm	[kg]
n	Mode index	[-]
N	Mode correction function	[-]
p	Pressure	[Pa]
p_0	Steady component of pressure	[Pa]
p'	Unsteady component of pressure	[Pa]
$\tilde{p}$	Complex pressure	[Pa]
p_l	Pressure at open-end	[Pa]
P	Maximum power	[W]
q	Total volume-velocity	[m^3 s^{-1}]
$\boldsymbol{q}$	Dipole source	[-]
q_d	Volume-velocity of driver	[m^3 s^{-1}]
q_l	Volume-velocity at open-end	[m^3 s^{-1}]
Q	Monopole source	[-]
Q_{es}	Driver electrical Q factor at f_s	[-]
Q_{ms}	Driver mechanical Q factor at f_s	[-]
Q_{ts}	Driver total Q factor at f_s	[-]
r	Distance between source and receiver	[m]

r_d	Radius of drive-unit	[m]
R	Acoustical empirical relation	[-]
R_1	Acoustical empirical relation	[-]
R_e	Voice coil electrical resistance	[Ω]
R_{ms}	Damping of driver suspension	[-]
R_s	Complex reflection coefficient of sample	[-]
S	Cross sectional area of *TLL* duct	[m^2]
S_d	Driver diaphragm surface area	[m^2]
S_l	Cross sectional area at open-end	[m^2]
t	Propagation time	[s]

Velocities

u	Particle velocity	[m s^{-1}]
$\tilde{u}$	Complex velocity	[m s^{-1}]
u_d	Velocity of driver diaphragm	[m s^{-1}]
u_l	Particle velocity at open-end	[m s^{-1}]
u_t	Total particle velocity	[m s^{-1}]

v	Variance of on-axis pressure	[-]
V	Terminal voltage	[V]
V_{as}	Equivalent volume of driver cone	[m^3]
x	Distance along the *x-axis* of *TLL*	[m]
x_1	Microphone location in impedance-tube	[m]
x_2	Microphone location in impedance-tube	[m]
X	Acoustical empirical relation	[-]
X_1	Acoustical empirical relation	[-]
X_{max}	Maximum diaphragm displacement	[m]
y	Distance along the *y-axis* of *TLL*	[m]
z	Distance along the *z-axis* of *TLL*	[m]

Impedances

Z	Characteristic impedance	[Pa s m^{-3}]
Z_a	Total acoustic impedance across driver	[Pa s m^{-3}]
Z_{ab}	Acoustic impedance on back of driver	[Pa s m^{-3}]
Z_{af}	Acoustic impedance on front of driver	[Pa s m^{-3}]
Z_{al}	Acoustic impedance at open-end	[Pa s m^{-3}]
Z_b	Backing impedance in impedance-tube	[Pa s m^{-3}]
Z_d	Driver nominal impedance	[Ω]
Z_e	Electrical impedance	[Ω]
Z_{eb}	Blocked-electrical impedance	[Ω]
Z_{ms}	Mechanical impedance of driver	[N s m^{-1}]
Z_s	Surface normal impedance of samples	[Pa s m^{-3}]

α	Empirical relation attenuation factor	[-]
α_1	Empirical relation attenuation factor	[-]
α_s	Absorption coefficient of sample	[-]
β	Empirical relation phase relation	[-]
β_1	Empirical relation phase relation	[-]
γ	Complex propagation coefficient	[Np m-1]
Δ	Magnitude difference of parameter	[-]
ϵ	Mode correction function	[-]
η	Root mean square pressure	[Pa]
λ	Wavelength	[m]
μ	Air viscosity	[Pa s]
ρ	Density of air medium	[kg m^{-3}]
ρ_0	Density, steady component	[kg m^{-3}]
ρ'	Density, unsteady component	[kg m^{-3}]
$\tilde{\rho}$	Complex density	[kg m^{-3}]
ρ_s	Density of fibrous sample	[kg m^{-3}]
σ	Flow-resistivity	[Pa s m^{-2}]
τ	Non-dimensional variable $\tau = \rho\frac{f}{\sigma}$	[-]

ϕ	Transduction coefficient	[Np A^{-1}]
ϕ_n	Pressure function	[Pa]
Φ_n	Normalization factor	[-]
φ	Acoustic phase shift $\varphi = arg\ \tilde{p}$	[rad]
ω	Angular frequency	[rad s^{-1}]
ω_n	Natural frequency	[rad s^{-1}]

Dedicated to my Teacher Xuelong Li, my Mother and Father for their infinite patience, continuous support and encouragements.

Chapter 1

Introduction

Loudspeakers are electroacoustical transducers which convert electrical energy to acoustical sound waves as a result of mechanical vibration of their diaphragm. The mechanism behind this conversion varies from loudspeaker to loudspeaker but, in most cases, involves some form of motor assembly attached to a diaphragm. The alternating force generated by the motor assembly, in response to the electrical signal, causes the diaphragm to vibrate. This in turn moves the air in contact with the diaphragm and gives rise to the radiation of the sound [1].

The low-frequency driver of the loudspeaker creates pressure fluctuation on both sides of the diaphragm. Therefore, a cabinet of some sort is required to control the sound radiation from the rear of the drive-unit, and prevent unwanted interference with that radiated from the front. Transmission-line loudspeaker cabinets are designed to use this rear driver radiation in order to achieve an extended low-frequency response [2].

Transmission-line loudspeakers rely on the use of sound absorbing materials and, although attempts at modelling the performance of these have been reported in the literature, most transmission-line loudspeakers are designed empirically, using a combination of experience and trial-and-error. This project is concerned with creating and evaluating an engineering method of accurately modelling the sound propagating inside the transmission-line loudspeaker cabinets [3].

1.1 Transmission-Line Loudspeakers

The efficiency of loudspeakers is quite poor at low-frequencies and therefore loudspeakers suffer by design from an insufficient low-frequency response [4–6]. One of the desirable factors for any high-fidelity loudspeaker system is having a flat frequency response. The transmission-line loudspeakers (*TLL*) are designed with the aim to extend the low-frequency response and consequently achieving the overall flat response for the loudspeaker [7, 8].

1.1.1 Infinite-Baffle

As mentioned previously, the low-frequency driver of the loudspeaker creates pressure fluctuation on both sides of the diaphragm. In order to control the sound radiation from the rear of the drive-unit, one needs to separate the front and backwards radiations of the drive-unit by mounting the loudspeaker unit on an infinite-baffle. The receiver therefore only perceives the front radiation of the drive-unit, as initially intended and the backwards radiations have been directed away from the receiver by the infinite-baffle that is dividing the front and backwards radiation of the drive-unit. Figure 1.1 illustrates the schematic model and the frequency response function of an idealised infinite-baffle loaded by an ideal drive-unit.

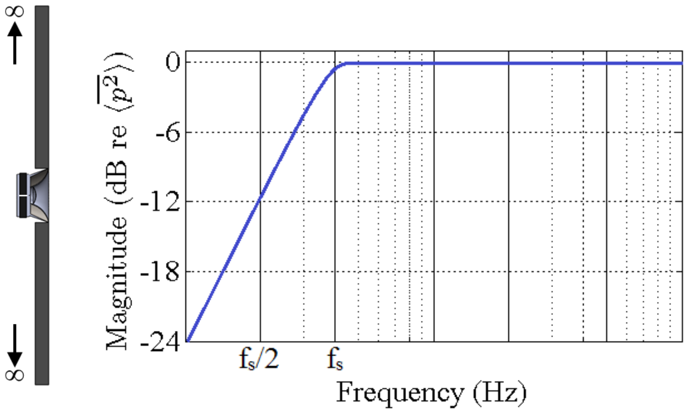

(a) (b)

FIGURE 1.1: Infinite-baffle. (a) Schematic model and (b) frequency response function with second-order roll-off (12 dB/octave slope).

The infinite-baffle radiates in half-space and has a second order roll-off or 12 dB/octave slope which can be observed in the frequency response in Fig. 1.1 (b) at the frequencies below the resonant frequency f_s, of the loudspeaker. Provided a drive-unit capable of true reproduction of the full range of audible frequencies between 20 to 20k Hz, with a flat frequency response has been mounted on an infinite-baffle, the true sound reproduction will be achieved. However, due to the limitation in implementing an infinite-baffle in a listening room, this idea for sound reproduction is considered impractical.

1.1.2 Infinite-Pipe

A variation of the infinite-baffle for controlling the aforementioned sound radiations from the rear of the loudspeaker driver, which was explained in Section 1.1.1, is to have an infinite-pipe attached to the back of the drive-unit so that the backwards radiations will be controlled by being emitted inside a pipe extended to infinity. Figure 1.2 illustrates the schematic model and the frequency response function of an infinite-pipe loaded by an ideal drive-unit.

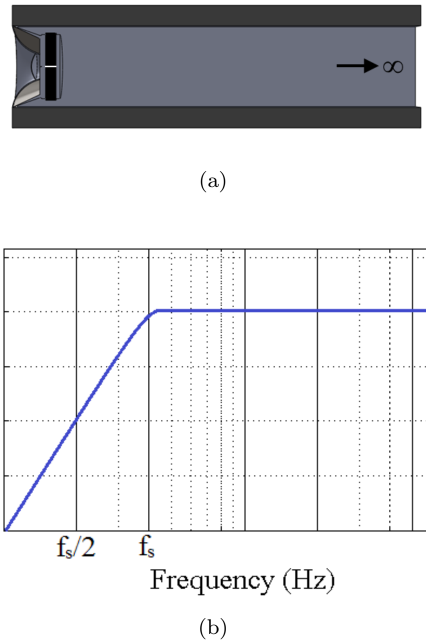

FIGURE 1.2: Infinite-pipe. (a) Schematic model and (b) frequency response function with second-order roll-off (12 dB/octave slope).

The radiation pattern of the infinite-pipe is unlike the case of the infinite-baffle explained in Section 1.1.1. The infinite-pipe radiates in full-space and hence it has 6 dB less in the magnitude of response in comparison to the infinite-baffle arrangement in Section 1.1.1. However, as in the previous case, a second order roll-off or 12 dB/octave slope can still be seen in the frequency response of the infinite-pipe in Fig. 1.2 (b) at the frequencies below the resonant frequency, f_s, of the loudspeaker. The idea of infinite-pipe also suffers from the practical implementation point of view, and therefore is also considered impractical.

1.1.3 Sealed-Cabinet

Another idea for controlling the backwards radiations of the loudspeaker driver is to have a cabinet wrapped around the drive-unit containing the unwanted backwards radiations. Figure 1.3 illustrates the schematic model and the frequency response function of a sealed-cabinet loudspeaker with the volume (V) loaded by an ideal drive-unit.

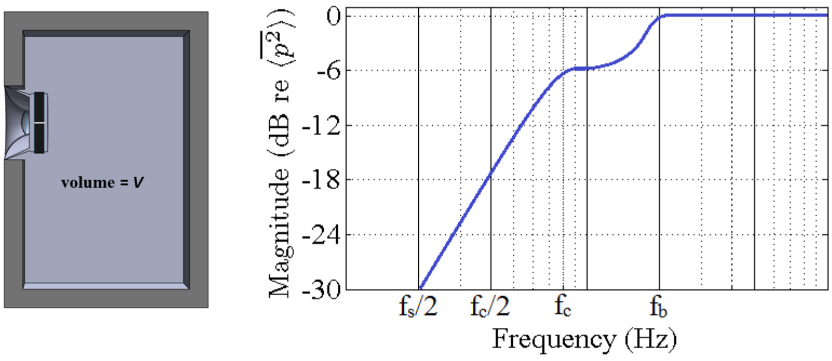

(a)

(b)

FIGURE 1.3: Sealed-cabinet. (a) Schematic model and (b) frequency response function with second-order roll-off (12 dB/octave slope).

However, by introducing a cabinet around the dive-unit, the efficiency of the loudspeaker output at low-frequencies will be further decreased. This is due to the added mechanical stiffness to the total loudspeaker system, which is the spring stiffness of air contained inside the cabinet. The increased stiffness in return pushes the resonant frequency, f_s, of the loudspeaker to a higher-frequency than that in the cases of infinite-baffle or infinite-pipe in Sections 1.1.1 or 1.1.2 respectively. In a closed-box loudspeaker, the air inside the box acts as a spring, returning the drive-unit cone to the zero-position in the absence of an audio signal applied to the driver. In order to reduce the unwanted mechanical stiffness, the internal volume of the loudspeaker cabinet should be considerably large. This idea however, is not the most practical solution since that would require a large loudspeaker cabinet. A 6 dB baffle-step, f_b, can be observed in the frequency response where the wavelength becomes comparable to that of the size of the loudspeaker cabinet. A second order roll-off or 12 dB/octave slope can also be seen in the frequency response of the sealed-cabinet in Fig. 1.3 (b) at the frequencies below the cabinet resonant frequency, f_c, of the loudspeaker. The sealed-cabinet radiation pattern is a frequency-dependent function. At the frequency range between the loudspeaker enclosure resonant frequency and the baffle-step, from f_c to f_b, where the wavelengths are considerably bigger than the size of the cabinet, the sealed-cabinet radiates in full-space such as in the case of the infinite-pipe in Section 1.1.5 and therefore has 6 dB less in the magnitude response. At frequencies above the baffle-step, f_b, where the size of the cabinet becomes comparable to that from the frequency's wavelengths, the loudspeaker system radiates such as in the case for the infinite-baffle in Section 1.1.1 in half-space and therefore a 6 dB increase in magnitude of response can be observed.

1.1.4 Ported-Cabinet

In order to avoid pushing the resonant frequency of the loudspeaker to a higher-frequency than that in the case of the infinite-baffle or infinite-pipe in Sections 1.1.1 or 1.1.2 respectively, a port can be added to the system. Figure 1.4 illustrates the schematic model and the frequency response function of a ported-cabinet loudspeaker with the volume (V) loaded by an ideal drive-unit.

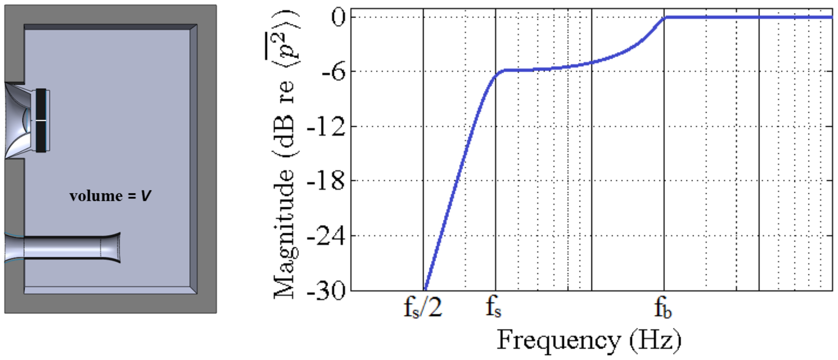

(a) (b)

FIGURE 1.4: Ported-cabinet. (a) Schematic model and (b) frequency response function with fourth-order roll-off (24 dB/octave slope).

As a result of adding the open-port to the loudspeaker enclosure system, the resonant frequency has been kept at f_s, but a fourth-order roll-off or 24 dB/octave slope can be observed in Fig. 1.4 (b) at the frequencies below the resonant frequency, f_s, of the loudspeaker. Adding the port also changes the mechanical system of the loudspeaker from a single-degree-of-freedom $(SDOF)$ system in the case of the sealed-cabinet in Section 1.1.3 to the two-degree-of-freedom $(TDOF)$ for the ported-cabinet. The ported-cabinet radiation pattern is also a frequency-dependent function. At the frequency range between the resonant frequency of the loudspeaker and the baffle-step, from f_s to f_b, where the wavelengths are considerably bigger than the size of the cabinet, the ported-loudspeaker radiates in full-space and therefore has 6 dB less in the magnitude of its response as for the infinite-pipe in Section 1.1.2. At frequencies above the baffle-step, f_b, where the size of the cabinet becomes comparable to that from the frequency's wavelengths, the loudspeaker system radiates such as in the case for the infinite-baffle in Section 1.1.1 in half-space and therefore a 6 dB increase in the magnitude of its response can be observed.

1.1.5 Finite-Pipe Closed-End

A modified case of the sealed-cabinet loudspeaker would be to replace the cabinet with a closed-end finite-pipe with the same volume (V). Figure 1.5 illustrates the schematic model and the frequency response function of a closed-end finite-pipe with the volume (V) loaded by an ideal drive-unit.

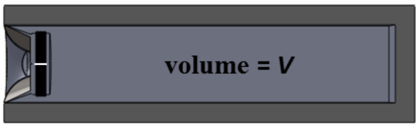

(a)

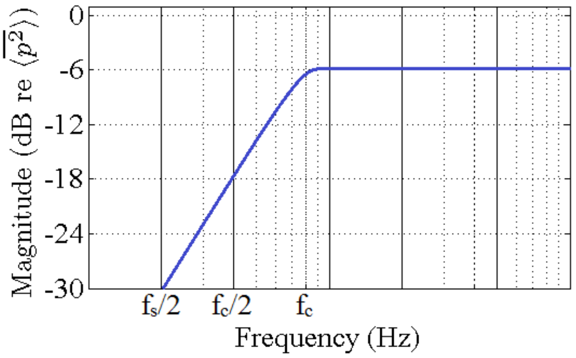

(b)

FIGURE 1.5: Finite-pipe with closed-end and volume (V). (a) Schematic model and (b) frequency response function with second-order roll-off (12 dB/octave slope). Standing wave resonances due to the reflection from the closed-end of the pipe have been ignored.

The frequency response of the finite-pipe with the closed-end exhibits a similarity to the cases of both the sealed-cabinet, as explained in Section 1.1.3, and to that of the infinite-pipe as explained in Section 1.1.2. At the frequencies below the cabinet resonant frequency, f_c, the finite-pipe behaves such as that in the sealed-cabinet loudspeaker with a second-order roll-off or 12 dB/octave slope, as can be seen in Fig. 1.5 (b) where the cabinet resonant frequency, f_c, depends on the volume and the sizes of the individual surfaces that made up the loudspeaker enclosure. At frequencies above the cabinet resonant frequency, f_c, the finite-pipe behaves such as that in the infinite-pipe and radiates in full-space. Therefore, it has 6 dB less in the magnitude of its response, as can be observed in Fig. 1.5 (b). It is also worth mentioning that the standing wave resonances due to the reflection from the close-end of the waveguide have been ignored. Also the main difference between the frequency response of the finite-pipe with the closed-end and the sealed-cabinet is that the baffle-step can no longer be seen in the frequency response, which is due to the shape of the loudspeaker enclosure, since it is similar to that of the infinite-pipe. Therefore, it exhibits the same response above its f_c frequency.

1.1.6 U-shaped *TLL* with Open End

Figure 1.6 illustrates the schematic model and the frequency response function of a U-shaped *TLL* with an open end and volume (V) loaded by an ideal drive-unit, where the length of the *TLL* duct is $L_x = \lambda/4$, where λ is the wavelength of the lowest frequency of interest.

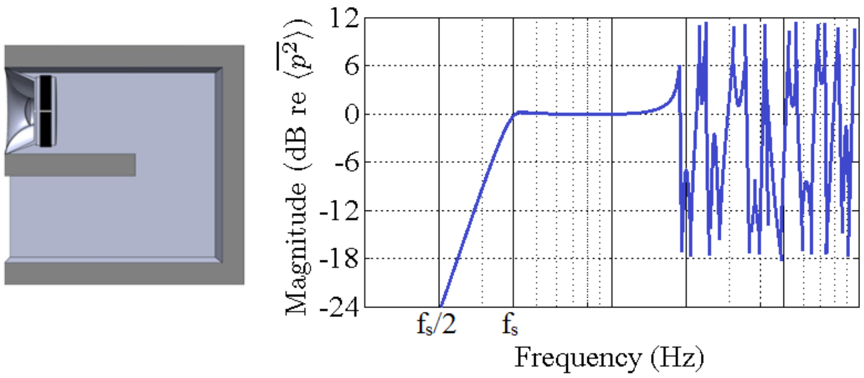

(a) (b)

FIGURE 1.6: U-shaped duct with hard-walled internal boundary condition. (a) Schematic model and (b) frequency response function with fourth-order roll-off (24 dB/octave slope).

The frequency response of the U-shaped *TLL* with the hard-walled boundary condition exhibits a fourth-order roll-off or 24 dB/octave slope, as can be observed in Fig. 1.6 (b) similar to that for the ported-cabinet as explained in Section 1.1.4. However, the addition of the waveguide behind the loudspeaker driver has different effects: the waveguides controls the unwanted sound pressures from the back of the driver and utilizes them to reinforce the overall low-frequency response of the *TLL*, and as a consequence at the low-frequency region from the resonant frequency, f_s, to the baffle-step, f_b, the *TLL* exhibits 6 dB higher in its overall response in comparison to that of the ported-cabinet in Section 1.1.4, which can be seen in Fig. 1.6 (b). On the other hand, addition of the waveguide also deteriorates the flat-frequency response of the U-shaped *TLL* from the baffle-step frequency, f_b, onwards, and therefore the current peaks and troughs can be observed in Fig. 1.6 (b). However, these peaks and troughs can be controlled by carefully optimizing the *TLL* waveguide through addition of the right amount of sound absorbing materials on the internal boundaries of the *TLL* duct.

1.1.7 Optimized *TLL* with Open End

A perfect transmission-line enclosure has an infinitely long duct attached to the back of the driver or a finite length, lined on the inside with the sound absorbing materials such that all the rear radiations of the loudspeaker driver is fully absorbed, down to the lowest frequency. Theoretically, the waveguide at the far-end could be either closed or open with no difference in the performance of the *TLL*. However, the packing density of the sound absorbing material used becomes critical, since too much absorbent materials will cause reflections of the backward radiations of the drive-unit, and the loudspeaker system acts as a closed-cabinet with small volume, whilst insufficient absorbent materials will allow the sound pressure to pass through to the duct. Consequently, often different sound absorbing materials with different packing densities have been used along the length of the duct from the back of the loudspeaker cone inside the *TLL* waveguide to the open end of the *TLL* duct. The peaks and troughs in Fig. 1.6 (b) in the frequency response of the *TLL*, which are generally associated with the addition of the waveguide behind the loudspeaker driver, can be controlled by optimizing the transmission-line loudspeaker cabinet using the correct amount of sound absorbing materials inside the cabinet. Figure 1.7 illustrates the schematic model and the frequency response function of an optimized transmission-line loudspeaker, with the open end and volume (V).[1]

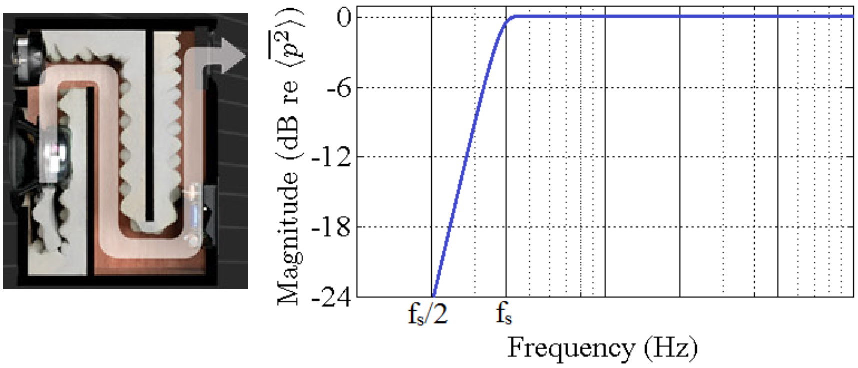

(a) (b)

FIGURE 1.7: Optimized *TLL*, lined on the internal boundaries with porous plastic, bulk-reacting sound absorbing liners. (a) Schematic model and (b) frequency response function with fourth-order roll-off (24 dB/octave slope).

In Fig. 1.7 (b) a fourth-order roll-off or 24 dB/octave slope can be observed. The radiation pattern of the *TLL* is also a frequency-dependent function and follows the same pattern as in the case of the ported-cabinet in Section 1.1.4. However, in comparison to the radiation pattern of the ported-cabinet in Fig. 1.4 in Section 1.1.4, at the frequency range between the loudspeaker resonant frequency, f_s, and the baffle-step, f_b, where the loudspeaker radiates in full-space and has 6 dB less in the magnitude of its response, in the optimized *TLL* this low-frequency inefficiency has been taken care of by the addition of the optimized transmission-line waveguide behind the loudspeaker driver. This effect is also known as the doubling effect of the transmission-line in the optimized frequency range which is generally between f_s and f_b. Above the baffle-step frequency, f_b, the optimized *TLL* radiates in half-space since the size of the cabinet becomes comparable to that from the frequency's wavelengths. At these frequencies the acoustically treated transmission-line waveguide absorbs

---

[1] Picture is courtesy of Professional Monitor Company *PMC*. $http://www.pmc-speakers.com$

all the propagated sound pressure within the duct. Therefore, the loudspeaker total volume-velocity consists of the direct radiated sound from the *TLL* woofer alone. Because the forward and backward radiations of the loudspeaker drive-unit are out-of-phase with each other, any interaction between these two sound pressures in the listening space creates distortion of the original signal, not intended to be reproduced. Additionally, because these two sound pressures travel different paths through the listening space, the sound waves would arrive at the listener's position at slightly different times, introducing frequency-dependent interference, which is again not part of the original sound. These unwanted effects can be taken care of by carefully optimizing the internal volume of the cabinet as well as the size-ratio of each of the panels comprising the *TLL* enclosure, also by optimizing the internal length of the *TLL* waveguide and most importantly the interior acoustic treatment in combination with the optimization of the separating distance between the loudspeaker driver and the open end of the *TLL* on the loudspeaker cabinet.

1.2 Literature Review

Transmission-line loudspeaker cabinets consist of a long, acoustically-lined, folded duct attached to the rear of a loudspeaker driver. The first documentation of a transmission-line system for obtaining extended low-frequency reproduction from a moving-coil loudspeaker was made by *A. R. Bailey* in 1965 [9]. *Bailey's* paper described the use of fibre-filled pipe, or transmission-line, which extended behind the drive-unit to absorb the propagation of acoustic sound waves [10]. However, due to the difficulty of successfully absorbing low-frequency energy, because of the large wavelengths involved, the length of the *TLL* duct and the density of the filling material were arranged such that the *TLL* waveguide effectively act such as a low-pass acoustic filter [10]. Thus the mid and high frequencies were subjected to a large attenuation within the duct but the low-frequencies re-emerged from the open end of the *TLL* with a phase such that the reinforcement with the direct radiated sound from the woofer would take place [9–11].

Figure 1.8 illustrates the schematic model of a transmission-line loudspeaker.

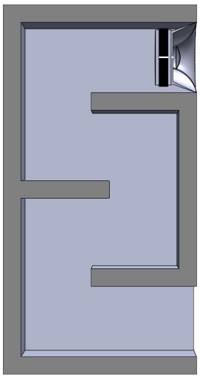

Figure 1.8: Schematic model of a *TLL*.

Bailey's papers, however, do not include the quantitative analysis of the combined effect of loudspeaker and fibre-field pipe and the effect of fibrous tangle on the propagation of an acoustic wave through a pipe (either uniform or otherwise) [10]. Later *L. J. S. Bradbury* in his paper analyzed the effects of fibrous materials on plane wave propagation in a uniform pipe by considering the aerodynamic properties of the fibres [12]. The formulation of a complete model for a transmission-line woofer system was first made by *R. M. Bullock and P. E. Hillman* which investigates the combined driver and uniform pipe system [13]. According to *J. Backman* a transmission-line loudspeaker enclosure can be defined as an enclosure with at least one acoustical wave tube that is not short when compared to the longest wave lengths reproduced by the loudspeaker, and which has cross sectional dimensions much smaller than its length [14]. The length of the transmission-line is selected so that the lowest resonant frequency (the quarter-wave resonance) is near the free-air resonance of the driver. The assumption was made that all other dimensions of the system except the length of the transmission-line are much smaller than the wave lengths of interest [14]. The concept of the transmission-line loudspeaker enclosure was introduced at the same time as the bass reflex loudspeaker in 1936 and described by *B. Olney* [15]. It also dates back to the acoustical labyrinth system as described by *Bailey* [9]. As mentioned previously, there are several types of enclosures that qualify for the term transmission-line. Basically, these are enclosures that are long enough in one internal dimension to accommodate at least one-quarter wavelength of the lowest frequency designed for the system. The path is usually folded and lined with damping material. The system is normally open at the end of the transmission-line, but when considerable damping material is employed there is little radiation from the end of the line or waveguide. In this case the system performs very much like a large well damped sealed enclosure. The conventional transmission-line approaches the bass-reflex loudspeaker, as the length of the waveguide approaches zero and the area of the labyrinth approaches the cross sectional area of the enclosure. If the area of the duct goes to zero the system approaches a sealed enclosure (assuming that the enclosure volume is bigger than zero) [14]. Another type of transmission-line loudspeaker, with sound radiated only through a transmission-line is dual-ported speakers. If the length of both of the ducts equals zero then the dual-port *TLL* is reduced to a conventional coupled-cavity system as described by *Backman* [14]. Transmission-line loudspeakers are also characterised by a sound-radiating at the end of the duct. However, a duct closed at the end could be used to model elongated loudspeaker enclosures or loudspeakers with large step changes in their cross-section [14]. Enclosures with one dimension much larger than the others can be regarded as a transmission-line loaded with a port small compared to the wave length, and if the port is long, the system can be regarded as an enclosure loaded with a transmission-line [14]. This project however, combines the effects of addition of fibrous or porous sound absorbing materials, bulk-reacting liners, on the internal boundaries, on the characteristic of sound propagation within a variety of straight, L-shaped and U-shaped *TLL* ducts. Within the scope of this investigation, the analytical results of straight ducts with hard-walled boundary conditions have been compared with the numerical models of the corresponding *TLL* waveguides. A selection of fibrous and porous sound absorbing materials were also investigated experimentally and their actual physical characteristics such as their density and flow-resistivity were implemented in the numerical models. Next in this project the numerical predictions of a variety of straight, L-shaped and U-shaped *TLL* ducts, acoustically treated with bulk-reacting liners, were compared and validated with the in-situ measurements on the similar range of ducts treated with the same samples of porous absorbing materials. Finally, using the numerical models developed and validated, novel acoustic treatment within U-shaped transmission-line loudspeaker has been proposed.

1.2.1 Uniform Duct *TLL*

Later on, *M. Roberts* in his paper assumes that at low-frequency that the pipe only supports plane wave propagation [10]. Therefore, the one-dimensional solution of the wave equation could be applied (see Eq. (A.1)).[2] The relationship between pressure, p, and particle velocity, u, is given by the Euler equation, which, in linear form, is as stated in Eq. (A.2). Therefore the particle velocity at the open end of the pipe, u_l, is as stated in Eq. (A.20). Having these expressions, *Roberts* derives the acoustic impedance at the open end of the duct as Z_{al} [10]:

$$Z_{al} = \frac{p_l}{u_l}, \tag{1.1}$$

where p_l is the pressure at the open end of the duct and u_l is the particle velocity at the open end of the duct. The acoustic impedance at the driver-end of the duct, $Z_{ab}|_{x=0}$, can also be found to be

$$\frac{Z_{ab}}{\rho c} = \frac{Ae^{jkL_x} + Be^{-jkL_x}}{Ae^{jkL_x} - Be^{-jkL_x}}, \tag{1.2}$$

where A and B are the magnitudes of the incident and reflected waves respectively, L_x is the length of the waveguide, k is the acoustic wavenumber, c is the speed of sound in free-air and ρ is the density of air medium. The electroacoustics analysis of the loudspeaker gives

$$V = IZ_{eb} + \phi u_d \tag{1.3}$$

$$F = u_d Z_{ms} - \phi I, \tag{1.4}$$

where V is the terminal voltage ($V = 2.83$ V *AES* for 1 W), I is the driving current, $\phi = B_v l_v$ is the transduction coefficient or force factor, Z_{eb} is the blocked electrical impedance, u_d is the velocity of driver diaphragm,

---

[2] The derivation of one-dimensional solution of the wave equation has been added to Appendix A.

F is the net force on the driver diaphragm, Z_{ms} is the open-circuit mechanical impedance not containing any of the acoustical elements, and can be found as described in Eq. (2.2). The blocked-electrical impedance, Z_{eb}, also can be found as described in Eq. (2.5). The driver velocity, u_d, can be found as Eq. (2.3). *Roberts* in his paper defines the pressure and particle velocity for the tapered transmission-line loudspeaker cabinet in terms of the complex wavenumber and the complex speed of sound respectively [10].

1.2.2 Maximum Sound Reinforcement

The main aim in adding a transmission-line waveguide to a loudspeaker is to extend the low frequency response of the speaker. Therefore, the frequency range where the maximum sound reinforcement occurs and the transmission-line is best effective needs to be determined. For a *TLL* with the hard-walled boundary condition on the interior boundaries, the lowest frequency that can propagate within it is determined by the length of the internal waveguide, where the lowest frequency has a wavelength, λ, four times the length of the loudspeaker internal waveguide, as explained by *G. Bank and J. Wright* in *chapter 7.3* of their book [16]. The wavelength of the sound, λ, inside the *TLL* duct can be found using:

$$\lambda = \frac{c}{f}. \tag{1.5}$$

Bank and Wright explained that at the frequency where the length of the transmission-line is equal to quarter of a wavelength, $\lambda/4$, the velocity at the opening would be in-phase with forward radiation from the driver. Therefore, the maximum reinforcement in the overall volume-velocity output of the loudspeaker occurs [16]. The practical performance of the system is also affected by the distance between the driver and the open end of the *TLL* on the loudspeaker cabinet. If they are separated by a distance greater than a quarter of a wavelength, the combination of volume-velocities will not be purely additive. This principle could also be applied to any multi-source loudspeaker system. The output of the *TLL* below the resonant frequency has similarities to that of the vented cabinet and therefore a fourth-order roll-off or 24 dB/octave slope can be observed in the frequency range below the resonant frequency of the loudspeaker [16]. Therefore the radiation impedance acting on the back of the driver, Z_{ab}, assuming the labyrinth as a pipe in which only plane waves propagate through it, becomes:

$$Z_{ab} = \frac{\rho c}{S}\left(\frac{Z_{al} + j(\rho c/S)\tan(kL_x)}{(\rho c/S) + jZ_{al}\tan(kL_x)}\right), \tag{1.6}$$

where Z_{ab} is acoustic impedance on the back of the driver and S is the cross sectional area of the *TLL* duct. At low frequencies the radiator can be treated as a piston (if the line is open ended and as a result radiates Z_{al}). Therefore:

$$Z_{ab} = 8j\omega\left(\frac{\rho r_d^3}{3S^2}\right), \tag{1.7}$$

where r_d is the radius of the driver diaphragm. If the line is rigidly terminated and is used simply as a superior mechanism for suppression of the rear radiation, as $Z_{al} \to \infty$, then Eq. (1.7) becomes [16]

$$Z_{ab} = \frac{\rho c}{S}\left(\frac{1}{j\tan(kL_x)}\right). \tag{1.8}$$

1.2.3 Effect of Sound Absorbing Materials

By lining the labyrinth with a suitable sound absorbent material, the mid and high frequencies could be attenuated and the significant resonances can be controlled. *Roberts* in his paper, uses the empirically found complex wavenumber, dependent on the diameter, density and packing density of the fibres used as sound absorbing materials [10]. *Roberts* outlines that, by lining the internal boundaries of the *TLL* waveguide with the sound absorbing materials, the speed of sound propagation in the duct will be reduced by a factor of the phase relation part of the empirically found complex wavenumber. In practice this means that the wavelengths of the signal in the pipe are effectively reduced by the same factor of the phase relation part. Consequently the required length of the duct that accommodates the lowest designed frequency is reduced. The wave amplitude also decays exponentially with distance according to the magnitude of the attenuation factor in the empirically found complex wavenumber [10, 16, 17].

1.2.4 Fibrous Sound Absorbing Materials

Bailey discovered that the behaviour of long-haired wool was very different from that of the other materials and offered far superior acoustic properties for his particular labyrinth type of loudspeaker design [9, 11]. He found that at a packing density of about 8 kg m^{-3} the specific acoustic impedance of this material above 100 Hz was close to that of air, so that the effective stiffness of the cabinet was not greatly influenced by the presence of the fibrous tangle, and yet the wool still had a high attenuation rate so that the shorter wavelength resonances that might otherwise have occurred within the cabinet were all damped [12]. On the other hand, at the low audio frequencies in the region of 30 Hz the wool appeared to reduce the speed of sound to about half its free-air value so that the half-wave-length labyrinth necessary to give an improved bass response was reduced in length from 9 m to 4.5 m for a 30 Hz wave [12]. *Bradbury* in his paper noted that the main effect which the fibrous material has on a sound wave passing through it arises from the drag on the fibres due to the sound wave [12]. *Bradbury* added that since the fibre diameters are much lower than the sound wavelengths at low frequencies, and at the very low air velocities which arise from sound waves, it is possible to show that this drag is proportional to the velocity of the air flowing past the fibres. For simple harmonic waves, a parameter $\omega M_f/D$ can be introduced where M_f is the mass of fibre per unit volume and D is the drag parameter, which is the ratio between the characteristic time required to set the fibres in motion to the period of the sound wave. When the frequency is sufficiently high so that the aforementioned ratio is much greater than 1, there is insufficient time during one cycle of a sound wave for the fibres to be set in motion and, under these circumstances, the sound waves pass through an essentially stationary fibrous frame. In this case the speed of sound is not greatly affected by the presence of the fibres, but because of the high drag, the sound wave is strongly attenuated.[3] By contrast, at low frequencies when $\omega M_f/D$ is much less than 1, the fibres have sufficient time during one cycle of a

---

[3] Fibrous material is assumed to have no mechanical stiffness of its own. Neglecting the stiffness of the fibrous frame requires that $E/(M_f c^2) \ll 1$, where E is the stiffness modulus of the fibrous tangle and c is the speed of sound in free-air. Even for densely packed fibres, the value of the above ratio has values only in the region of about 0.01.

wave to become virtually coupled with air movements, and the air and fibres move as one. Under these circumstances the drag is very small and the sound waves are only weakly attenuated.

1.2.5 Porous Sound Absorbing Materials

Porous plastic sound absorbing materials are another type of commonly used bulk-reacting liners. Some of their main physical characteristics used for the acoustic design and the optimization of the *TLL* waveguides are their density, Young's modulus, chemical composition, absorption coefficient and flow-resistivity which are discussed in more detail in Chapter 4.

1.3 Project Contributions

The contributions of this research have been listed below.

- *COMSOL Multiphysics* environment has been used to develop numerical models to analyse the sound propagation behaviour within a range of rectangular cross-section lined ducts at low-frequencies.[4] The created models are capable of correctly predicting the coupling between the treated region with the bulk-reacting sound absorbing liners and the free propagating region of the *TLL* [18].
- The lumped parameter model of the loudspeaker driver was constructed and combined with the numerical models of the sound propagation behaviour within a range of treated *TLL* as the excitation source. The acoustic impedance at the driver-end of the duct and the volume-velocity at the open end of the duct also have been estimated through using the developed numerical models.
- A variety of bulk-reacting sound absorbing materials, comprising of a range of fibrous and porous absorbers have been characterized by

---

[4] Standard numerical techniques within the *COMSOL Multiphysics* have been employed. The developed numerical models have been generated using the COMSOL version 4.2a.

their flow-resistivity and acoustic impedance. Then extensive in-situ measurements have been conducted on a variety of treated *TLL* in order to get the internal sound pressure and three-dimensional acoustic-intensity along the length of the duct.

- The prediction results of the numerical models have been then compared and validated with the in-situ measurement results of the sound pressure and three-dimensional acoustic intensity performed on a range of treated *TLL*.

- Finally, the developed numerical models have been used to create optimized design of transmission-line loudspeaker cabinet.

1.4 Thesis Structure

The structure of the following chapters of this thesis are explained here. In Chapter 2, the lump parameter model of the *TLL* driver have been constructed using the *Thiele-Small* parameters of the loudspeaker driver. Next, the sound propagation within a variety of rectangular cross-section straight lined ducts at low-frequencies with different boundary conditions on their internal boundaries of the *TLL* have been analyzed using the analytical models. Analysis of the further complicated ducts such as L-shaped or U-shaped ducts, treated with the bulk-reacting sound absorbing liners requires iteratively solving the transcendental equations describing them, which are analyzed numerically in Chapter 3 and validated with the in-situ measurements in Chapter 4. In Chapter 3, numerical models deal with the further complicated *TLL* waveguides in terms of their geometry such as straight, L-shaped and U-shaped ducts, and acoustic treatment such as bulk-reacting liners on the internal boundaries of the *TLL* ducts. In Chapter 4 the analytical and numerical models developed in Chapters 2 and 3 have been validated with the direct measurements results of the sound pressure and three-dimensional acoustic intensity conducted on a range of treated ducts. In Chapter 5 the numerical models developed in Chapter 3 have been used to design an optimized transmission-line loudspeaker cabinet. Chapter 6 gives the results of this project and concluding remarks. Finally, in Chapter 7, further work is suggested in order to improve the analysis and the optimization of the transmission-line loudspeakers. Appendix A contains the derivation of a simple acoustics model of sound propagating through the duct and the derivation of axial wavenumbers. Appendix B contains the detailed measurement results of the impedance-tube, DC-flow tests, numerical predictions and the in-situ measurements evaluating a range of treated *TLL*. Appendix C shows the detailed comparisons and validation results. The manuals and data sheets of the equipment used in performing the measurements in this project are provided in Appendix D.

1.5 Conclusion

In this chapter, the acoustical characteristics of the transmission-line loudspeakers have been introduced. Different loudspeaker enclosure designs have also been investigated, and their strength and weaknesses have been briefly explained in Section 1.1. The acoustical reasons behind the design of the transmission-line loudspeakers have also been outlined and in general their acoustical advantages and the frequency range in which the *TLL* are most effective have also been explained. Generally, since the loudspeakers have very low-efficiency at low-frequency the transmission-line waveguides have been used, aiming to extend the overall flat-frequency response of the loudspeakers. Looking at the frequency response of the transmission-line loudspeakers, they behave such as low-pass acoustic filters; therefore they have been designed such that the mid and high frequencies were subjected to a large attenuation within the *TLL* duct but the low-frequency sounds re-emerge from the open end of the duct with a phase such that the reinforcement with the direct radiated sound from the woofer would take place. The current literature regarding the transmission-line loudspeakers and their acoustic designs have been investigated in Section 1.2. In Chapter 2, the lump parameter model of a loudspeaker driver has been introduced. Using the *Thiele-Small* parameters of the driver some of the more complicated electroacoustical parameters such as the total stiffness of the driver suspension and the damping of the driver suspension have been found. Also, in

Chapter 2, the analytical models of the transmission-line loudspeakers are discussed.

Chapter 2

Analytical Models of *TLLs*

Lined ducts are used in a wide range of applications, including ventilation ducts, sound mufflers, aircraft engine ducts, and electroacoustics applications such as transmission-line loudspeaker cabinets. Knowledge and understanding of sound propagation within ducts with and without treatments is therefore essential in order to be able to create and analyse designs for the intended applications.

In this chapter, analytical models of simple transmission-line loudspeakers have been looked through. Since the driver lump parameter model can accurately predict its behaviour in the low-frequency region, using *Thiele-Small* parameters of the drive-unit the particle velocity at the back of the driver diaphragm inside the *TLL* duct can be predicted.

Next, the characteristics of sound propagation through a variety of two-dimensional and three-dimensional straight ducts with rectangular cross-sections at low-frequencies have been investigated. In the presented analytical models, two kinds of driver excitations, namely uniform (pistonic) and non-uniform excitations and three different internal boundary conditions, namely hard-walled, locally-reacting and bulk-reacting, along the length of the internal boundaries of the waveguides have been considered. The internal pressures have been plotted for the two and three-dimensional cases of straight ducts with the hard-walled boundary conditions.

Detailed analysis of the *TLL* ducts (straight, L-shaped and U-shaped), lined on the inside (internal boundaries) with the acoustic treatments have been investigated in Chapter 3. Instead of iteratively solving the transcendental equation describing the internal pressure along the length of the *TLL* ducts for each of the aforementioned cases, they have been solved numerically and are described in Chapter 3.

2.1 Drive-Unit Lump Parameter Model

The driver of the transmission-line loudspeaker has been modelled at low-frequencies using the lump parameter model of the drive-unit. The model assumes the motion of the drive-unit as a single degree of freedom (*SDOF*) system and this assumption is valid in the low-frequency region. Figure 2.1 illustrates the cross section of a loudspeaker driver and its analogous schematic of a *SDOF* system.[1]

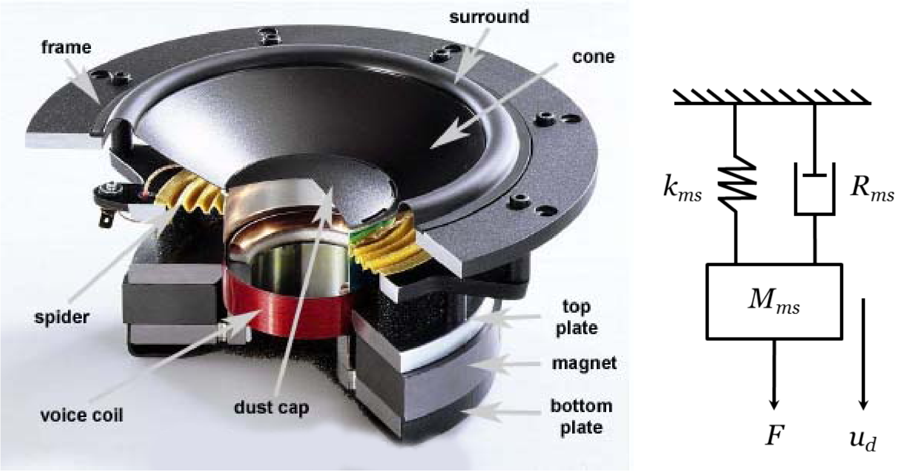

(a) (b)

FIGURE 2.1: (a) Loudspeaker driver cross section and (b) schematic model of single degree of freedom system.

A lumped element has been described using the idealized building-blocks such as mass, M_{ms}, spring stiffness, k_{ms}, and damper, R_{ms}, to represent the dynamic response of an electromechanical system (loudspeaker driver); the basic assumption is that the system's component being represented has dimensions much less than the relevant wavelength. A lumped

---

[1] Picture is courtesy of *Simply Speakers*. *http : //www.simplyspeakers.com*

element can be reactive which means it has no dissipation or resistive which means it has no stored energy. However, in the case of a lumped parameter model of a driver it has both resistive and reactive parts. The reactive elements are further categorized as springlike or masslike, where the springlike components store potential energy and the masslike components store kinetic energy [19]. The combination of the drive-unit spider and surround add up to give the stiffness of driver suspension, k_{ms}, and can be modelled as a springlike reactive element. The damping of the driver suspension, R_{ms}, can be modelled as a resistive component. The combination of drive-unit cone, dust cap and voice coil add up to give the effective moving mass of the driver, M_{ms}, and can be modelled as a masslike reactive component as illustrated in Fig. 2.1. Using the equation for the mass spring damper in the *SDOF* system with simple harmonic motion, it can be written as:

$$F = j\omega M_{ms} u_d + R_{ms} u_d + \frac{k_{ms} u_d}{j\omega}, \tag{2.1}$$

where F is the force applied to the loudspeaker driver-unit, u_d is the velocity of the driver diaphragm, ω is the angular frequency and equal to $\omega = 2\pi f$, f is the frequency parameter and $j = \sqrt{-1}$. The mechanical impedance (in a vacuum) is $Z_{ms} = F/u_d$ and can be found using the equation:

$$Z_{ms} = R_{ms} + j\left(\omega M_{ms} - \frac{k_{ms}}{\omega}\right). \tag{2.2}$$

The particle velocity, u_d, at the driver position can be found using the following equation:

$$u_d = \frac{\phi V}{Z_{eb} Z + \phi^2}, \tag{2.3}$$

where $\phi = B_v l_v$ is the transduction coefficient, B_v and l_v are magnetic flux density and the length of the voice coil wire in the gap respectively and V is the terminal voltage. The blocked-electrical impedance, Z_{eb}, can be found using:

$$Z_{eb} = R_e + j\omega L_e, \tag{2.4}$$

where R_e is the electrical resistance of the driver voice coil and L_e is the electrical inductance of the driver voice coil. The total impedance, Z, can be found to be:

$$Z = Z_{ms} + Z_a, \tag{2.5}$$

where $Z_a = Z_{af} + Z_{ab}$ is the total acoustic radiation impedance, Z_{af} and Z_{ab} are the acoustic radiation impedances in front and on the back of the driver respectively. The driver volume-velocity is $q_d = u_d S_d$ and the open end volume-velocity is $q_l = u_l S_l$, where u_d and S_d are the particle velocity and driver diaphragm surface area at position, $x = 0$, inside the *TLL* duct, and u_l and S_l are the particle velocity and the cross sectional area at the open end, at position, $x = L_x$, along the length of the *TLL* waveguide respectively. Assuming that the *TLL* driver and the open end of the duct are geometrically close compared to a wavelength, the total volume-velocity for the straight duct can be found to be:

$$q = u_d S_d - u_l S_l, \tag{2.6}$$

where the minus sign in Eq. (2.6) ensures that the total outward volume-velocity is positive. The on-axis pressure response at $r = 1$ m distance in front of the loudspeaker driver axis (far-field) can therefore be found to be [1]:

$$p(r, \omega) = \frac{j\rho ckqe^{-jkr}}{4\pi r}, \tag{2.7}$$

where ρ is the fluid density, c is the speed of sound. The acoustic wavenumber is $k = \omega/c$, and r is the on-axis distance between the source (loudspeaker driver) and the receiver (microphone). It is also worth mentioning that Eq. (2.7), represents the on-axis pressure for the half-space radiation such as the baffled case, as explained in Section 1.1.1 of Chapter 1.

2.1.1 Thiele-Small Parameters of Driver

Using the *Thiele-Small* parameters of the loudspeaker driver, the lump parameter model of a drive-unit was constructed. Table 2.1 shows the *Thiele-Small*, low-frequency parameters of a *Visaton* $B200$ 6 Ω driver, distributed by *Visaton the loudspeaker specialist.*[2]

Model	f_s [Hz]	Q_{ts} [-]	Q_{es} [-]	Q_{ms} [-]	V_{as} [m^3]	Z_d [Ω]	P [W]
$B200$ - 6 Ω	40	0.75	0.83	8.39	0.102	6	70

X_{max} [m]	R_e [Ω]	L_e [H]	S_d [m^2]	ϕ [Np A^{-1}]	M_{ms} [kg]	B_v [T]
$+/-0.0035$	5	0.0005	0.0214	3.9	0.0097	1.2

TABLE 2.1: *Thiele-Small*, low frequency parameters of *Visaton* $B200$ 6 Ω driver.

The physical descriptions and the units of all the variables in Table 2.1 can be found in the list of symbols. The resonant frequency of the driver in free-air is f_s. The Q_{ms} is the mechanical Q factor of the driver at f_s, when only the mechanical loss is considered and M_{ms} is the effective moving mass of the driver [20]. Using the equation of the resonant frequency of the loudspeaker driver, as described in Eq. (2.8) below, the total stiffness of the driver suspension, k_{ms}, was found to be [21]:

$$f_s = \frac{1}{2\pi}\left(\frac{k_{ms}}{M_{ms}}\right)^{1/2}. \tag{2.8}$$

Next using the equation of the mechanical Q factor Q_{ms} of the loudspeaker driver system, as described in Eq. (2.9) the damping of the driver suspension R_{ms} was found to be:

$$Q_{ms} = \frac{(k_{ms}M_{ms})^{1/2}}{R_{ms}}. \tag{2.9}$$

---

[2] Table is courtesy of *Visaton the loudspeaker specialist.* $http://www.visaton.com$

The force applied to the driver diaphragm F can be found using Eq. (2.1), or the following equation:

$$F = \phi I, \tag{2.10}$$

where I is the driving current applied to the driver. Therefore the driver velocity can be found by rearranging $Z = F/u_d$ as:

$$u_d = \frac{\phi I}{Z}. \tag{2.11}$$

The voltage across the driver terminals V can also be found using:

$$V = Z_{eb} I + \phi u_d. \tag{2.12}$$

Therefore, Eq. (2.3) describing the particle velocity at the loudspeaker driver position ($x = 0$) can be found using the rearranged form of Eq. (2.11) substituted for I into Eq. (2.12) to get the equation for driver velocity in terms of terminals voltage as presented in Eq. (2.3).

2.2 Duct Acoustics Background Theory

Starting with the propagation of sound within $2D$ hard-walled ducts, this investigation moves to the analytical models of $3D$ ducts with hard-walled boundary conditions. Two kinds of driver excitation have been considered, namely pistonic and non-uniform excitations. The analytical models look through straight ducts with rectangular cross-section with hard-walled and locally-reacting boundary conditions cases on the interior boundaries of the duct. Adding a waveguide without treatment on the inside of a loudspeaker cabinet creates a response such as non-optimized *TLL* as explained in Section 1.1.6. The equation for pressure inside the *TLL* waveguide with the hard-walled boundary conditions can be expressed as [22, 23]:[3]

$$p(x, \omega) = \frac{j\omega\rho}{\gamma} \left(\frac{e^{-\gamma x} - e^{\gamma(x-2L_x)}}{1 + e^{-2\gamma L_x}} \right) u_d, \tag{2.13}$$

---

[3] The derivation of one-dimensional solution of the wave equation has been included in Appendix A.

where x is the distance along the length of the TLL duct, ω is the angular frequency, ρ is the density of the medium, L_x is the length of the TLL duct, u_d is the driver velocity, γ is complex propagation coefficient of a progressive wave system given by $\gamma = \alpha + j\beta$, and α is the attenuation factor and β is the acoustic wavenumber [19]. The particle velocity inside the TLL duct with the hard-walled boundary conditions also can be described by [22, 23]:[4]

$$u(x, \omega) = \left(\frac{e^{-\gamma x} + e^{\gamma(x-2L_x)}}{1 + e^{-2\gamma L_x}} \right) u_d. \tag{2.14}$$

Therefore the ratio of the total velocity u_t, which is for the straight duct equal to $u_t = u_d - u_{Lx}$, normalized with respect to the velocity at the back of the driver u_d becomes [24]:[5]

$$\frac{u_t}{u_d} = 1 - \frac{2e^{-\gamma L_x}}{1 + e^{-2\gamma L_x}}. \tag{2.15}$$

Figure 2.2 illustrates the TLL response, where total velocity u_t in front of the loudspeaker is the sum of the driver and open end velocities, which has been normalized with respect to the driver velocity when the TLL duct has no acoustic treatment on the interior boundaries, for an extremely long length waveguide as described by Eq. (2.15) and explained in detail in Appendix A.

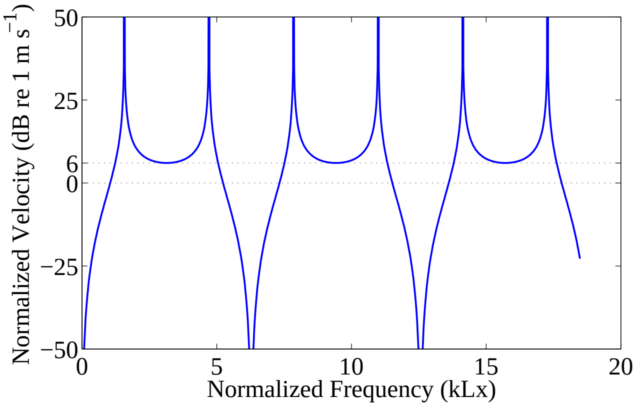

FIGURE 2.2: TLL response, total velocity normalized with respect to driver velocity, with no acoustic treatment on the interior boundaries.

---

[4] The derivation of particle velocity inside the TLL duct with hard-walled boundary conditions is included in Appendix A.

[5] The derivation of total velocity normalized with respect to the velocity at the back of the driver is included in Appendix A.

It can be seen in Fig. 2.2 that the peaks and troughs are tending towards infinity, since the driver damping and stiffness have not been considered and no damping or acoustic treatment has been added on the interior boundaries of the *TLL*. Another feature in Fig. 2.2 is a 6 dB boost in the base of the response which is the general characteristic of the *TLL*. Figure 2.3 illustrates the schematic model of a transmission-line loudspeaker, where A and B represent the complex amplitudes of incident and reflected waves respectively, as described in Eq. (2.16) and explained in detail in Appendix A.

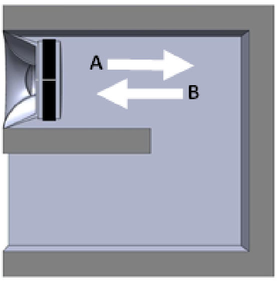

FIGURE 2.3: Schematic model of a *TLL*.

The pressure variation p inside the length of the duct has positive and negative propagating components and is given by [25]:

$$p(x,t) = Ae^{(j\omega t - \gamma x)} + Be^{(j\omega t + \gamma x)}, \tag{2.16}$$

where γ is the complex propagation coefficient of a progressive wave system given by $\gamma = \alpha + j\beta$, and α is the attenuation factor and β is the acoustic wavenumber [19]. It should be noted that the *TLL* ducts are 1 m length and have been excited with a pistonic excitation at the driver position $x = 0$, creating plane-wave propagating inside the duct, and also a pressure-release boundary condition $p = 0 \mid_{x=L_x}$ at the open end of the *TLL* duct $x = L_x$ have been assumed. Figure 2.4 illustrates the sound propagation within a *TLL* such as Fig. 2.3, when the length of the duct is equal to one-quarter of the wavelength of the sound propagating through it.

In Fig. 2.4, the phase relation, particle velocity and pressure along the length of a *TLL* duct can be observed, when it has been excited by a frequency that has a wavelength four times bigger than the duct length

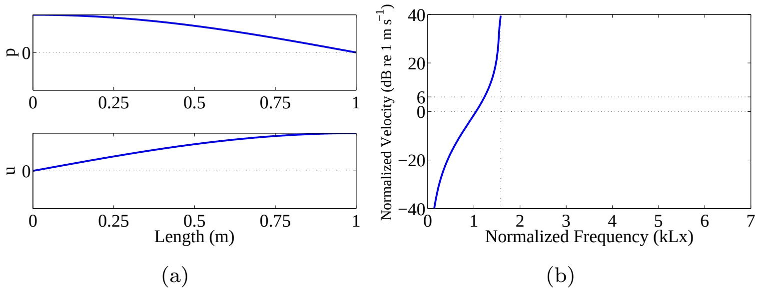

(a) (b)

FIGURE 2.4: Duct excited by a frequency with $\lambda = 4 \times$ duct length. (a) Phase relation between pressure (*top left*) and particle velocity (*bottom left*) and (b) normalized output.

$f = 85.7$ Hz. The output of the drive-unit and the open end of the duct are in-quadrature-phase $\emptyset = +90°$ and the magnitude of the output of the loudspeaker is dominated by the output of the open end of the waveguide. Hence, a peak on that frequency can be observed in Fig. 2.4 (b). Figure 2.5 illustrates the sound propagation within a *TLL*, such as shown in Fig. 2.3, when the length of the duct is equal to half of the wavelength of the sound propagating through it.

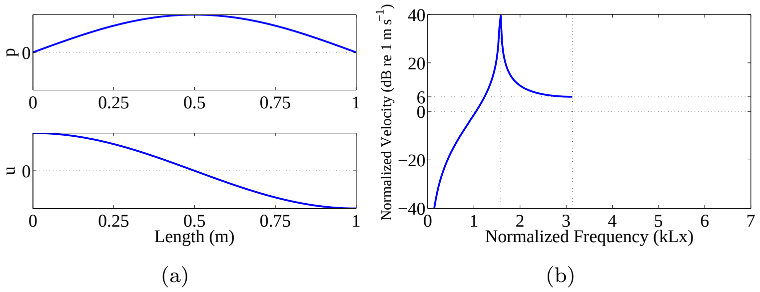

(a) (b)

FIGURE 2.5: Duct excited by a frequency with $\lambda = 2 \times$ duct length. (a) Phase relation between pressure (*top left*) and particle velocity (*bottom left*) and (b) normalized output.

In Fig. 2.5, the phase relation, particle velocity and pressure along the length of a *TLL* can be observed, when it has been excited by a frequency that has a wavelength twice the duct length $f = 171.5$ Hz. The output of the drive-unit and the open end of the *TLL* are in-phase $\emptyset = 0°$ due to the fold in the duct (refer to Fig. 2.3), and they are of a similar magnitude, since there is no damping or acoustic treatment added on the interior boundaries of the *TLL* duct [26]. Hence, a 6 dB increase in the output response of the *TLL* can be observed in Fig. 2.5 (b) on that frequency, also known as the doubling effect in the frequency response output. Figure 2.6 illustrates the sound propagation within the *TLL*, such as shown in Fig. 2.3, when the length of the duct is equal to three quarters of the wavelength of the sound propagating through it.

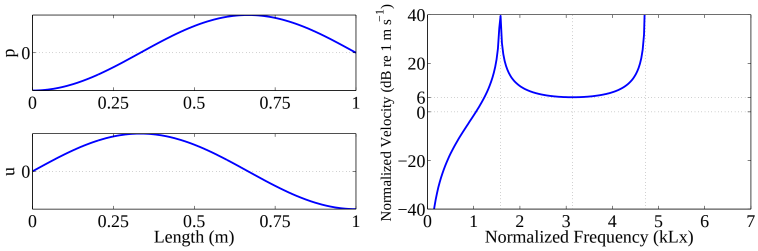

(a)

(b)

FIGURE 2.6: Duct excited by a frequency with $\lambda = 4/3 \times$ duct length. (a) Phase relation between pressure (*top left*) and particle velocity (*bottom left*) and (b) normalized output.

In Fig. 2.6, the phase relation, particle velocity and pressure along the length of a *TLL* duct can be seen, when it has been excited by a frequency that has a wavelength 4/3 times bigger than the duct length $f = 257.2$ Hz. The output of the drive-unit and the open end of the duct are in-quadrature-phase $\emptyset = -90°$ and the magnitude of the loudspeaker output is dominated by the output of the open end of the waveguide, due to the fold in the duct (refer to Fig. 2.3). Hence, a peak on the response of the *TLL* can be observed in Fig. 2.6 (b) on that frequency. Figure 2.7 illustrates the sound propagation within a *TLL* such as shown in Fig. 2.3, when the length of the duct is equal to the full wavelength of the sound propagating through it.

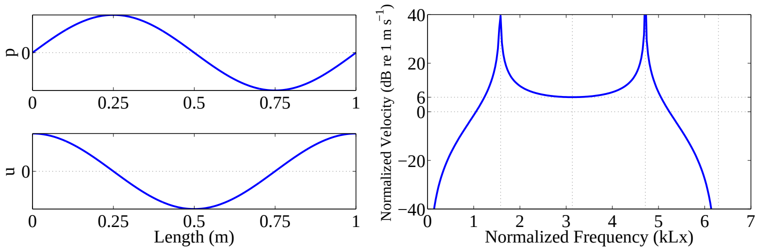

(a)

(b)

FIGURE 2.7: Duct excited by a frequency with λ = duct length. (a) Phase relation between pressure (*top left*) and particle velocity (*bottom left*) and (b) normalized output.

Finally, in Fig. 2.7 the phase relation, particle pressure and velocity along the length of a *TLL* can be noticed, when it has been excited by a frequency that has a wavelength equal to the duct length $f = 343.2$ Hz. The output of the drive-unit and the open end of the *TLL* are out-of-phase $\emptyset = 180°$, due to the fold in the duct (refer to Fig. 2.3), and they are of a similar magnitude, since there is no damping or acoustic treatment added on the interior boundaries of the *TLL*. Hence, a destructive interference in the total output of the *TLL* can be observed at that frequency. The addition of the acoustical treatment within the *TLL* waveguide however, has a direct effect on the imaginary length of the transmission-line, causing significant changes to the overall sound at the open end. By adding sound absorbers on the internal boundaries of the *TLLs*, the mid and high frequencies could be attenuated and the significant resonances can also be controlled [10]. Acoustic treatments are divided into locally-reacting and bulk-reacting liners as explained in Section 2.3, where the bulk-reacting liners are exhibiting far superior sound absorbing characteristics and consequently they are used in the audio applications such as optimized *TLLs*, hence, this project focuses on the bulk-reacting treatments. Historically, the fibrous bulk-reacting materials have been used as an acoustic treatments, as described by *Roberts* in his paper [10]. By lining the internal boundaries of the *TLL* with the acoustic treatment, the speed of sound propagation in the waveguide will be significantly reduced. In practice this means that the wavelengths of the sound signal in the pipe are effectively reduced. Consequently the required length of the duct that accommodates the lowest designed frequency is reduced. The wave amplitude also decays exponentially with the distance according to the magnitude of the attenuation factor in the empirically found complex wavenumber [10, 16]. However, due to the recent advances in the design and production of porous plastic open-cell foams, with specific flow-resistivity, density and other relevant physical properties desired, are far more commonly used by the industry as the acoustic absorbers, as explained by *Wu Qunli* [27]. Next, non-uniform excitations as described in Eq. (2.24) in Section 2.4.5, where one of the two triangles of the rolling piston has a positive normal acceleration while the other triangle is at rest and with the unit-velocity at the driver-end, has also been chosen as the main source of excitation throughout this project to ensure the excitation of a large number of modes within the *TLL* waveguides. Finally, the volume of air in the *TLL* enclosure, within the loudspeaker waveguides, constitutes an additive stiffness which is refereed to as an acoustic load. In low frequencies, this additive stiffness can be considerable compare with the stiffness of the loudspeaker cone itself. The internal air stiffness could be very high due to the hard-walled boundary conditions inside the *TLL* enclosure, since the present of the hard-walls imposes a boundary condition of zero particle velocity $u = 0$, that causes the internal stiffness to increase. The acoustic load inside the *TLL* waveguides depends on the internal volume of the duct, therefore as the size of the loudspeaker increases so as the acoustic load within the *TLL* waveguides. However, in the presented research in order to keep the presented models simple and robust the internal volume of all straight, L-shaped and U-shaped *TLL* waveguides have been kept constant with the same duct length of 1.6 m, and the effect of the acoustic loading of the loudspeaker motion within the analytical models and numerical predictions have not been accounted for.

2.3 Lined Waveguides

There are different possible scenarios of a lined-duct. Figure 2.8 illustrates the schematic model of a uniform duct with hard-walled boundary conditions. The pressure-release boundary condition $p = 0 \mid_{x=L_x}$ has been assumed for the open end of the duct. The velocity at the duct's hard-walled boundary conditions are $u = 0$ [28, 29].

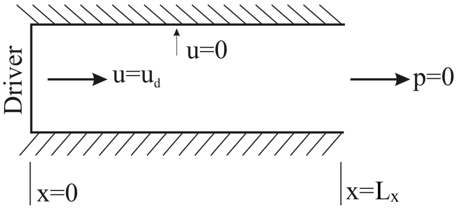

Figure 2.8: hard-walled duct.

Figure 2.9 illustrates the schematic model of a uniform duct lined with the locally-reacting boundary conditions on the interior boundaries. An example of locally-reacting liner would be when each cell in the acoustic liner behaves such as a *"Helmholtz resonance"* and therefore reducing designed frequencies [30].

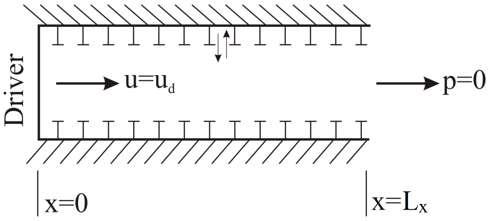

Figure 2.9: Duct lined with locally-reacting liner.

Figure 2.10 illustrates the schematic model of a uniform duct lined with the bulk-reacting boundary conditions on the interior boundaries.

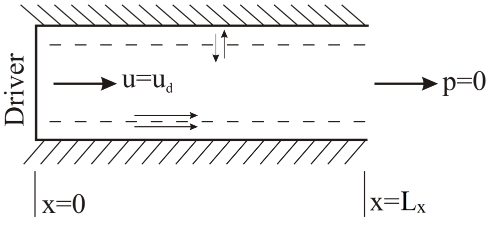

Figure 2.10: Duct lined with bulk-reacting liner.

As can be seen in Fig. 2.10 three distinct propagation modes can be observed within a lined duct treated with the bulk-reacting acoustic liner. The main mode propagates in the non-treated region of the duct. The second mode propagates within the sound absorbing layer[31]. There is a third mode propagating between the two layers of medium, on the surface of the sound absorbing liner and the non-treated region of the duct in the region where the speed of sound is almost the same between the free-region and sound absorbing layer [32, 33].

2.4 Analytical Models of Waveguides

The analytical models of *TLL* ducts lined with different acoustic treatments on the interior boundaries and excited with different diaphragm excitations is presented here [34]. Table 2.2 shows all the different possible scenarios in terms of acoustic treatments and source excitation, propagating within a *TLL* waveguide.

Cases	*Dimension*	*Boundary Condition*	*Diaphragm movement*
Variables	$2D$ $3D$	*hard-walled,* *Locally-Reacting,* *Bulk-Reacting*	*Pistonic,* *Non-Uniform*
1	$2D$	*Hard-Walled*	*Pistonic*
2	$3D$	*Hard-Walled*	*Pistonic*
3	$2D$	*Hard-Walled*	*Non-Uniform*
4	$3D$	*Hard-Walled*	*Non-Uniform*
5	$2D$	*Locally-Reacting*	*Pistonic*
6	$3D$	*Locally-Reacting*	*Pistonic*
7	$2D$	*Locally-Reacting*	*Non-Uniform*
8	$3D$	*Locally-Reacting*	*Non-Uniform*
9	$2D$	*Bulk-Reacting*	*Pistonic*
10	$3D$	*Bulk-Reacting*	*Pistonic*
11	$2D$	*Bulk-Reacting*	*Non-Uniform*
12	$3D$	*Bulk-Reacting*	*Non-Uniform*

TABLE 2.2: All different possibilities of *TLL* duct treatments and driver excitation.

2.4.1 *TLL* Assumptions Made and Carried Throughout the Project

The straight, L-shaped and U-shaped *TLL* uniform ducts considered in this research in $2D/3D$ cases of the numerical predictions or the in-situ measurements, have been designed and built with the square cross sectional area with the dimension of 0.3×0.3 m^2 and internal length of 1.6 m along (*x-axis*), and have hard-walled boundary conditions along the interior boundaries, and have been excited with a pistonic excitation at the driver position $x = 0$ with unit-velocity of 1 m s^{-1}, and pressure-release boundary condition $p = 0 \mid_{x=L_x}$ at the open end of the transmission-line waveguides $x = L_x$ for all the *TLL* ducts, unless it is been stated otherwise in the description of a specific figure.

2.4.2 Case 1: $2D$ Duct, Hard-Walled Boundary Condition and Pistonic Excitation

Assume a duct of width L_y and length L_x, with excitation at driver position $x = 0$, acoustically hard-walled at $y = 0$ and $y = L_y$, and a pressure-release boundary at the open end of the duct at $x = L_x$. The pressure $p(x, y)e^{j\omega t}$ is as shown in Eq. (2.17) and illustrated in Fig. 2.11 below [35, 36]. Figure 2.11 shows a $2D$ duct, with hard-walled boundary conditions on the interior boundaries as described for the cases 1 and 3 in Table 2.2.

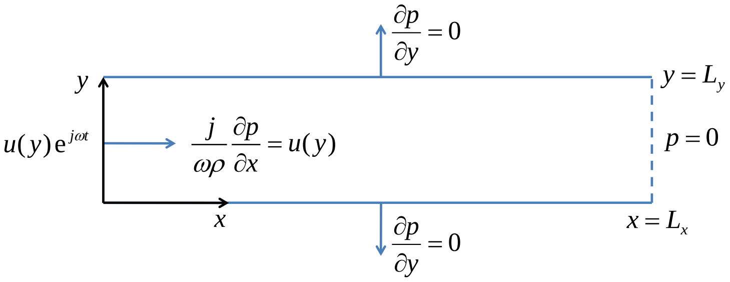

FIGURE 2.11: $2D$ duct, hard-walled case.

Suppose the driver velocity $u(y) = u_d$ is a constant; therefore there is a pistonic excitation propagating through the duct. Then only mode order 0 is excited, and the pressure field for a single frequency along the duct could be described by [22, 37]:[6]

$$\frac{p(x,y)}{\rho c^2} = -j\frac{u_d}{c}\frac{\sin\left(k\left(x-L_x\right)\right)}{\cos\left(kL_x\right)}, \tag{2.17}$$

where ρ is the fluid density, c is the speed of sound, and $k = \omega/c$ is the acoustic wavenumber. The parameters x and y refer to the locations along the length L_x and width L_y of the duct. Eq. (2.17) is the trigonometric representation of Eq. (A.17) presented in Appendix A, which is the exponential form of the particle pressure along the length of the *TLL* with rectangular cross section, pistonic excitation, hard-walled boundary conditions along the interior boundaries and a pressure-release boundary condition at the open end of the waveguide. Figure 2.12 shows the analytical results of pressure variation along the length of the duct, for $2D/3D$ cases [38].

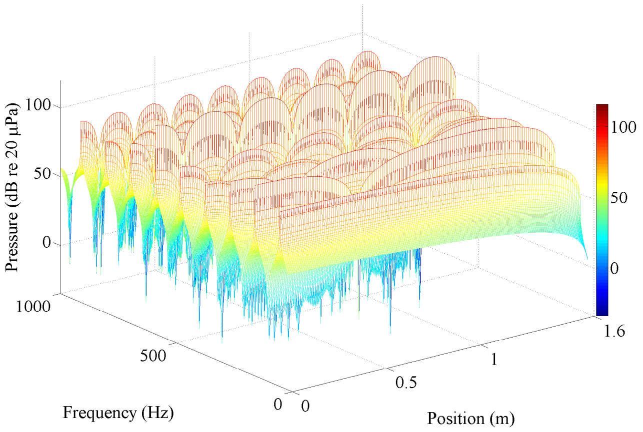

FIGURE 2.12: Pressure variation along the length of the duct (x-*axis*), for $2D/3D$ cases with hard-walled boundary conditions and pistonic excitation.

In Fig. 2.12 the pressure variation along the length of the *TLL* duct can be analyzed as the frequency increases. As the frequency progresses and the wavelength of the propagating sound shortens, a greater number of full-wavelengths can be observed to propagate within the pipe [39]. Also, at the low-frequency a natural decay of the sound pressure amplitude along the length of the duct can be observed with the lowest magnitude

---

[6] The derivation of one-dimensional solution of the wave equation is given in Appendix A.

at the 1.6 m length of the duct, which is due to the assumption of a pressure-release boundary condition at the open end of the duct.

2.4.3 Case 3: $2D$ Duct, Hard-Walled Boundary Condition and Non-Uniform Excitation

Suppose now there is a source excitation such as a “rolling piston” at the driver position $x = 0$, which can be described by:

$$u(y) = u_d \frac{2}{L_y}\left(y - \frac{L_y}{2}\right), \tag{2.18}$$

as sketched in Fig. 2.13 below. Figure 2.13 shows the schematic model of a rolling piston described in Eq. (2.18) for a non-uniform excitation described for $2D$ ducts in case 4 in Table 2.2.

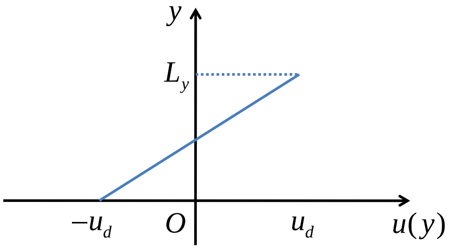

FIGURE 2.13: Schematic model of rolling piston for the $2D$ case.

The acoustic pressure is therefore described by [40, 41]:[7]

$$\begin{aligned}\frac{p(x,y)}{\rho c^2} = &-\frac{2ju_d}{c}\sum_{n=1}^{\infty}\frac{k}{k_{xn}}\epsilon_n\left(\frac{(-1)^n - 1}{(n\pi)^2}\right)\cdots \\ &\times \cos\left(\frac{n\pi y}{L_y}\right)\frac{\sin\left(k_{xn}\left(x - L_x\right)\right)}{\cos\left(k_{xn}L_x\right)},\end{aligned} \tag{2.19}$$

where the first term in brackets has the effect of removing all even-numbered modes. In this case there is no mode 0 excitation. All odd-numbered modes are excited, although only the lowest orders will be

---

[7] The derivation of acoustic pressure for a $2D$ case with hard-walled boundary conditions is an extension to the derivation of Eq. (2.17) given in Appendix A.

cut-on. The axial wavenumbers k_{xn} can be defined by [42]:[8]

$$k_{xn} = \left(k^2 - \left(\frac{n\pi}{L_y} \right)^2 \right)^{1/2}, \tag{2.20}$$

where n is mode index number and the normalization factor, ϵ, is described to ensure the average value of the mode shape function across the duct cross section is unity and is given by:

$$\epsilon = \begin{cases} 1 & for \quad n = 0, \\ 2 & for \quad n \neq 0. \end{cases} \tag{2.21}$$

Figure 2.14 shows the analytical results of pressure variation along the length of a $2D$ duct, with hard-walled boundary conditions on the interior boundaries and non-uniform excitation.

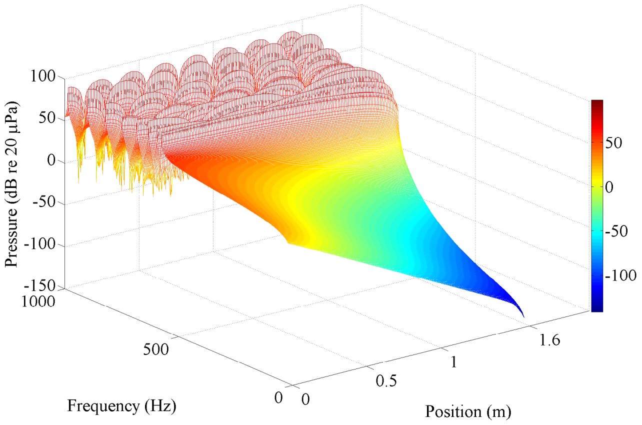

FIGURE 2.14: Pressure variation along the length of the duct (x-*axis*), for a $2D$ case with hard-walled boundary conditions and non-uniform excitation.

Once again in Fig. 2.14 the pressure variation along the length of the *TLL* duct can be analyzed as the frequency increases similar to the case in Fig. 2.12. As the frequency progresses and the wavelength of the propagating sound shortens, a greater number of full-wavelengths can be observed to propagate within the pipe [39]. Also, at the low-frequency a much more pronounced natural decay of the sound pressure amplitude along the length of the duct can be observed with the lowest magnitude at

---

[8] The derivation of axial wavenumbers is given in Appendix A.

the 1.6 m length of the duct which is due to the assumption of a pressure-release boundary condition at the open end of the duct in conjunction with the non-uniform excitation in a $2D$ duct which causes the excitation of higher order modes, which invariably pushes the decay envelope to a higher frequency range than that in Fig. 2.12. It has to be noted that the cut-on modes will be dominant, so the summation can be terminated at:

$$N = \frac{kL_y}{\pi}. \tag{2.22}$$

Figure 2.15 shows the analytical results of pressure variation along the cross section of the duct (y-*axis*), in the mid-point along the length of the duct for a $2D$ uniform duct, hard-walled boundary conditions along the interior boundaries and non-uniform excitation at the driver position.

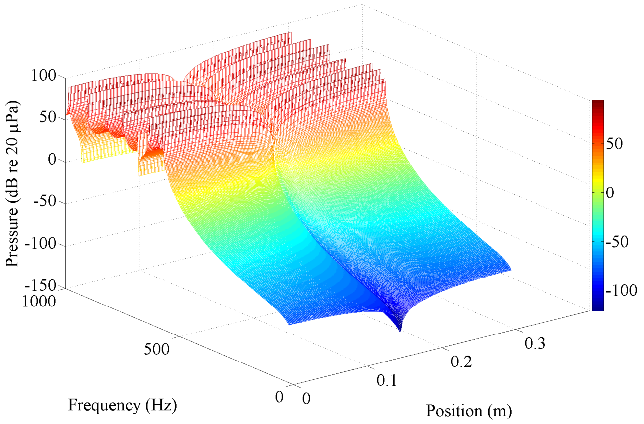

FIGURE 2.15: Pressure variation along the 0.3 m cross-section of the duct (y-*axis*), in the mid-point along the length of the *TLL*, $2D$ case with hard-walled boundary conditions and non-uniform excitation.

In Fig. 2.15 the pressure variation along the 0.3 m cross section of the $2D$ *TLL* duct (y-*axis*), in the mid-point along the length of the duct, with hard-walled boundary conditions and non-uniform excitation can be observed. There is a nodal line along the centre of the cross section of the duct which is the same as the frequency progresses [39]. Also, at low-frequencies a natural decay of the sound pressure amplitude along the internal boundaries of the cross section of the duct can be observed which is due to the hard-walled boundary conditions at the internal boundaries of the duct.

2.4.4 Case 2: $3D$ Duct, Hard-Walled Boundary Condition and Pistonic Excitation

Now assuming a duct of width L_y, height L_z and length L_x, with excitation at $x = 0$, acoustically hard-walled at $y = 0$, $y = L_y$, $z = 0$, $z = L_z$, and a pressure-release boundary condition at $x = L_x$. The pressure variation $p(x, y, z)e^{j\omega t}$ for the $3D$ duct with hard-walled boundary conditions on the interior boundaries and pistonic excitation can be found using Eq. (2.23). Figure 2.16 shows the schematic model of a $3D$ duct with hard-walled boundary conditions on the interior boundaries as described for cases 2 and 4 in Table 2.2.

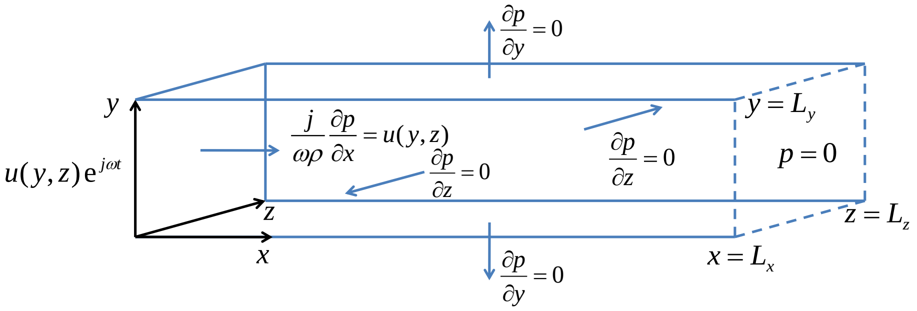

FIGURE 2.16: $3D$ duct, hard-walled case.

Suppose $u(y, z) = u_d$ is a constant, so there is a pistonic excitation at the driver position $x = 0$ along the waveguide. Then only mode order 0 is excited, and the pressure field within the $3D$ duct is:

$$\frac{p(x, y, z)}{\rho c^2} = -j\frac{u_d}{c}\frac{\sin\left(k\left(x - L_x\right)\right)}{\cos\left(kL_x\right)}, \tag{2.23}$$

which is identical to Eq. (2.17) for the $2D$ duct for case 1 in Section 2.4.2.

2.4.5 Case 4: $3D$ Duct, Hard-Walled Boundary Condition and Non-Uniform Excitation

Suppose now there is excitation such as a rolling piston, described by:

$$u\left(y, z\right) = u_d\frac{2}{L_y}\left(y - \frac{L_y}{2}\right)\frac{2}{L_z}\left(z - \frac{L_z}{2}\right). \tag{2.24}$$

Comparing Eq. (2.24) above with Eq. (2.18) for case 3 in Section 2.4.3, it can be noticed that Eq. (2.24) has another transverse direction z, associated with it. In this case there is no mode 0 excitation and there are two transverse directions, y and z, which require two mode indices, n and m, associated with the aforementioned directions respectively. All odd-numbered modes are excited, although only the lowest orders will be cut-on. Therefore, the axial wavenumbers can be defined by:

$$k_{xnm} = \left(k^2 - \left(\frac{n\pi}{L_y} \right)^2 - \left(\frac{m\pi}{L_z} \right)^2 \right)^{1/2}, \tag{2.25}$$

where k_{xnm} is the axial wavenumber in the x-direction along the length of the *TLL*, with the indices n and m, associated with their respective directions [43, 44]. The acoustic pressure is therefore given by:[9]

$$\begin{aligned} \frac{p\,(x,y,z)}{\rho c^2} &= -\frac{4ju_d}{c} \sum_{n=1}^{\infty} \sum_{m=1}^{\infty} \frac{k}{k_{xnm}} \epsilon_n \epsilon_m \left(\frac{(-1)^n - 1}{(n\pi)^2} \right) \left(\frac{(-1)^m - 1}{(m\pi)^2} \right) \cdots \\ & \times \cos\left(\frac{n\pi y}{L_y} \right) \cos\left(\frac{m\pi z}{L_z} \right) \frac{\sin\left(k_{xn}\left(x - L_x\right)\right)}{\cos\left(k_{xn} L_x\right)}, \end{aligned} \tag{2.26}$$

where ϵ_n and ϵ_m represent the predefined function ϵ as explained in Eq. (2.21) in Section (2.4.3), and associated with the transverse directions, y and z indicated by the two mode indices, n and m. Note that only the cut-on modes will be dominant, so the summation can be terminated for the cut-off modes. Cut-off modes have:

$$\left(\frac{n\pi}{L_y} \right)^2 + \left(\frac{m\pi}{L_z} \right)^2 > k^2. \tag{2.27}$$

Figure 2.17 shows the pressure variation along the length of a $3D$ uniform duct with hard-walled boundary conditions along the interior boundaries and non-uniform excitation.

Once again in Fig. 2.17 the pressure variation along the length of the *TLL* duct can be analyzed as the frequency increases similar to the cases in Fig. 2.12 and Fig. 2.14. As the frequency progresses and the wavelength of the propagating sound shortens, a greater number of full-wavelengths can

---

[9] The derivation of acoustic pressure for a $3D$ case with hard-walled boundary conditions is an extension to the derivation of Eq. (2.19) in Chapter 2.

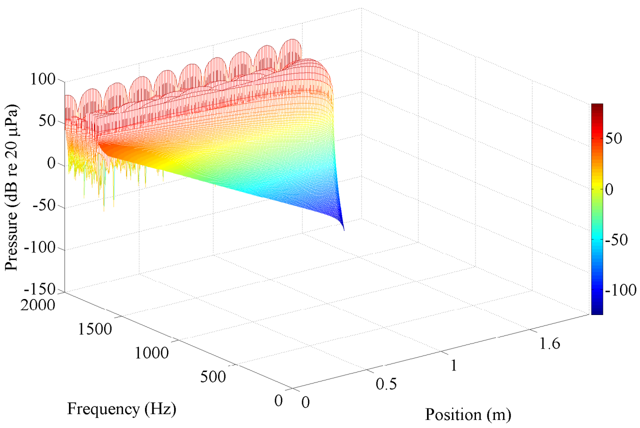

FIGURE 2.17: Pressure variation along the length of the duct (x-*axis*), of a $3D$ case with hard-walled boundary conditions and non-uniform excitation.

be observed to propagate within the pipe. Also, at low-frequencies a much more pronounced and very steep natural decay of the sound pressure amplitude along the length of the duct can be observed with the lowest magnitude at the 1.6 m length of the duct which is due to the assumption of a pressure-release boundary condition at the open end of the duct in conjunction with the non-uniform excitation in a $3D$ duct which causes the excitation of higher order modes, which invariably pushes the decay envelope to a higher frequency range than that in Fig. 2.12 and Fig. 2.14.

2.4.6 Case 5: $2D$ Duct, Locally-Reacting Boundary Condition and Pistonic Excitation

Next, there is a $2D$ duct as in cases 1 and 3, but with locally-reacting (LR) lined-walls (BC)at $y = 0$ and $y = L_y$, where the dimensionless admittance has been defined as $A_i = \rho c/Z_i$ [45]. Here Z_i is the wall impedance Z with index i, and the pressure is $p(x, y)e^{j\omega t}$. Figure 2.18 shows the schematic model of a $2D$ case with locally-reacting walls and a pressure-release boundary condition and an open end.

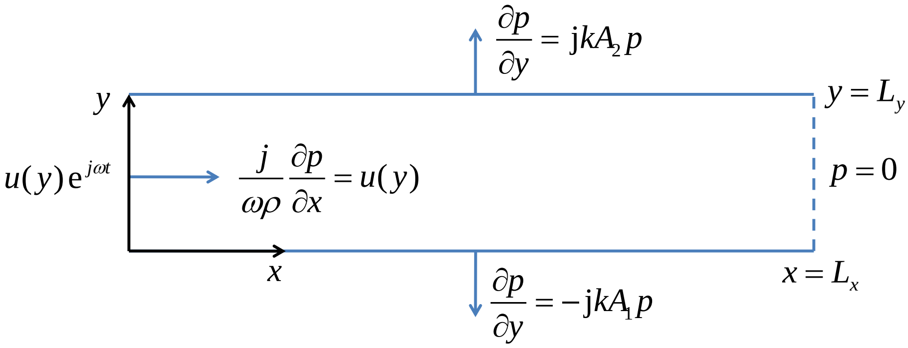

FIGURE 2.18: $2D$ duct with locally-reacting walls and a pressure-release boundary condition at the open end.

2.4.7 Eigenvalues

There exists an infinite set of transverse eigenvalues k_{yn}, which are solutions to the equation [46]:[10]

$$\left(k_{yn} + \frac{k^2 A_1 A_2}{k_{yn}}\right) \sin\left(k_{yn} L_y\right) + jk\left(A_1 + A_2\right)\cos\left(k_{yn} L_y\right) = 0. \quad (2.28)$$

It should be noted that all of the eigenvalues are complex, therefore only those which have a positive real part and a negative imaginary part have been considered.

---

[10] The transcendental Eq (2.28) is been solved numerically in Chapter 3 and its result has been implemented into the numerical models to get the p_0 at the $x = 0$ driver position and u_l at the $x = L_x$ open end of the TLL.

2.4.8 Axial Wavenumbers

For each of the transverse eigenvalues k_{yn}, there is a unique axial wavenumber k_{xn} given by:

$$k_{xn} = \left(k^2 - k_{yn}^2\right)^{1/2}. \tag{2.29}$$

All of the wavenumbers are also complex. The square root has been defined such that they all have a positive real part and a negative imaginary part. There is no longer a clear cut-off condition; all modes contain a decay factor. Now suppose there is pistonic excitation such as $u(y) = u_d$, at the driver position $x = 0$ with a constant value. Therefore, the pressure field can be described as [47]:

$$\frac{p(x,y)}{\rho c^2} = -j \sum_{n=0}^{\infty} \frac{k}{k_{xn}} \frac{L_y}{\Phi_n} F_n \phi_n(y) \frac{\sin\left(k_{xn}\left(x - L_x\right)\right)}{\cos\left(k_{xn} L_x\right)}, \tag{2.30}$$

where $\phi_n(y)$ is described by:

$$\phi_n(y) = \cos\left(k_{yn} y\right) - \frac{jkA_1}{k_{yn}} \sin\left(k_{yn} y\right), \tag{2.31}$$

where A_1 is the dimensionless surface admittance along the *x-axis* from $x = 0$ to $x = L_x$, as illustrated in Fig. 2.18, and the normalization factor Φ_n is:

$$\Phi_n = \int_0^{L_y} \left|\phi_n(y)\right|^2 dy, \tag{2.32}$$

and F_n is defined by:

$$F_n = \frac{u_d}{L_y c} \int_0^{L_y} \phi_n(y) dy. \tag{2.33}$$

It is worth mentioning that Eq. (2.30) describing the internal pressure along the length of the *TLL* ducts has been solved numerically and described in detail in Chapter 3.

2.4.9 Case 7: $2D$ Duct, Locally-Reacting Boundary Condition and Non-Uniform Excitation

Suppose $u(y)$ is a non-uniform excitation. Therefore the pressure field is the same as Eq. (2.30) for case 5 with pistonic excitation in Section 2.4.6. It is also worth mentioning that $\phi_n(y)$ is the same as Eq. (2.31) as in case 5 and the normalization factor Φ_n is also the same as Eq. (2.32) as mentioned previously in Section 2.4.6. However, F_n can be defined by:

$$F_n = \frac{1}{L_y c} \int\limits_0^{L_y} u(y)\phi_n(y)dy. \tag{2.34}$$

Table 2.2 describes different cases of treated *TLL* waveguides, cases 1 to 4 of have been explained in Sections 2.4.2 to 2.4.5 which deal with the *TLL* ducts with the hard-walled boundary conditions on their internal boundaries. Sections 2.4.6 and 2.4.9 explain cases 5 and 7, of Table 2.2, where cases 5 to 9 look into the case where the pressure fields within the *TLL* ducts have been treated with the locally-reacting liners. These have been added to this chapter for the purpose of completeness, since the bulk-reacting sound absorbing materials have far superior acoustical properties in terms of the absorption of the unwanted sound pressures. Therefore, the optimized transmission-line loudspeakers are acoustically treated with the bulk-reacting sound absorbing liners due to the better acoustical performance of the bulk-reacting liners in comparison to the locally-reacting treatments. However, instead of looking into the cases 9 to 12 analytically and iteratively solving the transcendental equations describing the internal pressure along the length of the *TLL* ducts for cases 9 to 12, they have been solved numerically and are described in Chapter 3.

2.5 Conclusion

In Chapter 2, the lump parameter model of the loudspeaker driver and the background theory of *TLL* ducts were introduced in Sections 2.1 and 2.2 respectively. Next, in Section 2.3, lined waveguides were looked at. The investigation continued with the analytical models of waveguides in

Section 2.4, and different possible scenarios were introduced in Table 2.2. The detailed analytical models of cases 1 to 5 and 7 from Table 2.2 have been looked at, and the pressure variation along the length of the *TLL* duct for cases 1 to 4 have been plotted in Sections 2.4.2, 2.4.3 and 2.4.5 respectively. In Chapter 3, the pressure field for the remaining cases in Table 2.2, have been looked at using the standard numerical techniques within the *COMSOL Multiphysics* environment through a series of developed numerical models.

Chapter 3

Numerical Models of *TLLs*

Standard numerical techniques within the *COMSOL Multiphysics* environment have been used to investigate the characteristics of sound propagation within a range of treated ducts. The modelling procedure in the *COMSOL* software is controlled through the *model builder* window, which includes a model tree with all the functionality and operations for building and solving the numerical models as well as displaying and exporting the results [18].

The numerical results were initially validated against the results of the analytical models for the basic cases of sound propagation within a *TLL*, since the analytical models look into the basic forms of the ducts, namely uniform straight ducts, with a variety of acoustic treatments, hard-walled and locally-reacting sound absorbing liners, and a variety of source excitations, namely pistonic and non-uniform excitation, as explained in detail in Chapter 2. Therefore, the numerical models begin with the investigation of some of the basic *TLL* ducts for the purpose of comparison and validation with the analytical results from Chapter 2.

The numerical predictions progress to more complicated cases of the ducts, namely L-shaped and U-shaped, lined on the interior boundaries with bulk-reacting acoustic liners. The results of these complicated cases were then compared with the in-situ measurement results. The in-situ tests were conducted on the similar cases of ducts treated with the same sound absorbing materials as described in detail in Chapter 4 using a variety of measurement techniques and microphone probes from *Microflown Technologies.*

3.1 Numerical Models of *TLL*

Beginning with the hard-walled case of different duct shapes, namely straight, L-shaped and U-shaped ducts, the numerical models advance to modelling of the same ducts treated with locally-reacting and bulk-reacting sound absorbing liners. The $3D$ duct geometries under consideration, straight, L-shaped and U-shaped ducts, have been drawn using the *Solidworks* $3D$ drawing package. The $3D$ geometries then have been transferred to the *COMSOL Multiphysics* environment using the function *live-link interface for Solidworks.* Next, using the function *form union* within *COMSOL* each waveguide geometry was unified. The sound absorbing materials of interest within the scope of this project have been assigned to the internal boundaries of each duct geometries. Within the scope of this project, the acoustic characteristics of a range of fibrous and porous sound absorbing materials were investigated as outlined in Tables 4.1 and 4.2 in Chapter 4, Section 4.1. The numerical models were designed with the aim of characterizing the sound propagation within a variety of treated *TLL* ducts. Therefore, the relevant physics, *pressure acoustics*, within *COMSOL* was selected for the purpose of these analyses. Two separate pressure acoustic models were added into the physics of the numerical models in *COMSOL.* One model to predict the sound propagation within the free acoustic medium and another pressure acoustics model for prediction of sound behaviour within the sound absorbing layer of the ducts. Next, the boundary conditions of different surfaces inside and outside the *TLL* ducts were specified depending on their location, where each boundary behaves as a *sound-hard-boundary* also known as the hard-walled boundary condition, such as all the external and internal layers of the duct, or a *sound-soft-boundary* also known as the pressure-release boundary condition, where the pressure is zero, such as the open end of the *TLL* waveguide. Therefore $p(x, \omega) = 0 \mid_{x=L_x}$, since the *TLL* waveguide experiences a sudden expansion in its cross sectional area. In the numerical models, the *TLL* driver was specified as a piston with the normal inwards acceleration, selecting one-end of the *TLL* duct [48, 49]. Depending on the numerical model, either a uniform acceleration as a pistonic source of excitation or a non-uniform source of excitation was chosen, as outlined in Table 2.2 and based on the analytical models developed in Chapter 2, Section 2.4.3 and represented in Eq. (2.18) and illustrated in the schematic Fig. 2.13.

3.1.1 Modelling Porous Materials

Depending on the numerical model, whether it is designed to model the sound propagation in a lined-duct treated with porous or fibrous materials, the first pressure acoustic model (which predicts the behaviour of propagation within the lined section of the duct) was set differently [50–52]. For the case when the duct is treated with the porous materials the coefficient of *Wu Qunli* were used in the fluid model of *COMSOL* for the *macroscopic empirical models* based on the paper by *Wu* [27]. The specific flow-resistivity per unit thickness, σ values, were measured at the Centre of Acoustic-Liner Technology of *Alenia Aermacchi* and have been added in the *COMSOL* models [53]. The values for density ρ and speed of sound c have been set to be taken from the material at 20°C. The temperature has been defined as 293.15 K and the absolute pressure as 10^5 Pa. The pressure acoustics model 1 is based on the following equation [18]:

$$\nabla . \frac{-1}{\tilde{\rho}} \left(\nabla p - \mathbf{q} \right) - \frac{\tilde{k^2} p}{\tilde{\rho}} = Q, \tag{3.1}$$

where $\nabla = \frac{\partial}{\partial x}\hat{\imath} + \frac{\partial}{\partial y}\hat{\jmath} + \frac{\partial}{\partial z}\hat{k}$ is the three dimensional Cartesian coordinates, $\tilde{\rho}$ is the air density defined by Eq. (3.3). The total pressure is defined as $p = p_0 + p'$, where p_0 is the ambient pressure and p' is the unsteady component of the pressure, $\mathbf{q}$ is the dipole source, Q is the monopole source. The acoustic wavenumber is defined as $\tilde{k^2} = (\omega/\tilde{c})^2$, where ω is the angular frequency and $\tilde{c}$ is the speed of sound. Therefore [18]:

$$\tilde{c} = c \left(1 + C_1 \left(\rho \frac{f}{\sigma} \right)^{-C_2} - jC_3 \left(\rho \frac{f}{\sigma} \right)^{-C_4} \right)^{-1}, \tag{3.2}$$

and

$$\tilde{\rho} = \frac{\rho c}{\tilde{c}} \left(1 + C_5 \left(\rho \frac{f}{\sigma} \right)^{-C_6} - jC_7 \left(\rho \frac{f}{\sigma} \right)^{-C_8} \right), \tag{3.3}$$

where f is the frequency, $C_1 - C_8$ are the constants and σ is the flow-resistivity. These equations, which describe the *pressure acoustics model* within the *COMSOL* environment, are based on the *Delany and Bazley* model in their paper [54]. It should be noted that the parameters $\tilde{\rho}$, $\tilde{c}$ and $\tilde{k^2}$ in Eqs (3.1), (3.2) and (3.3) could contain complex values and therefore they have been denoted by ($\tilde{}$) [31]. In modelling the treated *TLL* with the porous materials, the coefficients C_1 to C_8 have been taken from the *Wu Qunli's* model [27, 52, 55]. Table 3.1 shows the comparison between the two different coefficient values of *Wu Qunli* and *Delany and Bazley* which were used in the numerical models of the porous and fibrous materials respectively [27].[1]

Coefficients	*Wu Qunli*	*Delany and Bazley*
C_1	0.188	0.0978
C_2	0.554	0.700
C_3	0.163	0.189
C_4	0.592	0.595
C_5	0.209	0.0571
C_6	0.548	0.754
C_7	0.105	0.087
C_8	0.607	0.732

TABLE 3.1: Comparison of coefficients of *Wu Qunli* with *Delany and Bazley.*

Next, the imported geometries within *COMSOL* environment was meshed. The *free-tetrahedral* elements conform best to any random geometry and therefore have been chosen for this purpose. The size of the elements had to be small enough to resolve the highest frequency of interest so that any characteristic behaviour in the sound propagation could be observed and analyzed. Next, in the *study setting* of the numerical models, the frequency range of interest and its distribution steps were specified to be 20 to 1000 Hz, with the distribution of a single frequency. In the *compile equation* of the solver section, the frequency domain of the pressure acoustic models were chosen to be studied. The *relative tolerance* of the

---

[1] This table is courtesy of *Wu Qunli* from the paper [27].

models was set and optimized in the stationary solver, which controls the rate of divergence by setting the termination of the iterative solver processes for the direct linear system solvers. Finally, In the *memory allocation factor*, the amount of memory used by the computers and the type of solver were chosen to be 1.2 Gbit and *MUMPS* solver respectively, which controls directly the computational cost function. The *MUMPS* solver refers to the parallel sparse direct linear solver and it stand for the *MUltifrontal Massively Parallel sparse direct Solver*, which works on general systems of the form $Ax = b$ and is designed for the solution of large sparse systems of linear algebraic equations on distributed memory parallel computers. The software implements the multifrontal method, which is a version of Gaussian elimination for large sparse systems of equations, especially those arising from the *finite element method* (*FEM*). The *FEM* uses subdivision of a whole problem domain into simpler parts, called finite elements, and variational methods from the calculus of variations to solve the problem by minimizing an associated error function. Analogous to the idea that connecting many tiny straight lines can approximate a larger circle, *FEM* encompasses methods for connecting many simple element equations over many small subdomains, named finite elements, to approximate a more complex equation over a larger domain. The subdivision of a whole domain into simpler parts has several advantages such as accurate representation of a complex geometry, inclusion of dissimilar material properties, easy representation of the total solution and capturing the local effects within a complex geometry. The *MUMPS* solver uses several preordering algorithms to permute the columns and thereby minimize the fill-in. The *MUMPS* solver is multithreaded on platforms that support multithreading and also supports solving on distributed memory architectures and it includes out-of-core capabilities which can minimizes the internal memory usage of the computer [18].[2] Other modelling options including *boundary element method* (*BEM*) where the modelling is concentrating on the surface boundaries of the object under consideration, and therefore can not resolve the characteristic of sound propagation within the free-region of a *TLL* waveguide such as that in this project,

---

[2] The information regarding the *MUMPS* solver is courtesy of *COMSOL Multiphysics* help base on the COMSOL version 4.2a.

or *finite-difference time-domain* (*FDTD*) which is mainly used for modelling computational electrodynamics were also considered, but finally the *MUMPS* solver which uses the *FEM* was chosen.

3.1.2 Modelling Fibrous Materials

For the case when the duct is treated with the fibrous materials the coefficients of *Delany and Bazley* were implemented in the fluid model of *COMSOL* for the *macroscopic-empirical-models* based on their paper [54]. The specific flow-resistivity, σ values, of the fibrous samples, were measured at the Centre of Acoustic-Liner Technology of *Alenia Aermacchi* and have been used to create the required R_f values in Pa s m^{-2} in *COMSOL*. The values for density ρ, and speed of sound c, were set to be taken from the materials. Temperature has been defined as 293.15 K and absolute pressure as 10^5 Pa. The governing equations and the rest of the procedure was the same as for the case of porous sound absorbing materials and follows the same sequence as Eqs (3.1), (3.2) and (3.3).

3.1.3 Meshing Comparison

One of the important considerations in numerical modelling is the meshing of the geometry under consideration. Apart from controlling the frequency resolution of the numerical predictions, the size of the meshed elements has a direct effect on the computational cost-function. After comparing different meshing methods, such as *free-tetrahedral*, *swept-and-mapped*, as illustrated in Figs 3.1 and 3.2. Finally, the *free-tetrahedral* node meshing method was chosen to create the unstructured tetrahedral mesh [18]. The numbers, sizes and distributions of the elements were controlled by first choosing the *user-controlled mesh* system and then directly controlling the *size* and *distribution* subnodes functions in the numerical models. Using the *geometric-entity-level* function the area of each geometry was set for the specific meshing size and methods. The geometric domains, where the unstructured tetrahedral mesh have been created were defined using the *domain-selection* function in the *COMSOL* environment. In order to keep the numerical models accurate and robust, the *entire-geometry* option was set to create the unstructured *free-tetrahedral* mesh for the entire geometry, and the computational cost-function of the models are manageable for any ordinary computer when the models are meshed with the maximum resolution. The mesh quality can be conclusively determined based on the following factors within a numerical model. Starting with *rate of convergence*, the greater the rate of convergence, the better the mesh quality, which is an indication that the correct solution has been achieved faster. An inferior mesh quality may leave out certain important phenomena such as the boundary layer that occurs in fluid flow. In this case the solution may not converge or the rate of convergence will be impaired. Next, *solution accuracy*, a better mesh quality provides a more accurate solution. For example by refining the mesh at certain areas of the geometry where the gradients are high, thus increasing the fidelity of solutions in the region. On the other hand, if a mesh is not sufficiently refined then the accuracy of the solution is more limited. Thus, mesh quality is dictated by the required accuracy. Finally *CPU time required*, which is a necessary and yet undesirable factor. For a highly refined mesh, where the number of cells per unit area is at maximum, the CPU time required will be relatively large. Therefore, time will generally be proportional to the number of elements.

3.1.4 Scaling the Geometry

To scale the geometry during the meshing operation, the *x-scale*, *y-scale*, and *z-scale* of the imported geometries were set to positive real numbers. If any of the scale factors were not equal to one, the software scales the geometry in the x, y, and z directions before meshing; after meshing, it restores the geometry and the meshed element to fit the original size [18]. Figure 3.1 shows the comparison between the *free-tetrahedral* mesh and the *swept-and-mapped* mesh along the length of the straight duct in *z-axis*.

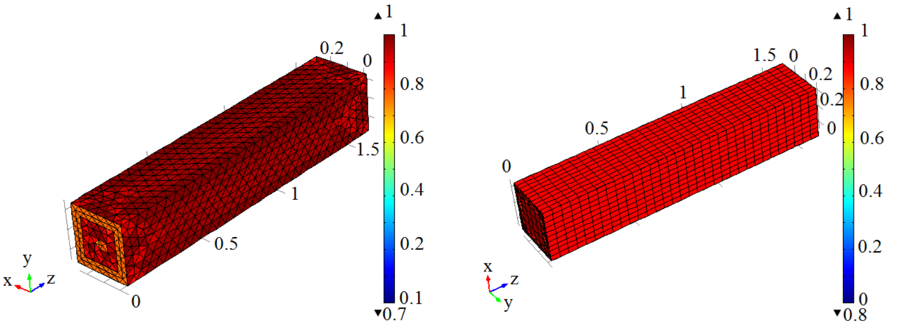

(a) (b)

FIGURE 3.1: Comparison of different meshing methods. (a) *Free-tetrahedral* and (b) *swept-and-mapped* meshing.

The scaling factors allow the generation of meshes that are anisotropic, and it is useful if the mesh generator creates many elements due to a thin geometry or if the mesh generation fails due to large aspect ratios in the geometry [18]. One of the first thing to consider in meshing is how to break the geometry into small pieces. There are different standard meshing techniques, but one of the most commonly used methods is the *free-tetrahedral*. As can be seen in Fig. 3.1 (a) the elements along the length of the duct have a tetrahedral setup whereas in Fig. 3.1 (b) the elements across the length of the *TLL* have a rectangular structure. Figure 3.2 shows the comparison of different meshing techniques, namely *free-tetrahedral* and *swept-and-mapped*, and meshing resolution (mesh-size) on the cross sections of transmission-line waveguides considered in this research.[3]

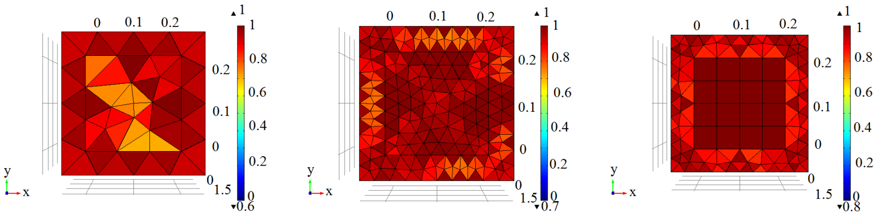

(a) (b) (c)

FIGURE 3.2: Comparison of cross section of different mesh size. (a) *Free-tetrahedral* mesh, (b) extra-fine *free-tetrahedral* mesh and (c) *swept-and-mapped* meshing method.

It has to be mentioned that in the *swept-and-mapped* method, first the cross section of the duct was meshed. The sound absorbing layer was meshed using the *free-triangular* meshing, and the free-region of the duct was mapped such that each node was located exactly on the position of the microphone during the in-situ measurements on the same duct, hence creating a matrix structure of 5 by 5 elements. Next the same pattern as the meshed cross section was swept through the whole structure of the duct. It can also be observed in Fig. C.7 in Appendix C, that in the *swept-and-mapped* method of meshing, the geometry of the elements along the length of the duct is rectangular whereas in the *free-tetrahedral* meshing method the geometry of elements is unstructured tetrahedral meshes. It was finally decided that for the numerical model under consideration the benefit of using the *swept-and-mapped* method in minimizing the computational cost-function is negligible. Hence, the more numerically accurate choice, the *free-tetrahedral* meshing, was chosen and carried forward for the rest of the numerical modelling. The unstructured *free-tetrahedral* meshing with a small enough element is proven to conform best to any random geometry, hence improving the accuracy of the numerical predictions.

---

[3] The detailed numerical results of different meshing methods have been added to Appendix C.

3.1.5 Relative Tolerance of Models

Another important factor in the computational cost-function of the numerical models is *relative-tolerance* which controls the speed of the divergence in the numerical model. The *relative-tolerance* has an adverse effect on the computational cost-function. As it decreases the computational cost-function increases and therefore it had to be optimized such that it does not compromise the accuracy of the numerical predictions and yet keeps the computational cost-function under control.

3.2 Comparison of Numerical Predictions and Analytical Models

Starting with the comparison of the pressure variation at the three different positions at the centre points of the cross section of the *TLL* waveguide, this investigation moves to the comparison of the numerical and analytical results. As explained in Section 2.4.1 the *TLLs* have 1.6 m length with the hard-walled boundary conditions with a pistonic excitation with unit-velocity and pressure-release boundary condition at the open end of the waveguides, unless it is been stated otherwise in the description of a specific figure. Figure 3.3 shows the comparison of the analytical results for the pressure variation at the centre points of the cross section for three different positions, namely drive-unit $x = 0$, halfway in the middle of the *TLL* $x = L_x/2$ and at the open end of the straight duct $x = L_x$.

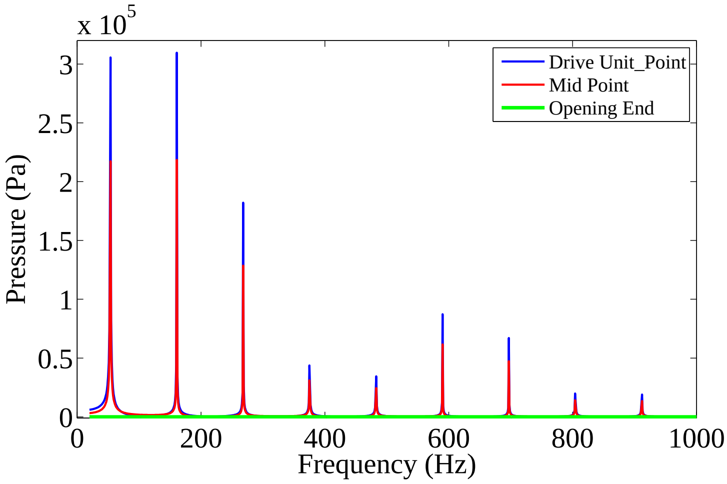

FIGURE 3.3: Comparison of analytical results at three different positions at the centre points across the cross-section of a straight duct. Drive-unit position $x = 0$ (*blue line*), middle of *TLL* along the length $x = L_x/2$ (*red line*) and the open end of the waveguide position $x = L_x$ (*green line*).

As can be seen in Fig. 3.3 the pressure amplitudes representing the driver (blue line) and middle positions (red line) decay as the frequency progresses; with the driver position having a higher amplitude than the middle position as expected, since it is located directly in front of the excitation source in the duct. The assumption of the pressure-release boundary condition causes the pressure variation at the open end to be a constant zero $p = 0 \mid_{x=L_x}$. Figure 3.4 shows the comparison of analytical and numerical results at centre points of the cross section positions at the drive-unit, half-way in the middle of the *TLL*, end of the waveguide and along the centre line of a straight *TLL* duct.

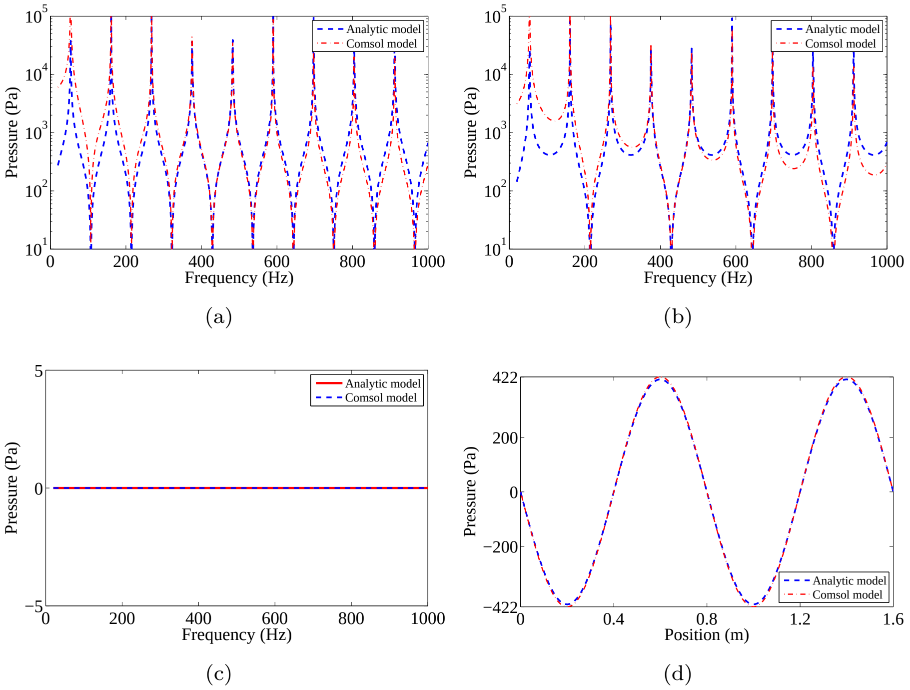

(a) (b)

(c) (d)

Figure 3.4: Comparison of the analytical and numerical results in a straight duct. (a) Drive-unit position, (b) middle of duct, (c) end of duct and (d) along the centre line of the duct length. Analytical results (*dashed line*) and *COMSOL* results (*dot dashed line*).

It can be seen from the results in Fig. 3.4 that the presented numerical model is capable of correctly predicting the characteristics of sound propagation behaviour within the *TLL* waveguide with hard-walled boundary conditions and pistonic excitation.

3.3 Case 10: $3D$ Straight Duct, Bulk-Reacting Boundary Condition and Pistonic Excitation

Next, the two-dimensional results of the pressure fluctuation along the length of the acoustically treated straight duct, excited with the pistonic source can be observed in Fig. 3.5 below, which is case 10 in Table 2.2. Figure 3.5 shows the results of a numerical model of pressure variation along the length of the straight duct, lined with a bulk-reacting liner sample $RG50/135$ (pink foam), for frequencies 100, 200, 300, 400, 600, 700, 800 and 900 Hz.

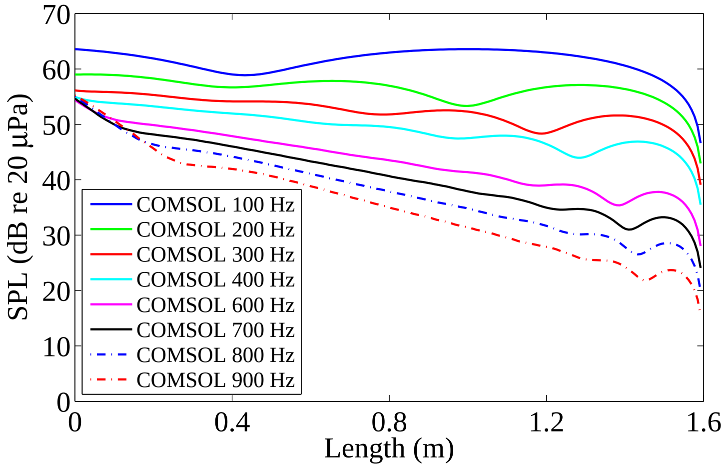

FIGURE 3.5: Numerical results of pressure variation, along the length of a straight duct, treated with sample $RG50/135$, for frequencies 100, 200, 300, 400, 600, 700, 800 and 900 Hz.

As expected Fig. 3.5 shows that the pressure variations decay along the length of the waveguide; also their amplitudes drop considerably as the frequency progresses [56]. There is almost a 25 dB decrease in the amplitude of the 600 Hz (solid pink line) in comparison to the 100 Hz (solid blue line) at 0.8 m, half way along the length of the *TLL* waveguide. It can be concluded that from 400 Hz onwards a lined duct with this size ($0.3 \times 0.3 \times 1.6$ m height by width by length), and this amount of sound absorbing materials ($0.3 \times 0.15 \times 1.6$ m height by width by length), experiences a high absorption along the duct, behaving as a low-pass acoustic filter, which confirms the general theory of the transmission-line loudspeakers. Also the pressure variation at all the frequencies tends to zero at the open end of the ducts which is due to the assumption of a pressure-release boundary condition in the numerical models. Figure 3.6 shows the comparison of numerical predictions for the sound pressure variation along the length of a straight *TLL* duct, lined with the bulk-reacting liners, sample *RG*50/135 (pink foam) and *RX*33/160 (green foam), for the frequencies 63, 125, 250, 500 and 1000 Hz.

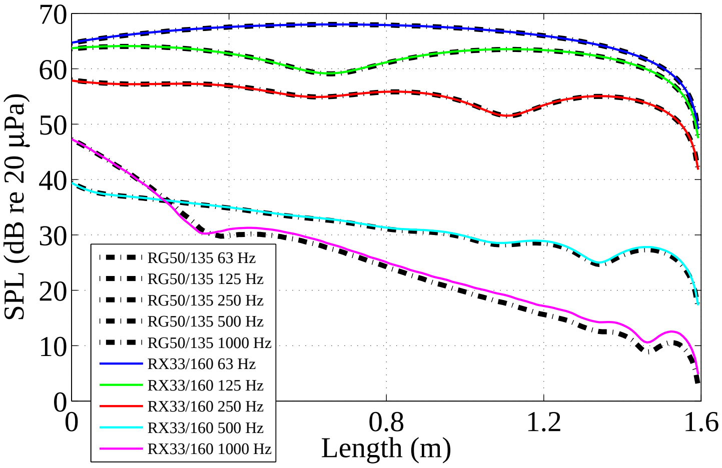

FIGURE 3.6: Comparison of numerical predictions of pressure variation along the length of a straight duct lined with samples *RG*50/135 (pink foam) (*dot dashed line*) and *RX*33/160 (green foam) (*solid line*), along the length, for frequencies 63, 125, 250, 500 and 1000 Hz.

It can be seen in Fig. 3.6 that the numerical predictions of the straight *TLL* duct lined with the same amount of two different sound absorbing materials, sample *RG*50/135 (pink foam) or *RX*33/160 (green foam), follows the same pattern and has almost the same values for the range of frequencies presented with the similar absorption pattern along the duct length, and there is no sudden change in the sound pressure variations along the length of the duct as the frequency progresses.

3.4 Straight Duct Models

Next, the numerical models are used to analyse the straight ducts with different internal boundary conditions along the interior boundaries of the waveguide. Figure 3.7 shows the duct geometry and the meshed element size of the straight duct, meshed with the unstructured *free-tetrahedral* method. At the cross section of the duct two triangles can also be observed, which represent the drive-unit of the *TLL* duct.

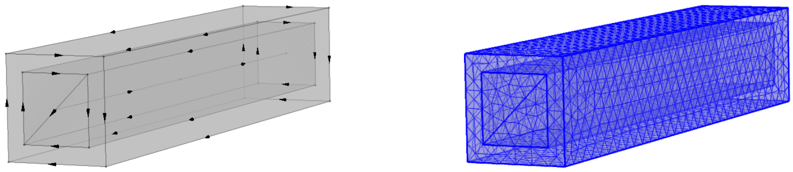

(a)

(b)

FIGURE 3.7: Straight duct. (a) Duct geometry and (b) size of the elements meshed with unstructured *free-tetrahedral* method.

A uniform layer of sound absorbing liner has been added to the internal boundaries along the length of the duct creating a layer wrapped around the free-region of the duct. There are two distinct regions that can be observed in Fig. 3.7: (1) the free-medium region in the centre of the duct which is filled with air and has two triangles at the beginning of the duct cross section representing the rolling piston motion as described in Eq. (2.24) in Section 2.4.5, and (2) a region representing the sound absorbing layer with a uniform thickness wrapped around the free-medium region. Figure 3.8 shows the acoustic pressure level variation along the length of the straight *TLL* duct, lined on the inside with the bulk-reacting acoustic liner, sample $RG50/135$, excited with a non-uniform excitation source, presented for the frequencies 300 and 1000 Hz respectively.[4]

It can be observed in Fig. 3.8 that the non-uniform excitation with unit-velocity at the driver-end has been modelled with a particular case of

---

[4] The detailed numerical results of straight duct models have been added to Appendix B.

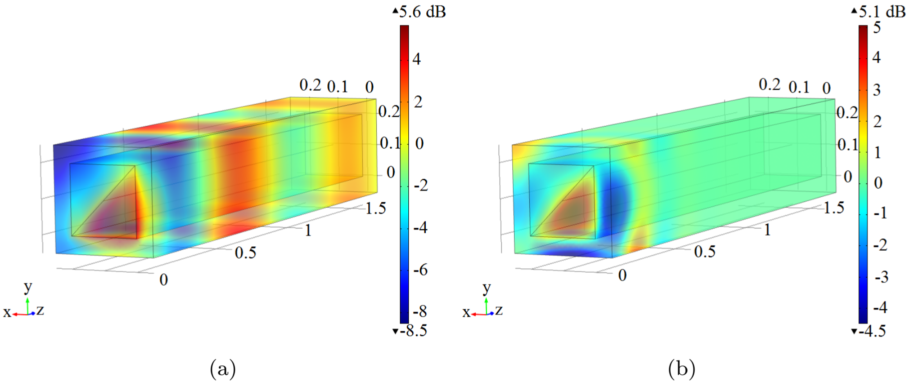

(a) (b)

FIGURE 3.8: Sound pressure level variation along the length of straight duct, with a non-uniform excitation, treated with sample *RG*50/135. (a) 300 Hz and (b) 1000 Hz.

excitation which has been chosen to excite a large number of modes within the *TLL* as described in Eq. (2.24) in Section 2.4.5, where one of the two triangles of the rolling piston has a positive normal acceleration while the other triangle is at rest. It can also be seen, as the frequency advances and the wavelength of the sound propagating shortens, in Fig. 3.8 (b) that the pressure variation along the duct tends to zero after a short distance away from the drive-unit (sound source in the duct). Figure 3.9 shows the isosurface acoustic pressure level variation along the length of the straight duct, lined with the bulk-reacting acoustic liner, sample *RG*50/135, excited with a non-uniform excitation source, presented for frequencies 200 and 300 Hz respectively.[5]

Once again in Fig. 3.9 all the features previously mentioned for the sound pressure level variation in Fig. 3.8, can be seen here but are more pronounced. A distinct triangular region of high-pressure illustrated with the dark-red colour in the isosurface plot, which represents the *TLL* driver as described in Eq. (2.24) in Section 2.4.5, can be observed to be wrapped by a region of low-pressure, which propagates through the waveguide. As mentioned in Sections 3.1.3 and 3.1.4, meshing is one of the most important considerations of any numerical modelling. The quality of the meshed structure with regards to the geometry under consideration and the frequency range of interest has been determined by the *COMSOL* environment and is presented in Fig. 3.10 below for the case of a straight

---

[5] The detailed numerical results of straight duct models have been added to Appendix B.

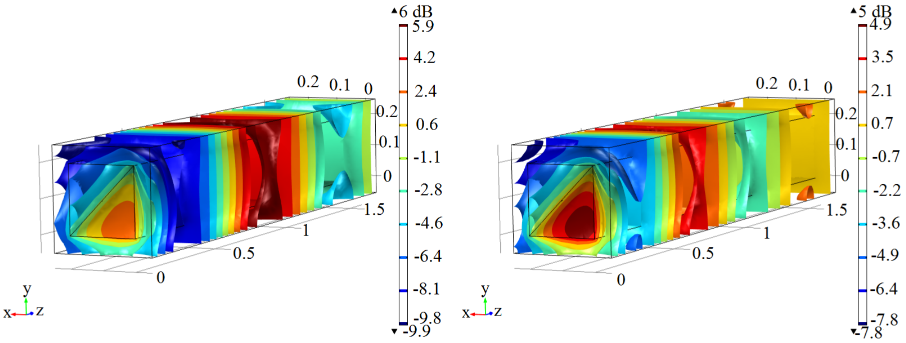

(a) (b)

FIGURE 3.9: Isosurface sound pressure level variation along the length of straight *TLL* duct, with non-uniform excitation at the driver-end, treated with sample *RG*50/135 (pink foam). (a) 200 Hz and (b) 300 Hz.

TLL duct, acoustically treated with the bulk-reacting sample *RG*50/135, excited with a non-uniform source. Figure 3.10 shows the mesh quality along the length and the cross section of the straight duct, lined with bulk-reacting liner sample *RG*50/135 (pink foam), with non-uniform excitation.

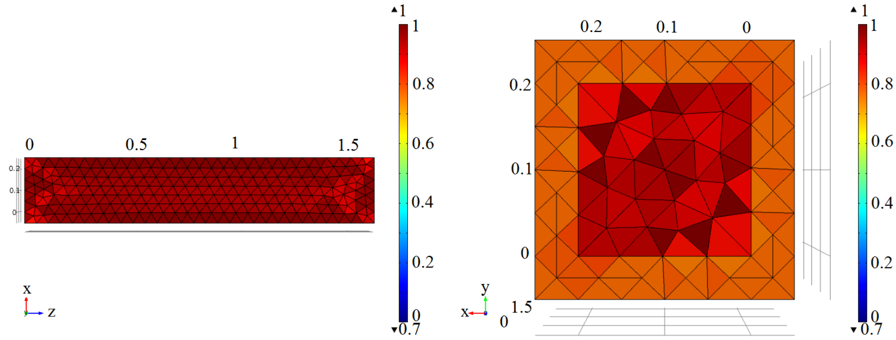

(a) (b)

FIGURE 3.10: Mesh quality along the length and the cross section of a straight duct, with non-uniform excitation, treated with sample *RG*50/135.

The quality of the meshed structure with regards to the geometry under consideration and the frequency range of interest has been determined by the *COMSOL* environment and has been presented in Fig. 3.10, for the case of straight duct, acoustically treated with the bulk-reacting sample *RG*50/135, excited with a non-uniform source.

3.5 L-Shaped Duct Models

The numerical results advance to consider the L-shaped duct. A uniform layer of sound absorbing liner has been added to the internal boundaries of the duct creating a second region wrapped around the free-medium, air region of the duct. Figure 3.11 shows the L-shaped duct geometry wire frame, with its drive-unit cross section which consist of two triangles, as well as duct centre line and the internal and external elements mesh size.

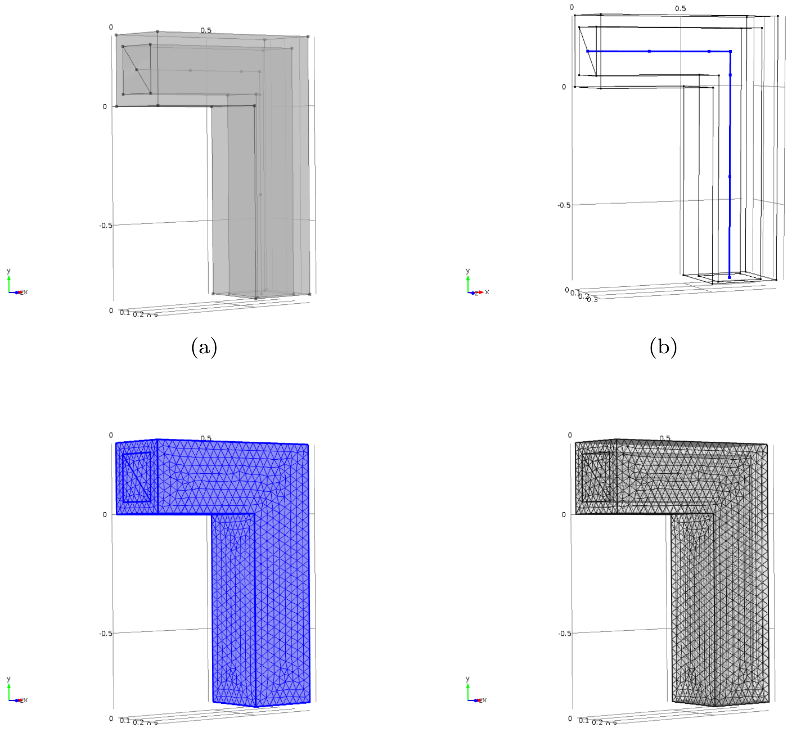

(a) (b) (c) (d)

FIGURE 3.11: L-shaped duct. (a) Duct geometry wire frame, (b) duct centre line, (c) external elements mesh size and (d) internal elements mesh size.

A uniform layer of sound absorbing liner has been added to the internal boundaries along the length of the duct creating a layer wrapped around the free-region of the duct. There are two distinct regions that can be observed in Fig. 3.11 (a): (1) the free-medium region in the centre of the duct which is filled with air and has two triangles at the beginning of the duct cross section representing the rolling piston motion as described in

Eq. (2.24) in Section 2.4.5, and (2) a region representing the sound absorbing layer with a uniform thickness wrapped around the free-medium region. Figure 3.12 shows the acoustic pressure level variation along the L-shaped duct, with a non-uniform excitation, lined with bulk-reacting sound absorbing liner sample $RG50/135$ at frequency 200 Hz.[6]

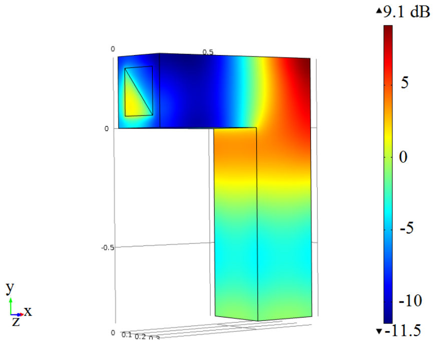

FIGURE 3.12: Variation of sound pressure level along the length of an L-shaped duct, with a non-uniform excitation at the driver-end, treated with the sample $RG50/135$ at 200 Hz.

A high-pressure region at the bend of the L-shaped duct can be observed at 200 Hz, in Fig. 3.12, with the concentration at the corner of the bend. Figure 3.13 shows the isosurface sound pressure level variations along the length of the L-shaped duct, lined with a bulk-reacting liner sample $RG50/135$, with a non-uniform excitation, at the frequencies 118 and 190 Hz.

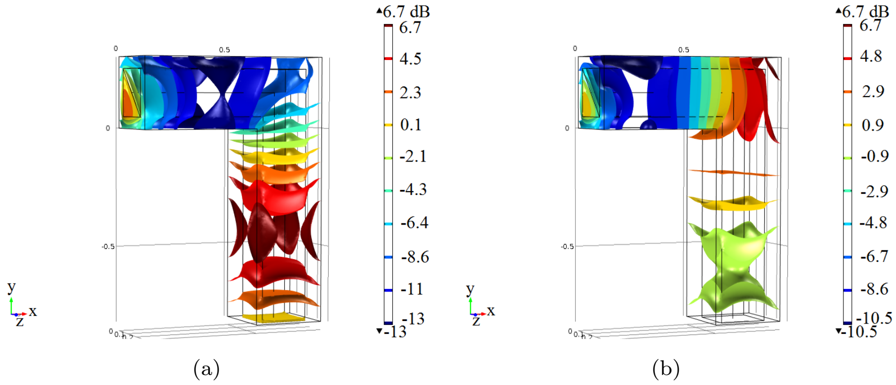

(a) (b)

FIGURE 3.13: Variation of isosurface sound pressure level along the length of an L-shaped *TLL* duct, with a non-uniform excitation, treated with the sample $RG50/135$. (a) 118 Hz and (b) 190 Hz.

---

[6] The detailed numerical results of L-Shaped duct models have been added to Appendix B.

In Fig. 3.13 the isosurface sound pressure level variations at 118 Hz and 190 Hz can be seen with more pronounced features. Figure 3.14 shows the mesh quality along the length and the cross-section of the L-shaped duct, lined with a bulk-reacting liner sample $RG50/135$ (pink foam), with a non-uniform excitation.

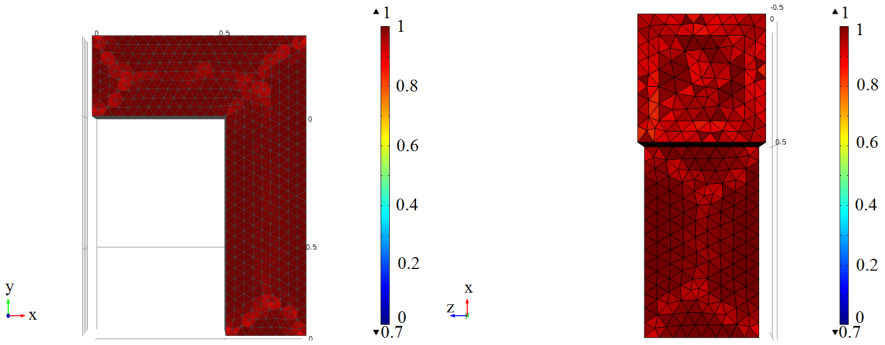

(a)

(b)

FIGURE 3.14: Mesh quality of an L-shaped duct treated with the bulk-reacting liner sample $RG50/135$ (pink foam), with a non-uniform excitation. (a) Duct length and (b) duct cross-section.

The quality of the meshed structure with regards to the geometry under consideration and the frequency range of interest has been determined by the *COMSOL* environment and has been presented in Fig. 3.14, for the case of an L-shaped *TLL* duct, acoustically treated with the bulk-reacting sample $RG50/135$, excited with a non-uniform source at the driver-end of the duct.

3.6 U-Shaped Duct Models

The numerical results advance to consider the U-shaped duct. A uniform layer of sound absorbing liner has been added to the internal boundaries of the duct creating a second region wrapped around the free-medium, air region of the duct. Figure 3.15 shows the U-shaped duct geometry wire frame, with its drive-unit cross section which consist of two triangles, as well as duct centre line and the internal and external elements mesh size.

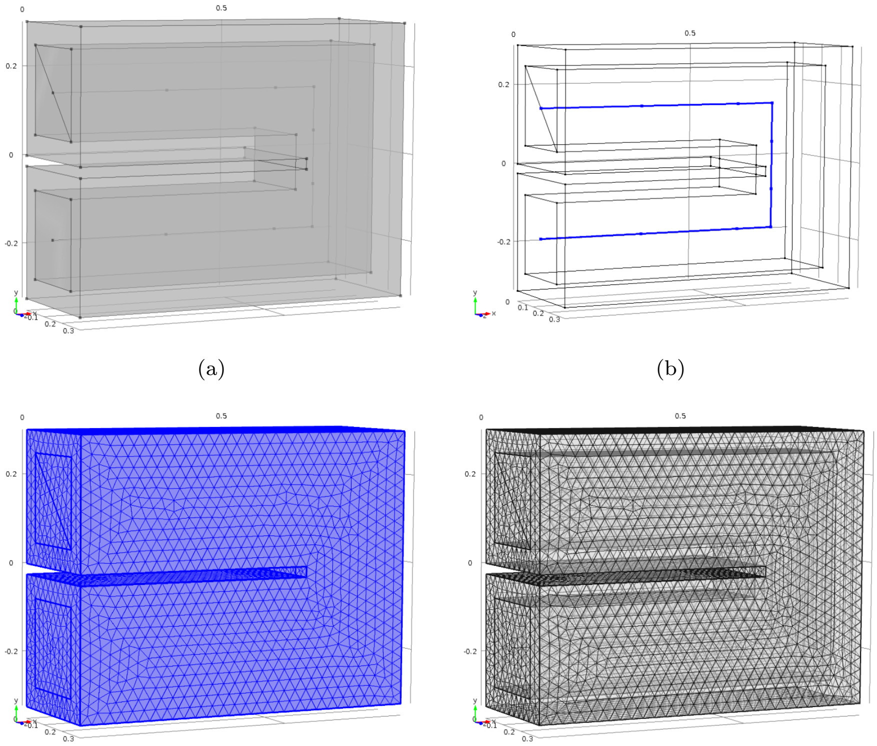

(a) (b)

(c) (d)

Figure 3.15: U-shaped duct. (a) duct geometry wire frame, (b) duct centre-line, (c) external elements mesh size and (d) internal elements mesh size.

As in Fig. 3.11 (a) there are once again two distinct regions that can be observed in Fig. 3.15 (a): (1) the free-medium region in the centre of the duct and (2) a region representing the sound absorbing layer with a uniform thickness wrapped around the free-medium region. Figure 3.16 shows the U-shaped duct geometry, normal accelerations 1 and 2, sound soft boundary, acoustic pressure models 1 and 2 respectively.

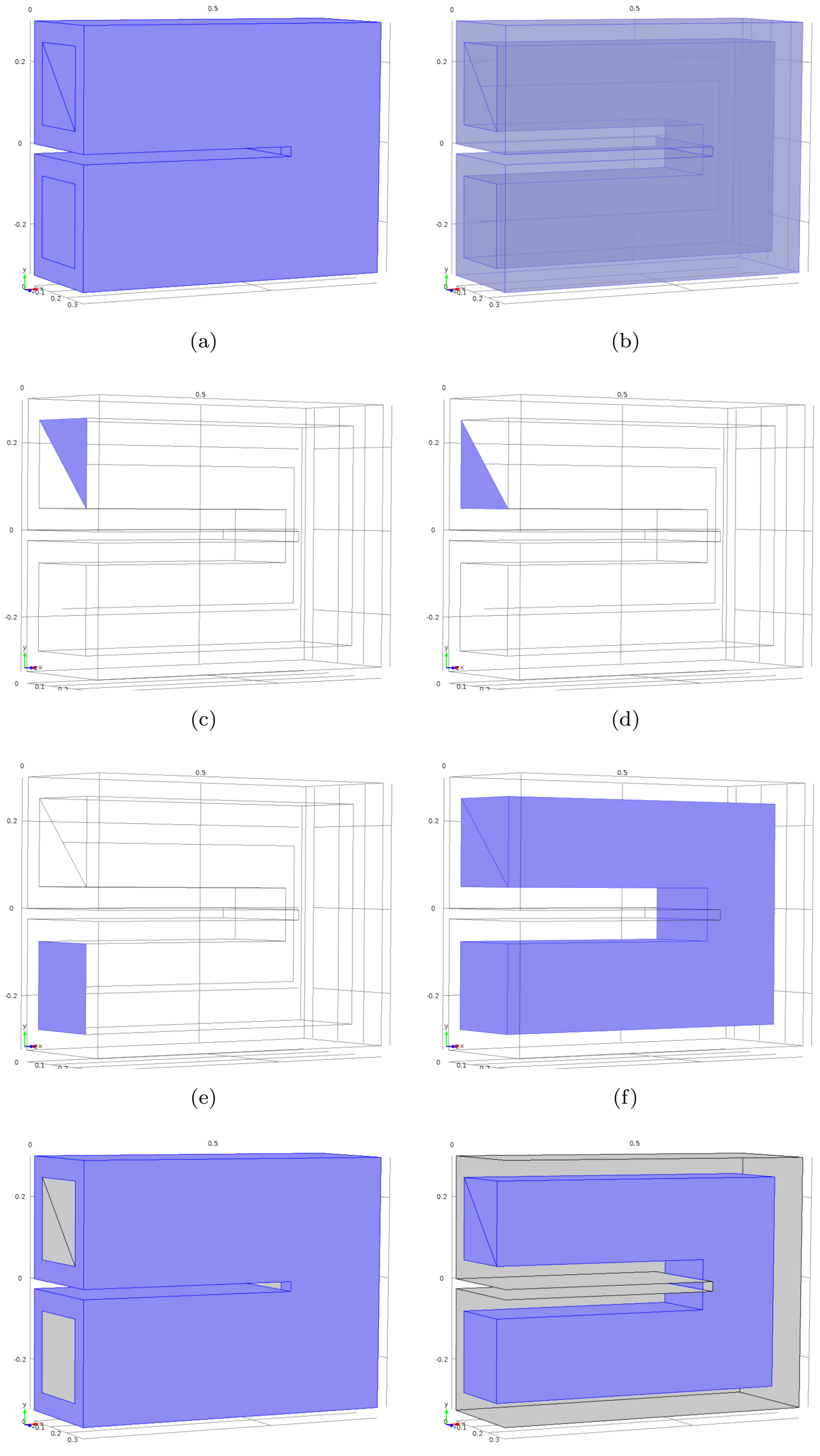

(a) (b)

(c) (d)

(e) (f)

(g) (h)

FIGURE 3.16: (a) U-shaped duct, (b) acoustic pressure model 1 and 2, (c) normal acceleration (rolling piston), (d) normal acceleration (rolling piston), (e) sound soft boundary condition (open end of the duct), (f) free-region of duct, (g) sound absorbing layer, and (h) combination of free-region and sound absorbing layer.

The U-shaped duct geometry can be seen in Fig. 3.16 (a) where the pressure acoustic regions of the U-shaped duct, one and two, within the *COMSOL* environment can be observed in Fig. 3.16 (b), (f), (g) and (h). The *TLL* drive-unit represented by a rolling piston, containing two triangles can also be observed in Fig. 3.16 (c) and (d). Finally, the open end of the U-shaped duct can be seen in Fig. 3.16 (e). Figure 3.17 shows the acoustic pressure level variation along the U-shaped duct, with a non-uniform excitation at the driver-end, lined on the interior boundaries with the bulk-reacting sound absorbing liner sample *RG*50/135 (pink foam), at the frequency 260 Hz.[7]

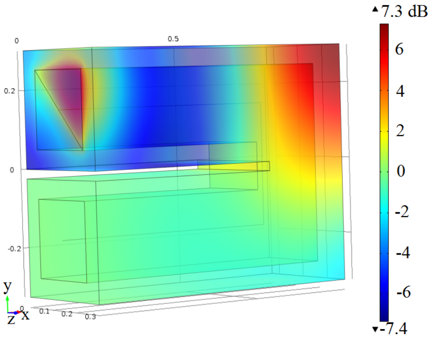

FIGURE 3.17: Variation of sound pressure level along the length of a U-shaped duct with a non-uniform excitation, treated with sample *RG*50/135 at 260 Hz.

The acoustic pressure level propagation within the U-shaped duct can be observed in Fig. 3.17 with a high-pressure region at the top corner of the bend of the U-shaped *TLL* at 260 Hz, with the concentration at the top corner of the bend. Figure 3.18 shows the isosurface acoustic pressure level variation along the length of the U-shaped duct, lined on the interior boundaries with the bulk-reacting acoustic liner sample *RG*50/135 (pink foam), with a non-uniform excitation, for a selected frequencies 180 Hz and 310 Hz.

In Fig. 3.18 the isosurface acoustic pressure level variation along the length of the U-shaped duct at 180 Hz and 310 Hz can be seen with more pronounced features. In Fig. 3.18 (a) the duct is accommodating the propagation of a full wavelength within its length, from driver position

---

[7] The detailed numerical results of U-Shaped duct models have been added to Appendix B.

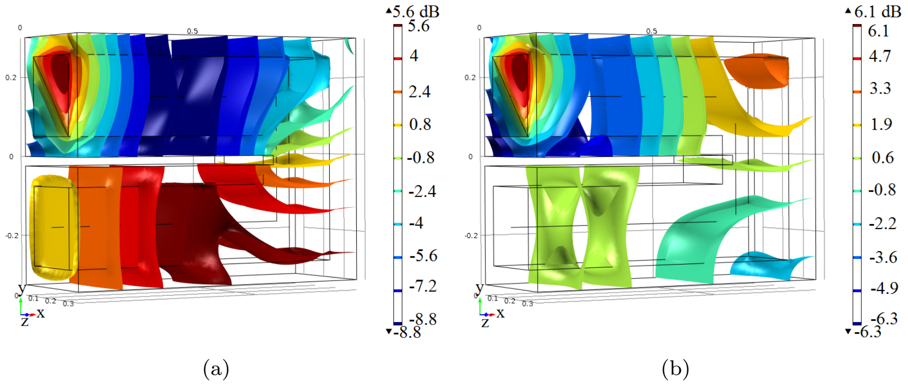

(a) (b)

FIGURE 3.18: Variation of isosurface sound pressure level along the length of a U-shaped *TLL* with non-uniform excitation, treated with sample *RG*50/135. (a) 180 Hz and (b) 310 Hz.

at $x = 0$ to the open end at $x = L_x$, where the first half of the duct length is accommodating a low-pressure region and the second half of the duct length is a high-pressure region. As the frequency progresses in Fig. 3.18 (b), a high-pressure region at the top corner of the bend can be observed with the pressure concentration at the top corner of the *TLL* and in the bottom corner a low-pressure region concentrated on the bottom corner can be observed. Figure 3.19 shows the mesh quality along the length of the U-shaped duct (side view), with a non-uniform excitation, lined with the bulk-reacting liner sample *RG*50/135.

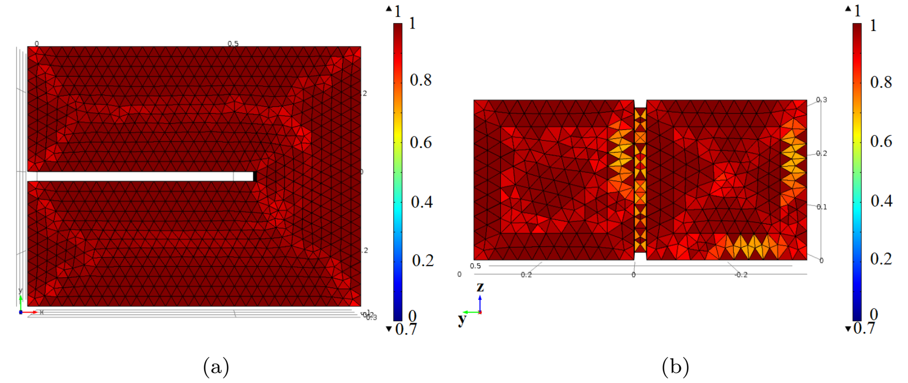

(a) (b)

FIGURE 3.19: Mesh quality along the length of the U-shaped duct with a non-uniform excitation, treated with sample *RG*50/135.

The quality of the meshed structure with regards to the geometry under consideration and the frequency range of interest has been determined by the *COMSOL* environment and is presented in Fig. 3.19, for the case of a

U-shaped *TLL* duct, acoustically treated with the bulk-reacting sample $RG50/135$, excited with a non-uniform source.

3.7 Modelling Limitation

There is a number of factors that contribute to the limitations of the numerical models. First, the $3D$ geometries under consideration, which are being drawn using *SolidWorks* $3D$ drawing package. There are many known and documented problems in transferring the $3D$ geometries between the *SolidWorks* and *COMSOL* environments. The drawing capability of the *COMSOL* package is quite limited and therefore a more versatile drawing environment, *SolidWorks*, has been used to offer more comprehensive controls over the $3D$ geometries drawn for the purpose of this project. However, the lines and parts of the imported geometries into the *COMSOL* software are numbered automatically by *COMSOL* and sometimes in a non-sequential order. This in turn creates problems when trying to evaluate the geometry under the consideration along those connected lines or parts. The numerical models use the results of a number of different measurements, one of which is the flow-resistivity, (σ) values, which is inserted for the R_f values in the *COMSOL* and therefore any inaccuracy in those data supplied by the Centre of Acoustic-Liner Technology *Alenia Aermacchi* will directly affect the accuracy of the numerical models. Another measurement result used in the presented numerical models are the coefficients of *Delany and Bazley* [54] used for the modelling of the fibrous absorbing materials and the coefficients of *Wu Qunli* [27] used for the modelling of porous absorbing materials. These measurements of the coefficients of *Delany and Bazley* or *Wu Qunli*, were conducted a long time ago with the measurement limitations of their own time and any inaccuracy of those experimental data will again directly affect the outcome of the numerical models presented here. In order to keep the computational cost-function of the presented models as low as possible, a pressure-release boundary condition has been assumed for the modelling of sound propagation at the open end of the duct. For the correct modelling of the open end however, the *TLL* should have been placed in a large cube, representing the listening room in which the *TLL* would be used; large enough to accommodate at least three or four full-wavelengths of the lowest-frequency of interest, 20 Hz, for the purpose of audio applications, and it should use the *model definition* of *perfectly matched layer* within the *COMSOL* environment instead of the *sound soft boundary* representing the pressure-release boundary condition for the open end of the duct. However, by adding this to the models, the size to aspect ratio would become considerably larger and in order to maintain the same modelling resolution the computational cost-function would increase considerably, which has been avoided in the models presented. It should also be noted that the pressure-release boundary condition is an acceptable and accurate approximation for the low-frequency range of interests as is the case in this project.

3.8 Conclusion

In this chapter, the numerical model of the transmission-line loudspeakers have been looked at in Section 3.1. The acoustic characteristics of sound propagation within the porous and fibrous absorbing materials were numerically modelled in Sections 3.1.1 and 3.1.2 respectively. Next, different meshing methods were compared in Section 3.1.3, and the scaling method of the geometries under consideration and the effect of relative tolerance on the computational cost-function were introduced in Sections 3.1.4 and 3.1.5 respectively. The numerical results of a straight duct with hard-walled boundary conditions were compared with the analytical models in Section 3.1.3. The acoustic pressure variation along the length of the straight duct treated with the bulk-reacting liner with pistonic excitation, which is case 10 in Table 2.2, has been analyzed in Section 3.3. Finally, different duct shapes, namely straight, L-shaped and U-shaped treated with bulk-reacting sound absorbing materials with a non-uniform excitation, which is case 12 of Table 2.2, were analyzed in Sections 3.4, 3.5 and 3.6 respectively. In Chapter 4 the numerical method has been benchmarked against measurement results, and it has been shown that the method can correctly predict the acoustic coupling between both the free-medium and the sound absorbing layer. However, there are a number of factors that increase the inaccuracy of numerical predictions. The assumption of a pressure-release boundary conditions at the open end of the *TLL* ducts contributes to the lack of complete accuracy between the numerical prediction and the in-situ measurements at that region of the duct, as discussed in detail in Section 3.7. The more comprehensive numerical model, however, should consider the end-correction for the duct by placing the *TLL* into a room, at least three or four times bigger than the size of the full-wavelength of the lowest-frequency of interest, and it should use the *model definition* of a *perfectly matched layer* within the *COMSOL* environment instead of the *sound soft boundary* representing the pressure-release boundary condition for the open end of the duct. The next assumption in the numerical model was that the driver motion at the low-frequency can be modelled as a uniform pistonic movement. Therefore, a uniform pistonic excitation was considered as the excitation source for the driver of the *TLL* in the numerical analysis. The uniform pistonic excitation of *COMSOL* models was later replaced by the lumped parameter model of the driver described in Chapter 2 to accurately predict the behaviour of the driver at the low-frequency which was the frequency range of interest in this project. However, numerical models capable of designing the transmission-line loudspeakers for the audio applications, should include the full audible frequency range 20 to $20k$ Hz. Therefore the driver modelling can no longer be satisfied by employing the lumped parameter model of the driver, since the lumped parameter model can only accurately predict the driver behaviour in the low-frequency range. Therefore, instead a full numerical driver model should be added to the models of the *TLL*.

Chapter 4

Experiments on *TLLs*

In this chapter, the analytical and numerical models presented in the previous Chapters 2 and 3 respectively, have been validated with direct measurements conducted on a variety of treated waveguides in order to get the internal sound pressure and three-dimensional acoustic-intensity along the length of the *TLL* ducts. The experimental validation began with carefully selecting a range of bulk-reacting sound absorbing materials, namely fibrous and porous absorbing materials, to be used for lining the internal boundaries of a range of ducts, namely straight and U-shaped ducts, built for the validation purpose.

Using the impedance-tube in the *ISVR* laboratory, impedance measurements were conducted on the selected range of fibrous and porous sound absorbing samples. The impedance data were then compared with the *Delany and Bazley* [54] and *Wu Qunli* [27] methods which were applied to the flow-resistivity measurements of the same range of fibrous and porous materials respectively, and conducted in the Centre of Acoustic-Liner Technology of *Alenia Aermacchi* in *Italy* using a DC-flow test, and have been used in Chapter 3 to construct the numerical models of the treated *TLL*.

Finally, a variety of microphone probes, namely *PU-match* and *USP-regular*, from *Microflown Technologies* were used to directly measure the in-situ sound pressure and three-dimensional acoustic-intensity inside a range of waveguides treated with a variety of bulk-reacting liners that had been previously selected and verified.

4.1 Sound Absorbing Samples

The sound absorbing characteristics of the selected range of the bulk-reacting liners were measured with a series of tests. Figure 4.1 shows the selected range of fibrous and porous sound absorbing materials used in lining the interior boundaries of a variety of *TLL* waveguides [57].

FIGURE 4.1: Sound absorbing samples. Samples are *RX*30/080, *RX*33/160, *RX*33/190, *RX*39/200, *RX*41/150, *RG*50/100, *RG*50-/135, *RG*50/230 and *needled felt - F1O*.

Tables 4.1 shows the range of porous materials selected for lining the internal boundaries of the constructed *TLL* waveguides.

	Sample Code	*Colour*	*Thickness* [m]	*Density* [kg m^{-3}]	*Hardness* [N m^{-2}]
1	*RX*30/080	*Light-Blue*	0.048	30	80
2	*RX*33/160	*Green*	0.051	33	160
3	*RX*33/190	*Aqua*	0.054	33	190
4	*RX*39/200	*Sky-Blue*	0.051	39	200
5	*RX*41/150	*Grey*	0.050	41	150
6	*RG*50/100	*Gold*	0.051	50	100
7	*RG*50/135	*Pink*	0.051	50	135
8	*RG*50/230	*White*	0.051	50	230

TABLE 4.1: Porous materials selected for lining the ducts.

The sample codes of each of the porous materials contains the information regarding its density, *Young's modulus* (hardness) and its chemical composition codes which can be seen in Table 4.1. The first two letters of each sample code represent the chemical composition code of that material. Samples with two different chemical compositions, namely *RX* and *RG*, were chosen and can be observed in Table 4.1 [50]. There are two sets of numbers in each sample code which represent the density and the Young's modulus of the samples respectively. The first two digits or the first set of numbers represent the density and the last three digits or second group of numbers represents the Young's modulus of each of the porous materials. Table 4.2 shows the range of fibrous materials selected for lining the internal boundaries of the constructed *TLL* waveguides.

	Sample Name	*Code*	*Colour*	*Thickness* [m]	*Density* [kg m^{-3}]
1	*Needled-Felt*	*F1O*	*Black/Blue*	0.008	17.75
2	*Cotton-Felt*	*F1B*	*White*	0.042	4.1
3	*Polyester-Wrap*	*S6B*	*White*	0.0255	10.04
4	*Polyester-Wrap*	*S6C*	*White*	0.014	42.64

TABLE 4.2: Fibrous materials selected for lining the ducts.

The fibrous samples are manufactured with different thicknesses. In order to have flow-resistivity data consistent and comparable with those of the porous samples measured, the fibrous materials were all rearranged to have 0.051 m thickness prior to the DC-flow tests. Physical characteristics such as the specific flow-resistivity per unit thickness, surface normal impedance, reflection coefficient and magnitude of absorption coefficient of the samples, were found using the DC-flow tests and impedance-tube measurements respectively. Accurate flow-resistivity measurements requires a fully calibrated DC-flow rig. The DC-flow tests were therefore performed by the external collaborator at the Centre of Acoustic-Liner Technology of *Alenia Aermacchi* in *Italy.* The flow-resistivity values were measured for a range of flow-speed as shown in Tables 4.3, 4.4 and 4.5 in Section 4.4. The flow-resistivity data, σ values, of the selected range of fibrous and porous sound absorbing samples were then combined with either the *Delany and Bazley* [54] or the *Wu Qunli* [27] coefficients and their corresponding methods respectively, for the cases of the *TLL* ducts lined on their internal boundaries with the fibrous or porous samples, and compared with the impedance-tube measurements, conducted in the

ISVR laboratory. The measured flow-resistivity data were used to construct the numerical models presented in Chapter 3 which models the sound propagation within a variety of hard-walled cases and treated *TLL* [58]. Finally, in Chapter 4, the numerical predictions of treated *TLL* waveguides from Chapter 3 have been compared and validated with the direct measurement results of the sound pressure and 3*D* sound-intensity measured in-situ on a variety of treated *TLL* ducts.

4.2 Surface Normal Impedance of Sound Absorbing Samples

Surface normal impedance, absorption coefficient and magnitude of reflection coefficient for a range of fibrous and porous materials were measured using an impedance-tube in the *ISVR* laboratory. *ISO* 10534 specifies a method for the determination of the sound absorption coefficient, reflection factor and surface impedance or surface admittance of materials and objects and this procedure was followed [59].[1] Figure 4.2 shows the *ISVR* impedance-tube test rig.

FIGURE 4.2: *ISVR* impedance-tube test rig.

The Impedance-tube rig used in the measurements has a length of $l = 1$ m and cross sectional diameter of $\varnothing = 0.1$ m. The impedance values of the

---

[1] *BS EN ISO* 10534-1:2001 *"Acoustics – Determination of sound absorption coefficient and impedance in impedance tubes – Part 1 Method using standing wave ratio"*.

samples were determined for the surface normal sound incidence by evaluating the standing wave pattern of the plane-wave propagating inside the tube, which was generated by the superposition of an incident sinusoidal plane-wave, with the plane-wave reflected from the test object [60–62]. This method can be used for the determination of the sound absorption coefficient of sound absorbers with the normal sound incidence [61]. In using the impedance-tube, the wavenumbers are $k = 2\pi f/c$, where f is the frequency parameter of the sound signal and c is the speed of sound in the medium. Therefore the reflection coefficient of the samples R_s, can be found using:

$$R_s = \frac{e^{jkx_1} - He^{jkx_2}}{He^{-jkx_2} - e^{-jkx_1}}, \tag{4.1}$$

where x_1 and x_2 are the first and second locations of the microphone inside the impedance-tube respectively. The transfer function H can be expressed as $H = H_1/H_2$, which is the ratio of the transfer functions H_1 and H_2, corresponding to x_1 and x_2, the microphone locations inside the impedance-tube duct. Therefore the impedance of the sample Z_s becomes:

$$Z_s = \frac{1 + R_s}{1 - R_s}. \tag{4.2}$$

The absorption coefficient of the samples α_s also becomes:

$$\alpha_s = 1 - |R_s|^2. \tag{4.3}$$

By rearranging Eq. (4.2) the real part of the sample impedance R can be found to be:

$$R_s = \frac{Z_s - 1}{Z_s + 1}, \tag{4.4}$$

now combining $Z_s = R + jX$ with the Eqs (4.4) and (4.3) gives the following expression for the absorption coefficient of the samples α_s:

$$\alpha_s = \frac{4R}{(1 + R^2) + X^2}. \tag{4.5}$$

This method can further be used for the determination of the acoustical surface impedance or surface admittance of the sound absorbing materials [63]. The impedance-tube method is well suited for parameter studies and for the design of sound absorbers, because only a small sample of the absorber materials is needed which should be the size of the cross-sectional area of the impedance-tube duct [50]. There are some characteristic differences between this method and the measurement of sound absorption in a reverberation room based on *IS*0 354 [64].[2] The impedance tube-method can be used for the determination of the reflection factor and also the impedance or admittance of the samples. In the impedance-tube measurement the sound incident is normal to the test object surface whereas for the reverberation room method the sound incidents arrive at the test object at random angels of incidents. The reverberation room method will, under idealized conditions, determine the sound absorption coefficient of the samples for random sound incidences. The impedance-tube method on the other hand relies on the existence of a plane incident sound wave and gives exact values under this condition (measuring and mounting errors excluded). The evaluation of the sound absorption coefficient in a reverberation room is based on a number of simplifying and approximate assumptions concerning the sound-field and the size of the absorber under consideration. Consequently sound absorption coefficients exceeding the value of 1 are sometimes obtained using the reverberation room method. Figure 4.3 shows the magnitude of the reflection coefficient of a range of porous and fibrous absorbing materials which have been measured respectively using the impedance-tube of the *ISVR*.

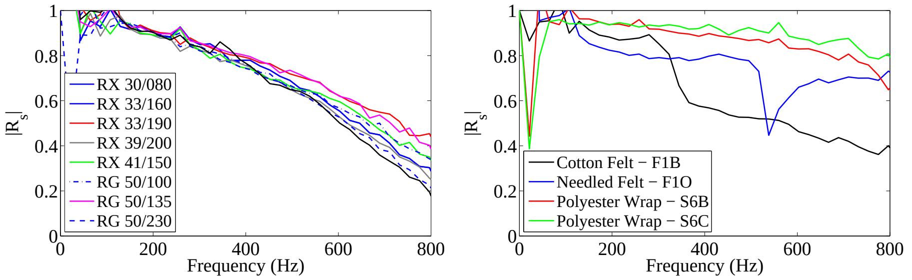

(a) (b)

FIGURE 4.3: Magnitude of reflection coefficient of a selected range of sound absorbing materials. (a) Porous samples: *RX*30/080, *RX*33/160, *RX*33/190, *RX*39/200, *RX*41/150, *RG*50/100, *RG*50/135 and *RG*50/230 and (b) fibrous samples: *needled felt - F1O*, *cotton felt - F1B*, *polyester wrap - S6B* and *polyester wrap - S6C*.

---

[2] *BS EN ISO* 354:2003 *"Acoustics – Measurement of sound absorption in a reverberation room"*.

The magnitude of the reflection coefficients of a range of porous materials can be observed in Fig. 4.3 (a) and it can be seen that they all follow the same pattern of decrease in their magnitude with increasing frequency. In Fig. 4.3 (b) fibrous samples *polyester wrap - S6B*, *polyester wrap - S6C* and *needled felt - F1O* shows a similar decrease of their magnitude of reflection coefficients except for a trough in the frequency range of 515 – 640 Hz in the response of the *needled felt - F1O* which could be associated with an error such as sudden increase of the noise floor which had occurred during the measurement of that particular sample. The *cotton felt - F1B* sample shows a much more pronounced decrease from the frequency of 320 Hz onwards which could be associated with high absorption of that particular sample above that frequency, otherwise it follows the same pattern as the rest of the fibrous samples. Figure 4.4 shows the absorption coefficients for a range of porous and fibrous absorbing materials respectively measured in the impedance tube of the *ISVR*.

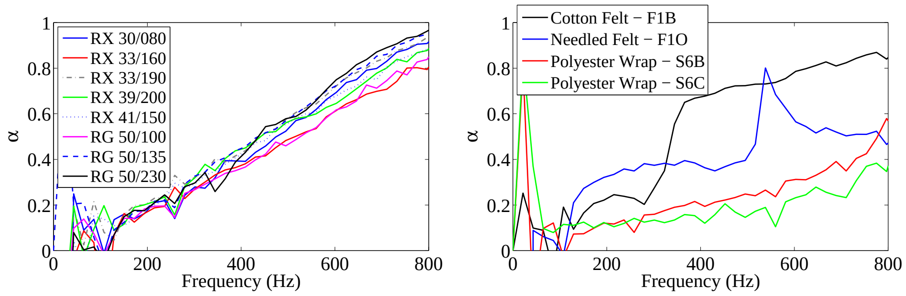

(a)

(b)

FIGURE 4.4: Absorption coefficient of a selected range of sound absorbing materials. (a) Porous samples $RX30/080$, $RX33/160$, $RX33/190$, $RX39/200$, $RX41/150$, $RG50/100$, $RG50/135$ and RG-$50/230$ and (b) fibrous samples *needled felt - F1O*, *cotton felt - F1B*, *polyester wrap - S6B* and *polyester wrap - S6C*.

It can be seen from Fig. 4.4 (a) that all porous samples follow the same pattern similar to the case for the magnitude of reflection coefficients of the samples in Fig. 4.3 (a). The porous samples, exhibit a gradual increase in their absorption coefficient as the frequency advances. In Fig. 4.4 (b) fibrous sample *polyester wrap - S6B*, *polyester wrap - S6C* and *needled felt - F1O* shows a similar increase of their absorption coefficients except for a peak in the frequency range of 515 to 640 Hz in the response of the *needled felt - F1O* which could be associated with an error such as a sudden increase of the noise floor which had occurred during the measurement of that particular sample. The *cotton felt - F1B* sample shows much more increase from the frequency of 320 Hz onwards which could be associated with high absorption of that particular sample above that frequency, otherwise it follows the same pattern as the rest of the fibrous samples.

4.3 Flow-Resistivity of Samples

Specific flow-resistivity per unit thickness of the same range of fibrous and porous sound absorbing materials were found.[3] The samples were cut into cylinders of $\varnothing = 0.1$ m in diameter, which is the internal diameter of the flange of the DC-flow rig. The samples were then sent to the Centre of Acoustic-Liner Technology of *Alenia Aermacchi* in *Italy.* The test was done using the *Aermacchi's* DC-flow test rig *Raylometer-tube*, to measure the flow-resistivity per unit thickness of the sound absorbing samples. Figure 4.5 shows the *Aermacchi* DC-flow rig. The flange of the *Raylometer-tube* is loaded with sample of porous material [53].[4]

FIGURE 4.5: *Aermacchi* DC-flow rig loaded with porous sample.

The air flow was pumped into a monitored tube with the controlled pressure and velocity, in a controlled environment. The regularized air then

---

[3] Resistivity is equal to resistance per unit thickness of the sound absorbing samples.

[4] Picture is courtesy of *Alenia Aermacchi*, Centre of Acoustic-Liner Technology. $http://www.aleniaaermacchi.it$

passes through the flange which contains the sample of sound absorbing material. The air was pumped downstream and the air pressure was measured before and after it passed through the sample of sound absorbing materials. The whole system is completely calibrated and controlled by computer. The difference in the air pressures, before and after it has passed over each of the sound absorbing samples, is then divided by the air flow-speed to give the flow-resistivity value for that specific air velocity for each of the different materials [65]. The flow-resistivity per unit thickness $\sigma = \Delta p/u$ is measured in MKS Rayls at the specified increasing flow-speeds in m s^{-1} relative to the two different measurements performed on each side of each of the absorbing samples (two surfaces areas 1 and 2 of each sample). This was performed by inserting each sample twice from each side into the *Raylometer-tube*. Figure 4.6 shows the *Aermacchi* DC-flow rig.[5]

FIGURE 4.6: *Aermacchi*DC-flow rig.

The flow-resistance of the samples are corrected to standard environmental conditions, for the temperature of 21.11°C and the atmospheric

---

[5] Picture is courtesy of *Alenia Aermacchi*, Centre of Acoustic-Liner Technology. *http : //www.aleniaaermacchi.it*

pressure of 1013.25 mbar. The air velocity is regulated at certain speeds and with certain intervals, which in turn gives the value for the flow-resistivity per unit thickness of each sample at that particular flow-speed. At a high flow-speed of $u = 3$ m s^{-1} the differential pressure transducer was sometimes subjected to the overloads; therefore the measured flow-resistance decreases with the flow-speed. In order to minimize the measurement error, the system is completely airtight and measurements were performed on both sides (both surface areas) of each sample of sound absorbing material. The flow-resistivity of the samples were measured for the flow-speeds of 0.2, 0.4, 0.6, 1.05, 1.5, 2 and 3 m s^{-1}. For the purpose of electroacoustics applications such as loudspeaker design as in this project, the flow-resistivity values corresponding to the flow-speed of zero has been considered. The flow-resistivity values corresponding to the air flow-speeds of 0, 0.01, 0.02, 0.03, 0.04 and 0.05 m s^{-1} were found by extrapolating the line from the straight section of each graph (the part that exhibits increases in σ values) in Fig. B.3, B.4 and B.5 backwards to zero.[6] Table 4.3 shows the flow-resistivity values for the samples $RX30/080$, $RX33/160$, $RX33/190$ and $RX39/200$ respectively in MKS Rayls, extrapolated downwards to zero air flow-speed, measured using the DC-flow test.

Flow-Speeds [m s^{-1}]	*Light Blue* $RX30/080$ [Pa s m^{-2}]	*Green* $RX33/160$ [Pa s m^{-2}]	*Aqua* $RX33/190$ [Pa s m^{-2}]	*Sky Blue* $RX39/200$ [Pa s m^{-2}]
0.00	45700	30200	48600	35000
0.01	46700	30600	49300	35400
0.02	47600	31100	50100	35900
0.03	48600	31500	50800	36300
0.04	49600	31900	51500	36800
0.05	50500	32400	52200	37300

TABLE 4.3: Flow-resistivity σ values for samples $RX30/080$, $RX33$-/160, $RX33/190$ and $RX39/200$ in MKS Rayls extrapolated downward to zero air flow-speed.

---

[6] The complete flow-resistivity data, measured in the Centre of Acoustic-Liner Technology *Alenia Aermacchi*, is been included in Appendix B.

Table 4.4 shows the flow-resistivity values for samples *RX*41/150, *RG*50/100, *RG*50/135 and *RG*50/230 respectively in MKS Rayls, extrapolated downwards to zero air flow-speed, measured using the DC-flow test.

Flow-Speeds [m s^{-1}]	*Grey* *RX*41/150 [Pa s m^{-2}]	*Gold* *RG*50/100 [Pa s m^{-2}]	*Pink* *RG*50/135 [Pa s m^{-2}]	*White* *RG*50/230 [Pa s m^{-2}]
0.00	38200	25500	32900	32000
0.01	38700	25900	33400	32800
0.02	39200	26400	33900	33600
0.03	39700	26800	34400	34400
0.04	40200	27200	34900	35200
0.05	40700	27600	35400	36000

TABLE 4.4: Flow-resistivity σ values for samples *RX*41/150, *RG*50-/100, *RG*50/135 and *RG*50/230 in MKS Rayls extrapolated downward to zero air flow-speed.

Table 4.5 shows the flow-resistivity values for samples *cotton felt - F1B*, *needled felt - F1O*, *polyester wrap - S6B* and *polyester wrap - S6C* respectively in MKS Rayls, extrapolated downwards to zero air flow-speed, measured using the DC-flow test.

Flow-Speeds [m s^{-1}]	*Cotton-Felt F1B* [Pa s m^{-2}]	*Needled-Felt F1O* [Pa s m^{-2}]	*Polyester-Wrap S6B* [Pa s m^{-2}]	*Polyester-Wrap S6C* [Pa s m^{-2}]
0.00	152000	441000	10600	5820
0.01	153000	443000	10600	5850
0.02	154000	444000	10700	5880
0.03	154000	446000	10700	5910
0.04	155000	447000	10800	5940
0.05	156000	449000	10800	5970

TABLE 4.5: Flow-resistivity σ values for samples *cotton felt - F1B*, *needled felt - F1O*, *polyester wrap - S6B* and *polyester wrap S6C* in MKS Rayls extrapolated downward to zero air flow-speed.

It can be seen from Tables 4.3 and 4.4 that the flow-resistivity per unit thickness of porous materials is more or less consistent and in the same range of values whereas the fibrous samples have a wide range of values, as can be seen in Table 4.5. The *cotton felt - F1B* and *needled felt -*

F1O have much higher values than those of porous samples whereas the flow-resistivity per unit thickness of *polyester wrap - S6B* and *polyester wrap S6C* has lower values than those of porous samples. It is worth mentioning that the flow-speeds of the *Aermacchi Raylometer-tube* have been optimized for the aeroacoustic applications and therefore it has been designed for much higher flow-speeds than those of interest in this project. In this research on the acoustics of the *TLL* however, the low-flow-speeds are of particular interest and therefore the average of the two measured flow-resistivity per unit thickness for each of the specific air flow-speeds were found and the trend of the flow-resistivities for each of the materials were then extrapolated backwards to zero flow-speed to give the variation of flow-resistivity corresponding to the flow-speeds of 0 to 0.05 m s^{-1} as presented in Tables 4.3, 4.4 and 4.5. It is also notable that in order to keep the position of the test articles in the DC-flow rig, it was necessary to insert each sample in the upper part of the *Raylometer-tube*, interposing between the tube flanges a mesh, characterised by negligible flow-resistance, clamped between the rubber sealing.

4.4 Estimating Absorption Coefficients from Measured Flow-Resistivity

The propagation of sound in an isotropic homogeneous material is determined by two complex quantities, the characteristic impedance Z_0 and the propagation coefficient γ [66]. For a plane-wave propagation in a given direction, the isotropy requirement may be relaxed since most available fibrous or porous sound absorbing materials can be considered to be sufficiently homogeneous for practical purposes [54]. *Delany and Bazley* showed that for a duct uniformly lined with the sound absorbing materials of surface normal-incidence impedance Z_s and a finite thickness h as shown in Fig. 4.10 the surface normal-incidence impedance Z_s is given by [54]

$$\frac{Z_s}{Z} = \frac{Z_b \cosh(\gamma h) + Z \sinh(\gamma h)}{Z \cosh(\gamma h) + Z_b \sinh(\gamma h)}, \tag{4.6}$$

where the complex propagation coefficient of a progressive wave system is the quantity $\gamma = \alpha + j\beta$ where α is the attenuation factor and non-zero for lossy media and β is the phase relation and represents k which is the acoustic wavenumber in the propagation direction, where $k = \omega/c$ and $j = \sqrt{-1}$ [19]. By determining the surface normal-incidence impedance of the samples Z_s for two different values of backing impedance or two different values of thickness h of the liner by measurement or prediction, both the characteristic impedance Z and the propagation coefficient γ may be evaluated. A particular case of Eq. (4.6) of interest in this thesis is when $Z_b = \infty$ for a rigidly backed medium. In Eq. (4.6) letting $Z_b \to \infty$ we get:

$$Z_s = Z \coth(\gamma h), \tag{4.7}$$

where $\coth(\gamma h)$ is:

$$\coth(\gamma h) = \frac{e^{\gamma h} + e^{-\gamma h}}{e^{\gamma h} - e^{-\gamma h}}. \tag{4.8}$$

The *Delany and Bazley* empirical relations containing coefficients R, X, α and β can also be found to be [54]:

$$R = \rho c \left(1 + 0.0571 \left(\frac{\rho f}{\sigma}\right)\right)^{-0.754}, \tag{4.9}$$

$$X = -0.087\rho c \left(\frac{\rho f}{\sigma}\right)^{-0.732}, \tag{4.10}$$

$$\alpha = 0.189\frac{\omega}{c}\left(\frac{\rho f}{\sigma}\right)^{-0.595}, \tag{4.11}$$

$$\beta = \frac{\omega}{c}\left(1 + 0.0978\left(\frac{\rho f}{\sigma}\right)^{-0.7}\right), \tag{4.12}$$

where ρ is the density of the air medium, c is the speed of sound in air, f is the frequency parameter, σ is the flow-resistivity and the angular frequency is $\omega = 2\pi f$. Therefore the characteristic impedance Z and complex propagation coefficient γ will be:

$$Z = R + jX, \tag{4.13}$$

and

$$\gamma = \alpha + j\beta, \tag{4.14}$$

where α is the attenuation factor, β is the acoustic wavenumber [19].

Table 4.6 shows the comparison of empirical relations between acoustical properties and flow-resistivity from three independent studies *Delany and Bazley*, *Dunn and Davern* and *Wu Qunli* [27].[7]

Acoustical properties	*Delany and Bazley*	*Dunn and Davern*	*Wu Qunli*
$(R_1/\rho c) - 1$	$0.0571\tau^{-0.754}$	$0.114\tau^{-0.369}$	$0.209\tau^{-0.548}$
$X_1/\rho c$	$-0.087\tau^{-0.732}$	$-0.0985\tau^{-0.758}$	$-0.105\tau^{-0.607}$
α_1/k	$0.189\tau^{-0.595}$	$0.168\tau^{-0.715}$	$0.163\tau^{-0.592}$
$(\beta_1/k) - 1$	$0.0978\tau^{-0.700}$	$0.136\tau^{-0.491}$	$0.188\tau^{-0.554}$

TABLE 4.6: The comparison of empirical relations from three independent studies *Delany and Bazley*, *Dunn and Davern* and *Wu Qunli*.

The empirical relations of acoustical properties have been expressed with a non-dimensional variable $\tau = \rho f/\sigma$, where f is the frequency parameter, σ is the flow-resistivity of the samples and ρ is the density of air medium. The coefficients of *Delany and Bazley* have been found by experimenting on mainly the fibrous samples and the coefficients of *Wu Qunli* have been found by experimenting on mainly the porous plastic open-cell samples. However, the coefficients of *Dunn and Davern* have been found by experimenting on foams but it focuses on different range of flow-resistivity values. Table 4.7 shows the correlation coefficients of acoustical properties in Table 4.6 with the non-dimensional variable τ [27].[8]

Acoustical properties	*Correlation coefficient*
$(R_1/\rho c) - 1$	0.85
$X_1/\rho c$	0.95
α_1/k	0.99
$(\beta_1/k) - 1$	0.94

TABLE 4.7: Correlation coefficients of acoustical properties and flow-resistivity.

The characteristic impedance and the propagation coefficient of the porous plastic open-cell foams correlate well with the flow-resistivity. The correlation coefficients of acoustical properties are shown in Table 4.6 with the

---

[7] This table is courtesy of *Wu Qunli* from the paper [27].

[8] This table is courtesy of *Wu Qunli* as described in the paper [27].

non-dimensional variable τ ranges from 0.85− to 0.99 shown in Table 4.7. In this research the *Wu Qunli's* coefficients have been used in the numerical models of ducts lined on the interior boundaries with the porous sound absorbing materials and the *Delany and Bazley's* coefficients have been used for the models of ducts lined with the fibrous samples. The empirical relations established by *Wu Qunli* in Table 4.6 are suitable for the calculation of acoustical properties of porous plastic open-cell foams with medium flow-resistivity. *Dunn and Davern's* results, however, are suitable only for the calculation of acoustical properties of foams with low flow-resistivity [27].

4.4.1 Estimating Absorption Coefficient of Fibrous Samples Using the *Delany and Bazley* Method

Figure 4.7 shows the comparison of measured absorption coefficients using the impedance-tube with the empirical absorption coefficients of *Delany and Bazley* in conjunction with the measured flow-resistivity values from DC-flow test for a selected range of fibrous materials.

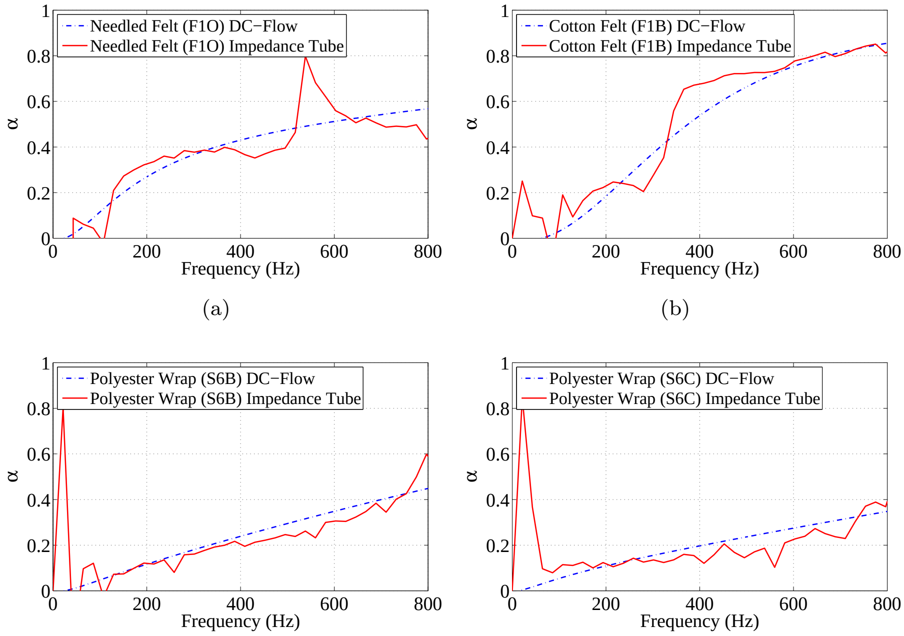

(a) (b) (c) (d)

FIGURE 4.7: Comparison of absorption coefficient of fibrous materials. Impedance-tube measurements (*solid line*) and empirical absorption coefficient of *Delany and Bazley* combined with the flow-resistivity measurements (*dot dashed line*). (a) *Needled felt - F1O*, (b) *cotton felt - F1B*, (c) *polyester wrap - S6B* and (d) *polyester wrap - S6C*.

As can be seen in Fig. 4.7 (a) *needled felt - F1O*, the empirical absorption coefficient and the impedance-tube measurement, are more or less following the same trend as the frequency progresses, with the empirical absorption coefficient (dot dashed line) showing a gradual increase in its response whereas the impedance-tube measurement (solid line) in comparison showing a smooth peak; overestimating the empirical result by about 0.06 between the frequency range of 130 to 323 Hz, followed by a decrease in its response underestimating the empirical data by about 0.08 between the frequency range of 370 to 520 Hz. The impedance-tube measurement then experiences a sudden peak of about 0.3 in magnitude between the frequency range of 520 to 635 Hz, and from that point onwards the impedance-tube data start to steadily decrease again and underestimate the empirical results by about 0.13 at 800 Hz. Once again in Fig. 4.7 (b) *cotton felt - F1B*, the empirical absorption coefficients and the impedance-tube measurements, are following the same trend through out the whole frequency range, with the impedance-tube data underestimating the empirical result by about 0.1 in the frequency range of 230 to 332 Hz followed by a 0.15 overestimation between the frequency range of 332 to 560 Hz. From that point onwards the impedance-tube result follows the same trend as the empirical absorption coefficient, where finally the impedance-tube data underestimates the empirical results by about 0.05. In Fig. 4.7 (c) *polyester wrap - S6B*, the empirical absorption coefficients and the impedance-tube measurements, are following the same trend through out the whole frequency range once again, with the impedance-tube data underestimating the empirical result by about 0.04 in the frequency range of 240 to 750 Hz, and from that point onwards the impedance-tube measurements start to exhibit steady increase and overestimate the empirical results by about 0.15 at 800 Hz. A sharp peak that can be noticed at the 20 Hz region is due to the noise floor below the resonant frequency of the impedance-tube drivers [67]. Similarly in Fig. 4.7 (d) *polyester wrap - S6C*, the empirical absorption coefficients and the impedance-tube measurements, are following the same trend through out the whole frequency range, with the impedance-tube data underestimating the empirical data by about 0.04 in the frequency range of 260 to 740 Hz, and from that point onwards the impedance-tube data start to increase and overestimate the empirical results by about 0.03 at 800 Hz. A sharp peak that can be noticed at the 20 Hz region is due to the noise floor below the resonant frequency of the impedance-tube drivers [39, 68]. As can be seen in Fig. 4.7, overall for all the fibrous samples the empirical data, which is the combination of the *Delany and Bazley* method applied into the flow-resistivity measurements, and the impedance-tube measurements follow the same trend and show a close agreement throughout the whole frequency range [69].

4.4.2 Estimating Absorption Coefficient of Porous Samples Using the *Wu Qunli* Method

Figure 4.8 shows the comparison of measured absorption coefficients using the impedance-tube with the empirical absorption coefficients of *Wu Qunli* in conjunction with the measured flow-resistivity values from the DC-flow test for a selected range of porous materials [50, 66].

As can be seen in Fig. 4.8 (a) sample $RX30/080$, the empirical absorption coefficient and the impedance-tube measurement are more or less following the same trend along the frequency range presented, with some peaks and troughs in the impedance-tube measurement at the low frequency region up to the 410 Hz which could be associated with the noise floor during the impedance-tube measurement of that particular sample. From that point onwards the impedance-tube data in comparison starts to exhibit a steady increase and overestimate the empirical data by about 0.1 at the 800 Hz frequency. Similarly, in Fig. 4.8 (b) sample $RX33/160$, the empirical absorption coefficient and the impedance-tube measurement are following the same trend, with the impedance-tube measurement overestimating the empirical data by about 0.1 uniformly along the frequency range presented. Once again in Fig. 4.8 (c) sample $RX33/190$, the empirical absorption coefficient and the impedance-tube measurement are following the same trend along the frequency range presented, with are some peaks and troughs in the impedance-tube measurement at the low frequency region up to the 150 Hz which could be associated with the noise floor during the impedance-tube measurement of that particular sample, where the peaks and troughs around the 20 Hz region is due to the noise floor below the resonant frequency of the impedance-tube drivers. From that point onwards the impedance-tube measurement overestimates the empirical result by about 0.03 along the whole frequency range presented. Once again In Fig. 4.8 (d) sample $RX39/200$, the empirical absorption coefficient and the impedance-tube measurement are following the same trend along the frequency range presented, with are some peaks and troughs in the impedance-tube measurement at the low frequency region up to the 107 Hz which could be associated with the noise floor during the impedance-tube measurement of that particular sample, where the peaks and troughs around the 20 Hz region is due

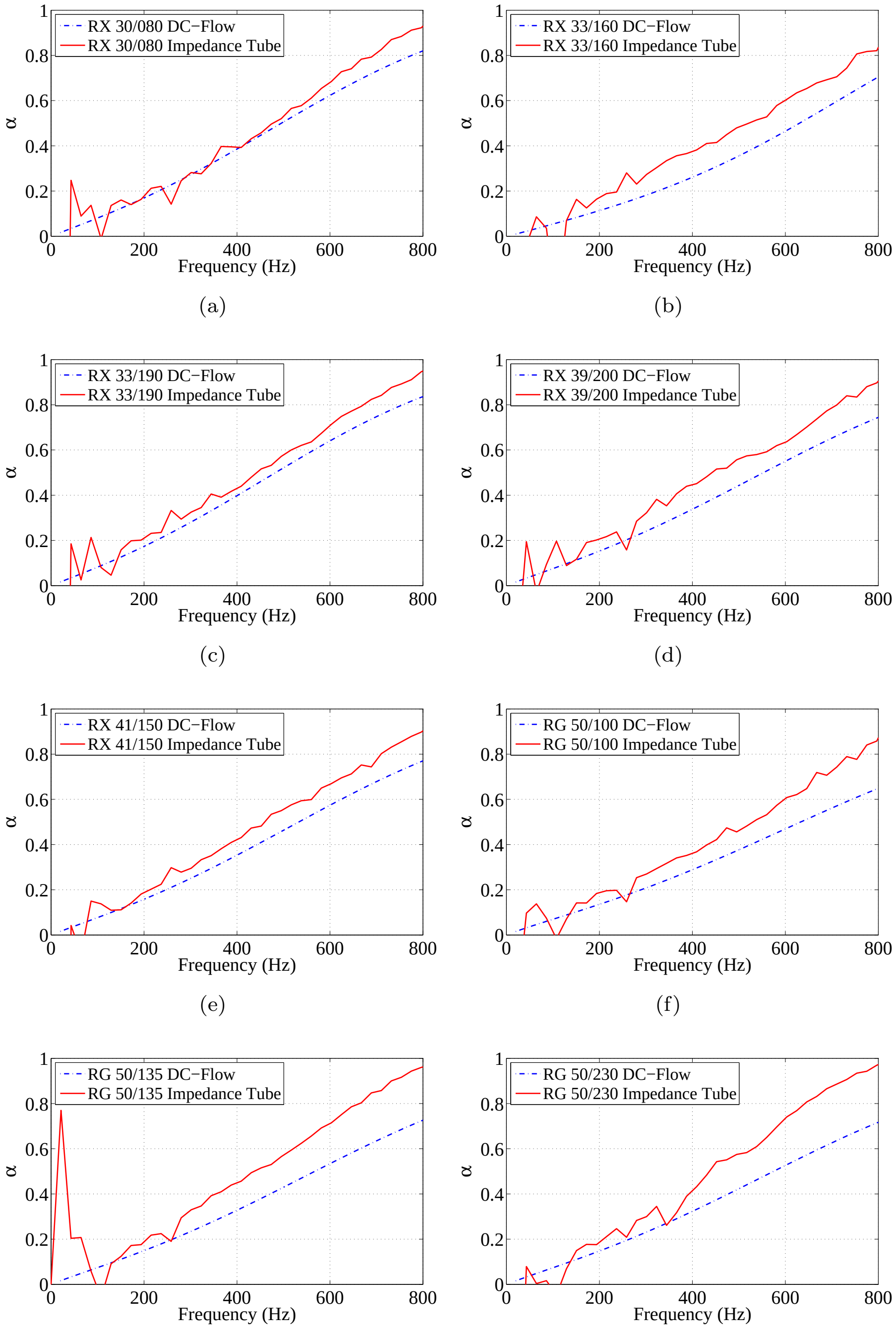

(a) (b) (c) (d) (e) (f) (g) (h)

FIGURE 4.8: Comparison of absorption coefficient of porous materials. Impedance tube measurements (*solid line*) and empirical absorption coefficient of *Wu Qunli* combined with the flow-resistivity measurements (*dot dashed line*). (a) $RX30/080$, (b) $RX33/160$, (c) $RX33/190$, (d) $RX39/200$, (e) $RX41/150$, (f) $RG50/100$, (g) $RG50/135$ and (h) $RG50/230$.

to the noise floor below the resonant frequency of the impedance-tube drivers. From that point onwards the impedance-tube measurement overestimates the empirical result by about 0.13 along the whole frequency range presented. Samples $RX41/150$, as can be seen in Fig. 4.8 (e), show a close similarity between the empirical absorption coefficient and the impedance-tube measurement along the frequency range presented, with the impedance-tube measurement exhibiting a steady increase in comparison in the frequency range of 150 to 800 Hz where it is overestimating the empirical result by about 0.13. In Fig. 4.8 (f) sample $RG50/100$, the empirical absorption coefficient and the impedance-tube measurement are following more or less the same trend along the frequency range presented, with some peaks and troughs in the impedance-tube measurement at the low-frequency region up to 280 Hz which could be associated with the noise floor during the impedance-tube measurement of that particular sample. From that point onwards the impedance-tube measurement overestimates the empirical result by about 0.08 until it finally overestimates the empirical result to about 0.2 at 800 Hz. In Fig. 4.8 (g) sample $RG50/135$, the empirical absorption coefficient and the impedance-tube measurement are once again following the same trend in the frequency range presented, with the impedance-tube measurement exhibiting a higher magnitude of absorption coefficient along the whole frequency range and overestimating the empirical result by about 0.09 at the frequency of 280 Hz, and steadily increasing the difference to about 0.24 at 800 Hz frequency. A sharp peak that can be noticed at the 20 Hz region is due to the noise floor below the resonant frequency of the impedance-tube drivers. Finally, in Fig. 4.8 (h) sample $RG50/230$, the empirical absorption coefficient and the impedance-tube measurement exhibit less similarity with each other, specially in comparison with the other porous samples presented in Fig. 4.8. Apart from some erratic behaviour in the frequency range of 138 to 345 Hz in the impedance-tube response, from that point onwards it exhibits a steady increase in its magnitude in comparison to the empirical result presented to about 0.26 at 800 Hz frequency. It should be noticed that in Fig. 4.8, despite the fact that all samples show more or less close and reasonable agreement with the empirical results yet they are overestimating the empirical results in all cases presented.

4.5 Experimental Evaluation of *TLL*

Using a variety of microphone probes, namely *PU-match* and *USP-regular*, from *Microflown Technologies* and their specifically designed measurement methods, the in-situ measurements on a range of the *TLL* waveguides, namely straight and U-shaped ducts, treated with a variety of porous plastic open-cell foams, bulk-reacting liners, were conducted to find the sound pressure and three-dimensional sound-intensity within the *TLL* cabinets [70, 71]. Figure 4.9 illustrates the schematic model of the measurements conducted on a variety of acoustically treated uniform straight and U-shaped ducts considered in this research for evaluating the characteristic of sound propagation inside the waveguides.

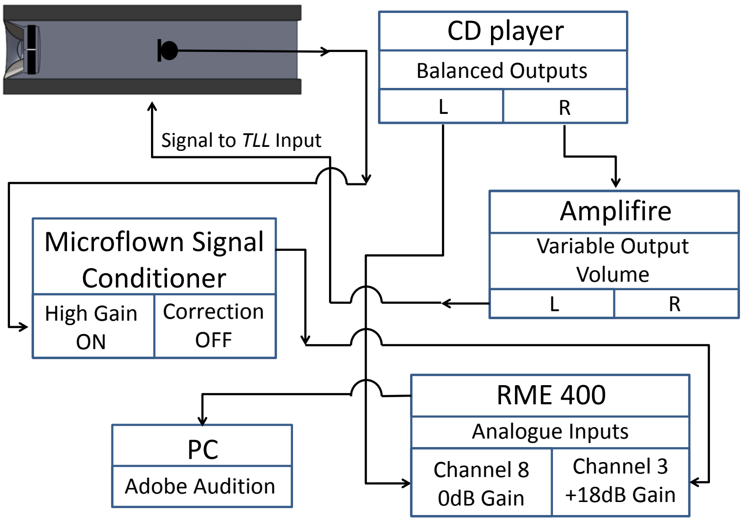

FIGURE 4.9: Schematic model of in-situ measurements for evaluating a range of acoustically treated straight and U-shaped waveguides.

The experimental setup in Fig. 4.9 shows the arrangement used to evaluate a range of acoustically treated, on their interior boundaries, straight and U-shaped uniform *TLL* cabinets [72]. For the measurements conducted on the straight ducts the *Microflown PU-match* was used. A two-ways collocated pressure/velocity sensor which was used in combination with a specific purpose built two-ways *Microflown* signal conditioner, as outlined in Section 4.5.2. In the measurements conducted on the U-shaped ducts, the *Microflown USP-regular* was used. A four-ways collocated pressure and three-dimensional particle velocity sensors, consisting of three individual particle velocity sensors, orthogonally placed, each measuring the particle velocity from the respected x, y and z directions, which was used in conjunction with the specific four-ways *Microflown* signal conditioner as outlined in Section 4.5.5. The straight and U-shaped ducts were acoustically lined with a variety of porous sound absorbing materials, namely $RX33/160$ (green foam) and $RG50/135$ (pink foam) as outlined in Table 4.1 in Section 4.1. Design and manufacturing of bulk-reacting liners has advanced recently resulting in far better controls over their designing with a particular flow-resistivity and density, consequently the porous materials are more commonly used by the industry as an acoustic absorbent [27]. Table 4.8 shows the list of equipment used for the experiments on a range of acoustically treated *TLL* ducts, to evaluate the in-situ sound pressure and sound-intensity inside the cabinets [73].

Equipment list	*Model*
CD player	*Marantz Professional* $PMD321$
Amplifier	*Yamaha Power Amplifier* $H5000$
Sound card	*RME Fireface* 400
Signal conditioner	*Microflown signal conditioner* 2/4 *channels*
Microphones	*Microflown PU-match/USP-regular probes*
Data acquisition	*Standard PC, Adobe Audition*
Video recorder	*Standard camera Canon*

Table 4.8: List of equipment used for the in-situ measurements performed on a range of acoustically treated waveguides, namely straight and U-shaped ducts.

4.5.1 Measurement Precision

The square cross sectional area of the uniform *TLL* ducts, straight, L-shaped and U-shaped, had a total internal dimensions of 0.3×0.3 m^2 and consisted of two regions, namely acoustically treated region which was filled with the variety of porous plastic open-cell foams, bulk-reacting sound absorbing materials, and the free-region which was filled with air. The free-region of the *TLL* ducts had a cross sectional area of 0.2×0.2 m^2, in the straight duct measurements, it was divided into squares of 0.05 × 0.05 m^2 resulting in 25 measurement lines with 0.05 m distance apart from one another across the length of the duct, as shown in Fig. 3.2 (c). The exact location of each of these 25 lines across the length of the *TLL* waveguide was found with a $3D$ surface laser with precision tolerance of ±0.0002 m per metre distance from the $3D$ laser unit, using a *Bosch GLL 3-80P*, as can be seen in Fig. 4.10 [74].[9] The in-situ measurements on a range of acoustically treated *TLL* ducts were conducted in the large anechoic chamber of the *ISVR* in order to simulate the free-field conditions and therefore eliminating any acoustical effects that the laboratory environment could have on the sound-field at the open end region of the *TLL* ducts [75]. For the in-situ measurements performed on the U-shaped ducts, the selected free-region of the duct around the bend as can be seen in Fig. 4.20 was divided into a matrix of 5 × 5. With spacing of 0.05 m starting from the surface area of the sound absorbing liners, 72 point measurements were conducted in each of the five acoustic surface layers inside the U-shaped duct to evaluate the collocated pressure and $3D$ particle velocity around the bend of the *TLL* duct. The exact location of these 72 points were found using the aforementioned $3D$ surface laser. Figure 4.10 shows the straight *TLL* duct rig, lined on the internal boundaries with a variety of porous plastic open-cell foams, $RX33/160$ (green foam), prepared for the in-situ measurements of sound pressure and $3D$ sound-intensity in the anechoic chamber to simulate the free-field condition at the open end of the waveguide.

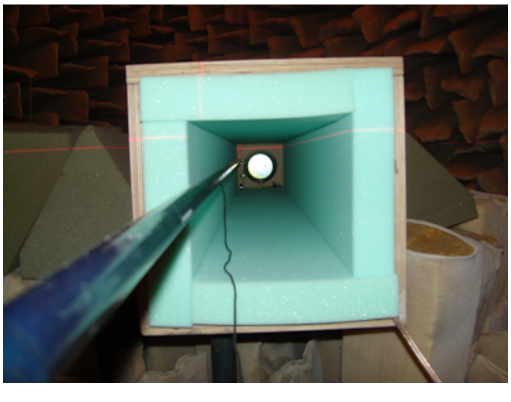

FIGURE 4.10: Straight duct lined with sample $RX33/160$ (green foam) in the anechoic chamber. The red cross on the surface area of the duct is one of the positions marked by the $3D$ surface laser.

---

[9] Full technical details of the *Bosch GLL 3-80P*, $3D$ surface laser used in the in-situ measurements can be found at $http://www.lawson-his.co.uk$.

4.5.2 Scan and Paint Method

The straight waveguide has been evaluated using a measurement method developed by *Microflown Technologies* and their collocated pressure/velocity probe, *PU-match*, to measure the sound pressure and particle velocity at any points within the free space of the duct [76]. Figure 4.11 illustrates the physical size of the *Microflown PU-match* used to directly measure the sound pressure and particle velocity within a range of acoustically treated straight *TLL* duct.[10]

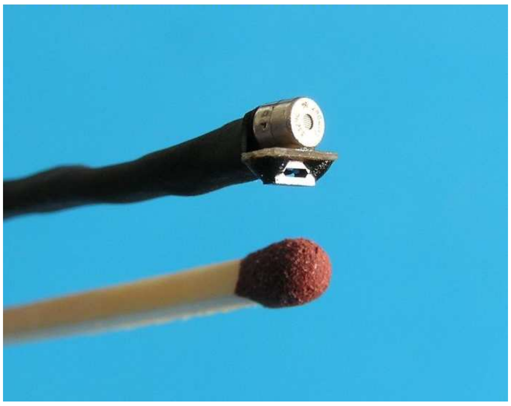

FIGURE 4.11: Physical size of the *Microflown PU-match* probe.

In order to minimize the physical disturbance of the recording transducer on the sound-field the *Microflown PU-match* probe was used [77]. The microphone was attached to the end of a rod on a rolling stand with 0.07 m distance between the rod and the tip of the microphone. The miniaturized size of the *PU-match* probe and the distance between the microphone and its stand was chosen in order to make sure the acquisition setup had the minimum effect on the sound-field [78]. The purpose built microphone stand could be adjusted in height with the range of 0.05 to 0.25 m to cover all the possible points along the length of the 0.2×0.2 m^2 cross section of the straight *TLL* duct. The straight duct rig had a square cross section which was lined uniformly with the same thickness of sound absorbing materials along the interior boundaries of the duct. Therefore, assuming the centre line of the duct cross section as the axial frame of reference in the *x-axis* direction, along the length of the duct, reduces the required measurement area across the duct cross

---

[10] Picture is courtesy of *Microflown Technologies*. $http://www.microflown.com$

section to one quarter of the total cross sectional area which then could be mirrored to the other quadrants respectively. Figure 4.12 illustrates the size of the *Microflown PU-match* on the purpose built stand used to directly measure the sound pressure and particle velocity along the length of the straight *TLL* duct treated with the variety of bulk-reacting sound absorbing liners.

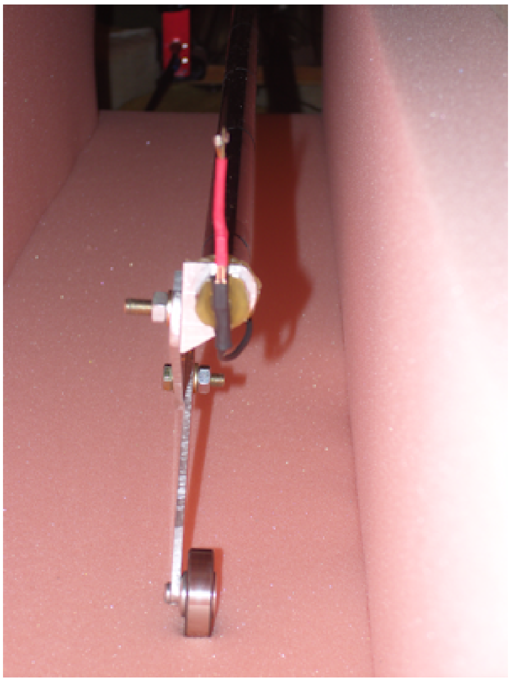

FIGURE 4.12: *Microflown PU-match* probe on its purpose built stand inside the straight duct, lined with sample $RG50/135$ (pink foam).

Figure 4.13 shows the sound pressure, particle velocity and sound-intensity within the length of the straight *TLL* duct lined with the porous plastic open-cell foam, sample $RG50/135$ (pink foam), using the *Microflown PU-match* probe for a range of frequencies presented. The in-situ measurements were conducted in the free-region of the *TLL* which is filled with air.

In Fig. 4.13, in-situ measurement results exhibit a behaviour such as experiencing a sudden expansion in the acoustic boundary at the open end of the waveguide which can be seen more prominently specially at the frequencies of 500 and 1000 Hz where the size of the wavelengths becomes comparable to that of the open end of the *TLL* duct. As can be

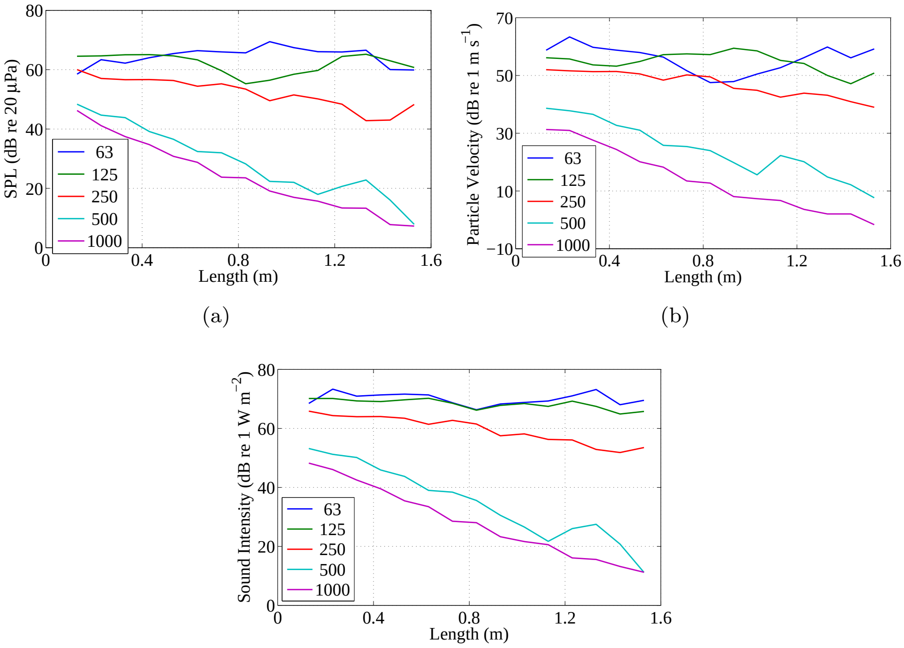

(a)

(b)

(c)

FIGURE 4.13: In-situ measurement of sound pressure, particle velocity and sound-intensity within a straight *TLL* duct acoustically treated with sample *RG*50/135 (pink foam), using *PU-match* for frequencies 63, 125, 250, 500 and 1000 Hz. (a) Sound pressure, (b) particle velocity and (c) sound intensity.

seen in Fig. 4.13 (a) sound pressure, (b) particle velocity and (c) sound-intensity, the frequencies $63, 125$ and 250 Hz show almost negligible decay along the length of the duct. However, as the frequency progresses the rate of the decay increases, where at 63 Hz there is almost no decay along the *TLL* duct length, at 250 Hz there is about 12 dB decay can be observed. The rate of the decay increases and for the 500 and 1000 Hz, it is about 40 dB. Figure 4.14 shows the pressure variation in dB re 20 μPa, inside the straight-duct treated with bulk-reacting liner, sample *RG*50/135 (pink foam), measured using *Microflown PU-match.*[11]

As can be seen in Fig. 4.14 (a) there is a high pressure behind the driver which drops by about 15 dB at 0.55 m away from the driver. After that point the pressure starts to rise again to the maximum amount of 75 dB

---

[11] The detailed experimental results of in-situ measurements performed on the straight duct lined with the porous sample *RG*50/135, for the frequency range of 40 to 1000 Hz has been added to Appendix B.

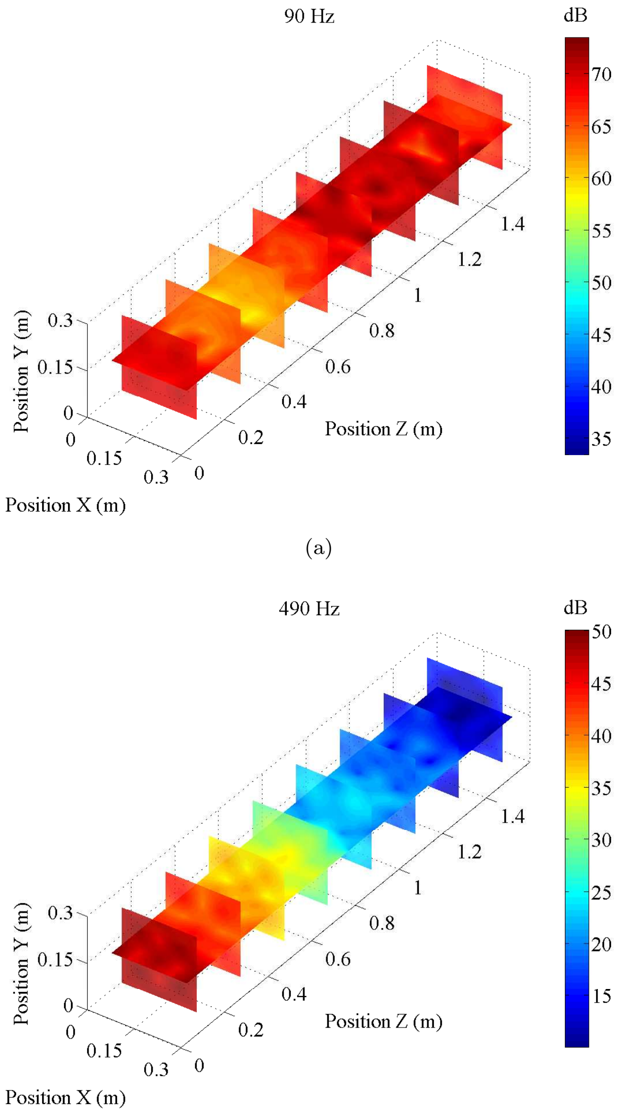

(a)

(b)

FIGURE 4.14: Pressure variation in dB re 20 μPa, for a straight duct treated with the bulk-reacting sample $RG50/135$, measured using *PU-match*. (a) 90 Hz and (b) 490 Hz.

at 1.1 m away from the driver and it starts to decay from that point onwards to the open end of the duct by about 12 dB. In Fig. 4.14 (b) the pressure magnitude exhibits about 40 dB drops in its value uniformly along the length of the *TLL* duct.

4.5.3 Measurement Resolutions

The one dimensional *PU-match* probe consists of a *Microflown* acoustical particle velocity sensor and a collocated miniature sound pressure transducer *Knowles FG series* placed without packaging. This transducer is the smallest available intensity probe, as can be seen in Fig. 4.11 in Section 4.5.2. Due to the small size of the probe it is possible to measure the sound-field with the least amount of acoustical disturbance and with extreme high spatial resolution which otherwise could not be possible [79]. During these measurements the straight-duct was lined on the inside with a variety of different bulk-reacting liners. The acoustic absorbent treatments were chosen from the selection of fibrous and porous materials with different densities, ρ, flow-resistivities, σ, and Young's modulus, E. In the *scan and paint measurement method* developed by the *Microflown Technologies*, the miniature *PU-match* probe was used mounted on a purpose built stand rolling along the length of the duct sweeping the sound-field from the back of the driver position to the open end of the waveguide, as can be seen in Fig. 4.12, during the measurements for each of the samples. In the evaluation and analysis of the measurement data a windowing space frame along the length of the duct had to be chosen with a reasonable overlapping, in order to correctly resolve the sound-field under consideration. The choice of windowing space was important since a window which is too small results in too much overlapping of the measured data and consequently the results would appear as if the sound-field was too erratic which would not be a correct representative of the acoustic sound-field under analysis. On the other hand, a windowing with the size bigger than necessary would result in huge inaccuracy in resolving the sound-field under consideration again and consequently should have been avoided. Figure 4.15 shows the comparison of windowing resolution for sound pressure results, which was then also applied during the analysis of the particle velocity and the sound-intensity data, on the in-situ measurements conducted on straight-duct lined on the interior boundaries with a sample of a sound absorbing material *RG*50/135 (pink foam), for a range of frequencies presented. The solid-line, dash-line and dotted-line corresponds to 0.1 m, 0.06 m and 0.03 m windowing sections along the length of the *TLL* duct respectively.

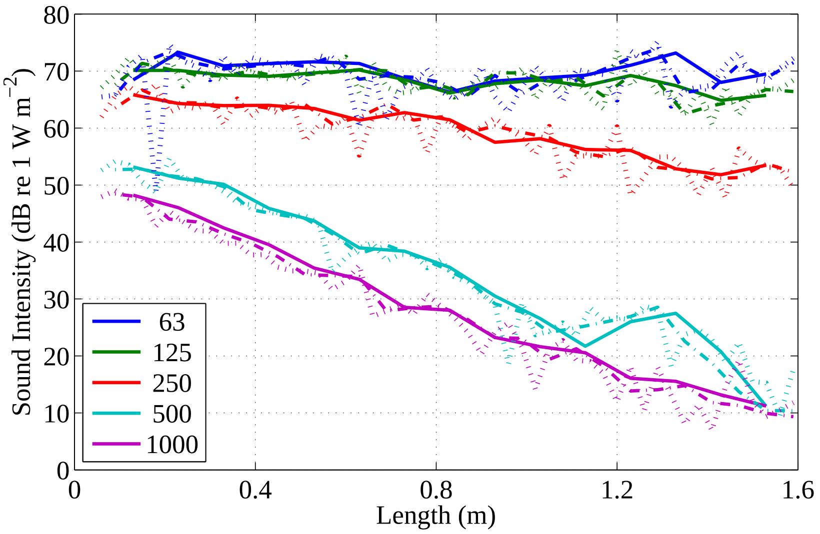

FIGURE 4.15: Comparison of windowing resolution in sound-intensity within a straight duct treated with sample *RG*50/135, using *Microflown PU-match*. Lines corresponds to 0.1 m (*solid lines*), 0.06 m (*dashed lines*) and 0.03 m (*dotted lines*) for the frequencies 63, 125, 250, 500 and 1000 Hz.

As can be seen in Fig. 4.15, the 0.03 m windowing represented by the (dotted lines), shows too erratic behaviour and therefore was excluded in the analysis of the measurement results. The 0.1 m (solid lines) and 0.06 m (dashed lines) however, show more or less the same trend but overall the 0.1 m (solid lines) exhibited better representation of the measurement data and therefore it was chosen as the windowing resolution of the in-situ measurements. The internal cross sectional area of the *TLL* ducts were made 0.3×0.3 m^2, lined on the inside with the sound absorbing materials of 0.05 m thickness. The remaining free-area of the duct would be 0.2×0.2 m^2 which was divided into a matrix of 5×5 as shown in Fig. 3.2 (c). The highest frequency of interest in this project was 1000 Hz and the broadband excitation signal to the *TLL* driver was 20 to 2000 Hz; therefore the 0.05 m spacing for the in-situ measurements of the sound pressure and sound-intensity along the length of the duct was sufficient enough to resolve any changes in the acoustic environment of the sound-field within the *TLL* waveguide. With the spacing of 0.05 m starting from the surface area of the sound absorbing liner, 25 lines were swept to evaluate the collocated pressure and particle velocity along the length of the straight duct. The measurements were repeated for a variety of the sound absorbing liners added on the internal boundaries of the waveguide. The direct measurements were then plotted with zero interpolation and have been presented in this chapter. Figure 4.16 illustrates the sound pressure results for a straight duct treated with the sample $RX33/160$ (green foam), for a range of frequencies presented.

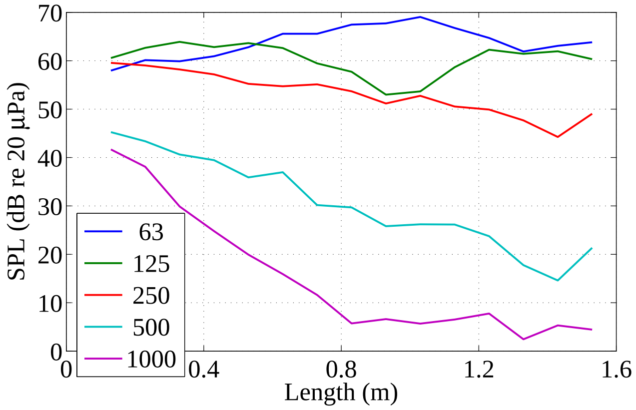

FIGURE 4.16: Sound pressure results for straight duct, treated with sample $RX33/160$ (green foam), for frequencies 63, 125, 250, 500 and 1000 Hz.

The effect of a pressure-release boundary condition at the open end of the duct, which can be more clearly observed for the frequencies of 500 and 1000 Hz, could be associated with the comparable size of open end of the duct and the size of the wavelength of the aforementioned frequencies. It can be seen in Fig. 4.16 that the response is similar to that of Fig. 4.13 (a). At the frequencies of 63, 125 and 250 Hz the magnitude of the sound pressure shows very little decay along the 1.6 m length of the duct. However, as the frequency progresses the rate of the decay increases, where at 63 Hz there is almost no decay along the duct length, at 250 Hz there is almost 10 dB decay can be observed. The rate of decay increases further and for the 500 and 1000 Hz, it is about 30 dB.

4.5.4 Comparison of Scan and Paint and Numerical Predictions

The results of the *scan and paint* measurement method have been compared with the numerical predictions of evaluating the straight duct treated on the internal boundaries with the different sound absorbing materials which have been developed and presented in Chapter 3. Figure 4.17 illustrates the comparison between the numerical predictions and the direct measurements of sound pressure along the length of the straight-duct, treated with sample $RX33/160$ (green foam), for a range of frequencies presented. Solid lines in the figure correspond to the *COMSOL* results and dashed lines correspond to the in-situ measurement results.

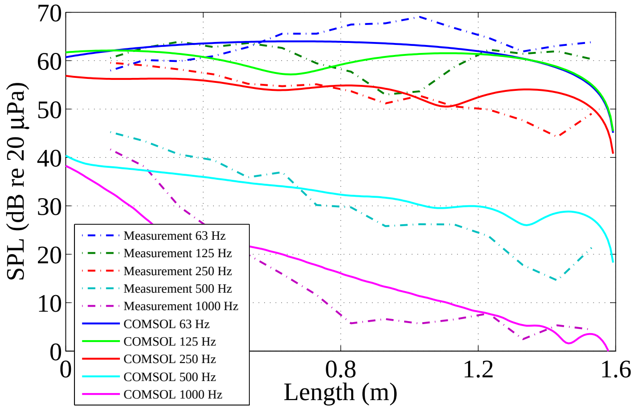

FIGURE 4.17: Comparison of the numerical prediction and the in-situ measurements of sound pressure along the straight-duct length, treated with sample $RX33/160$ (green foam), for frequencies 63, 125, 250, 500 and 1000 Hz. *COMSOL* results (*solid lines*) and measurement results (*dot dashed lines*).

In Fig. 4.17 a pistonic excitation was considered as the source excitation in the numerical model. The in-situ measurement results exhibit a pressure-release boundary condition $p = 0 \mid_{x=L_x}$ at the open end of the duct which can be observed more clearly at the frequencies of 500 and 1000 Hz. This could be associated with the comparable physical size of the open end of the duct and the wavelengths of the aforementioned frequencies [80]. These findings also correspond well with the known and published theory about the principle behind the acoustically treated transmission-line waveguides. As the theory states, and due to the difficulty of successfully absorbing low-frequency energy because of the large wavelengths involved, the length of the *TLL* duct and the density of the filling material were arranged such that the *TLL* waveguide effectively acts such as a low-pass acoustic filter [10]. Thus the mid and high frequencies were subjected to a large attenuation within the duct but the low-frequencies re-emerged from the open end of the *TLL* with a phase such that the reinforcement with the direct radiated sound from the woofer would take place [9–11]. In Fig. 4.17 frequencies 63, 125 and 250 Hz exhibit close similarity in their trends between the numerical prediction and the direct measurements. The comparison of the 250 Hz is almost the same apart from the dissimilarity at the open end of the duct. It is also worth mentioning that in all of the numerical predictions illustrated in Chapter 3, a pressure-release boundary condition at the open end of the *TLL* duct has been assumed. Therefore the acoustic-impedance at the open end of the duct is $Z_{al} = 0$, and consequently the acoustic pressure at the open end is $p = 0 \mid_{x=L_x}$. This acoustical condition was assumed since a duct with a small opening experiences a sudden expansion in the cross sectional area of the duct; therefore the pressure at the open end of the duct tends to zero. This assumption was also made to keep the numerical models presented in Chapter 3 as robust as possible, which has been explained in more detail in Chapter 3. In Fig. 4.17 the 500 and 1000 Hz on the other hand show far less similarity in their comparison of the magnitude of the sound pressure between the predicted and measured values. Figure 4.18 illustrates the comparison between the numerical results and direct measurements of sound pressure along the straight-duct length, treated with sample *RG*50/135 (pink foam), for a range of frequencies presented. Solid lines in the figure correspond to the *COMSOL* results and dashed lines correspond to the in-situ measurement results.

As in the previous case in Fig. 4.17, the in-situ measurement results exhibit a pressure-release boundary at the open end of the duct. This effect can be observed more clearly for the frequencies of 500 and 1000 Hz, which is due to the sudden expansion in the acoustic boundary at the open end of the waveguide. In Fig. 4.18 frequencies 63, 125 and 250 Hz exhibit close similarity in their trends between the numerical prediction and direct measurements, with the comparison of 250 Hz being almost

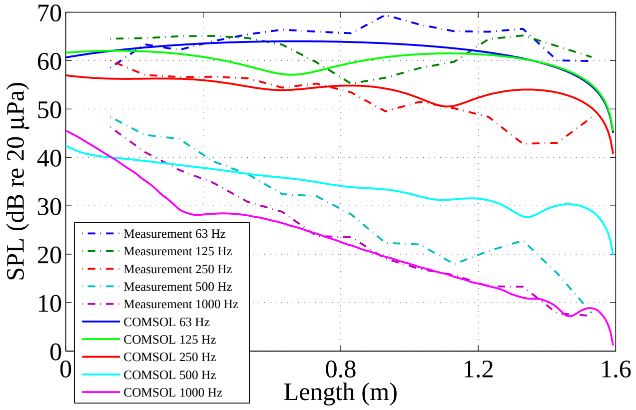

FIGURE 4.18: Comparison of numerical prediction and direct measurements of sound pressure along the straight duct, treated with sample *RG*50/135 (pink foam), for the frequencies 63, 125, 250, 500 and 1000 Hz. *COMSOL* results (*solid lines*) and measurement results (*dot dashed lines*).

the same apart from the prediction at the open end of the duct, which was due to the assumption of a pressure-release boundary condition for the open end of the duct. The 500 Hz shows far less similarity in comparison of magnitude of the sound pressure between the predicted and measured values. The 1000 Hz has almost identical response for both prediction and measurements from 0.7 to 1.5 m across the length of the duct. It has to be noticed that Fig. 4.17 and Fig. 4.18 are showing the comparison of two different porous plastic sound absorbing liners with their corresponding numerical predictions, and as can be seen both treatment show very good agreement with the numerical predictions.

4.5.5 In-situ Sound Intensity Method

The U-shaped duct has been evaluated using a measurement method developed by *Microflown Technologies* and their collocated pressure/velocity *USP-regular* probe to measure the sound pressure and three dimensional particle velocity within the free space of the duct [81]. The $3D$ half inch *USP-regular* probe consists of three orthogonally placed *Microflown* acoustic particle velocity sensors and a collocated miniature sound pressure microphone at their centre. The actual sensor configuration without its cap has a volume less than $0.005 \times 0.005 \times 0.005$ m^3. Figure 4.19 shows the *Microflown USP-regular* probe and the location of the collocated miniature pressure transducer and three orthogonally placed particle velocity sensors, used to directly measure the sound pressure and the $3D$ particle velocity within the U-shaped duct.[12]

FIGURE 4.19: Physical size of the *Microflown USP-regular* sensor and the configuration of the three orthogonally placed particle velocity sensors and the collocated miniature pressure transducer in their centre can be observed.

Any acoustic sound-field can be described by two complementary acoustic properties: the sound pressure (scalar value) and the particle velocity (vector value) [82]. The *USP-regular* probe of the *Microflown* is capable of directly measuring the acoustic particle velocity in the sound-field under consideration, and is used as an acoustic-vector-sensor (*AVS*). Using the *USP-regular* probe and the measurement technique developed by *Microflown Technologies*, the three dimensional sound-intensity, energy, power and acoustic-impedance can be measured in-situ, under realistic

---

[12] Picture is courtesy of *Microflown Technologies*. $http://www.microflown.com$

conditions for the near-field measurements. Also, the *USP-regular*, can be used within closed cavities, such as ventilation ducts or *TLL* waveguides, without the need for anechoic conditions and the problems of pressure over intensity index has been resolved for this sensor. It should also be noted that, the susceptibility of the *USP-regular*, compared to other microphones, to the background noise and the reflections is -40 dB.[13] Figure 4.20 shows the schematic model of the U-shaped duct analysed in this project, the selected area around the bend shows the location where the detailed in-situ measurements were conducted.

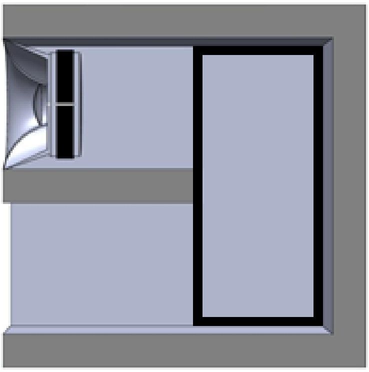

FIGURE 4.20: Schematic model of the U-shaped duct. The selected area was analysed in details with conducting the in-situ measurements of sound pressure and 3*D* acoustic-intensity for the frequency range of 40 to 1000 Hz.

The acoustic behaviour of sound propagation within a straight *TLL* duct lined on the inside (the internal-boundaries) with a variety of sound absorbing materials has been measured directly and analysed earlier in Section 4.5.2. Next, the focus was placed on the sound behaviour around the bends inside the U-shaped transmission-line loudspeaker cabinets. Here an assumption has been made that the acoustical behaviour within the straight sections of the *TLL* duct before and after the bend area is similar to the corresponding parts described earlier in Section 4.5.2. Figure 4.21 shows the comparison of the in-situ measurements using the *Microflown USP-regular* probe and the numerical prediction of pressure variation inside the U-shaped duct, for the frequencies of 300, 345 and 390 Hz.[14]

---

[13] The *USP-regular* information are courtesy of *Microflown Technologies*. $http://www.microflown.com$

[14] Detailed experimental results of the in-situ measurements performed on the U-shaped duct for the frequency range of 40 to 1000 Hz has been added to Appendix B.

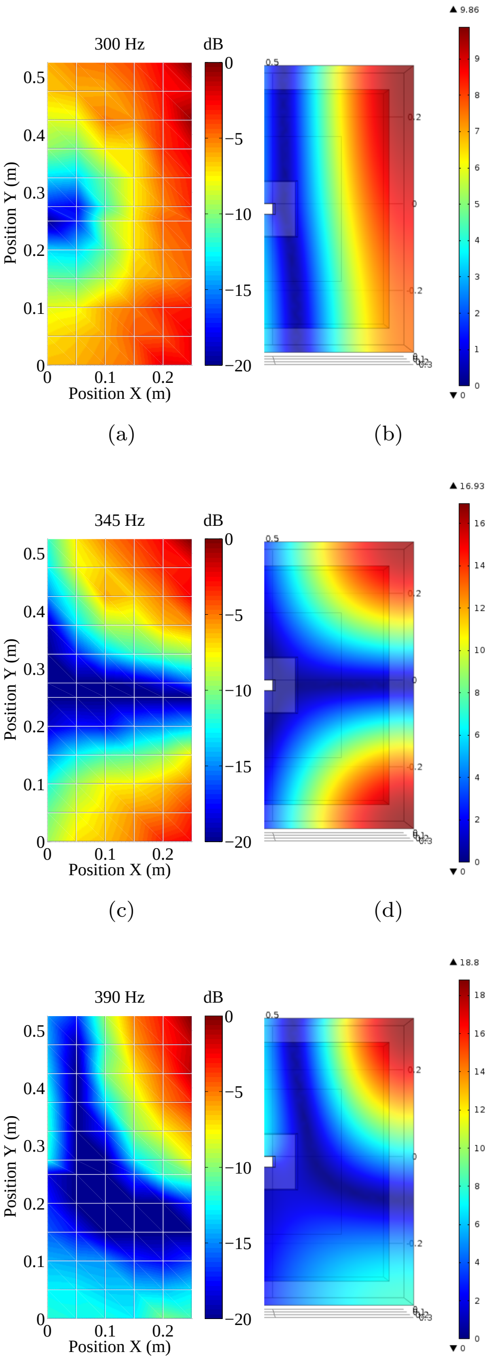

(a) (b)

(c) (d)

(e) (f)

FIGURE 4.21: Comparison of in-situ measurement using *USP-regular* sensor with numerical predictions of pressure variation inside the U-shaped duct lined with the sample $RX33/160$ (green foam). (a) 300 Hz, (b) 300 Hz, (c) 345 Hz, (d) 345 Hz, (e) 390 Hz, and (f) 390 Hz; (a), (c) and (e) correspond to the in-situ measurements and (b), (d) and (f) correspond to the numerical predictions.

The comparison of the in-situ measurements, using the *USP-regular* probe and the numerical prediction, of pressure variation around the bend region inside the U-shaped duct can be observed in Fig. 4.21 at three different frequencies, where Fig. 4.21 (a), (c) and (e) refer to the in-situ measurements and Fig. 4.21 (b), (d) and (f) represent the numerical results. Comparing the results in Fig. 4.21 (a) with the selected area in Fig. 4.20, it can be seen that at 300 Hz, there is a low-pressure region around the tip of the separating panel in the U-shaped duct, and a high-pressure region encapsulating it concentrated on the internal back panel of the *TLL* loudspeaker with the highest pressure concentration at the two right-side corners of the bend area. The concentration of high pressure around the bend and more specifically in the right-side corners are expected since the top right corner is in front of the loudspeaker drive, excitation source, creating an obstacle in front of the movement of the sound pressure and the bottom right corner is again causing the change in the direction of the sound pressure. Comparing the results in Fig. 4.21 (a) and (b), it can be seen that they do not matching completely at this frequency, 300 Hz. Despite the fact that, the same as in Fig. 4.21 (a) a low-pressure region can be noticed around the separating panel of the U-shaped duct and a high-pressure region with its concentration on the top right corner as can be observed in Fig. 4.21 (b), it is clear that the high-pressure region in Fig. 4.21 (b) no longer encapsulates the low-pressure region. The low-pressure region also seems to have spread across both top and bottom sections of the duct. The amplitude difference of the excitation source between the in-situ measurement and the numerical results could be associated as the main cause of this inaccuracy at this particular frequency. In Fig. 4.21 (c) as the frequency progresses to 345 Hz, the low-pressure region located around the separating panel in Fig. 4.21 (a) is growing, creating two distinct regions of high-pressures concentrated on the two right-side corners of the waveguide bend. In Fig. 4.21 (d), the numerical results exhibit a very close similarity with the in-situ measurement at this particular frequency. In Fig. 4.21 (e) as the frequency increases further to 390 Hz, the low-pressure region around the separating panel in Fig. 4.21 (a) is growing even further, but since the frequency is getting close to the standing wave frequency within the bend area in the U-shaped duct distinct high and low-pressure regions have been created at the two right-side corners of the duct bend. Once again comparing Fig. 4.21 (f) with (e) a close similarity can be observed showing that the numerical result is following the same pattern as the in-situ measurement at that frequency. The distinct high and low-pressure regions as a result of the standing wave pattern within the bend area of the duct as discussed in Fig. 4.21 (e) can be observed more clearly in Fig. 4.21 (f).

4.5.6 Measurement Resolutions

Using the measurement method developed by *Microflown Technologies*, the *in-situ sound-intensity*, and the *USP-regular* sensor was used in the U-shaped bend region inside the *TLL* duct to directly measure the sound pressure and three dimensional particle velocities resulting in the direct measurements of the three dimensional acoustic-intensities. Detailed experimental results of the in-situ measurements performed on the acoustically treated U-shaped duct have been added in Appendix B. The internal cross sectional area of the *TLL* ducts were made 0.3×0.3 m^2, lined on the inside with the sound absorbing materials of 0.05 m thickness. The remaining free-region of the duct therefore would be 0.2×0.2 m^2 which was divided into a matrix of 5×5. With spacing of 0.05 m starting from the surface area of the sound absorbing liners, 72 point measurements were conducted in each of the five acoustic surface layers inside the U-shaped duct to evaluate the collocated pressure and $3D$ particle velocity around the bend of the *TLL* duct. It should also be noted that in the results presented in Section 4.5.5 the white grids correspond to the exact location of the *Microflown USP-regular* sensor which was used for the measurements conducted on each position in each of the acoustic layers. The direct results of the consecutive points have been interpolated to create the surface plots of the acoustic behaviour of the sound propagation within the U-shaped region of the *TLL* waveguide.

4.6 Measurement Limitation

There was a number of different factors in the measurements conducted that created and increased the measurement errors. One of the main limiting factors was the precision of the microphone locations during the measurements in all of the *TLL* waveguides. In the *scan and paint* method used for the measurement conducted on the straight ducts and presented in Section 4.5.2 the *PU-match* microphone was mounted at the end of a 7 m long rod which was rolled backward from the driver position at $x = 0$ to the open end of the duct at $x = L_x$. Due to the long length of the rod also including the microphone stand, the microphone was vibrating as it was rolled backwards to the open end of the waveguide hence reducing the accuracy of the measurements. In the *in-situ sound-intensity* method used for the measurements conducted on the U-shaped ducts, the position of the *USP-regular* microphone mounted on a miniature tripod was changed for each measurement point. Due to the required high number of repetition of the microphone alignments, there was a possibility of mis-aligning the $3D$-sensor at some of the locations. Next in the list of limiting factors was the signal-to-noise ratio during the data acquisition. For the *scan and paint* method the measurement was performed in the anechoic chamber whereas for the U-shaped duct measurements the tests were performed in the listening room laboratory. Therefore the noise floor was considerably higher than the measurement done in the anechoic chamber. Another limiting factor was the inherent microphone inaccuracy that each and every microphone suffers from. The general inaccuracy in the repeatability of the measurement conditions was another limiting factor in the measurement errors. Also the loudspeaker drivers never behave completely pistonic; hence modelling the drive-unit with the pistonic excitation introduces further inaccuracy and error between the numerical predictions and the direct measurements conducted and presented in Chapter 4. The next error factor was the measured low-frequency response of the sound-field inside the *TLL* ducts which were directly affected by the resonant frequency of the loudspeaker driver. In measuring the U-shaped ducts, the point by point measurement technique was used. The separation distance between the measurement points was another limitation factor. In the case of the *scan* *and paint* method which was used for the straight duct measurements the microphone was rolled backwards from the back of the driver position to the open end of the duct. Finally, the availability of the measurement facilities, laboratories and equipment could be the other main factors increasing the overall limitation of these presented measurements. Within the scope of this project it became necessary to liaise with many different companies to borrow equipment and samples and to conduct measurements in parts in collaboration. The measurement equipment had to be borrowed from the manufacturer the *Microflown Technologies*, since the variety of the measurement probes used were extremely expensive and beyond the available budget for this project. Therefore the measurement equipment was used for a very short period of time. Consequently, extensive in-situ measurements could not be performed on all range of available sound absorbing materials. The analysis could be further solidified by adding further extensive data acquisition on the range of treated waveguides.

4.7 Conclusion

In Chapter 4, direct measurements were conducted on a variety of sound absorbing materials in order to characterise their behaviour. Using the *ISVR* impedance-tube, the impedance measurements were conducted on the selected range of fibrous and porous sound absorbing samples. Two different kinds of bulk-reacting samples were chosen, namely fibrous and porous absorbing materials, for lining of the internal boundaries of a range of ducts, namely straight and U-shaped ducts. The impedance measurements were then compared with with the *Delany and Bazley* [54] and *Wu Qunli* [27] methods which were applied to the flow-resistivity measurements of the same range of fibrous and porous materials respectively, and conducted in the Centre of Acoustic-Liner Technology of *Alenia Aermacchi* in *Italy* using a DC-flow test,and have been used in Chapter 3 to construct the numerical models of the treated *TLL*. Next, the direct measurements were conducted on a range of treated waveguides in order to get the internal sound pressure and three-dimensional acoustic-intensity along the length of the *TLL* ducts which were then compared with the analytical and numerical models, presented in Chapters 2 and 3 respectively. A variety of measurement methods and microphone probes were used, namely *PU-match* sensor in combination with the *scan and paint* method and *USP-regular* sensor in combination with the *in-situ sound intensity* method, from *Microflown Technologies* to measure the straight and U-shaped ducts respectively. Next, in Chapter 5 the developed numerical models presented in Chapter 3, which have been compared with the direct measurements in Chapter 4, were used to apply simple optimization on the transmission-line loudspeaker cabinets.

Chapter 5

Optimization of *TLLs*

In this chapter, the numerical models, presented in Chapter 3 and validated with the in-situ measurements in Chapter 4, have been used to apply acoustical optimization on a simple-geometry transmission-line loudspeaker cabinet. The *TLL* consists of an acoustically treated waveguide attached to the back of the loudspeaker driver in order to extend the overall low-frequency response of the loudspeaker. The audio performance of the *TLL* can be acoustically optimized by accordingly controlling the internal sound pressure along the length of the *TLL* waveguide.

The optimization began with carefully selecting a range of bulk-reacting sound absorbing materials, namely fibrous and porous absorbers, to be used for lining the internal boundaries of a selection of straight and U-shaped *TLL* ducts. The sound absorbing materials were then characterized using their flow-resistivities which were measured in the Centre of Acoustic-Liner Technology of *Alenia Aermacchi* in *Italy* using a DC-flow test, presented in Chapter 4. The flow-resistivity data were then used to construct the numerical models of the treated *TLL*, presented in Chapter 3 to correctly estimate the effects and the contribution of the acoustical treatments added into the waveguide at the back of the transmission-line woofers.

The audio optimization of the *TLL* can be grouped into the optimization of the cabinet geometry and the optimization of the internal acoustical treatments. Transmission line loudspeakers rely on the use of sound absorbing materials and, although attempts at modelling the performance of these have been reported in the literature, most *TLLs* are designed empirically, using a combination of experience and trial-and-error. In this research the effect of cabinet geometry has been ignored and the emphasis has been placed on the optimization of the acoustic liners along the internal boundaries of the transmission-line waveguides.

5.1 Optimization Variables

The *TLL* designs have been used in a wide range of audio applications such as high-quality studio monitoring used in the *BBC* studios and high-end *HiFi* audio systems for the audiophiles. Figure 5.1 shows a cross section of an acoustically treated and fully optimized floor-stand transmission-line loudspeaker.[1]

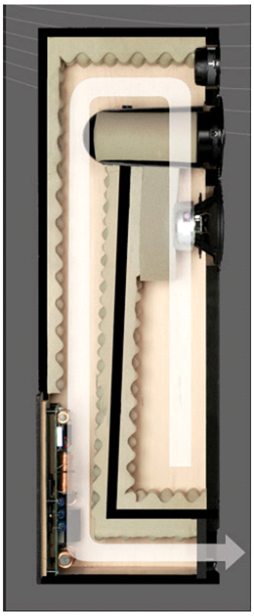

Figure 5.1: An acoustically treated and optimized floor-stand *TLL*.

As can be seen in Fig. 5.1, the internal tubing of the loudspeaker has been lined by a selection of the bulk-reacting sound absorbing liners (porous-plastic open-cell foams). It is also noticeable in Fig. 5.1, that the thickness of the sound absorbing liner is varying along the internal length of the waveguide attached to the back of the *TLL* drivers. To this

---

[1] Picture is courtesy of Professional Monitor Company *PMC*.
http : //www.pmc − speakers.com

date, any new *TLL* has been designed by trial and error and prototyping since the complete understanding of the acoustical behaviour of a treated transmission-line waveguide has not been available in the literature [83]. One of the main objectives of this project was to find and evaluate a numerical method capable of correct prediction and detailed analysis of the sound propagation within a treated transmission-line waveguide. The acoustical optimization parameters are the location, thickness and the flow-resistivity of the different bulk-reacting sound absorbing liners. In this project, a simple U-shaped *TLL* duct, as in Fig. 5.3 (a), has been chosen. The splitting surfaces and the corner areas inside the *TLL* waveguides are some of the obvious locations to apply the acoustical treatments with the variable thicknesses of sound absorbing materials. These locations are of high priority due to the high concentrations of the acoustic pressure in those areas as could be seen in Fig. 4.21. The flow-resistivity values corresponding to different flow-speeds for each of the different liners has been illustrated and explained in detail in Tables 4.3, 4.4 and 4.5 in Chapter 4. It is worth mentioning that the presented numerical models can be further enhanced by considering a more comprehensive *model definition* within the *COMSOL Multiphysics* environment which is the *perfectly matched layer*, instead of the *sound soft boundary* for the open ends of the *TLL* ducts which represents the pressure-release boundary condition, so that predictions could include the end-corrections as a result of any reflection interactions at that region. However, it should be noted that the pressure-release boundary condition is an acceptable and accurate approximation for the low-frequency range of interests as is the case in this project. Also, by further advancing the *model definitions* of the numerical models, the computational cost function would have increased considerably; hence, after consideration the presented models were opted out of the addition of the *perfectly matched layer*.

5.2 Cabinet Geometry

The geometrical optimization of the *TLL* cabinets can be divided into three main areas, namely cabinet volume, the separating distance between the loudspeaker driver (sound source) and the open end of the

TLL duct and the transmission-line length (length of the internal waveguide). Needless to say, all these specific transmission-line cabinet considerations still have to be combined with the general loudspeaker cabinet design considerations such as the cabinet edge diffractions and the interferences caused by the contribution of the cabinet panels vibration to the on-axis pressure within the listening sound field, to name but a few. This project, focuses specifically on the understanding of an acoustically treated transmission-line waveguide and places emphasis on creating and validating a numerical model capable of correct prediction and detailed analysis of the sound propagation within a loaded *TLL*. Therefore, the volume of the loudspeaker cabinets have been kept constant and the effects of the geometrical optimizations on the *TLL* cabinets have been ignored. Similarly, the effect of any kind of optimization on the separating distance between the *TLL* driver and the open end of the waveguide has also been ignored.

5.2.1 Transmission-Line Length

The main characteristic of any transmission-line loudspeaker cabinet is having an internal waveguide attached to the back of the loudspeaker driver to redirect the backward radiations of the driver and use the generated pressure in order to extend the overall low-frequency response of the loudspeaker. The transmission-lines of the *TLL* cabinets can be divided into two main categories, namely uniform and tapered ducts. This project investigates the *TLL* with the uniform ducts. Since the main focus of this project is on the effects of the acoustical treatments within the transmission-lines, the physical length of the internal ducts have been kept constant and the effects of its geometrical optimization has been ignored. However, the addition of the acoustical treatment within the *TLL* waveguide has a direct effect on the imaginary length of the transmission-line, causing significant changes to its overall sound output at the open end of the duct. Therefore, the overall optimization of the length of the transmission-line could be divided into two parts, namely optimization of their internal physical length and the optimization of the acoustical treatments along the internal boundaries of the transmission-line waveguide, which have been looked at in detail in Section 5.3.3.

5.3 Acoustic Treatments

Acoustic treatment within the *TLL* waveguide has a direct effect on the overall audio performance of any transmission-line loudspeaker. Adding a suitable sound absorbent material within the internal boundaries of the *TLL* duct, the mid and high frequencies could be attenuated and the significant resonances can be controlled. *Roberts* in his paper [10] explains that, an empirically found complex wavenumber dependent on the diameter, density and packing density of the fibres of the fibrous sound absorbing samples can be used to model the acoustic treatment within the *TLL* waveguide. *Roberts* also outlines that, by lining the internal boundaries of the *TLL* waveguide with the sound absorbing materials, the speed of sound propagation in the duct will be significantly reduced. In practice this means that the wavelengths of the sound signal in the pipe are effectively reduced. Consequently the required length of the duct that accommodates the lowest designed frequency is reduced. The wave amplitude also decays exponentially with the distance according to the magnitude of the attenuation factor in the empirically found complex wavenumber [10, 16].

5.3.1 Types of Acoustic Treatments

In this category there are two main types of acoustic treatments, based on their design structure and materials, namely locally-reacting and bulk-reacting liners, as explained in Section 2.3, in Chapter 2. The bulk-reacting liners are further divided into two main category, namely fibrous and porous absorbing samples, as in Tables 4.1 and 4.2. It is worth mentioning that the bulk-reacting liners are far more superior to the locally-reacting liners as an acoustic absorbent material and since the audio applications such as the optimization of the *TLL* ducts do not specifically require the use of the locally-reacting liners, such as the aeroacoustic applications, then, this project focuses on the use of the bulk-reacting liners as an acoustic treatment for the optimization. Historically, the fibrous bulk-reacting liners have been used as an acoustic liner such as the research done by *Roberts*, as described in his paper [10].

However, more recently, due to the advances in the design and production of porous plastic open-cell foams, and also since there are far better controls in designing a specific porous plastic foam with a particular flow-resistivity values and density and other relevant physical properties desired, porous materials are far more commonly used by the industry as an acoustic absorbent, as explained by *Wu Qunli* in his paper [27].

5.3.2 Size and Location of Acoustic Treatments

One of the most desirable characteristics of the output (audio sound) from any loudspeaker is to have an on-axis flat frequency response within the whole audible frequency range from 20 to 20 kHz, when the measurement is conducted in an anechoic chamber with the microphone positioned at 1 m distance away from the loudspeaker. The acceptable tolerance for achieving this objective within the audiophile community is ±3 dB [84]. Therefore, in this project the optimization objective has been set to minimize the variability of the on-axis frequency response of the loudspeakers 1 m away from the loudspeaker front panel. Starting with the *TLL* duct completely empty, without any acoustic treatment as in case 1 in Table 5.1, this investigation moves to the case of a *TLL* waveguide completely filled with the sound absorbing materials, as in case 2 in Table 5.1 and then continues to explore the best possible scenario as presented in Table 5.1. In achieving this the cost function Jp can be defined by the equation

$$Jp = \frac{v}{\eta}, \tag{5.1}$$

where v is the variance of the on-axis pressure and can be defined by:

$$v = \left(\frac{1}{\Delta f} \int_{20}^{20kHz} \left(\overline{p^2}(f) - \langle \overline{p^2}(f) \rangle \right)^2 df \right)^{1/2} . \tag{5.2}$$

The on axis pressure is p, $\Delta f = f_{\max} - f_{\min}$ and the $\eta = \langle \overline{p^2}(f) \rangle$ and could be defined by:

$$\eta = \frac{1}{\Delta f} \int_{20}^{20kHz} \overline{p^2}(f) df. \tag{5.3}$$

Figure 5.2 shows the optimization cost functions of a selected range of U-shaped *TLL* ducts, varying in their internal boundary conditions from the *TLL* ducts with hard-walled boundary (zero acoustic treatment, case 1) to the cases acoustically treated with the bulk-reacting liners (cases 2 to 10). It is worth mentioning that the description of the different cases presented in Fig. 5.2 is presented in detail in Table 5.1 below.

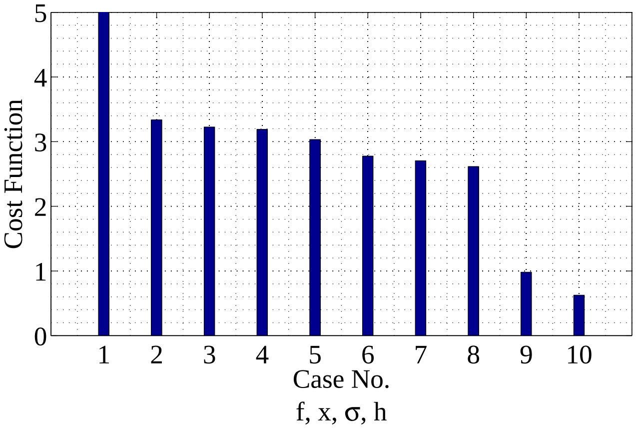

FIGURE 5.2: Optimization cost functions of a selected range of U-shaped *TLLs*. Case 1 exhibit a value of 30.7, whereas case 10 has a value of 0.67.

It can be seen in Fig. 5.2 that the *TLL* duct completely filled (case 2 in Table 5.1), with the value of 3.34, is performing considerably better, almost by a factor of 10, than the *TLL* duct without any acoustic treatment (case 1 in Table 5.1), with the value of 30.7. Also, it should be mentioned that the best presented case 10, with the value of 0.67, is almost lower by a factor of 45 than the worst case 1, with the value of 30.7, in terms of their variability of the on-axis frequency response in 1 m distance away from the loudspeaker front panel. Next, the completely filled *TLL* duct, case 2, is almost higher by a factor of 5 from the best optimized and lowest value presented case 10 in terms of their variability value. These finding indicate, since minimizing the variability of the on-axis frequency response of the loudspeakers is one of the most desired audio characteristic for any loudspeaker and consequently one of the main aims for this project, and by looking at Table 5.1 and Fig. 5.2, that there is a huge variety of cases and acoustical optimization considerations between cases 2 to 10. Therefore, the knowledge and understanding of the necessary and right amount and right location of the sound absorbing liners within the *TLL* waveguide becomes crucial for any acoustical consideration in designing an optimized transmission-line loudspeaker. Table 5.1 shows the complete descriptions of the acoustic lining and the values of the optimization cost-functions *Jp* of a selected range of treated U-shaped *TLL* ducts shown in Fig. 5.2.

Case	*Acoustic Lining Description*	*Cost Function*
1	Hard-walled boundary condition where the duct is completely empty.	30.7
2	Bulk-reacting boundary condition where the duct is completely filled.	3.34
3	Single layer of absorber on all internal boundaries.	3.23
4	Single layer of absorber on all internal boundaries, with an extra layer on the top and bottom corners and on the end of the separating surface.	3.19
5	Single layer of absorber on top and bottom surfaces, and double layers on the separating surface.	3.03
6	Single layer of absorber on top and bottom surfaces, and triple layers on the separating surface.	2.78
7	Double layers of absorber on top and bottom surfaces, and single layer on the back and separating surfaces.	2.70
8	Double layers of absorber on top, bottom and back surfaces and single layer on the separating surface.	2.61
9	Single layer of absorber on all internal boundaries, and quadruple layers covering the open end.	0.98
10	Single layer of absorber on all internal boundaries, and double layers covering the open end.	0.63

TABLE 5.1: Acoustic lining descriptions and the values of the optimization cost-functions *Jp* of a selected range of a treated U-shaped *TLL* ducts as shown in Fig. 5.2.

A selected range of acoustic linings have been presented in Table 5.1 and Fig. 5.2, which represent a huge possibility and different variety of the locations and the amount of sound absorbing materials that can be added inside the *TLL* waveguide. Figure 5.3 shows the schematic model of a *TLL* duct, along with the 3*D* geometry of an acoustically treated *TLL* with a single layer of sound absorbing liner on all of the internal boundaries of the duct and double layers of acoustic lining covering the open end of the waveguide as in cases 1 and 10 respectively in Table 5.1.

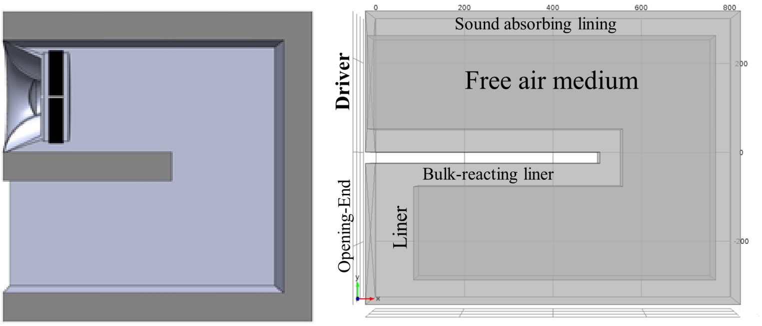

(a)

(b)

FIGURE 5.3: (a) Schematic model of a U-shaped *TLL* duct with hard-walled boundary condition (*as in case* 1) and (b) a *TLL* acoustically treated with a single layer of sound absorbing liner on all its internal boundaries and double layers covering the open end (*as in case* 10). The dark-grey area corresponds to the free-air medium and the light-grey area corresponds to the sound absorbing lining.

In Fig. 5.3 (a), a schematic model of a U-shaped duct with hard-walled boundary conditions on its interior boundaries can be observed. Also, in this figure an acoustical condition within a *TLL* waveguide such as that in case 1 in Table 5.1 can be observed. In Fig. 5.3 (b), the 3*D* geometry of a *TLL* duct, with the dimensions of $0.3 \times 0.3 \times 1.6$ m can be observed, acoustically treated with a single layer of sound absorbing material with the thickness of 0.05 m on its interior boundaries. It should be noted that the open end of the *TLL* duct has also been covered by double layers of acoustic lining. In Fig. 5.3 (b), the dark-grey parts represent the free-air medium within the *TLL* duct and the light-grey area represents the layer of acoustical sound absorbent. Also, in this figure an acoustical condition within a *TLL* waveguide such as that in case 10 in Table 5.1 can be observed. Figure 5.4 shows the 3*D* geometry of an acoustically treated U-shaped *TLLs*. In case (a) waveguide is treated with a single layer of sound absorbing liner on all the internal boundaries apart from the separating surface, and the separating surface is encapsulated by triple layers of sound absorbing liners. The open end of the *TLL* is left untreated without any acoustic lining, as in case 6 in Table 5.1. In case (b) the *TLL* is lined with a single layer of sound absorbing liner on all of the internal boundaries and an extra block of acoustic liner on the top and bottom corners around the U-shaped bend of the duct and the tip of the separating surface, as in case 4 in Table 5.1.

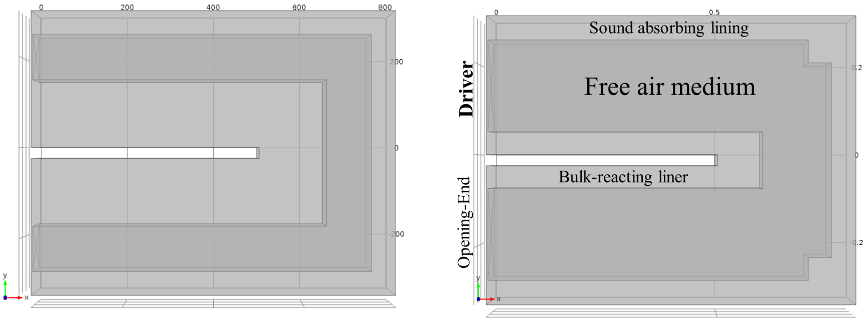

(a)

(b)

FIGURE 5.4: Acoustically treated U-shaped ducts. (a) Duct treated with a single layer of sound absorber on all of the internal boundaries apart from the separating surface, and triple layers of acoustic lining is encapsulating the separating surface (*as in case* 6). (b) Duct treated with single layer of sound absorbing material on all the internal boundaries and an extra block of acoustic liner on the top and bottom corners around the U-shaped bend and the tip of the separating panel (*as in case* 4). The dark-grey area corresponds to the free-air medium and the light-grey area corresponds to the sound absorbing lining.

Once again in Fig. 5.4 (a), the $3D$ geometry of a *TLL* duct, with the dimensions of $0.3 \times 0.3 \times 1.6$ m can be observed, acoustically treated with a single layer of sound absorbing material with the thickness of 0.05 m on its interior boundaries around the top and bottom and back panel. Also, it can be seen that the separating panel of the U-shaped duct has been encapsulated by triple layers of acoustic lining with the thickness of 0.15 m. It should be noted that the open end of the *TLL* has been left untreated in this case. In Fig. 5.4 (a), the dark-grey parts represent the free-air medium within the *TLL* duct and the light-grey area represents the layer of acoustical sound absorbent. Also, in this figure an acoustical condition within a *TLL* waveguide such as that in case 6 in Table 5.1 can be observed. In Fig. 5.4 (b), the $3D$ geometry of a *TLL* duct, with the dimensions of $0.3 \times 0.3 \times 1.6$ m can be observed, acoustically treated with a single layer of sound absorbing material with the thickness of 0.05 m on its interior boundaries. Also, as can be seen, an extra block of acoustic lining with the dimension of 0.05×0.05 m has been added to the top and bottom right corners, as well as the tip of the separating panel within the U-shaped duct. Also, once again the open end of the *TLL* duct has been left untreated in this case. In Fig. 5.4 (b), the dark-grey parts represent the free-air medium within the *TLL* duct and the light-grey area represents the layer of acoustical sound absorbent. Also in this figure, an acoustical condition within a *TLL* waveguide such as that in case 4 in Table 5.1 can be observed. Figure 5.5 shows the on-axis frequency response function of an acoustically optimized U-shaped *TLL*, where the duct has been acoustically treated with the sample $RG50/135$, with a single layer of acoustic lining on all of its internal boundaries, and double layers covering its open end as described in case 10 in Table 5.1 and can be seen in Fig 5.3, and has been excited with loudspeaker driver.

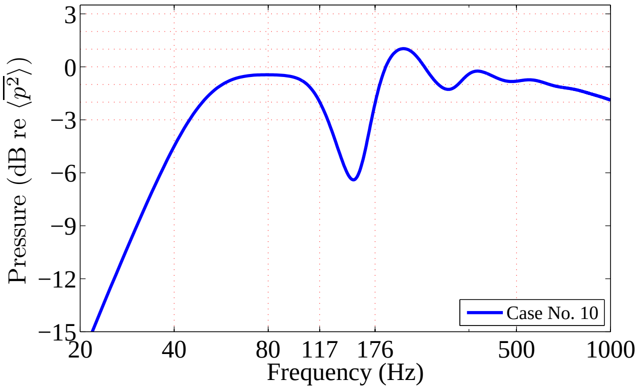

FIGURE 5.5: On-axis frequency response function of an acoustically treated U-shaped *TLL* with the acoustic lining sample $RG50/135$, as described in case 10 in Table 5.1 and can be seen in Fig 5.3 with a driver excitation.

In Fig. 5.5, the on-axis frequency response function of an acoustically optimized transmission-line loudspeaker at low-frequency can be observed as in case 10 in Table 5.1. The on-axis frequency response functions p were found using the Eq. (2.7) where the total volume velocity q, is the combination of the driver volume-velocity $q_d = u_d S_d$, and the open end volume-velocity $q_l = u_l S_l$, where u_d and S_d are the particle velocity and driver diaphragm surface area at position $x = 0$ inside the *TLL* duct, and u_l and S_l are the particle velocity and the cross sectional area at the open end, at position $x = L_x$ along the length of the *TLL* waveguide respectively, as explained in Section 2.1 [1]. The particle velocity at the back of the driver u_d, was found using the lumped parameter model of the driver in conjunction with the *Thiele-Small* parameters of the loudspeaker driver [1]. The particle velocity at the open end u_l, was found using the numerical predictions as explained in Chapter 3. As mentioned previously in Section 5.3.2, the most desired audio characteristic of any loudspeaker system is to have a flat on-axis frequency response at 1 m distance in front of the loudspeaker front panel within the accepted *HiFi* tolerance (±3 dB) [85]. The *Thiele-Small*, low-frequency parameters of a *Visaton B*200 6 Ω driver was used in modelling the loudspeaker driver of the presented optimized *TLL*, as in Table 2.1 in Chapter 2. It should be noted that the resonance frequency, f_s, of the driver used, in free-air is 40 Hz and as can be observed in the frequency response of the optimized *TLL*, the resonance frequency has been pushed up to about 70 Hz. The *TLL* response exhibits 45 Hz at -3 dB, which is increasing to -0.4 dB at 70 Hz. It can be noticed that the optimized response is within the acceptable *HiFi* tolerance of ±3 dB apart from the frequency range of 117 to 176 Hz, where a -6 dB trough can be observed. This trough can be optimized by looking at the geometrical optimization of this *TLL* cabinet and mainly the separation distance between the sound source (driver) and the open end of the *TLL*. However, within the scope of this project, the geometrical optimization has not been considered, as explained in Section 5.2. Figure 5.6 shows the comparison of the on-axis frequency response functions of an acoustically optimized *TLL*, as in case 10, with an acoustically hard-walled boundary condition, as in case 1 from Table 5.1. In case 10 the *TLL* duct is acoustically treated with the sample *RG*50/135, and in both cases 10 and 1 the ducts have been excited with a loudspeaker driver.

In Fig. 5.6, the comparison of the on-axis pressure responses between cases 10 and 1 from Table 5.1 has been shown here, where in case 1 the duct has a hard-walled boundary condition and is completely empty and in case 10 duct is acoustically treated with the sample *RG*50/135. Both cases have a driver excitation. As can be seen in Fig. 5.6, the peaks and

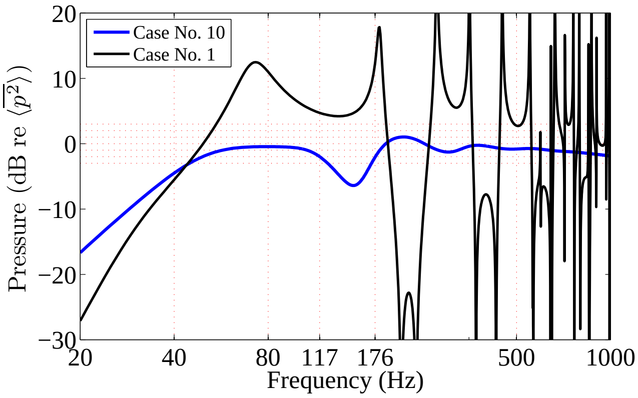

FIGURE 5.6: Comparison of the on-axis frequency response functions of cases 10 and 1 from Table 5.1, where in case 1 the duct has a hard-walled boundary condition and is completely empty and in case 10 duct is acoustically treated with the sample $RG50/135$. Ducts are excited with a loudspeaker driver.

troughs in the response of the *TLL* with hard-walled boundary condition, as in case 1, has been smoothed out in comparison with the response of the acoustically optimized *TLL*, as in case 10. The resonance frequency, f_s, of the loudspeaker driver in free-air is 40 Hz whereas the resonance frequency of case 1 exhibits 0 dB at 50 Hz, and the case 10 exhibits -3 dB at 44 Hz. From that point their difference increases where at 73 Hz the case 1 shows 12.5 dB, whereas case 10 exhibits -0.4 dB. The wide trough that can be seen in the response of the case 1 between the frequency range of 73 to 182 Hz has been completely smoothed out and been slightly shifted to the lower-frequency range at 58 to 110 Hz for the case 10. The shift in the frequency range of the aforementioned trough is due to the acoustic treatments added on the internal boundaries of the case 10, causing the *TLL* to act as if it has an imaginary longer internal length waveguide. It should be noted that the quarter wavelength resonance frequency, $\lambda/4$, in the presented *TLL* duct with the 1.6 m length, correspond to approximately frequency of ≈ 53.6 Hz, which is lower than the maximum output seen in Fig. 5.6 for case 1 at about ≈ 72 Hz. This however, is due to the presence of a very high pressure at the back of the driver position, $x = 0$, inside the waveguide causing a reduction of the driver velocity, resulting in a reduction in the loudspeaker system output, as can be seen in Fig. 2.4 and explained in details in Section 2.2. Therefore, the maximum output that can be observed around the frequency of ≈ 72 Hz is not strictly a resonance frequency of the *TLL* waveguide.

Next, from 180 Hz onwards the case 1 experiences an erratic behaviour which has been smoothed out in case 10 as can be seen in Fig. 5.6. As expected once again the steep and long trough in the response of the case 1 in the frequency range of 182 to 273 Hz has been massively smoothed out by about 20 dB in the response of case 10 and also has been shifted to the lower-frequency range of 117 to 176 Hz. From 273 Hz onwards the response of the acoustically hard-walled case 1, shows an erratic behaviour whereas the optimized *TLL*, case 10, exhibits a smooth response, well within the accepted *HiFi* tolerance (±3 dB), to the end of the frequency presented. Figure 5.7 shows the comparison of the on-axis frequency response functions of an acoustically optimized *TLL*, as in case 10 in Table 5.1, with the two cases 9 and 2, where in case 9 the duct has been acoustically treated with a single layer of sound absorbing liner on all internal boundaries and quadruple layers covering the open end, and in case 2 the *TLL* duct is completely filled with the acoustic absorber. The *TLL* ducts have been acoustically treated with the sample $RG50/135$, with a driver excitation.

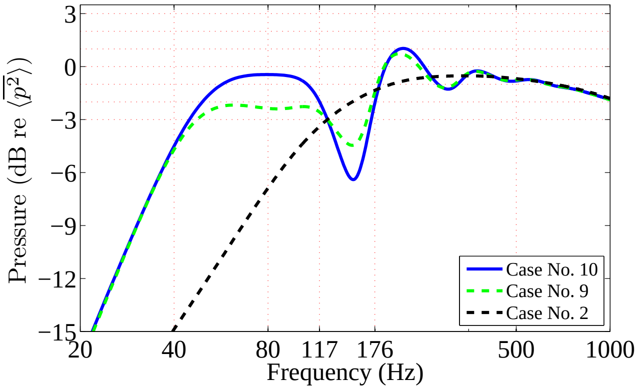

FIGURE 5.7: Comparison of the on-axis frequency response functions of cases 10, 9 and 2 in Table 5.1. In all cases the ducts have been acoustically treated with the sample $RG50/135$, with a driver excitation.

In Fig. 5.7, the frequency response of case 10 in Table 5.1, the optimized *TLL* has been compared with the cases 9 and 2. The ducts have been acoustically treated with the sample $RG50/135$ (pink foam), with a loudspeaker driver excitation. Cases 10 and 9 both have a single layer of acoustic absorbent material with the thickness of 0.05 m on their internal boundaries. However, in case 10 the open end of the *TLL* is covered by double layers of sound absorbing materials, as can be seen in Fig. 5.3 (b), but in case 9 the open end is covered by quadruple layers of acoustic absorbent material, as described in Table 5.1. As their response in Fig. 5.7 indicates, covering the open end with quadruple layers of acoustic liners instead of double layers has smoothed the trough that can be seen in the frequency range of 117 to 176 Hz by about 2 dB from -6.39 to -4.45 Hz. However, the smoothing of this trough has cost the decrease of response in the frequency range of 44 to 117 Hz in case 9 and consequently this acoustic lining design is not the current optimum design, as indicated in Table 5.1. From 117 Hz onwards the cases 9 and 10 exhibit exactly similar response to the end of frequency presented in Fig. 5.7. Case 2 in comparison is over-damped, behaving as a closed-cabinet, since the transmission-line has been uniformly filled by the acoustic absorbent materials sample $RG50/135$. As a result the resonant frequency, f_s, of the TLL in case 2 has been pushed up to the frequency of 117 Hz as can be seen in Fig. 5.7. Also, as a result of over-damped condition in case 2 the peaks and troughs that can be noticed in the response of cases 10 and 9 between the frequency range of 117 to 500 Hz has been smoothed out. From 500 Hz onwards all three cases 10, 9 and 2 follow the exact same pattern. As mentioned previously, the smoothing of the frequency range of 117 to 500 Hz, is at the expenses of pushing the resonant frequency of the loudspeaker system in case 2 to much higher frequency and therefore this acoustic design shows very poor ranking in terms of overall optimization, as can be seen in Table 5.1. Figure 5.8 shows the comparison of the on-axis frequency response functions of an acoustically optimized TLL, as in case 10 in Table 5.1, with the cases 3, 4, 5, 6, 7, and 8 in Table 5.1 in Section 5.3.2. The TLL ducts have all been acoustically treated with the sample $RG50/135$, with a driver excitation.

In Fig. 5.8, the frequency response of case 10 in Table 5.1, the optimized TLL has been compared with the cases 3, 4, 5, 6, 7 and 8. The ducts have been acoustically treated with the sample of porous plastic open-cell foam, $RG50/135$ (pink foam), with a loudspeaker driver excitation. Case 10 has a single layer of acoustic absorbent material with the thickness of 0.05 m on their internal boundaries; also the open end of the TLL is covered by double layers of sound absorbing materials, as can be seen in Fig. 5.3 (b). The description of acoustic lining of cases 3, 4, 5, 6, 7

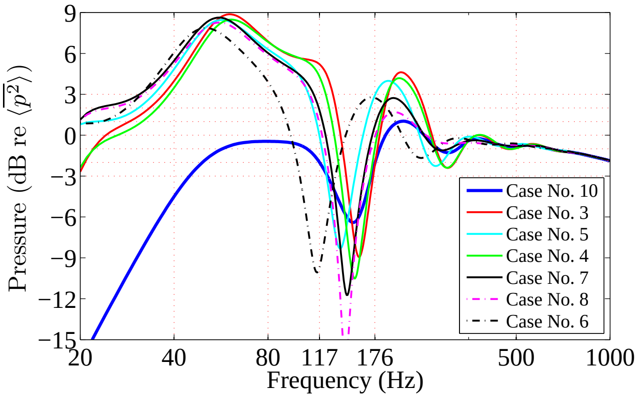

FIGURE 5.8: Comparison of the on-axis frequency response functions of cases 10, with cases 3, 4, 5, 6, 7 and 8 in Table 5.1. In all cases the ducts have been acoustically treated with the sample $RG50/135$, with a driver excitation.

and 8 has been added in Table 5.1. As mentioned previously in Fig. 5.5, the resonance frequency, f_s, of the driver used, in free-air is 40 Hz and as can be observed the resonance frequency of cases 3, 4, 5, 6, 7 and 8 has been pushed up to about 53 Hz. From their resonance frequency at about 53 Hz up to the 500 Hz the responses of the aforementioned cases show an erratic behaviour, with an almost 15 dB trough in the frequency range of 117 to 176 Hz apart from the case 6 where the *TLL* is covered with a single layer of sound absorber around the duct and triple layers encapsulating the separating panel of the duct where the aforementioned trough occurs in the frequency range of 80 to 170 Hz. From 500 Hz onwards, all cases including case 10 follow the exact same trend up to the end of the frequency presented 1000 Hz.

5.3.3 Effect of Acoustic Treatments on Transmission-Line Length

Since generally any loudspeaker system suffers from an insufficient low-frequency response, due to their inefficiency at the low-frequencies, the transmission-line loudspeakers rely on the use of sound absorbing materials added on their internal boundaries to extend their overall response of the loudspeaker at the low-frequency region [86]. As mentioned in Section 5.2.1, one of the main characteristics of any transmission-line loudspeaker is having an internal waveguide attached to the back of the driver to redirect the backward radiations of the driver and use the generated pressure, as a result of driver movement, to extend the overall low-frequency response of the loudspeaker. The addition of the acoustical treatment on the internal boundaries of the *TLL* waveguide also has a secondary direct effect on the imaginary length of the transmission-line, causing significant changes to its overall sound output at the open end of the duct. Figure 5.9 shows the comparison of the on-axis frequency response functions of the analytical and the numerical models of a straight duct with hard-walled boundary condition on the internal boundaries of the duct. In both models, ducts have a driver excitations.

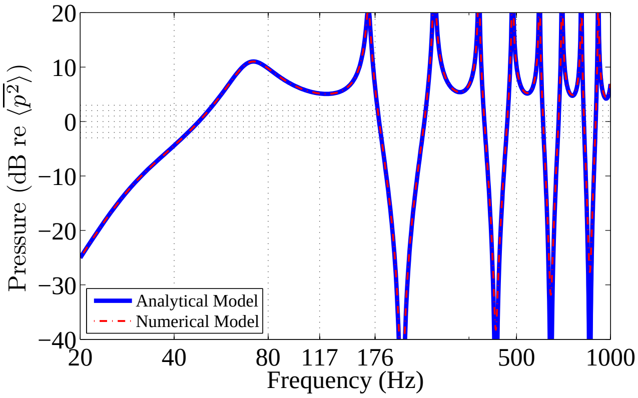

FIGURE 5.9: Comparison of the on-axis frequency response functions of analytical and numerical models of a straight duct with hard-walled boundary condition and driver excitation. Analytical result (*solid line*) and numerical result (*dot dashed line*).

In Fig. 5.9, the analytical and numerical models of a straight duct with the hard-walled boundary condition on the internal boundaries have been compared. In both cases, ducts have a driver excitations. As can be seen in Fig. 5.9, the analytical and numerical models follow the exact same trend throughout the whole frequency range presented. The *Thiele-Small*, low-frequency parameters of a *Visaton B*200 6 Ω driver was used in modelling the loudspeaker driver of the presented models, as in Table 2.1 in Chapter 2. It should be noted that the resonance frequency, f_s, of the driver used, in free-air is 40 Hz. As can be observed in the frequency response of the analytical and numerical models in Fig. 5.9, the resonance frequency has been pushed up to about 48 Hz. A wide trough can be observed in the frequency range of 70 to 165 Hz, and from that point onward the response of the models exhibits an erratic behaviour with steep peaks and troughs to the end frequency presented. It also should be noted that these peaks and troughs have been smoothed out by the addition of the acoustic treatment, optimizing the overall output of the duct, as can be seen in Fig. 5.5. Figure 5.10 shows the comparison of the on-axis frequency response functions of a straight and a U-shaped TLL, (as in case 3 in Table 5.1), where for each of the geometries, two different scenarios have been considered, namely acoustically treated and hard-walled boundary conditions. The acoustically treated ducts, straight and U-shaped, have been lined with a single layer of sound absorber, sample $RG50/135$, on their internal boundaries. All cases have driver excitations.

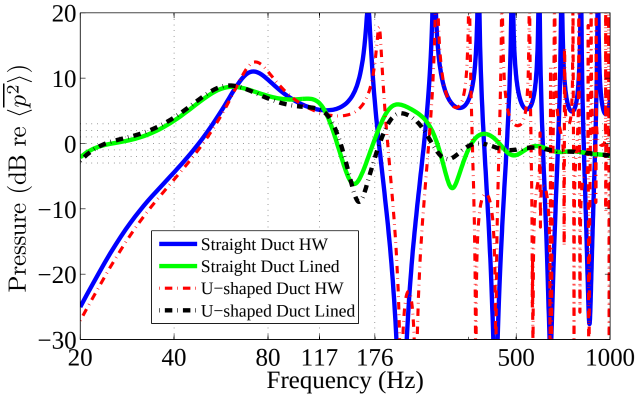

FIGURE 5.10: Comparison of the on-axis frequency response functions of a straight and a U-shaped ducts (as in case 3 in Table 5.1). For each geometry both acoustically hard-walled and treated boundary conditions have been considered. The acoustically treated cases have been lined with the sample $RG50/135$. All cases have a loudspeaker driver excitations. Straight duct results (*solid line*) and U-shaped ducts results (*dot dashed line*).

In Fig. 5.10, the comparison of the on-axis frequency response of straight and U-shaped ducts, (as in case 3 in Table 5.1), can be observed. For each geometry both acoustically hard-walled and teated boundary conditions have been considered. The acoustically treated cases have been lined with the sample $RG50/135$. All cases have a driver excitations. As can be seen in Fig. 5.10, both straight and U-shaped TLL with either of their considered acoustic boundary conditions, hard-walled or lined, follow the same trend along the frequency range presented. The resonance frequency of the straight duct with hard-walled boundary condition exhibits 0 dB at 48 Hz whereas the U-shaped TLL exhibits 0 dB at 50 Hz.

There is 12.5 dB peak at 73 Hz in the response of both straight and U-shaped ducts, where the U-shaped duct response is higher by about 1.5 dB. From that frequency, a wide trough can be noticed in the responses of both ducts where in the case of the straight duct it peaks at 166 Hz and in the case of U-shaped ducts it peaks at 181 Hz. There is also a close similarity in the responses of the straight and U-shaped duct that have been acoustically treated throughout the whole frequency range presented. In both cases, straight and U-shaped duct, the acoustically treated ducts exhibit shift in their response compared to their hard-walled scenarios as can be seen in Fig. 5.10 for the trough in the frequency range of 169 to 275 Hz in the hard-walled cases which has shifted to the lower frequency range of 120 to 207 Hz in the acoustically treated cases. This shift in the frequency response of the acoustically lined ducts indicates that the speed of sound within those ducts has been considerably slowed down and duct is acting as if it has a much longer internal duct. Figure 5.11 shows the effect of acoustic treatment on the imaginary length of the *TLL* waveguide by comparing two scenarios of acoustically treated U-shaped *TLL* with the hard-walled case: when in the first scenario, the ducts have the same internal length of 1.6 m and in the second scenario, the acoustically treated U-shaped *TLL* is 1.6 m and the hard-walled duct is 2.1 m long.

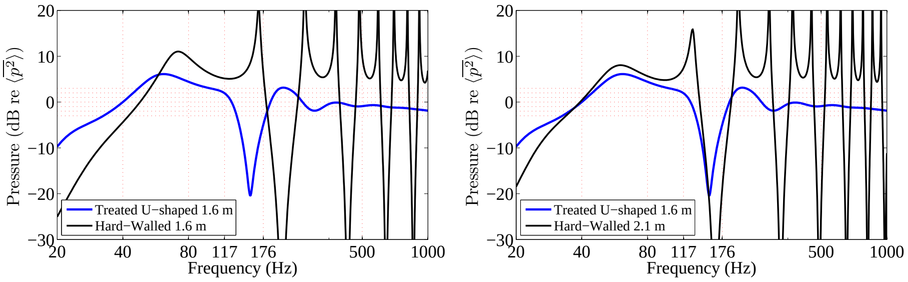

(a) (b)

FIGURE 5.11: The effect of acoustic treatment on the imaginary length of the *TLL* waveguide. (a) Comparison of acoustically treated U-shaped *TLL* with the hard-walled case when both ducts have the same physical duct length of 1.6 m and (b) comparison of acoustically treated U-shaped *TLL* with 1.6 m duct length with the hard-walled case with 2.1 m duct length.

In Fig. 5.11, the effects of acoustic lining on the imaginary length of the internal waveguide within a *TLL* has been illustrated. As can be seen in Fig. 5.11 (a), when the length of the hard-walled case is the same as the acoustically treated U-shaped *TLL*, 1.6 m for both cases, the steep trough that can be seen in the response of the hard-walled case in the frequency range of 169 to 269 Hz, correlates with the damped, yet still steep trough in the response of the acoustically treated U-shaped *TLL* in the frequency range of 117 to 203 Hz. This shift in the frequency response of the acoustically treated U-shaped *TLL* is due to the addition of acoustic lining, causing the speed of sound within its waveguide to considerably slow down acting as if the treated waveguide had a much longer internal duct [87]. It should also be noted that the resonance frequency of the treated U-shaped duct is exhibiting 0 dB at 40 Hz whereas the resonance frequency of the hard-walled case is 48 Hz. Now in contrast, in Fig. 5.11 (b), when the length of the hard-walled case is extended to 2.1 m, so its resonance frequency matches the one from the treated duct with 1.6 m length, at 40 Hz, which is also the resonance frequency of the driver used (*Visaton B*200 6 Ω shown in Table 2.1 in Chapter 2), it can be seen that the aforementioned trough, initially in Fig. 5.11 (a) in the frequency range of 117 to 203 Hz, has been narrowed and shifted to the frequency range of 130 to 203 Hz. This clearly indicates the effects of acoustic treatment on the imaginary length of the waveguide within the transmission-line loudspeakers corresponding well with the documented literature, as *Roberts* also outlines that, by lining the internal boundaries of the *TLL* waveguide with the sound absorbing materials, the speed of propagating sound within the duct will be significantly reduced [10]. In practice this means that the wavelengths of the sound signal in the pipe are effectively reduced. Consequently the required length of the duct that accommodates the lowest designed frequency is reduced. The wave amplitude also decays exponentially with the distance according to the magnitude of the attenuation factor in the empirically found complex wavenumber [10, 16]. Also, it can be easily calculated that for a *TLL* duct, acoustically hard-walled boundary condition on the internal boundaries, with the length of 2.1 m the lowest frequency that can propagate within it is 40 Hz. This calculation corresponds well with the documented requirement for the length of the waveguide which has to be at least a quarter of a wavelength of the lowest frequency of interest, in this case 40 Hz, since this is the lowest frequency that the drive-unit is capable of producing.

5.4 Optimized Transmission-Line Loudspeakers

Finally, applying an acoustic treatment, by considering the optimization requirements and constraint as explained in Section 5.3, an acoustically optimized design can be made. Figure 5.12 shows the $3D$ geometry as well as the on-axis frequency response function of an acoustically optimized U-shaped TLL, where the TLL duct has been acoustically treated with a single layer of acoustic lining on all of the internal boundaries, and double layers covering the open end as described in case 10 in Table 5.1. The TLL duct is acoustically treated with the sample $RG50/135$, and has a driver excitation.

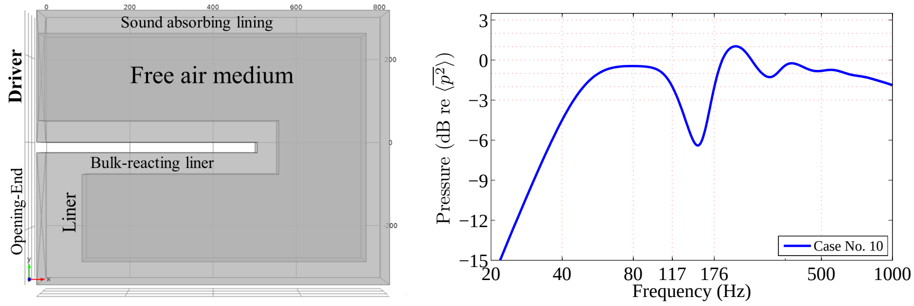

(a) (b)

FIGURE 5.12: Acoustically optimized U-shaped TLL. (a) An acoustically treated U-shaped TLL with a single layer of sound absorbing liner on all its internal boundaries and double layers covering the open end (*as in case* 10 *in Table 5.1*). The dark-grey area corresponds to the free-air medium and the light-grey area corresponds to the sound absorbing lining. (b) On-axis frequency response function of an acoustically treated U-shaped TLL with the acoustic lining sample $RG50$-/135, and a driver excitation.

In Fig. 5.12, the on-axis frequency response function of an acoustically optimized transmission-line loudspeaker at low-frequency can be observed as in case 10 in Table 5.1. As mentioned previously in Section 5.3.2, the most desired audio characteristics of any loudspeaker system is to have a flat on-axis frequency response at 1 m distance in front of the loudspeaker front panel within the accepted *HiFi* tolerance (±3 dB). The *Thiele-Small*, low-frequency parameters of a *Visaton* $B200$ 6 Ω driver was used in modelling the loudspeaker driver of the presented optimized *TLL*, as in Table 2.1 in Chapter 2. It should be noted that the resonance frequency, f_s, of the driver used, in free-air is 40 Hz and as can be observed in the frequency response of the optimized *TLL*, the resonance frequency has been pushed up to about 70 Hz. The *TLL* response exhibits 45 Hz at -3 dB, which is increasing to -0.4 dB at 70 Hz. It can be noticed that the optimized response is within the acceptable *HiFi* tolerance of ± 3 dB apart from the frequency range of 117 to 176 Hz, where a -6 dB trough can be observed. This trough can be optimized by looking at the geometrical optimization of this *TLL* cabinet and mainly the separation distance between the sound source (driver) and the open end of the *TLL*. However, within the scope of this project, the geometrical optimization has not been considered, as explained in Section 5.2. Figure 5.13 shows a cross section of an acoustically treated and fully optimized bookshelf transmission-line loudspeaker.[2]

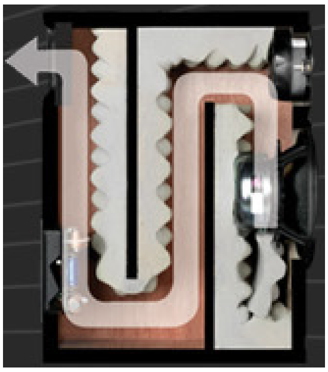

FIGURE 5.13: An acoustically treated and optimized bookshelf *TLL*.

As can be seen in Fig. 5.13, the internal tubing of the loudspeaker has been lined by a selection of the bulk-reacting sound absorbing liner (porous-plastic open-cell foams). It is also noticeable in Fig. 5.13, that the thickness of the sound absorbing liner is varying along the internal length of the waveguide attached to the back of the *TLL* drivers.

---

[2] Picture is courtesy of Professional Monitor Company *PMC*.
$http://www.pmc-speakers.com$

5.5 Conclusion

In this chapter the optimization parameters of a transmission-line loudspeaker was introduced to be the geometrical and the acoustical optimizations. The geometrical optimization of the *TLL* cabinets was further divided into three main groups, namely cabinet volume, the separating distance between the loudspeaker driver and the open end of the *TLL* and the length of the internal waveguide as explained in detail in Section 5.2. It should also be noted, that these specific geometrical optimizations still have to be combined with the general optimizations of the loudspeaker cabinet. However, this project focuses specifically on the understanding of an acoustically treated *TLL* and places emphasis on creating and validating a numerical model capable of correct prediction and detailed analysis of the sound propagation within a loaded *TLL*. Therefore, the effects of the geometrical optimizations on the *TLL* cabinets were ignored. The acoustic treatments within the *TLL* waveguide also have direct effects on the overall audio performance of the *TLL* as explained in detail in Section 5.3. The acoustical optimization parameters were further divided into location, thickness and type of different sound absorbing liners. Also, it was proved that by adding suitable sound absorbing materials within the internal boundaries of the *TLL* duct, the mid and high frequencies could be attenuated and the significant resonances can be controlled. In Table 5.1 selected cases of the U-shaped *TLL* ducts have been looked at, starting from a hard-walled boundary condition case to the best optimized case, as in case 10. Also in Section 5.3.3 the effects of sound absorbing materials on the imaginary length of the *TLL* duct was looked at. It was also proved that by lining the internal boundaries of the *TLL* waveguide with the sound absorbing materials, the speed of sound propagation in the duct will be significantly reduced, which in practice means that the wavelengths of the sound signal in the pipe are effectively reduced. Consequently the required length of the duct that accommodates the lowest designed frequency has been reduced. The wave amplitude also decays exponentially with the distance according to the added sound absorbing materials.

Chapter 6

Conclusion

Loudspeakers are electroacoustical transducers converting electrical energy to acoustical sound waves, as a result of mechanical vibration of their drivers. In most cases this conversion mechanism involves some form of motor assembly attached to a diaphragm. The alternating force generated by the motor assembly, in response to the electrical signal, causes the diaphragm to vibrate. This in turn moves the air in contact with the diaphragm and gives rise to the radiation of the sound. The loudspeaker driver creates acoustic pressure on both sides of the diaphragm. Therefore, a cabinet of some sort is needed to control the sound radiations from the back of the loudspeaker driver. Transmission-line loudspeakers are designed to use the backward radiations of the driver diaphragm, by redirecting them to re-emerge from the open end of the *TLL*, consequently extending the overall low-frequency response of the loudspeaker. Loudspeaker systems suffer from an insufficient low-frequency response, due to their inefficiency at the low-frequencies. Transmission-line loudspeakers rely on the use of sound absorbing materials added on the internal boundaries of their waveguide to extend the overall low-frequency response of the loudspeaker. Therefore, they are most effective at the frequency range of f_s to 1000 Hz, where f_s is the resonance frequency of the *TLL* driver. The response of the transmission-line waveguides indicates, that they act such as low-pass acoustic filters; therefore they have been designed and optimized such that the mid and high frequencies were subjected to a large attenuation within the *TLL* duct but the low-frequency sounds re-emerge from the open end of the duct with a phase such that the reinforcement with the direct radiated sound from the woofer would take place as explained in detail in Chapter 1.

Standard numerical techniques within the *COMSOL Multiphysics* environment were used to investigate the characteristics of sound propagation within a range of rectangular cross-section lined ducts at low-frequencies. The numerical results were initially validated against the results of the analytical models for the basic cases of sound propagation within a *TLL* as explained in detail in Chapter 3. It was shown that the created models are capable of correctly predicting the coupling between both the free propagating region and the acoustically treated region with the bulk-reacting sound absorbing liners of the *TLL* as explained in detail in Chapter 4. The analytical models looked into the basic forms of the ducts, namely uniform straight ducts, with a variety of acoustic treatments, hard-walled and locally-reacting sound absorbing liners, and a variety of source excitations, namely pistonic and non-uniform excitation, as explained in detail in Chapter 2. Next, the lumped parameter model of the loudspeaker driver was constructed and combined with the numerical models of the sound propagation behaviour within a range of treated *TLL* as a excitation source. Using the *Thiele-Small* low-frequency parameters of the loudspeaker driver, some of the more complicated electroacoustical parameters such as the total stiffness of the driver suspension and the damping of the driver suspension were found, as explained in detail in Chapter 2. The acoustic impedance at the driver-end, inside the *TLL* duct and the volume-velocity at the open end of the *TLL* waveguide were also estimated using the developed numerical models. A variety of bulk-reacting sound absorbing materials, comprising of a range of fibrous and porous absorbers were characterized by their flow-resistivity and acoustic impedance. Using the impedance-tube in the *ISVR* laboratory, impedance measurements were conducted on the selected range of fibrous and porous sound absorbing samples. The impedance data were then compared with the *Delany and Bazley* [54] and *Wu Qunli* [27] methods which were applied to the flow-resistivity measurements of the same range of fibrous and porous materials respectively, and conducted in the Centre of Acoustic-Liner Technology of *Alenia Aermacchi* in *Italy* using a DC-flow test, and have been used in Chapter 3 to construct the numerical models of the treated *TLL*. Next, the numerical predictions progressed to more complicated cases of ducts, namely L-shaped and U-shaped, lined on the interior boundaries with bulk-reacting acoustic liners. Then extensive in-situ measurements were conducted on a variety of treated *TLL* using a variety of microphone probes, namely *PU-match* and *USP-regular*, from *Microflown Technologies* in order to directly measure the internal sound pressure and $3D$ acoustic-intensity along the length of the *TLL* ducts. The prediction results of the numerical models were then compared with the in-situ measurement results of the sound pressure performed on a range of treated *TLL* as explained in detail in Chapter 4.

Finally, the developed numerical models were used to apply acoustical optimization on a simple-geometry transmission-line loudspeaker cabinet. The *TLL* consist of an acoustically treated waveguide attached to the back of the loudspeaker driver in order to extend the overall low-frequency response of the loudspeaker. The audio performance of the *TLL* can be acoustically optimized by accordingly controlling the internal sound pressure along the length of the *TLL* waveguide. The acoustic treatments within the *TLL* waveguide have direct effects on the overall audio performance of the *TLL* as explained in detail in Section 5.3. The acoustical optimization parameters were further divided into location, thickness and type of different sound absorbing liners. Also, it was proved that by adding a suitable sound absorbing material within the internal boundaries of the *TLL* duct, the mid and high frequencies could be attenuated and the significant resonances could be controlled. In Section 5.3.3, the effects of sound absorbing materials on the imaginary length of the *TLL* duct was looked at. It was also proved that by lining the internal boundaries of the *TLL* waveguide with the sound absorbing materials, the speed of sound propagation in the duct will be significantly reduced, which in practice means that the wavelengths of the sound signal in the *TLL* waveguide are effectively reduced. Consequently the required length of the duct that accommodates the lowest designed frequency is reduced. The wave amplitude also decays exponentially with distance according to the sound absorbing materials used on the internal boundaries.

Chapter 7

Further Work

The work presented in this thesis can be further continued and improved, mainly in three areas: the numerical models, the in-situ measurements performed on the transmission-line loudspeakers and the optimization of *TLL*.

7.1 Numerical Models

There is a number of factors that contribute to the limitations of the numerical models. First, the $3D$ geometries under consideration, which are being drawn using *SolidWorks* $3D$ drawing package. There are many known and documented problems in transferring the $3D$ geometries between the *SolidWorks* and *COMSOL* environments. The drawing capability of the *COMSOL* package is quite limited and therefore a more versatile drawing environment, such as *SolidWorks*, had to be used to offer more comprehensive controls over the $3D$ geometries drawn for the purpose of this project. However, the lines and parts of the imported geometries into the *COMSOL* software are numbered automatically by *COMSOL* and sometimes in a non-sequential order. This in turn creates problems when trying to evaluate the geometry under the consideration along those connected lines or parts. Further research could be done in finding a $3D$ drawing environment that matches better with the *COMSOL* package hence avoiding the aforementioned problems. Next in line of the numerical limitation is that the numerical models use the results of a number of different measurements, one of which is the flow-resistivity, (σ) values, which is inserted for the R_f values in the *COMSOL* and therefore any inaccuracy in those data supplied by the external company, Centre of Acoustic-Liner Technology *Alenia Aermacchi*, will directly affect the accuracy of the numerical models. Also the measure flow-resistivities were measured for the range of flow speed specifically designed for the aeroacoustic applications which was not the case in this project. In the continuation of this project the flow-resistivities could be measured with the specific flow speed suitable for the purpose of the audio applications. Another measurement result used in the presented numerical models were the coefficients of *Delany and Bazley* [54] used for the modelling of the fibrous absorbing materials and the coefficients of *Wu Qunli* [27] used for the modelling of porous absorbing materials. These measurements of the coefficients of *Delany and Bazley* or *Wu Qunli*, were conducted a long time ago with the measurement limitations of their own time and any inaccuracy of those experimental data will again directly affect the outcome of the numerical models presented here. It would be recommended to double check those experimental findings of *Delany and Bazley* and *Wu Qunli* with a new round of measurements on the corresponding materials. Another numerical limitation was that in order to keep the computational cost-function of the presented models as low as possible, a pressure-release boundary condition has been assumed for the modelling of sound propagation at the open end of the duct. The assumption of a pressure-release boundary condition at the open end of the *TLL* ducts contributes to the lack of complete accuracy between the numerical prediction and the in-situ measurements at that region of the duct, as discussed in detail in Section 3.7. For the correct modelling of the open end however, the *TLL* should have been placed in a large cube, representing the listening room in which the *TLL* would be used; large enough to accommodate at least three or four full-wavelengths of the lowest-frequency of interest, 20 Hz, for the purpose of audio applications, and it should use the *model definition* of *perfectly matched layer* within the *COMSOL* environment instead of the *sound soft boundary* representing the pressure-release boundary condition for the open end of the duct. However, by adding this to the models, the size to aspect ratio would become considerably larger and in order to maintain the same modelling resolution the computational cost-function would increase considerably, which has been avoided in the models presented. It should also be noted that the pressure-release boundary condition is an acceptable and accurate approximation for the low-frequency range of interests as is the case in this project. However, due to the intended application of audio research, it is necessary to look at the full-range of audible frequency, 20 to $20k$ Hz; therefore the assumption of pressure-release boundary condition would no longer be applicable. Also as mentioned in Section 2.2 the volume of air in the *TLL* enclosure constitutes an additive stiffness which is refereed to as an acoustic load. The acoustic load inside the waveguides depends on the internal volume of the duct, therefore as the size of the loudspeaker increases so as the acoustic load within the waveguides. In this investigation, to keep the presented models simple and robust, the internal volume of all the *TLL* waveguides have been kept constant and with the same duct length. However, the effect of the acoustic loading of the loudspeaker motion within on the numerical predictions have not been accounted for, which should be included in the future and further advanced numerical models of the *TLLs*.

7.2 In-situ Measurements

There are several different factors in the measurements conducted that created and increased the measurement errors. One of the main limiting factors was the precision of the microphone locations during the measurements in all of the *TLL* waveguides. In the *scan and paint* method used for the measurement conducted on the straight ducts and presented in Section 4.5.2, the *PU-match* microphone was mounted at the end of a 7 m long rod which was rolled backward from the driver position at $x = 0$ to the open end of the duct at $x = L_x$. Due to the long length of the rod also including the microphone stand, the microphone was vibrating as it was rolled backwards to the open end of the waveguide hence reducing the accuracy of the measurements. In the *in-situ sound-intensity* method used for the measurements conducted on the U-shaped ducts, the position of the *USP-regular* microphone mounted on a miniature tripod was changed for each measurement point. Due to the required high number of repetitions of the microphone alignments, there was a possibility of mis-aligning the $3D$-sensor at some of the locations. Next in the list of limiting factors was the signal-to-noise ratio during the data acquisition. For the *scan and paint* method the measurement was performed in the anechoic chamber whereas for the U-shaped duct measurements the tests were performed in the listening room laboratory. Therefore the noise floor was considerably higher than the measurement done in the anechoic chamber. Another limiting factor was the inherent microphone inaccuracy that each and every microphone suffers from. The general inaccuracy in the repeatability of the measurement conditions was another limiting factor in the measurement errors. Also the loudspeaker drivers never behave completely pistonic; hence modelling the drive-unit with the pistonic excitation introduces further inaccuracy and error between the numerical predictions and the direct measurements conducted and presented in Chapter 4. There are different source excitations which have been considered within the presented numerical models in Chapter3, such as pistonic or non-uniform excitations. The pistonic source excitations were then further advanced to use the lumped parameter model of the actual driver used in the measurement using the *Thiele-Small* low-frequency parameters of the loudspeaker driver. However, the current numerical models can be further advanced by including a model of a full-range loudspeaker driver capable of accurately modelling the driver in the frequency range of 20 to $20k$ Hz. The next error factor was the measured low-frequency response of the sound-field inside the *TLL* ducts which were directly affected by the resonant frequency of the loudspeaker driver. In measuring the U-shaped ducts, the point by point measurement technique was used. The separation distance between the measurement points was another limitation factor. A denser measurement with higher resolution can improve that possible error. In the case of the *scan and paint* method which was used for the straight duct measurements the microphone was rolled backwards from the back of the driver position to the open end of the duct. It was not possible within the availability of this project to do an extensive measurement on all ranges of available sound absorbing materials. The analysis could be further solidified by adding further extensive data acquisition on the whole range of treated waveguides.

7.3 Optimization

In this project the optimization was applied on the simple geometry U-shaped *TLL*, and focused only on the acoustical optimization and the geometrical optimization was completely ignored. Further research should include the investigation on the effect of geometrical optimization combined with the acoustical optimization. For example as can be seen in the on-axis frequency response function of an acoustically optimized *TLL* at low-frequency in Fig. 5.5, it can be noticed that the optimized response is within the acceptable *HiFi* tolerance of ±3 dB apart from the frequency range of 117 to 176 Hz, where a -6 dB trough can be observed. This trough can be optimized by looking at the geometrical optimization of this *TLL* cabinet and mainly the separation distance between the sound source (driver) and the open end of the *TLL*. Next, the advanced optimized models should be further validated through a series of direct comparison with the in-situ measurements on the *TLL* cabinets corresponding with the newly developed models. Finally, since this work could be applied in a wide variety of the applications such as ventilation ducts in the architectural design, sound mufflers in the automotive engineering or aircraft engine ducts in the aerospace and aeronautical applications to name but a few, therefore, the future research should also look into those area in order to cover any specific requirement within those aforementioned applications.

Appendix A

Derivations

A.1 Derivation of Analytical Models of *TLL*

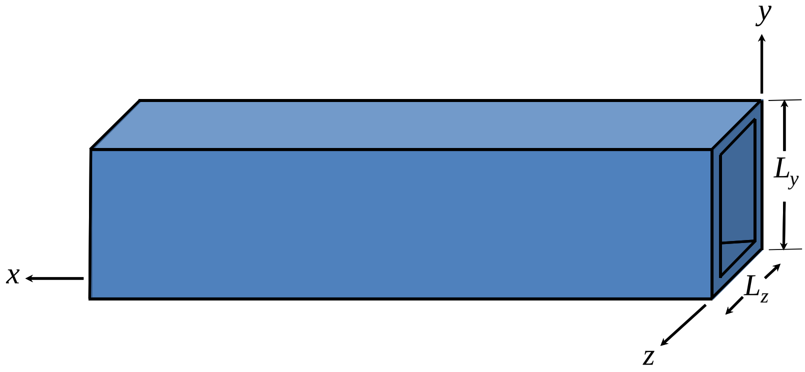

FIGURE A.1: Schematic model of straight duct.

Beginning with a simple acoustics model of sound propagating through the duct at a single frequency ω, the complex form of harmonic solution for the acoustic pressure of a plane wave, where the pressure variation p in the duct has positive and negative propagating components, is given by the following equation [25]:

$$p(x,t) = Ae^{(j\omega t - \gamma x)} + Be^{(j\omega t + \gamma x)}, \tag{A.1}$$

where γ is complex propagation coefficient of a progressive wave system given by $\gamma = \alpha + j\beta$ where α is the attenuation factor, β is the acoustic wavenumber and $j = \sqrt{-1}$ [19]. The angular frequency is $\omega = 2\pi f$ and

c is the speed of sound in free-air, f is the frequency parameter and x represents the distance from the source along the axis of the pipe. The parameters A and B are the complex amplitudes of the incident and reflected waves respectively and t is time. The relationship between the pressure p and the particle velocity u is given by the Euler equation. The linear form of the Euler equation is stated in Eq. (A.2). Assuming that fluid quantities consist of a steady component (ambient) denoted by subscript $(_0)$ and a small unsteady component denoted by superscript $(')$, therefore total pressure is $p = p_0 + p'$ and total density is $\rho = \rho_0 + \rho'$, where $p' \ll p_0$ and $\rho' \ll \rho_0$, the linearized Euler equation is given by the following equation [25]:

$$\rho \frac{\partial u}{\partial t} = -\nabla p, \tag{A.2}$$

where $\nabla = \frac{\partial}{\partial x}\hat{\imath} + \frac{\partial}{\partial y}\hat{\jmath} + \frac{\partial}{\partial z}\hat{k}$ in the three dimensional cartesian coordinates, and

$$\hat{\imath} = \begin{bmatrix} 1 \\ 0 \\ 0 \end{bmatrix}, \; \hat{\jmath} = \begin{bmatrix} 0 \\ 1 \\ 0 \end{bmatrix}, \; \hat{k} = \begin{bmatrix} 0 \\ 0 \\ 1 \end{bmatrix}$$

are the unit vectors codirectional with the x, y and z axes respectively. ρ is the total density of the air medium. For sound of single frequency ω, Eq. (A.2) can be solved to give the particle velocity $u(x, \omega)$ with respect to the pressure $p(x, \omega)$

$$j\omega\rho u(x, \omega) = -\nabla p(x, \omega) \tag{A.3}$$

where $p(x, \omega)$ and $u(x, \omega)$ now refer to the complex amplitudes of the pressure and particle velocity respectively. Now substituting for p from $p(x, \omega) = Ae^{-\gamma x} + Be^{\gamma x}$, from Eq. (A.1) into Eq. (A.3) gives the velocity $u(x, \omega)$ to be

$$u(x, \omega) = \frac{-j\gamma}{\omega\rho}\left(Ae^{-\gamma x} - Be^{\gamma x}\right). \tag{A.4}$$

The characteristic impedance is $Z = p/u$. Using Eq. (A.1) and Eq. (A.4) it can be written as

$$Z(x, \omega) = \frac{j\omega\rho}{\gamma}\left(\frac{Ae^{-\gamma x} + Be^{\gamma x}}{Ae^{-\gamma x} - Be^{\gamma x}}\right). \tag{A.5}$$

Evaluating $Z(x, \omega)$ at the back of the driver, inside the *TLL* where $x = 0$ gives the radiation impedance at the back of the driver $Z(x, \omega) \mid_{x=0} = Z_{ab}$

to be

$$Z_{ab} = \frac{j\omega\rho}{\gamma}\left(\frac{A+B}{A-B}\right). \tag{A.6}$$

Now let $r = B/A$ where r is the complex reflection coefficient at the back of the driver. Substituting this into Eq. (A.6) gives

$$Z_{ab} = \frac{j\omega\rho}{\gamma}\left(\frac{1+r}{1-r}\right). \tag{A.7}$$

By rearranging Eq. (A.7) the reflection coefficient r can be found to be

$$r = \frac{(\gamma/j\omega\rho)\,Z_{ab} - 1}{(\gamma/j\omega\rho)\,Z_{ab} + 1}. \tag{A.8}$$

In a lossless medium, $\gamma = jk$, where and $k = \omega/c$, Eq. (A.8) evaluates to [19]:

$$r = \frac{(Z_{ab}/\rho c) - 1}{(Z_{ab}/\rho c) + 1}. \tag{A.9}$$

A.1.1 Applying Boundary Conditions

Applying the boundary condition of continuity of particle velocity at $x = 0$, the velocity at the back of the driver becomes $u(x,\omega)\mid_{x=0}= u_d$. Substituting this into Eq. (A.4) gives

$$u_d = \frac{-j\gamma}{\omega\rho}\left(A - B\right). \tag{A.10}$$

Calculating the complex amplitude B of the reflected wave with respect to A the complex amplitude of the incident wave gives

$$B = A - \left(\frac{j\omega\rho}{\gamma}\right)u_d. \tag{A.11}$$

At $x = L_x$, where L_x is the length of the *TLL* waveguide, the radiation impedance at the open end of the duct is $Z_{al} = p(l)/u(l)$. At the open end of the *TLL* duct a pressure-release boundary condition has been assumed, therefore $Z_{al} = 0$. This condition is assumed since a duct with a small opening experiences a sudden expansion in the cross sectional area, therefore the pressure at the open end of the duct tends to zero and hence:

$$p(x,\omega)\mid_{x=L_x}= p_l = Ae^{-\gamma L_x} + Be^{\gamma L_x} = 0 \tag{A.12}$$

and therefore,

$$B = -Ae^{-2\gamma L_x}. \tag{A.13}$$

Equating Eq. (A.11) and Eq. (A.13) results in

$$A = \frac{j\omega\rho}{\gamma}\left(\frac{u_d}{1+e^{-2\gamma L_x}}\right). \tag{A.14}$$

Eq. (A.14) can be rearranged to give the velocity at the driver-end $u(x,\omega)\mid_{x=0}= u_d$ to be

$$u_d = \frac{-j\gamma}{\omega\rho}\left(1+e^{-2\gamma L_x}\right)A. \tag{A.15}$$

A.1.2 Pressure and Velocity Along the Length of *TLL*

Substituting for B from Eq. (A.13) into Eq. (A.1) gives

$$p(x,\omega) = A\left(e^{-\gamma x} - e^{\gamma(x-2L_x)}\right). \tag{A.16}$$

Now substituting for A from Eq. (A.14) in Eq. (A.16) gives the equation for pressure inside the *TLL* waveguide

$$p(x,\omega) = \frac{j\omega\rho}{\gamma}\left(\frac{e^{-\gamma x} - e^{\gamma(x-2L_x)}}{1+e^{-2\gamma L_x}}\right)u_d. \tag{A.17}$$

To find the equation for the particle velocity inside the *TLL* cabinet, substituting for B from Eq. (A.13) into Eq. (A.4) gives

$$u(x,\omega) = \frac{-j\gamma}{\omega\rho}\left(e^{-\gamma x} + e^{\gamma(x-2L_x)}\right)A. \tag{A.18}$$

Now substituting for A from Eq. (A.14) in Eq. (A.18) gives the equation for the particle velocity inside the *TLL* duct

$$u(x,\omega) = \left(\frac{e^{-\gamma x} + e^{\gamma(x-2L_x)}}{1+e^{-2\gamma L_x}}\right)u_d. \tag{A.19}$$

Using Eq. (A.19) the velocity at the open end of the *TLL* duct become $u(x,\omega)\mid_{x=L_x}= u_l$. Therefore u_l can be found to be

$$u_l = \left(\frac{2e^{-\gamma L_x}}{1+e^{-2\gamma L_x}}\right)u_d. \tag{A.20}$$

The driver volume-velocity is $q_d = u_d S_d$ where u_d is the driver velocity and S_d is the surface area of the driver diaphragm. The volume-velocity at the open end of the *TLL* is $q_l = u_l S$ where u_l is the velocity at the open end of the waveguide and S is the cross sectional area of the open end of the duct. The total volume-velocity q of the *TLL* can be found to be

$$q = u_d S_d - u_l S. \tag{A.21}$$

The total velocity of the *TLL* is $u_t = u_d - u_l$. Therefore the total velocity normalized with respect to the driver velocity is

$$\frac{u_t}{u_d} = 1 - \frac{u_l}{u_d}. \tag{A.22}$$

Therefore the ratio of the total velocity u_t to the velocity at the back of the driver u_d becomes

$$\frac{u_t}{u_d} = 1 - \frac{2e^{-\gamma L_x}}{1 + e^{-2\gamma L_x}}. \tag{A.23}$$

In a lossless medium equation (A.23) becomes:

$$\frac{u_t}{u_d} = \frac{\cos(kL_x) - 1}{\cos(kL_x)}. \tag{A.24}$$

Appendix B

Measurement Results

B.1 Real and Imaginary parts of Impedance-Tube Results

Figure B.1 show the real parts of impedance results of porous and fibrous samples respectively.

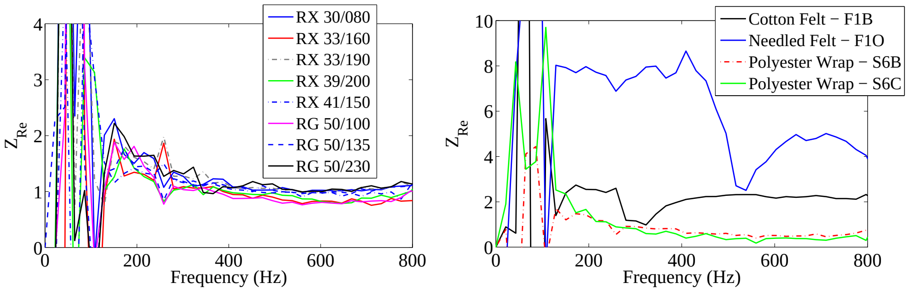

(a)

(b)

Figure B.1: Real parts of impedance results. (a) Porous samples $RX30/080$, $RX33/160$, $RX33/190$, $RX39/200$, $RX41/150$, $RG50/100$, $RG50/135$ and $RG50/230$ and (b) fibrous samples *cotton felt - F1B*, *needled felt - F1O*, *polyester wrap - S6B* and *polyester wrap - S6C*.

Figure B.2 show the imaginary parts of impedance results of porous and fibrous samples respectively.

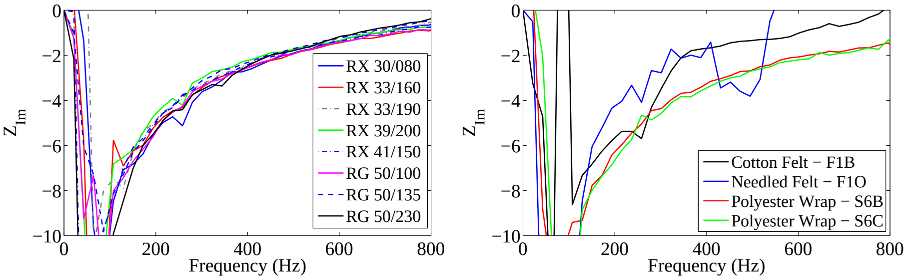

(a) (b)

Figure B.2: Imaginary parts of impedance results. (a) Porous samples $RX30/080$, $RX33/160$, $RX33/190$, $RX39/200$, $RX41/150$, $RG50/100$, $RG50/135$ and $RG50/230$ and (b) fibrous samples *cotton felt - F1B*, *needled felt - F1O*, *polyester wrap - S6B* and *polyester wrap - S6C*.

B.2 DC-Flow Results

The data presented here are the results of flow-resistivity measurements performed by centre of acoustic-liner technology of *Alenia Aermacchi* on a range of fibrous and porous materials.

Table B.1 shows the flow-resistivity values measured using DC-flow test for the samples $RX30/080$, $RX33/160$, $RX33/190$ and $RX39/200$ respectively.

Figure B.3 shows the flow-resistivity values measured using DC-flow test for the samples $RX30/080$, $RX33/160$, $RX33/190$ and $RX39/200$ respectively.

Table B.2 shows the flow-resistivity values measured using DC-flow test for the samples $RX41/150$, $RG50/100$, $RG50/135$ and $RG50/230$ respectively.

Figure B.4 shows the flow-resistivity values measured using DC-flow test for the samples $RX41/150$, $RG50/100$, $RG50/135$ and $RG50/230$ respectively.

Table B.3 shows the flow-resistivity values measured using DC-flow test for the samples *cotton felt - F1B*, *needled felt - F1O*, *polyester wrap - S6B* and *polyester wrap - S6C* respectively.

Figure B.5 shows the flow-resistivity values measured using DC-flow test for the samples *cotton felt - F1B*, *needled felt F1O*, *polyester wrap - S6B* and *polyester wrap - S6C* respectively.

	Area 1	*Area 2*	*Average*
Flow-Speeds [m s^{-1}]	*Light Blue* $RX30/080$ [Pa s m^{-2}]	*Light Blue* $RX30/080$ [Pa s m^{-2}]	*Light Blue* $RX30/080$ [Pa s m^{-2}]
0.20	67900	67700	67800
0.40	84100	83400	83700
0.60	102900	101000	101900
1.05	148000	144700	146300
1.50	195100	191200	193100
2.00	179200	179900	179500
3.00	117400	118800	118100
Flow-Speeds [m s^{-1}]	*Green* $RX33/160$ [Pa s m^{-2}]	*Green* $RX33/160$ [Pa s m^{-2}]	*Green* $RX33/160$ [Pa s m^{-2}]
0.20	40500	40100	40300
0.40	47200	46600	46900
0.60	55500	54500	55000
1.05	75000	73800	74400
1.50	96600	94600	95600
2.00	121800	119200	120500
3.00	119300	119100	119200
Flow-Speeds [m s^{-1}]	*Aqua* $RX33/190$ [Pa s m^{-2}]	*Aqua* $RX33/190$ [Pa s m^{-2}]	*Aqua* $RX33/190$ [Pa s m^{-2}]
0.20	67000	62600	64800
0.40	79600	73500	76500
0.60	93600	86100	89800
1.05	128300	116400	122300
1.50	164300	148900	156600
2.00	176800	176500	176600
3.00	119400	117300	118300
Flow-Speeds [m s^{-1}]	*Sky Blue* $RX39/200$ [Pa s m^{-2}]	*Sky Blue* $RX39/200$ [Pa s m^{-2}]	*Sky Blue* $RX39/200$ [Pa s m^{-2}]
0.20	45100	45000	45000
0.40	53200	52700	52900
0.60	62500	60900	61700
1.05	83600	80800	82200
1.50	106000	102000	104000
2.00	132900	126700	129800
3.00	118500	118900	118700

TABLE B.1: Flow-resistivity values of samples $RX30/080$, $RX33/160$, $RX33/190$ and $RX39/200$ respectively for a range of flow speed.

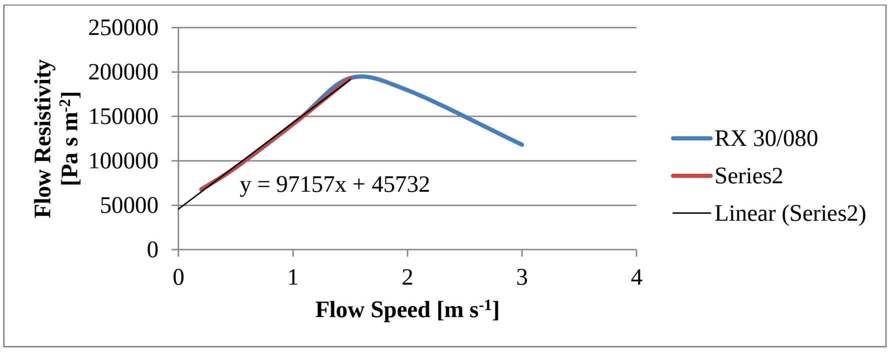

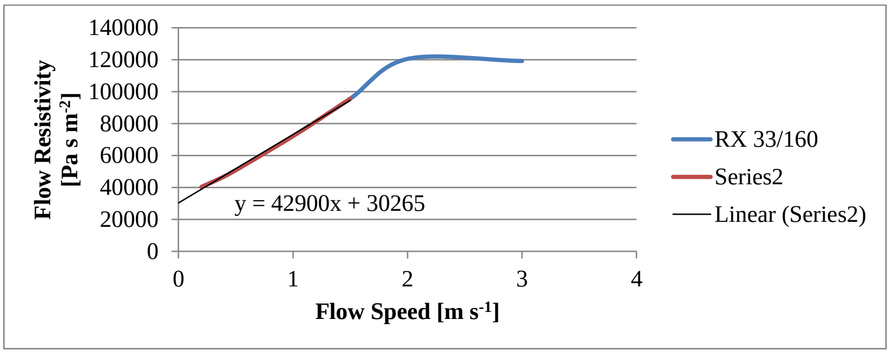

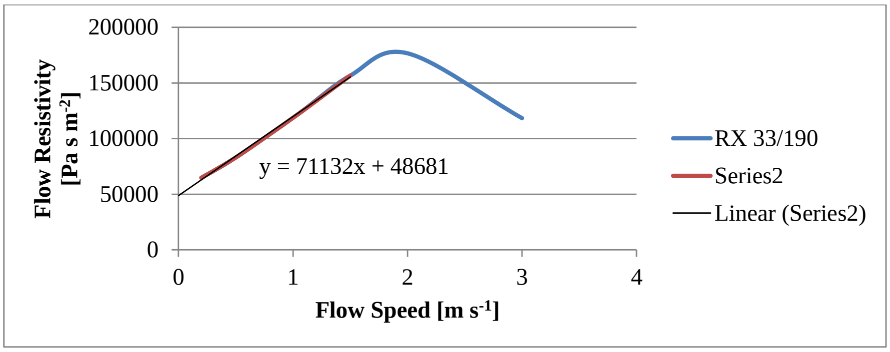

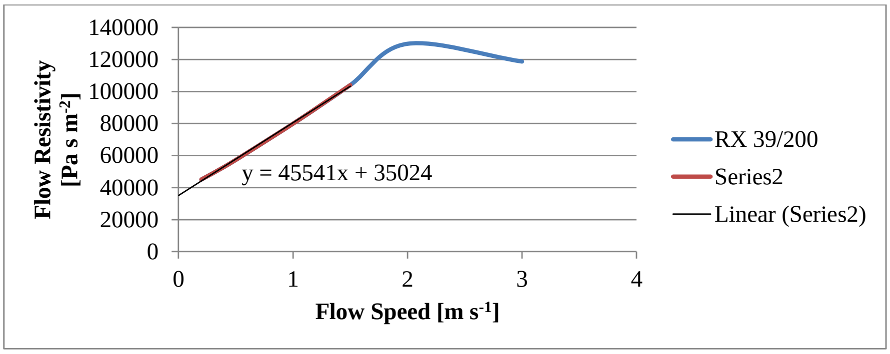

FIGURE B.3: Flow-resistivity values of $RX30/080$, $RX33/160$, $RX33$-$/190$, $RX39/200$ respectively.

	Area 1	*Area 2*	*Average*
Flow-Speeds [m s^{-1}]	*Grey* $RX41/150$ [Pa s m^{-2}]	*Grey* $RX41/150$ [Pa s m^{-2}]	*Grey* $RX41/150$ [Pa s m^{-2}]
0.20	49500	49200	49300
0.40	57900	57400	57600
0.60	67200	66400	66800
1.05	89100	88900	89000
1.50	113100	112900	113000
2.00	140800	140800	140800
3.00	119100	118800	118900
Flow-Speeds [m s^{-1}]	*Gold* $RG50/100$ [Pa s m^{-2}]	*Gold* $RG50/100$ [Pa s m^{-2}]	*Gold* $RG50/100$ [Pa s m^{-2}]
0.20	35300	35200	35200
0.40	42700	42000	42300
0.60	51100	49800	50400
1.05	70900	68400	69600
1.50	92200	89100	90600
2.00	117800	113200	115500
3.00	119600	119100	119300
Flow-Speeds [m s^{-1}]	*Pink* $RG50/135$ [Pa s m^{-2}]	*Pink* $RG50/135$ [Pa s m^{-2}]	*Pink* $RG50/135$ [Pa s m^{-2}]
0.20	43700	44800	44200
0.40	51800	53000	52400
0.60	61100	62200	61600
1.05	83300	84600	83900
1.50	107600	108900	108200
2.00	135600	137100	136300
3.00	118800	119100	118900
Flow-Speeds [m s^{-1}]	*White* $RG50/230$ [Pa s m^{-2}]	*White* $RG50/230$ [Pa s m^{-2}]	*White* $RG50/230$ [Pa s m^{-2}]
0.20	50900	49200	50000
0.40	65100	61800	63400
0.60	81000	76300	78600
1.05	119700	111400	115500
1.50	159500	147900	153700
2.00	176800	176900	176800
3.00	117300	118900	118100

TABLE B.2: Flow-resistivity values of samples $RX41/150$, $RG50/100$, $RG50/135$ and $RG50/230$ respectively for a range of flow speed.

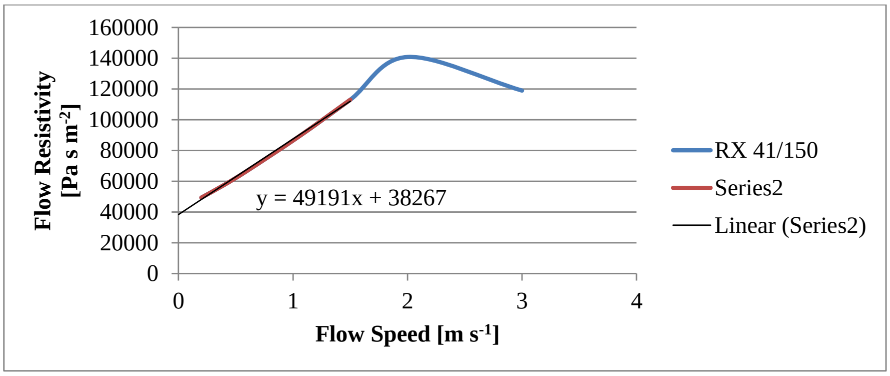

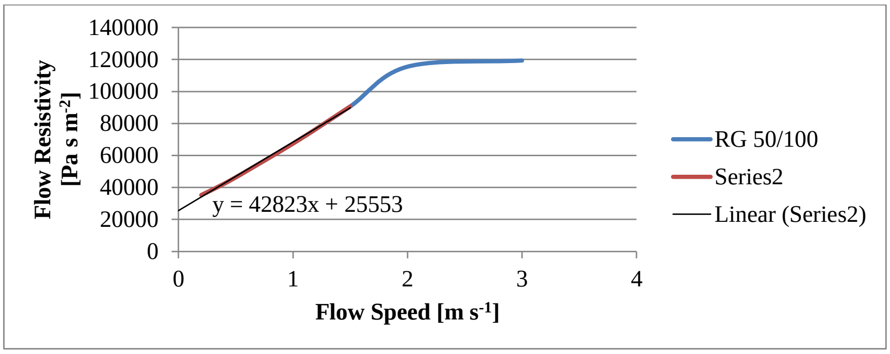

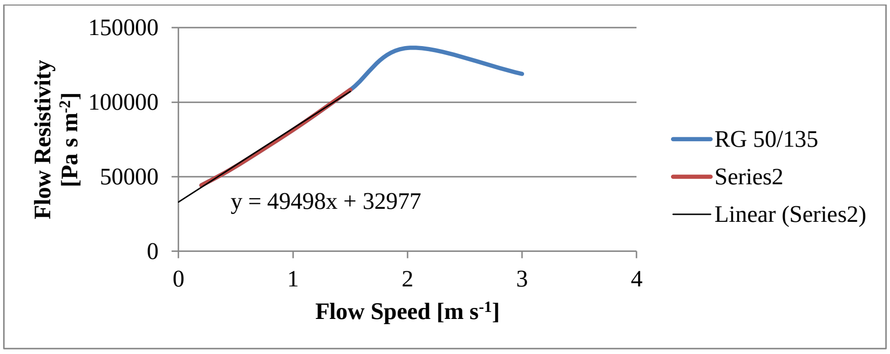

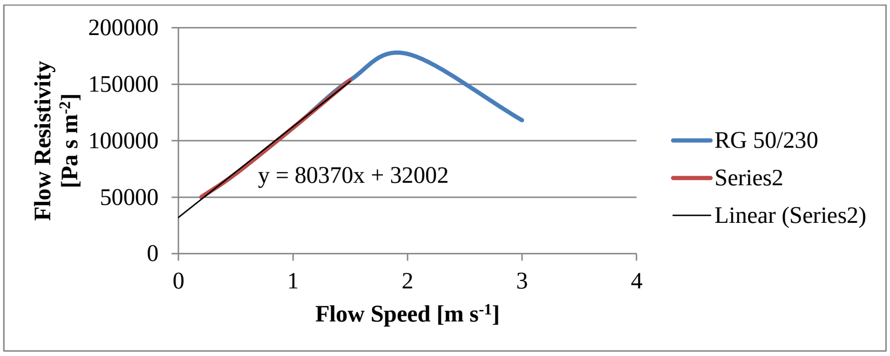

FIGURE B.4: Flow-resistivity values of $RX41/150$, $RG50/100$, $RG50$-$/135$, $RG50/230$ respectively.

	Area 1	*Area 2*	*Average*
Flow-Speeds [m s^{-1}]	*Cotton Felt F1B* [Pa s m^{-2}]	*Cotton Felt F1B* [Pa s m^{-2}]	*Cotton Felt F1B* [Pa s m^{-2}]
0.20	166600	169800	168200
0.40	180600	185100	182800
0.60	195500	199100	197300
1.05	229100	235700	232400
1.50	237000	237500	237200
2.00	176400	176600	176500
3.00	119300	118900	119100
Flow-Speeds [m s^{-1}]	*Needled Felt F1O* [Pa s m^{-2}]	*Needled Felt F1O* [Pa s m^{-2}]	*Needled Felt F1O* [Pa s m^{-2}]
0.20	495100	446100	470600
0.40	523500	482100	502800
0.60	549500	509800	529600
1.05	345600	342900	344200
1.50	240000	238700	239300
2.00	177600	175900	176700
3.00	119700	119400	119500
Flow-Speeds [m s^{-1}]	*Polyester Wrap S6B* [Pa s m^{-2}]	*Polyester Wrap S6B* [Pa s m^{-2}]	*Polyester Wrap S6B* [Pa s m^{-2}]
0.20	11100	11300	11200
0.40	12300	12600	12400
0.60	13600	13700	13600
1.05	16000	16200	16100
1.50	18300	18500	18400
2.00	20600	20800	20700
3.00	25000	25100	25000
Flow-Speeds [m s^{-1}]	*Polyester Wrap S6C* [Pa s m^{-2}]	*Polyester Wrap S6C* [Pa s m^{-2}]	*Polyester Wrap S6C* [Pa s m^{-2}]
0.20	6200	6100	6100
0.40	7100	6900	7000
0.60	7800	7600	7700
1.05	9300	9100	9200
1.50	10700	10600	10600
2.00	12100	11900	12000
3.00	14800	14700	14700

TABLE B.3: Flow-resistivity values of samples *Cotton Felt - F1B*, *Needled Felt - F1O*, *Polyester Wrap - S6B* and *Polyester Wrap - S6C* respectively for a range of flow speed.

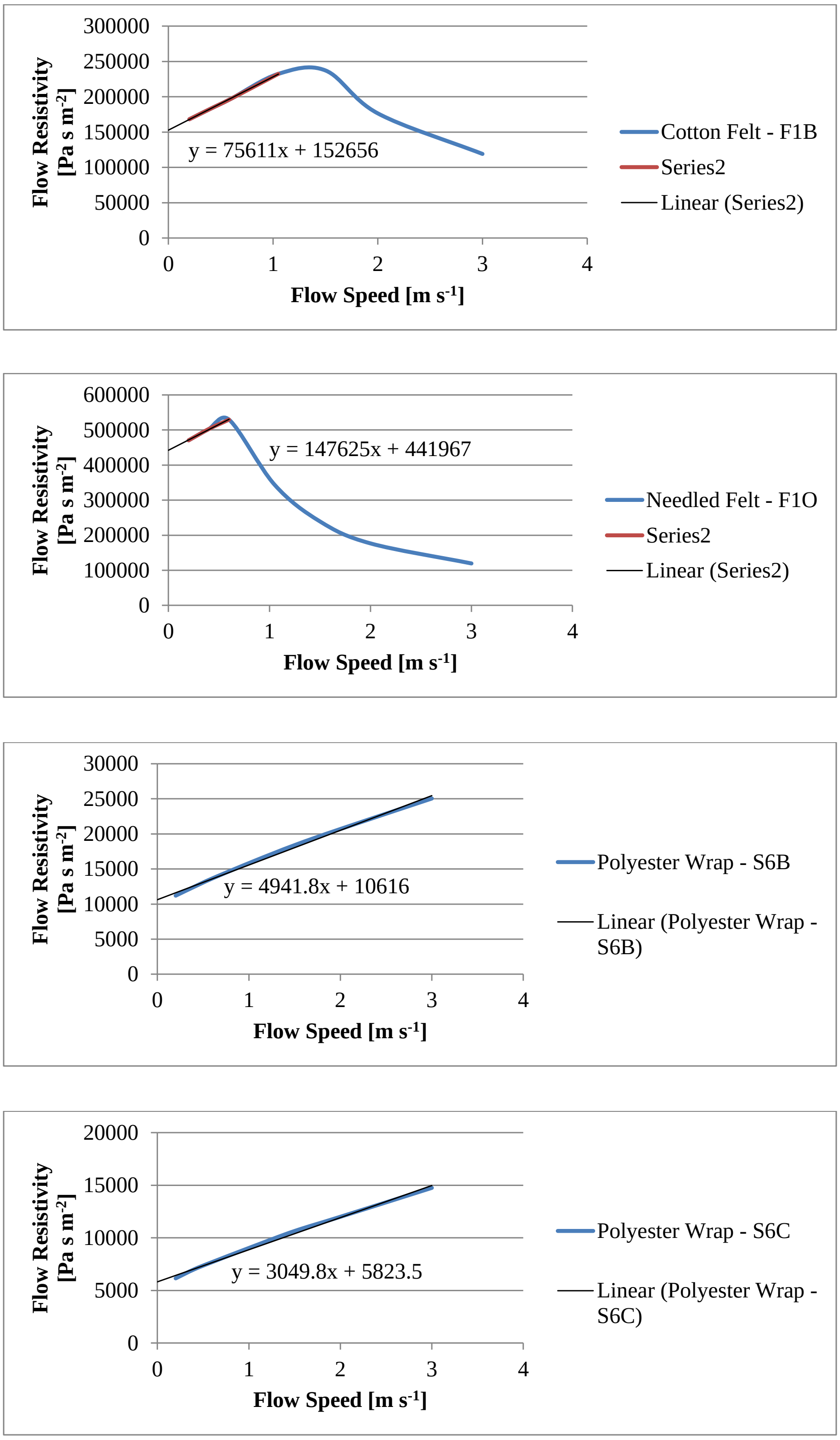

FIGURE B.5: Flow-resistivity values of *cotton felt - F1B*, *needled felt - F1O*, *polyester wrap - S6B* and *polyester wrap - S6C* respectively.

B.3 Numerical Models

B.3.1 Numerical Prediction L-shaped Duct

Figures B.6 and B.7 show the acoustic pressure variation along the length of a L-shaped duct, with non-uniform excitation, lined with a bulk-reacting sound absorbing liner sample $RG50/135$.

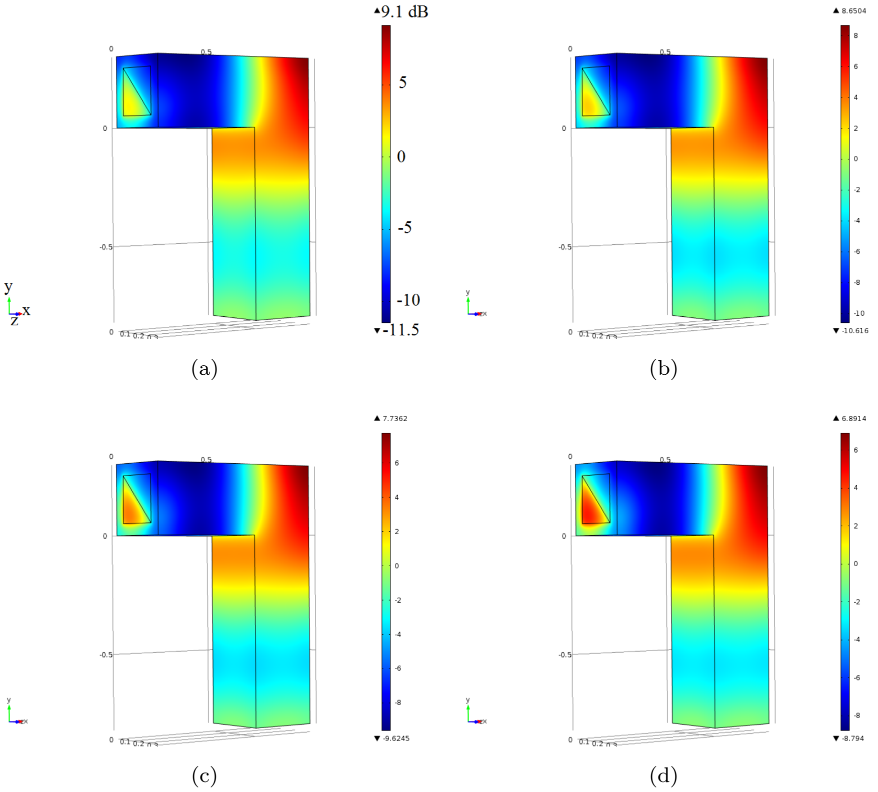

(a)

(b)

(c)

(d)

FIGURE B.6: Acoustic pressure variation along the length of a L-shaped duct, with non-uniform excitation, and acoustically treated with sample $RG50/135$ (pink foam). (a) 200 Hz, (b) 210 Hz, (c) 220 Hz and (d) 230 Hz.

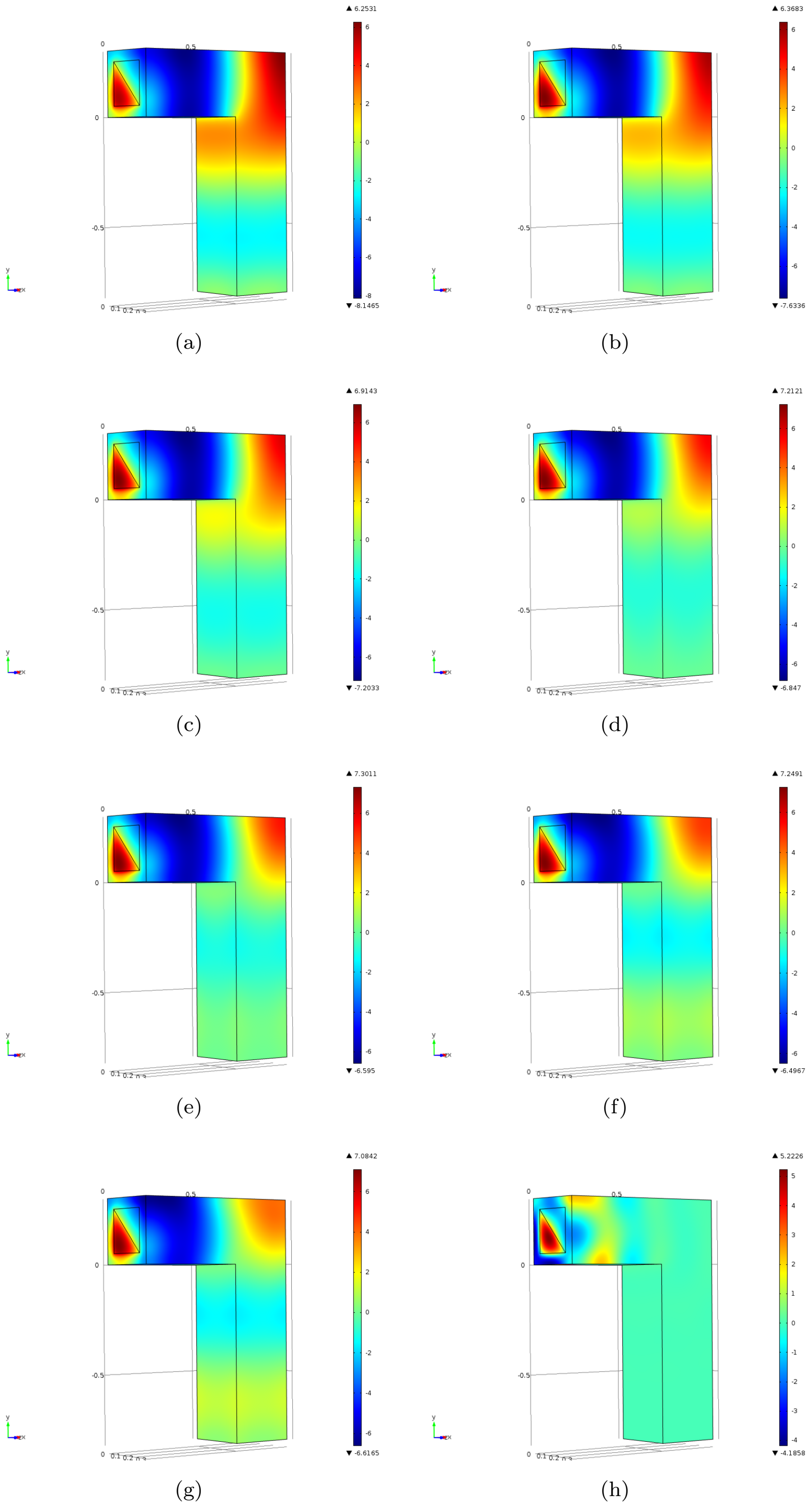

(a) (b) (c) (d) (e) (f) (g) (h)

FIGURE B.7: Acoustic pressure variation along the length of a L-shaped duct, with non-uniform excitation, treated with sample $RG50/135$. (a) 240 Hz, (b) 250 Hz, (c) 260 Hz, (d) 270 Hz, (e) 280 Hz, (f) 290 Hz, (g) 300 Hz and (h) 1000 Hz.

B.3.2 Numerical Models U-shaped Duct

Figures B.8 to B.9 show the acoustic pressure variation along the length of a U-shaped duct, with non-uniform excitation, lined with a bulk-reacting sound absorbing liner sample $RG50/135$, for the frequency range of 20 to 1000 Hz.

B.3.3 Numerical Models U-shaped Duct Isosurface

Figure **??** shows the isosurface variation of acoustic pressure along the length of the U-shaped duct, with non-uniform excitation, lined with a bulk-reacting sound absorbing liner sample $RG50/135$, for the selected frequencies within the range 120 to 310 Hz.

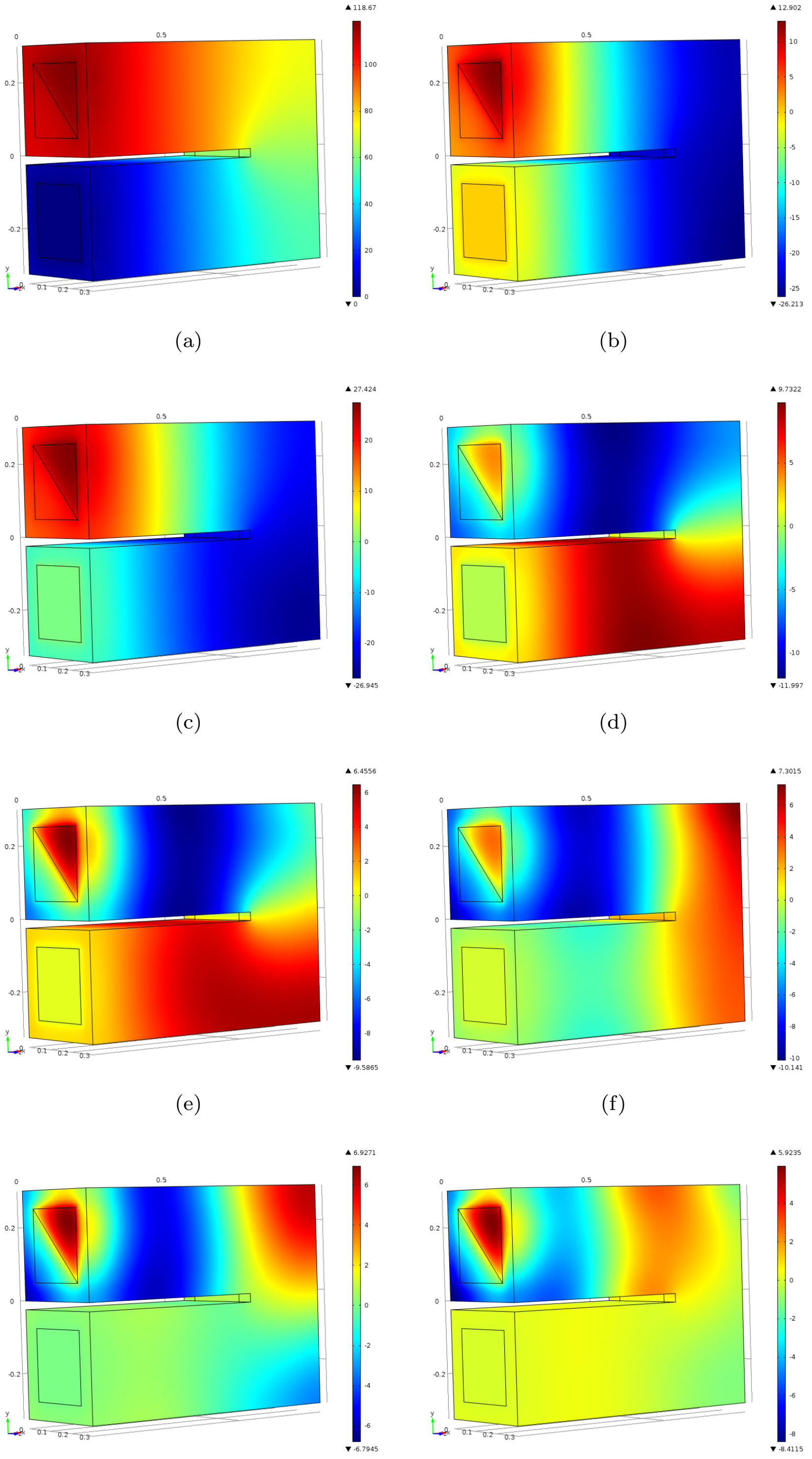

(a) (b)

(c) (d)

(e) (f)

(g) (h)

FIGURE B.8: Acoustic pressure variation along the length of a U-shaped duct, treated with sample *RG*50/135, with non-uniform excitation. (a) 20 Hz, (b) 80 Hz, (c) 100 Hz, (d) 160 Hz, (e) 180 Hz, (f) 200 Hz, (g) 280 Hz and (h) 330 Hz.

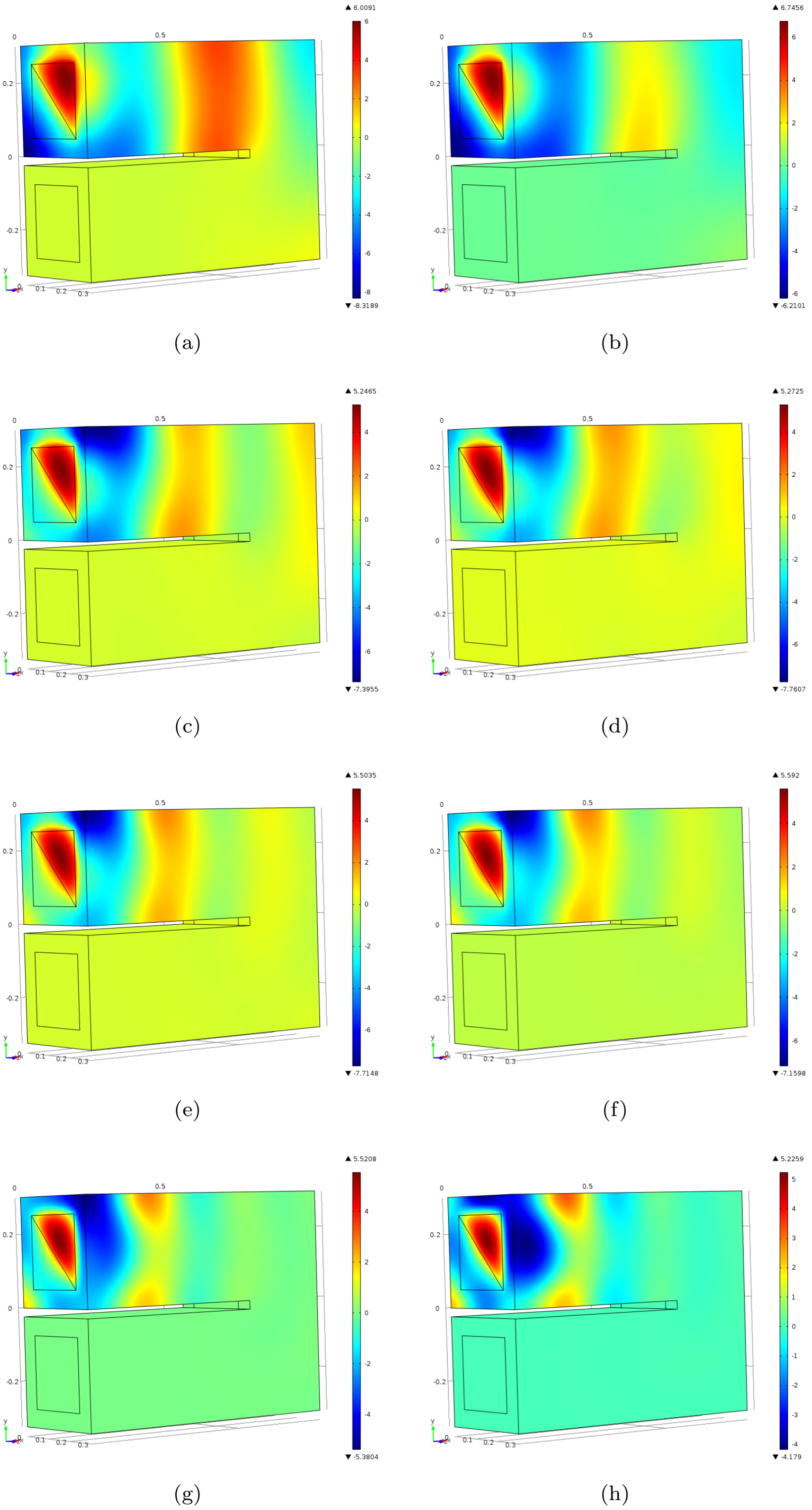

(a) (b) (c) (d) (e) (f) (g) (h)

FIGURE B.9: Acoustic pressure variation along the length of a U-shaped duct, treated with sample *RG*50/135, with non-uniform excitation. (a) 400 Hz, (b) 450 Hz, (c) 570 Hz, (d) 640 Hz, (e) 740 Hz, (f) 800 Hz, (g) 900 Hz and (h) 1000 Hz.

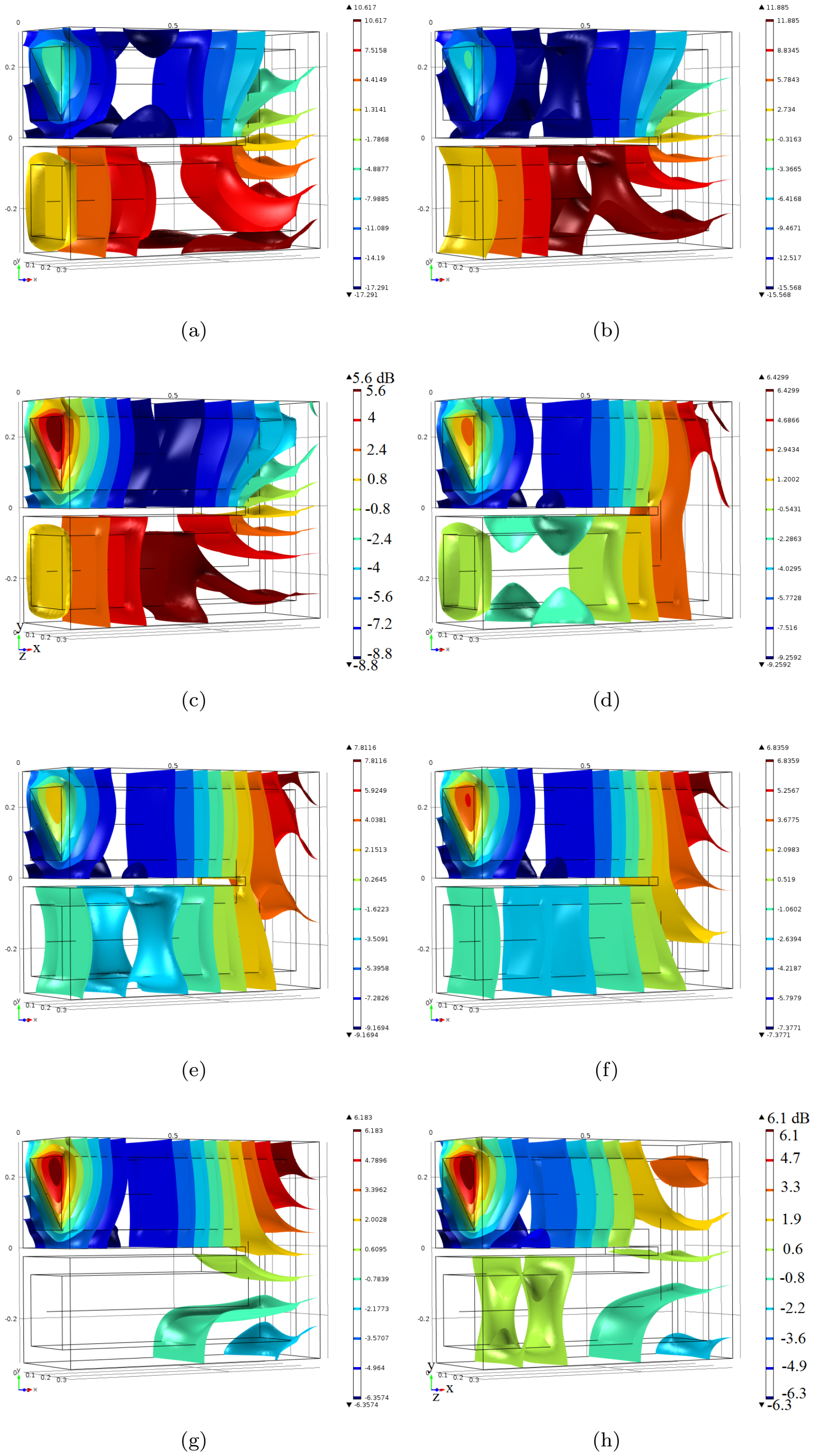

FIGURE B.10: Isosurface acoustic pressure variation along the length of a U-shaped duct, treated with sample $RG50/135$, with non-uniform excitation. (a) 120 Hz, (b) 140 Hz, (c) 180 Hz, (d) 200 Hz, (e) 210 Hz, (f) 240 Hz, (g) 270 Hz and (h) 310 Hz.

B.4 Experimental Evaluation of Ducts

B.4.1 Straight-Duct Pressure Variation Results

Figures B.11 to B.12 illustrate the results of in-situ pressure measurements along the length of the straight duct treated with sample $RG50/135$, at the specified frequencies using the *Microflown PU-Match* sensor.

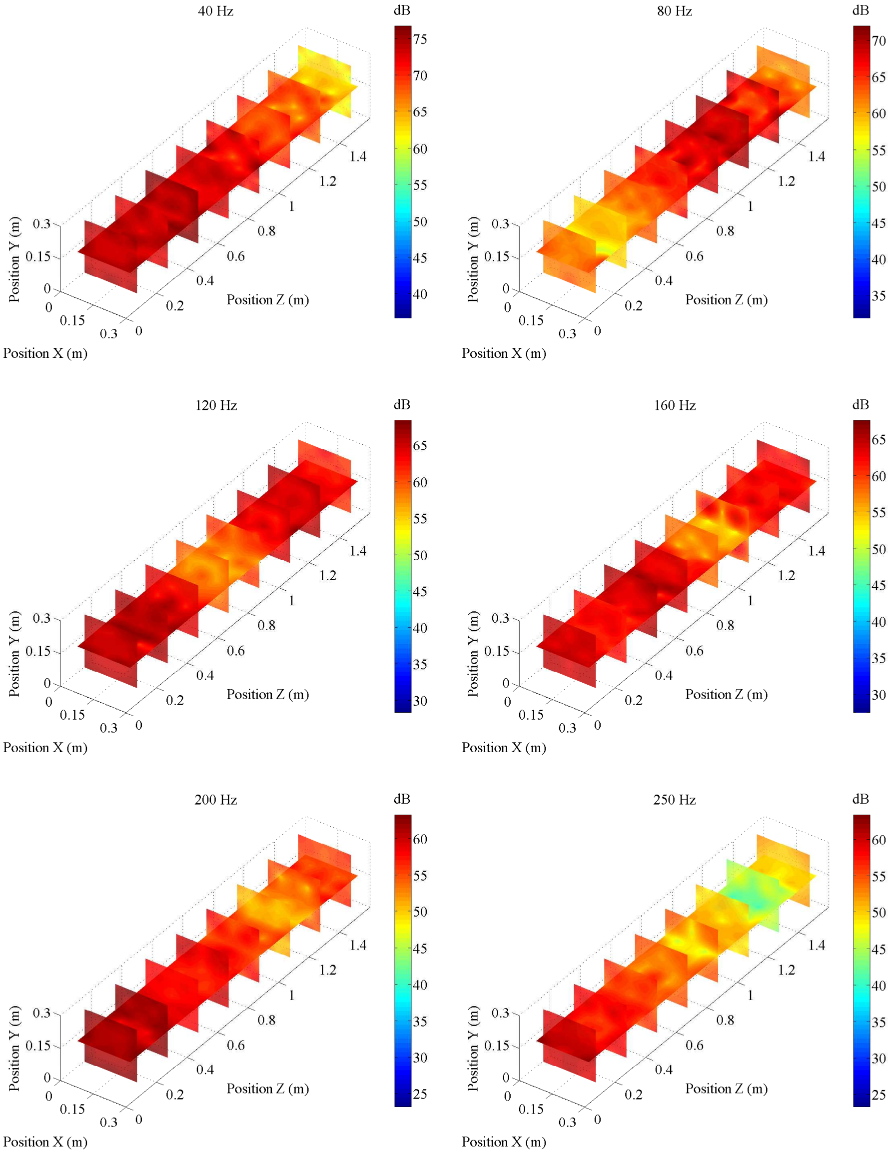

FIGURE B.11: Pressure variation along the length of a straight duct treated with sample $RG50/135$ for a frequency range of 40 to 250 Hz.

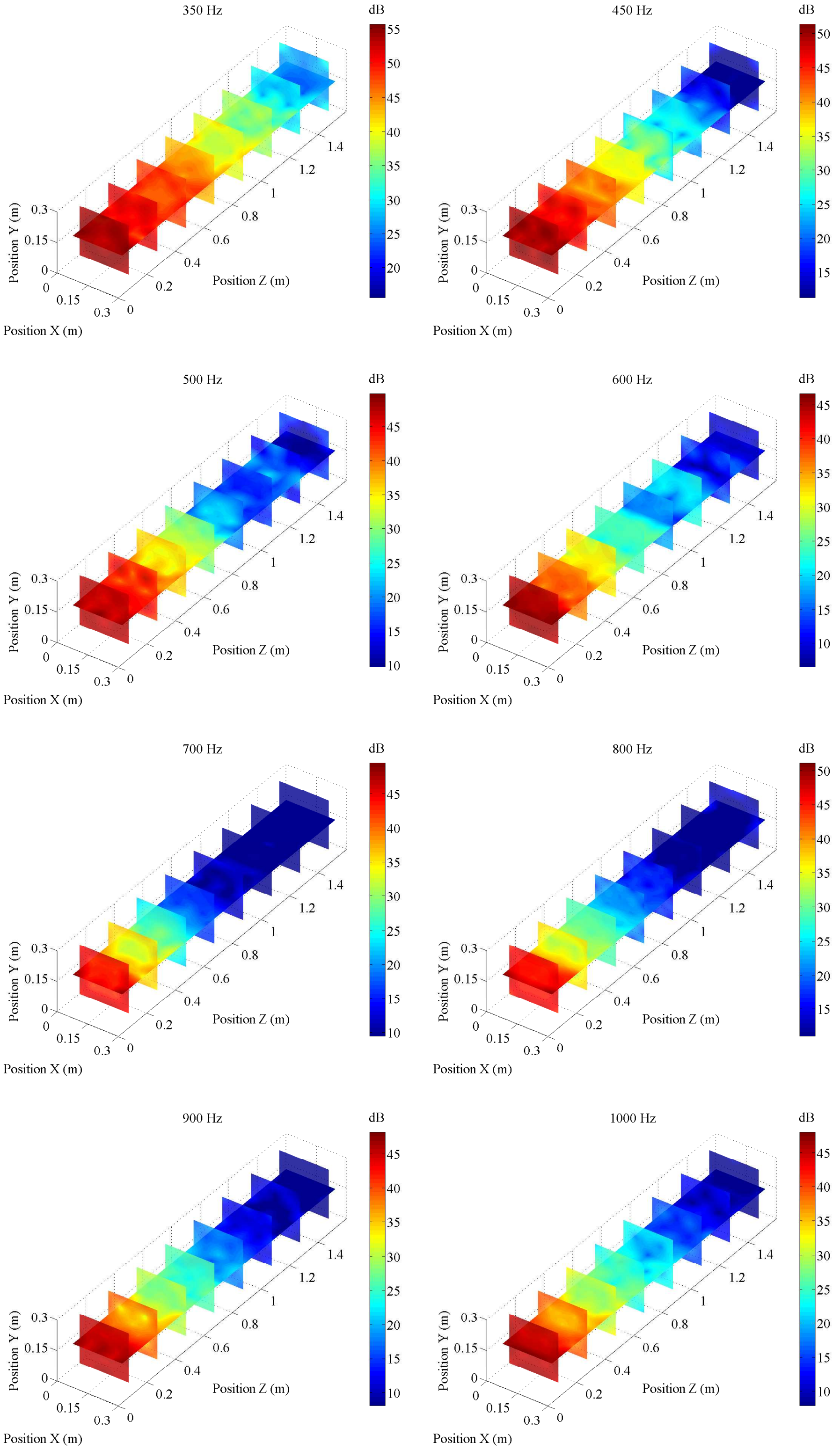

Figure B.12: Pressure variation along the length of a straight duct treated with sample $RG50/135$ for a frequency range of 350 to 1000 Hz.

B.4.2 Detailed Experimental Results Using ***Microflown USP-Regular*** $3D$ Sensor

Detailed experimental results using a *Microflown USP-regular* sensor are described here. Figure B.13 shows the schematic of a U-shaped duct. The selected area in Fig. B.13 where the bend in the U-shaped duct is located, has been measured with high resolution and displayed in the following figures for the frequency range of 40 to 1000 Hz.

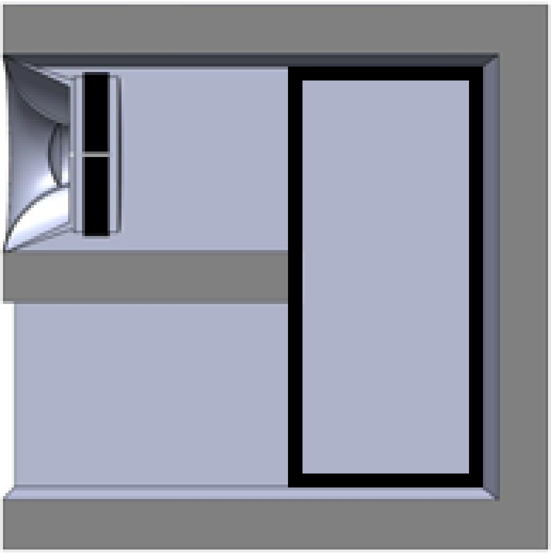

FIGURE B.13: Schematic model of a U-shaped duct. The selected area has been measured in detail for the frequency range $40 - 1000$ Hz.

B.4.3 U-Duct Pressure Results

Figures B.14 to B.15 illustrate pressure measurements of a U-shaped duct with the hard-walled case at a height position 0.25 m at the specified frequencies.

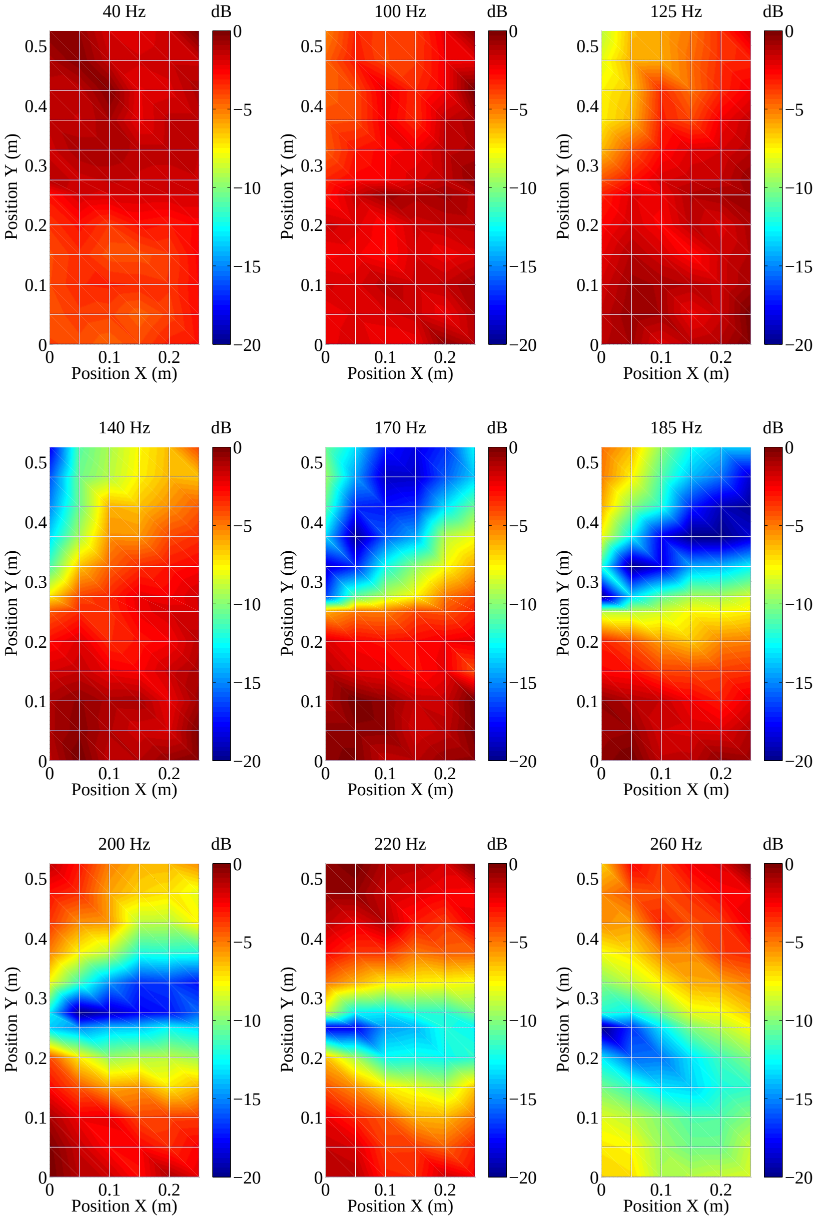

FIGURE B.14: Pressure variation for the U-shaped duct, hard-walled case for a frequency range 40 to 260 Hz.

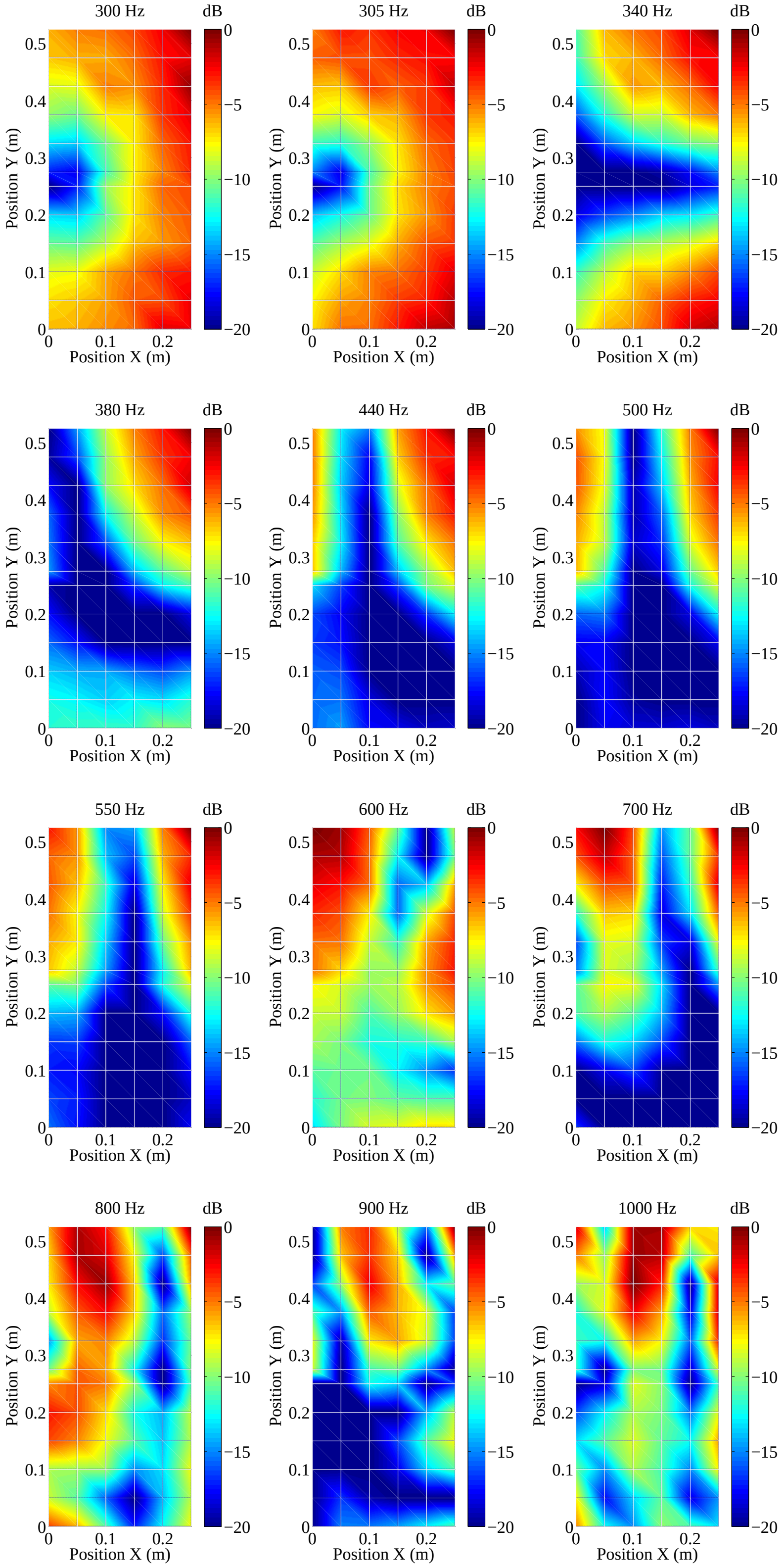

Figure B.15: Pressure variation for the U-shaped duct, hard-walled case for a frequency range 300 to 1000 Hz.

B.4.4 U-Duct Active Intensity Results

Figure B.16 shows the in-situ measurements of the active-intensity inside the U-shaped duct, measured using the *Microflown USP-regular* probe for the frequencies of 145, 385 and 850 Hz [88].

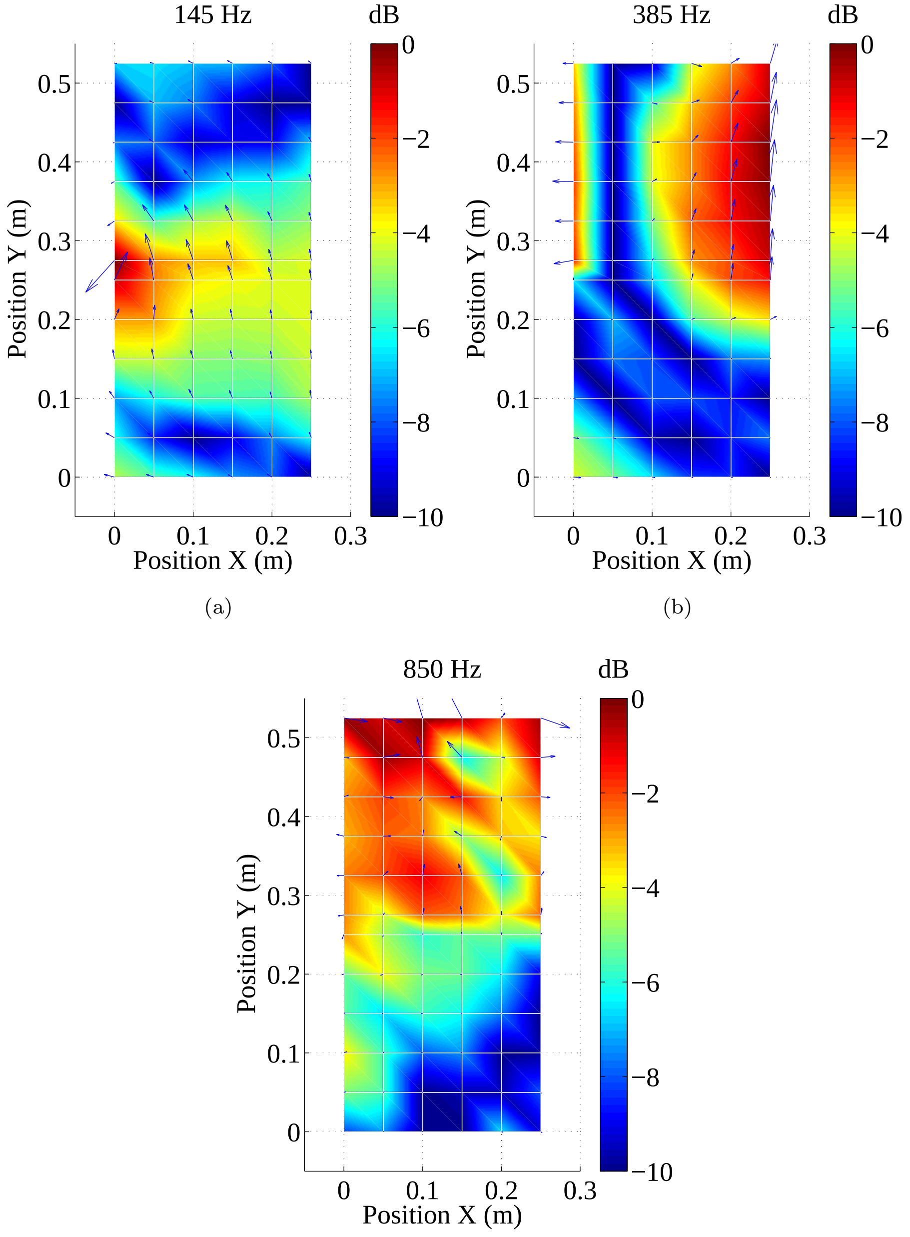

(a)

(b)

(c)

Figure B.16: Active-intensity variation inside the U-shaped duct, measured using the *USP-regular* probe. (a) 145 Hz, (b) 385 Hz and (c) 850 Hz.

The active-intensity variation around the bend region inside the U-shaped *TLL* duct can be seen in Fig. B.16 at three different frequencies. Comparing the results in Fig. B.16 (a) with the selected area in Fig. 4.20, it can be seen that there is a region of high-active-intensity at 145 Hz around and at the tip of the separating panel in the U-shaped duct. It can also be seen that there are two regions of low-active-intensity encapsulating the high-active-intensity region around the separating panel of the duct, with the lowest intensity concentration at the two corners of the bend area. It should also be noted that the arrows in Fig. B.16 show the direction that the active-intensity is tending towards. In Fig. B.16 (b) as the frequency progresses to 385 Hz, the high-intensity region located around and at the tip of the separating panel in Fig. B.16 (a) is now transformed to the low-active-intensity at the tip of the separating panel and creates a distinct region of high-intensity as well, which is concentrated on the top-right corner of the waveguide bend. In Fig. B.16 (c) as the frequency increases even further to 850 Hz, the low-intensity region at the tip of the separating panel in Fig. B.16 (b) has moved to the bottom-right corner of the U-shaped duct creating two regions of high and low active-intensities. It is worth mentioning that the active-intensity is an equivalent term for acoustic intensity, interpreted as a time-average quantity. The term is mainly applied to single-frequency sound fields, where it is useful to contrast active and reactive-intensity components. It should be noted that if the acoustic pressure and particle velocity in a single-frequency $3D$ sound-field are represented by [19]

$$\begin{aligned} p &= Re[\tilde{p}(x)e^{j\omega t}], \\ u &= Re[\tilde{u}(x)e^{j\omega t}], \end{aligned} \tag{B.1}$$

where $\tilde{p}$ and $\tilde{u}$ are the complex pressure and velocity amplitudes at vector position x respectively, then the active-intensity vector, I_A, is [19]

$$I_A = \frac{1}{2} Re[\tilde{p} * \tilde{u}], \tag{B.2}$$

where $*$ is the complex conjugate. An equivalent expression based on the rms pressure, p_{rms}, and the phase gradient, $\nabla\varphi$, is [19]

$$I_A = -\frac{p_{rms}^2}{\omega\rho} \nabla\varphi, \tag{B.3}$$

where φ is the arg $\tilde{p}$, and where ρ is the fluid density. It should also be noted that these relations apply to lossless fluids with no mean flow [19]. Figures B.17 and B.18 illustrate active intensity measurements of the U-shaped duct for the hard-walled case at a height position 0.25 m at the specified frequencies.

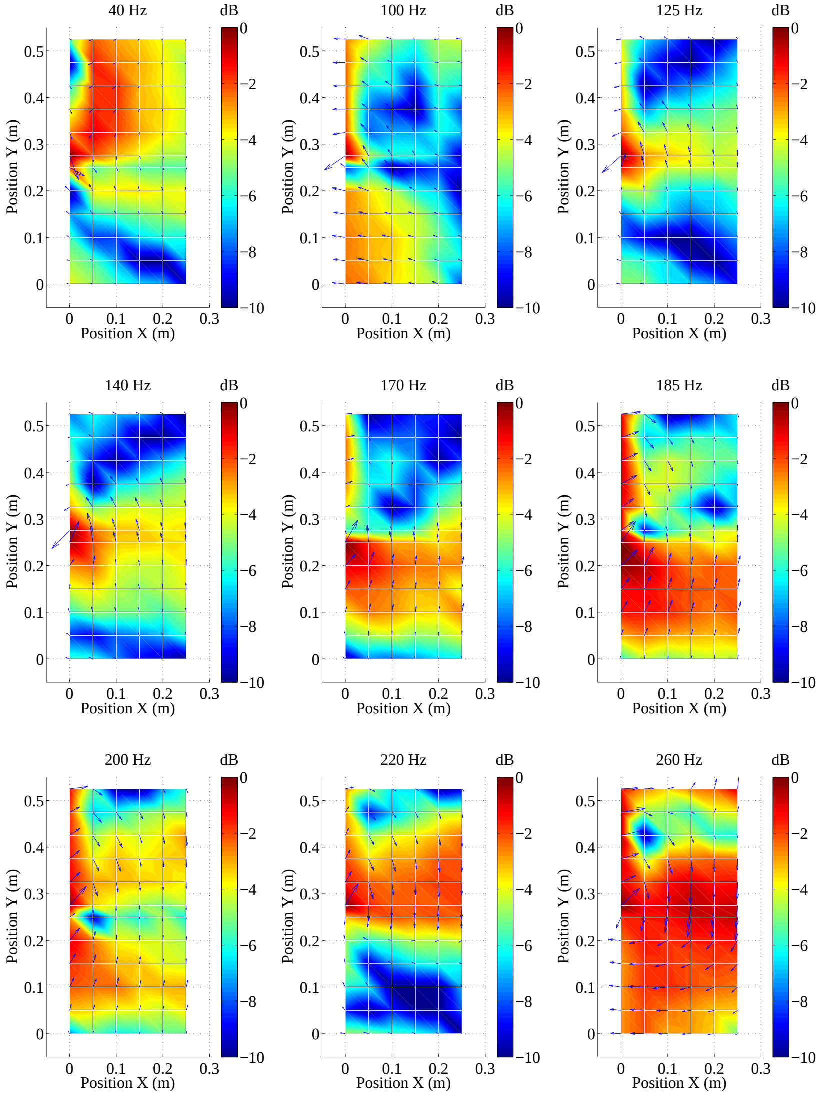

Figure B.17: Active intensity measurements for the U-shaped duct, hard-walled case for frequency range 40 to 260 Hz.

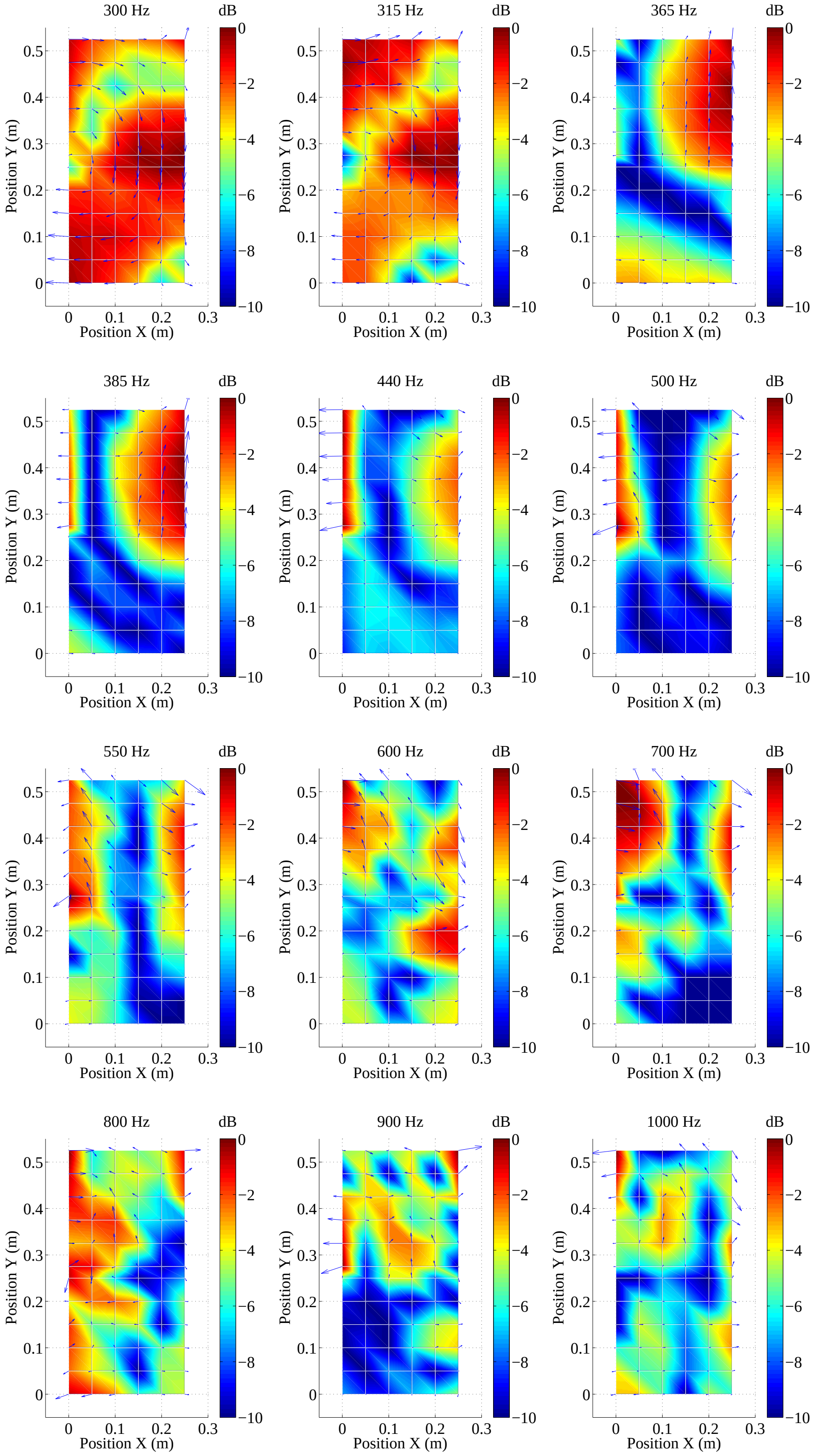

FIGURE B.18: Active intensity measurements for the U-shaped duct, hard-walled case for frequency range 300 to 1000 Hz.

B.4.5 U-Duct Reactive Intensity Results

Figure B.19 shows the in-situ measurements of the reactive-intensity inside the U-shaped duct, measured using the *Microflown USP-regular* probe for the frequencies of 130, 210 and 580 Hz [88].

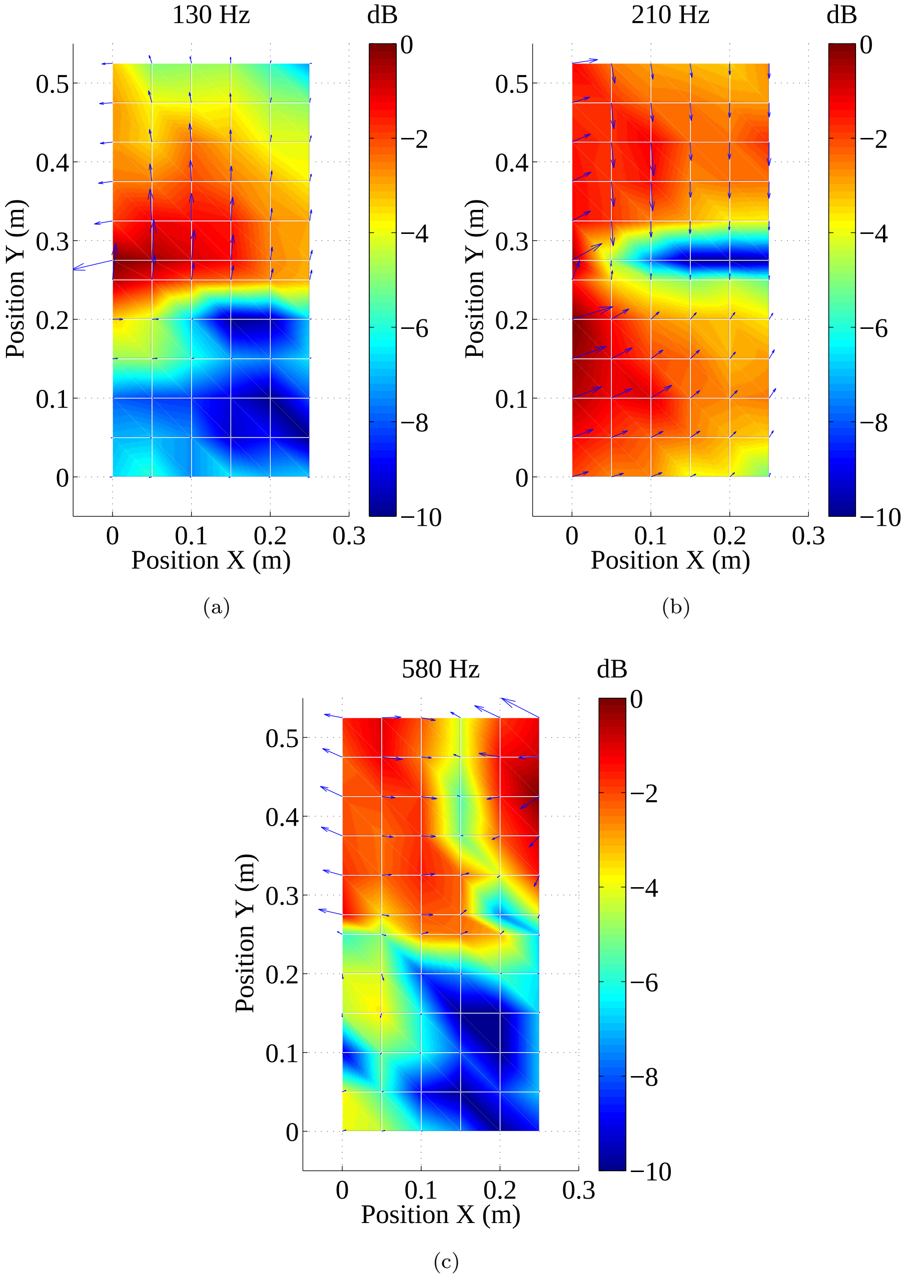

(a)

(b)

(c)

Figure B.19: Reactive-intensity variation inside the U-shaped duct measured using the *USP-regular* probe. (a) 130 Hz, (b) 210 Hz and (c) 580 Hz.

The reactive-intensity around the bend region inside the U-shaped *TLL* duct can be observed in Fig. B.19 at three different frequencies. Comparing the results in Fig. B.19 (a) with the selected area in Fig. 4.20, it can be seen that there is a region of high-reactive-intensity at 130 Hz around and at the tip of the separating panel in the U-shaped duct. It can also be seen that there is a region of low-reactive-intensity encapsulating the high-intensity region, with the lowest intensity concentration at the bottom-right corner of the bend area. In Fig. B.19 (b) as the frequency progresses to 210 Hz, the high-reactive-intensity region located around the separating panel in Fig. B.19 (a) has advanced, covering almost the entire bending region of the U-shaped duct. It can further be noticed that there is sharp and narrow region of low-reactive-intensity in front of the separating panel in the U-shaped duct, separating the two high-reactive-intensity regions. As in the previous case the arrows in Fig. B.19 show the direction that the reactive-intensity is tending towards. In Fig. B.19 (c) as the frequency increases even further to 580 Hz, the high-intensity region is concentrated on the top-right corner and a low-intensity region is developed at the bottom-right corner of the U-shaped duct as well. It is worth mentioning that the reactive-intensity is a measure of the oscillatory instantaneous acoustic intensity associated with particle velocity components in quadrature with the acoustic pressure. The term is generally restricted to harmonic sound-fields, where it contrasted with active-intensity. For a single-frequency sound-field whose acoustic pressure and particle velocity position x are represented by Eq. B.1, the reactive-intensity vector, J_R, at point x may be written in terms of the complex numbers, $\tilde{p}$, and $\tilde{u}$, as

$$J_R = -\frac{1}{2} Im[\tilde{p} * \tilde{u}], \tag{B.4}$$

or the mean square pressure, p_{rms}^2, and its gradient, as

$$J_R = -\frac{1}{2\omega\rho} \nabla (p_{rms})^2. \tag{B.5}$$

Here ω is the angular-frequency, and ρ is the density.

Figures B.20 and B.21 illustrate the reactive intensity measurements of a U-shaped duct for the hard-walled case at 0.25 m height position at the specified frequencies.

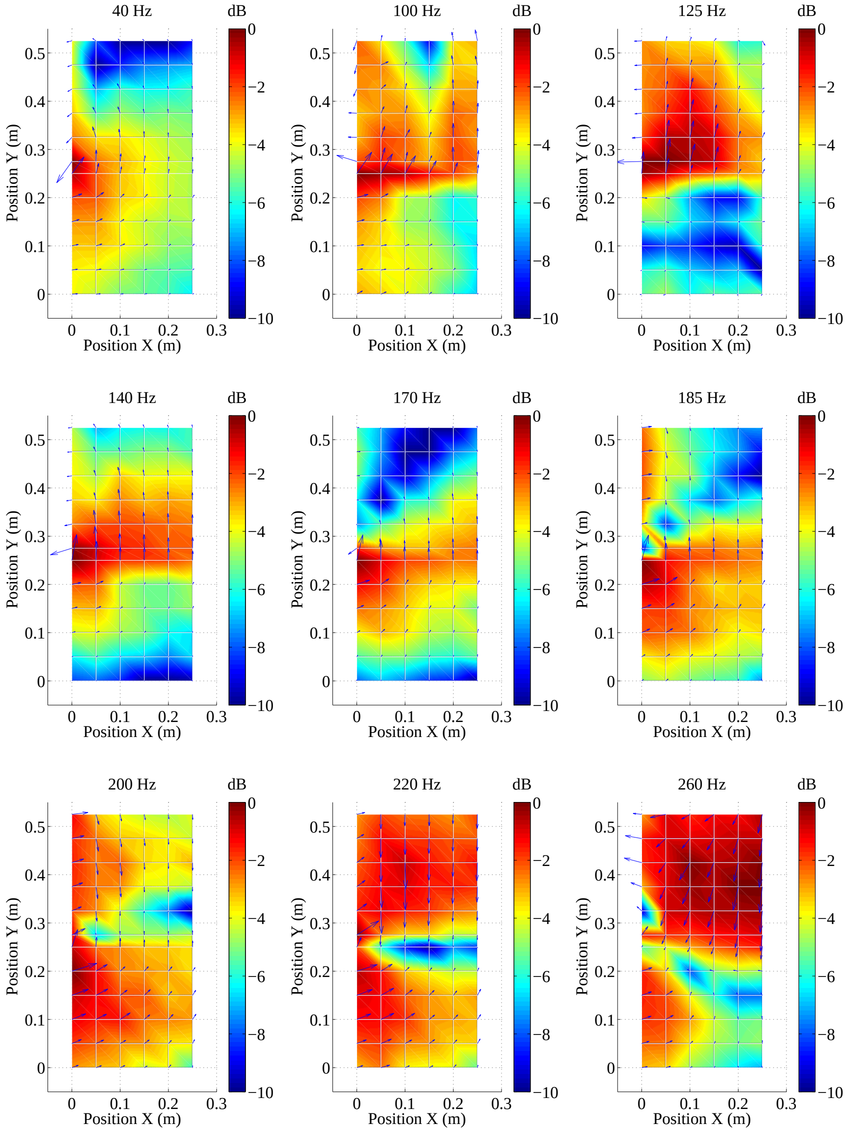

FIGURE B.20: Reactive intensity measurements for the U-shaped duct, hard-walled case for frequency range of 40 to 260 Hz.

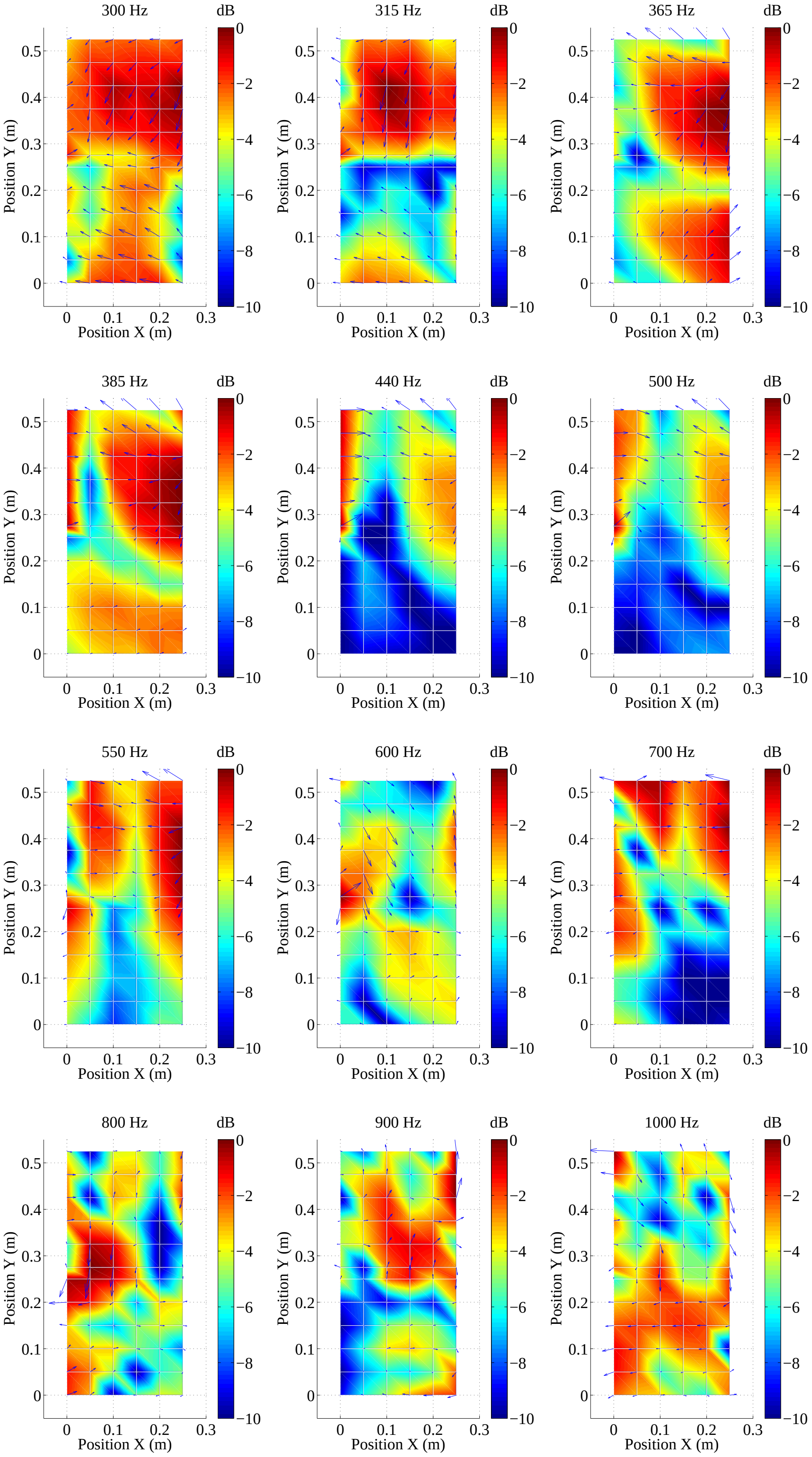

Figure B.21: Reactive intensity measurements for the U-shaped duct, hard-walled case for frequency range of 300 to 1000 Hz.

B.4.6 U-Duct Global Intensity Results

Figure B.22 shows the in-situ measurements of the global-intensity inside the U-shaped duct measured using the *USP-regular* sensor for frequencies of 175, 225 and 545 Hz [88].

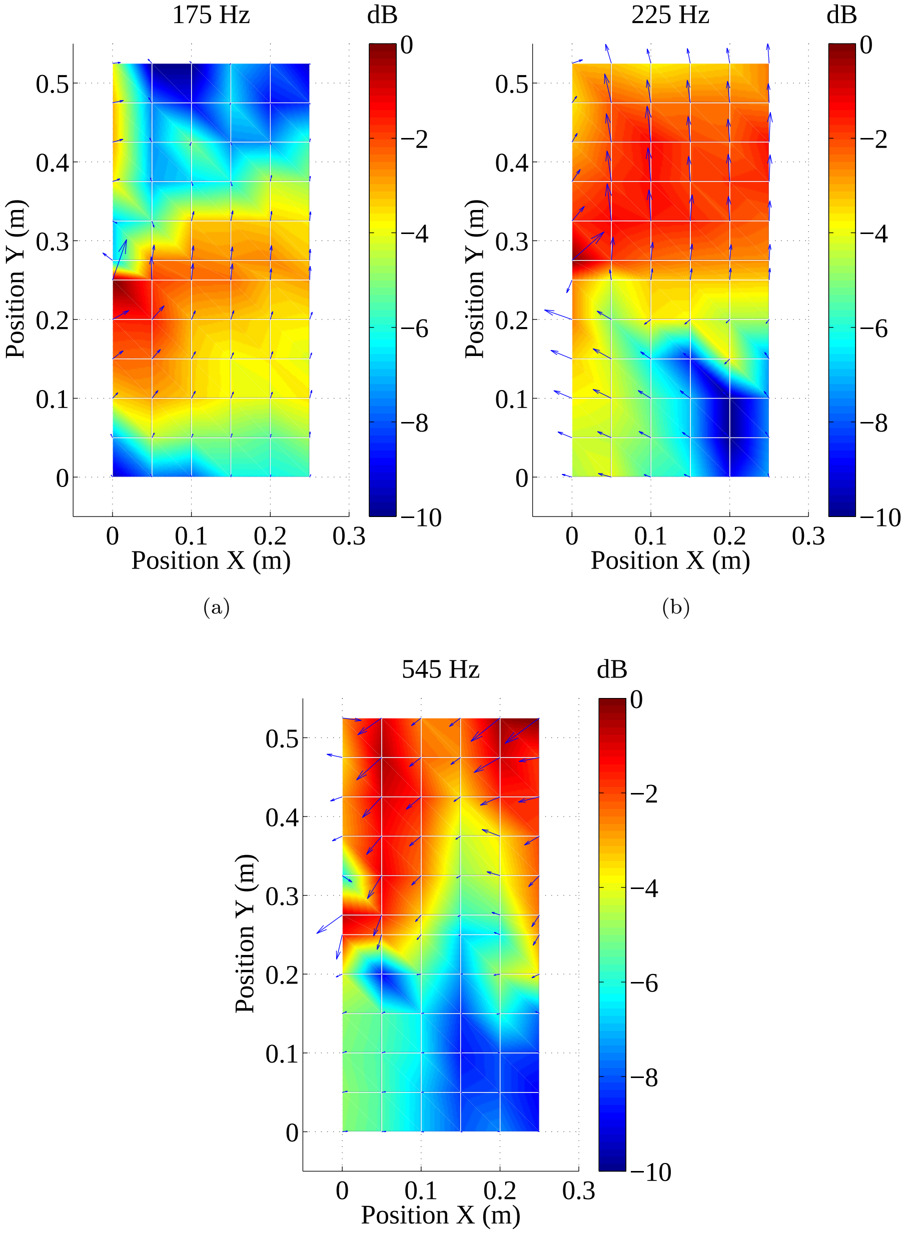

(a)

(b)

(c)

FIGURE B.22: Global-intensity variation inside the U-shaped duct measured using the *USP-regular* probe. (a) 175 Hz, (b) 225 Hz and (c) 545 Hz.

The global-intensity variation around the bend region inside the U-shaped *TLL* duct can be seen in Fig. B.22 at three different frequencies. Comparing the results in Fig. B.22 (a) with the selected area in Fig. 4.20 it can be seen that there is a region of high-global-intensity at 175 Hz around the separating panel in the U-shaped duct. It can also be seen that there are two regions of low-global-intensity on the top and bottom sides of the U-shaped duct, with the lowest intensity concentration at the top-right corner of the bending region. In Fig. B.22 (b) as the frequency progresses to 225 Hz, the high intensity region located around the separating panel in Fig. B.22 (a) has been moved to the top-half of the U-shaped duct creating two distinct regions of high and low global-intensity on the bend area of the duct with the lowest concentration of the global-intensity being located at the bottom-right side of the U-shaped duct. As in the previous case, the arrows in Fig. B.22 show the direction that the global-intensity is tending towards. In Fig. B.22 (c) as the frequency increases even further to 545 Hz, the high and low intensity regions in Fig. B.22 (b) is further concentrated on the top and bottom corners of the duct creating two distinct regions of high and low global-intensity.

Figures B.23 and B.24 illustrate the global intensity measurements of a U-shaped duct for the hard-walled case at 0.25 m height position at the specified frequencies.

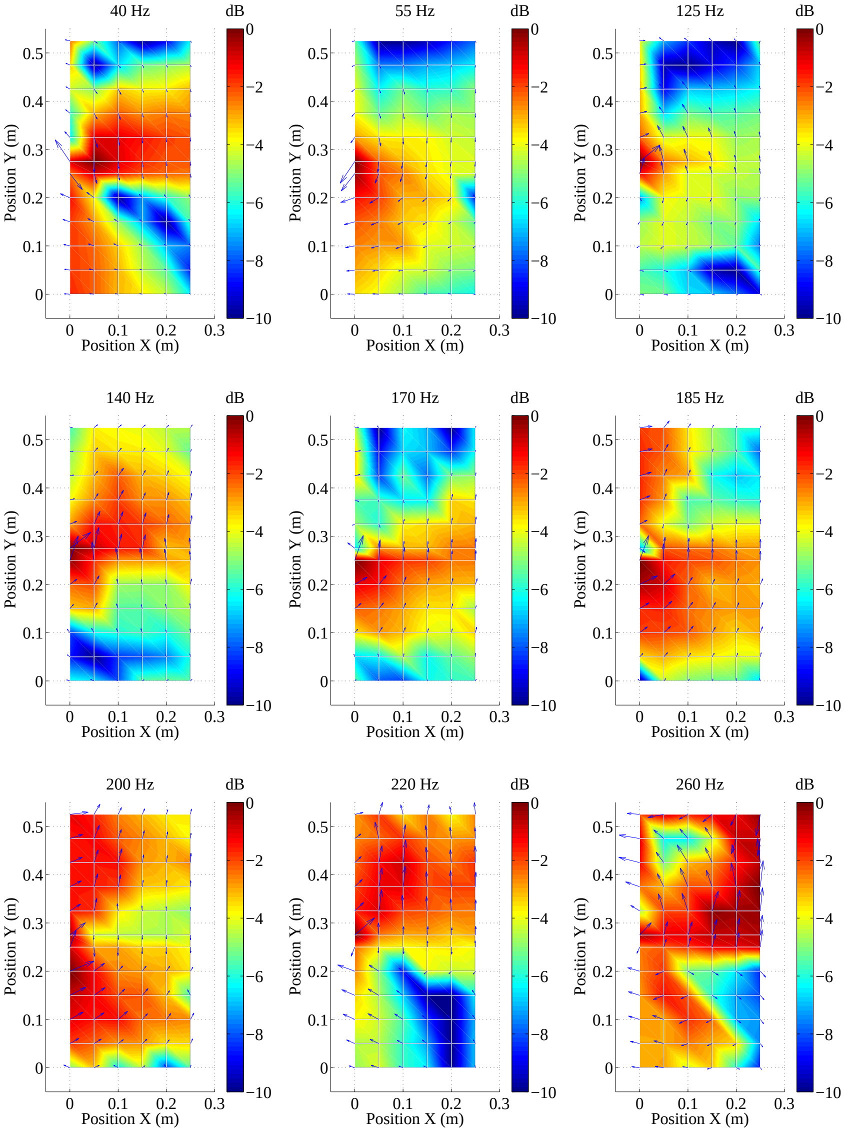

FIGURE B.23: Global intensity measurements for the U-shaped duct, hard-wall case for frequency range 40 to 260 Hz.

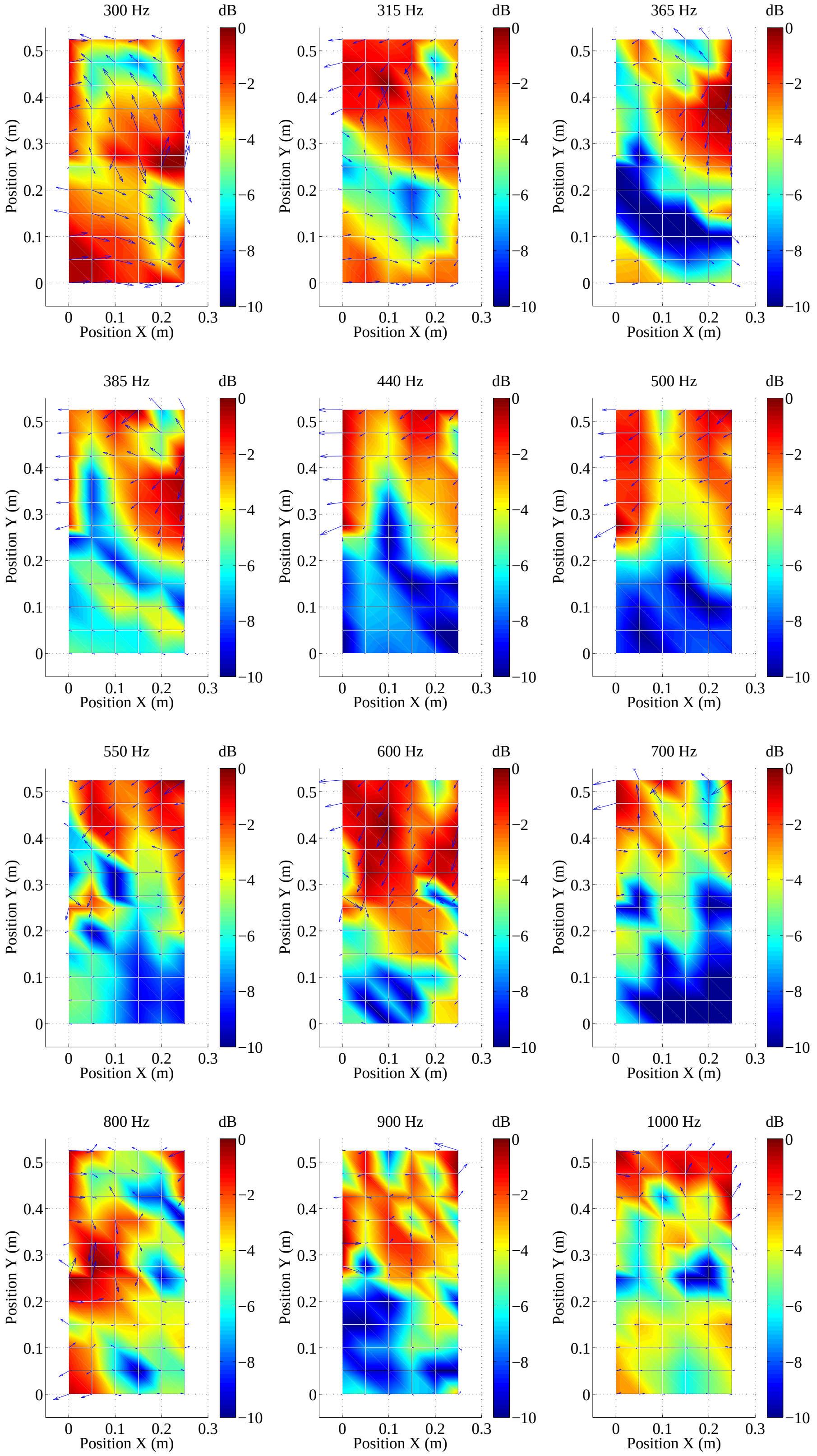

FIGURE B.24: Global intensity measurements for the U-shaped duct, hard-wall case for frequency range 300 to 1000 Hz.

Appendix C

Comparison and Estimation

C.1 Comparison of DC-Flow and Impedance-Tube Data

C.1.1 Estimating Magnitude of Reflection Coefficient and Absorption Coefficient of Fibrous Samples Using the *Delany* and *Bazley* Method

Figure C.1 shows the comparison of magnitude of reflection coefficients of a range of fibrous materials measured using DC-flow tests with impedance-tube measurements [54].

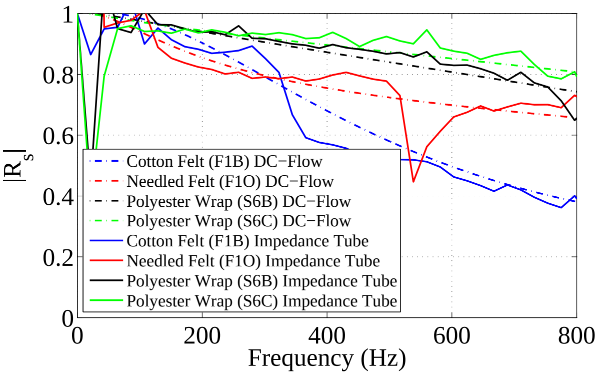

FIGURE C.1: Comparison between the magnitude of reflection coefficient of fibrous materials. Impedance-tube measurements (*solid line*) and DC-flow measurements (*dot dashed line*). Compared samples *cotton felt - F1B*, *needled felt - F1O*, *polyester wrap - S6B* and *polyester wrap - S6C*.

Figure C.2 shows the comparison of magnitude of reflection coefficients of range of fibrous materials measured using DC-flow tests with impedance-tube measurements. Impedance-tube measurements correspond to the solid lines and DC-flow measurements correspond to the dot dashed lines in the presented figure. Compared samples are as follows: (a) *needled felt - F1O*, (b) *cotton felt - F1B*, (c) *polyester wrap - S6B* and (d) *polyester wrap - S6C* [54].

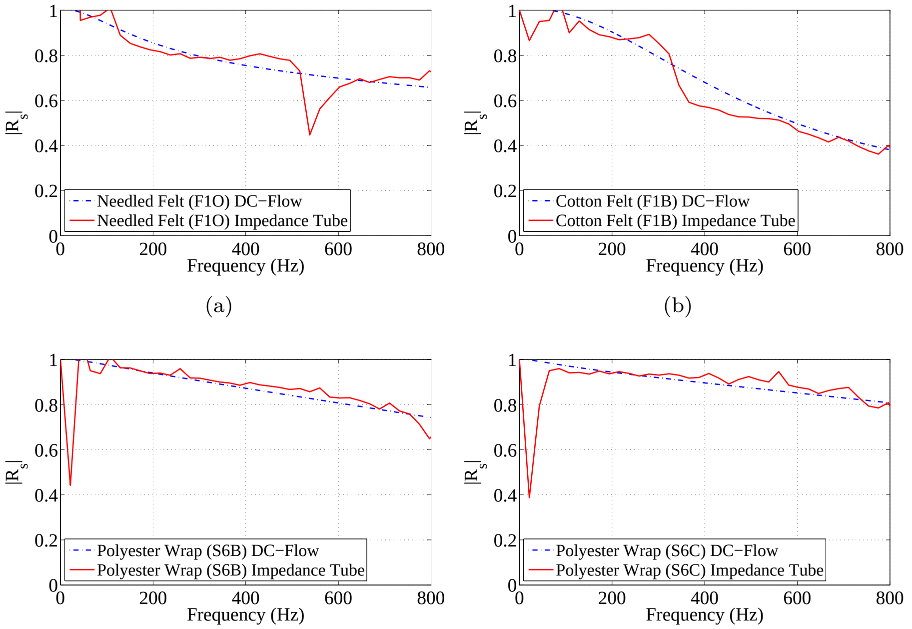

(a) (b)

(c) (d)

FIGURE C.2: Comparison of magnitude of reflection coefficient of fibrous materials. Impedance-tube measurements (*solid line*) and DC-flow measurements (*dot dashed line*). (a) *needled felt - F1O*, (b) *cotton felt - F1B*, (c) *polyester wrap - S6B* and (d) *polyester wrap - S6C*.

Figure C.3 shows the comparison of absorption coefficients of a range of fibrous materials measured using the DC-flow test with impedance-tube measurements. Impedance-tube measurements correspond to the solid lines and DC-flow measurements correspond to the dot dashed lines in the presented figure. Compared samples are as follows: (a) *cotton felt - F1B*, b) *needled felt - F1O*, (c) *polyester wrap - S6B* and (d) *polyester wrap - S6C* [54].

It can be observed that the measured impedance-tube data are following the same trend and varying by a small amount. However the comparison

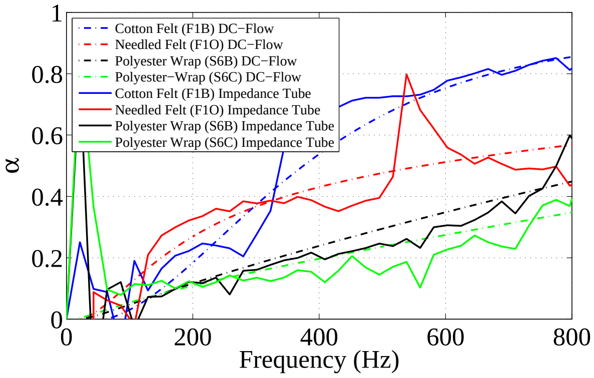

FIGURE C.3: Comparison between absorption coefficient of fibrous materials. Impedance tube measurements (*solid line*) and DC-flow measurements (*dot dashed line*). Compared samples *cotton felt - F1B*, *needled felt - F1O*, *polyester wrap - S6B* and *polyester wrap - S6C*.

between the impedance-tube data and DC-flow measurements are not always very good. The comparison between the measured results for the cotton felt and needled felt are showing very good agreement whereas the comparison for both polyester-wrap samples (S6B and S6C) are not in great agreement.

C.1.2 Estimating Absorption Coefficient and Magnitude of Reflection Coefficient of Porous Samples Using the *Wu Qunli* Method

Figure C.4 shows the comparison of absorption coefficients of a range of porous materials measured using the DC-flow test with impedance-tube measurements [27].

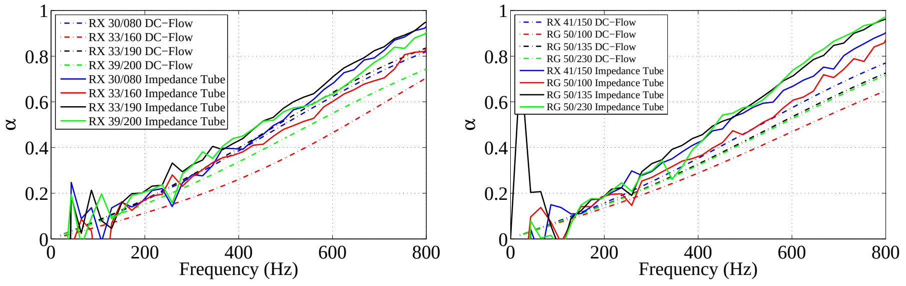

(a) (b)

Figure C.4: Comparison between absorption coefficient of porous samples. Impedance-tube measurements (*solid line*) and DC-flow measurements (*dot dashed line*). (a) $RX30/080$, $RX33/160$, $RX33/190$, $RX39/200$, and (b) $RX41/150$, $RG50/100$, $RG50/135$, $RG50/230$.

Figure C.5 shows the comparison of magnitude of reflection coefficients of a range of porous materials measured using the DC-flow test with impedance-tube measurements [27].

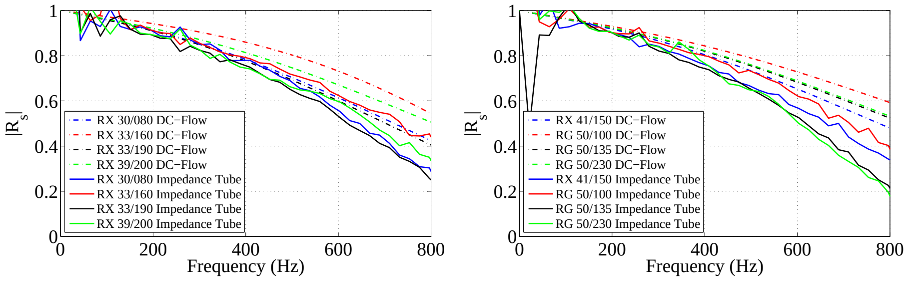

(a) (b)

Figure C.5: Comparison between magnitude of reflection coefficient of porous materials. Impedance-tube measurements (*solid line*) and DC-flow measurements (*dot dashed line*). (a) $RX30/080$, $RX33/160$, $RX33/190$, $RX39/200$, and (b) $RX41/150$, $RG50/100$, $RG50/135$, $RG50/230$.

Figure C.6 shows the comparison between magnitude of reflection coefficients of fibrous samples measured using the impedance tube with DC-flow measurements. Compared samples are as follows: (a) $RX30/080$, (b) $RX33/160$, (c) $RX33/190$, (d) $RX39/200$, (e) $RX41/150$, (f) RG-$50/100$, (g) $RG50/135$ and (h) $RG50/230$ [27].

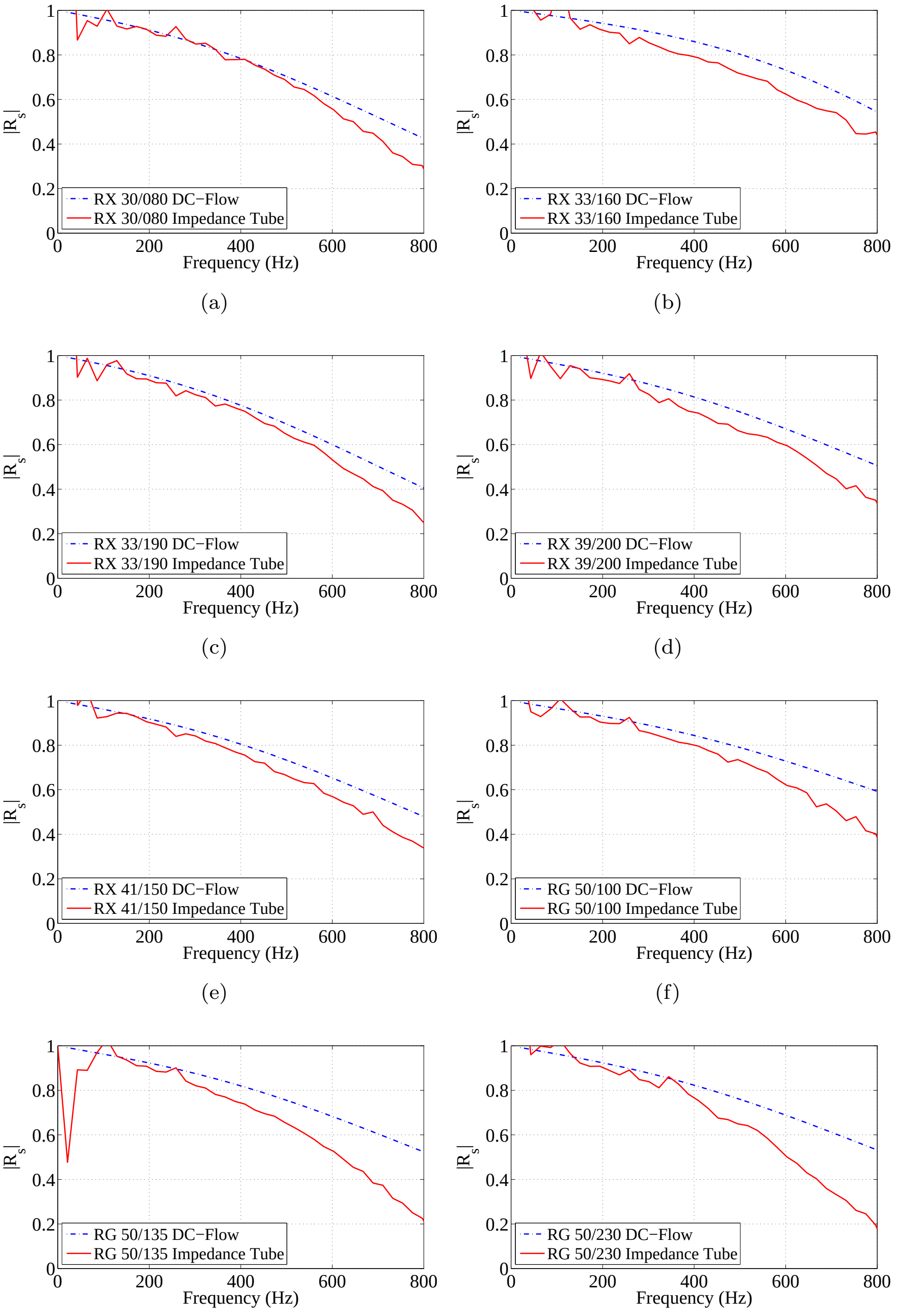

(a) (b)

(c) (d)

(e) (f)

(g) (h)

FIGURE C.6: Comparison of magnitude of reflection coefficient of a range of porous materials. Impedance-tube measurements (*solid line*) and DC-flow measurements (*dot dashed line*). (a) *RX*30-/080, (b) *RX*33/160, (c) *RX*33/190, (d) *RX*39/200, (e) *RX*41/150, (f) *RG*50/100, (g) *RG*50/135 and (h) *RG*50/230.

C.2 Numerical Models

C.2.1 Comparison of Mashing Size and Techniques

Figure C.7 shows the comparison between three meshing sizes of external and internal elements of straight ducts using the *free-tetrahedral* method (a to f) and the *swept-and-mapped* method of meshing (g and h).

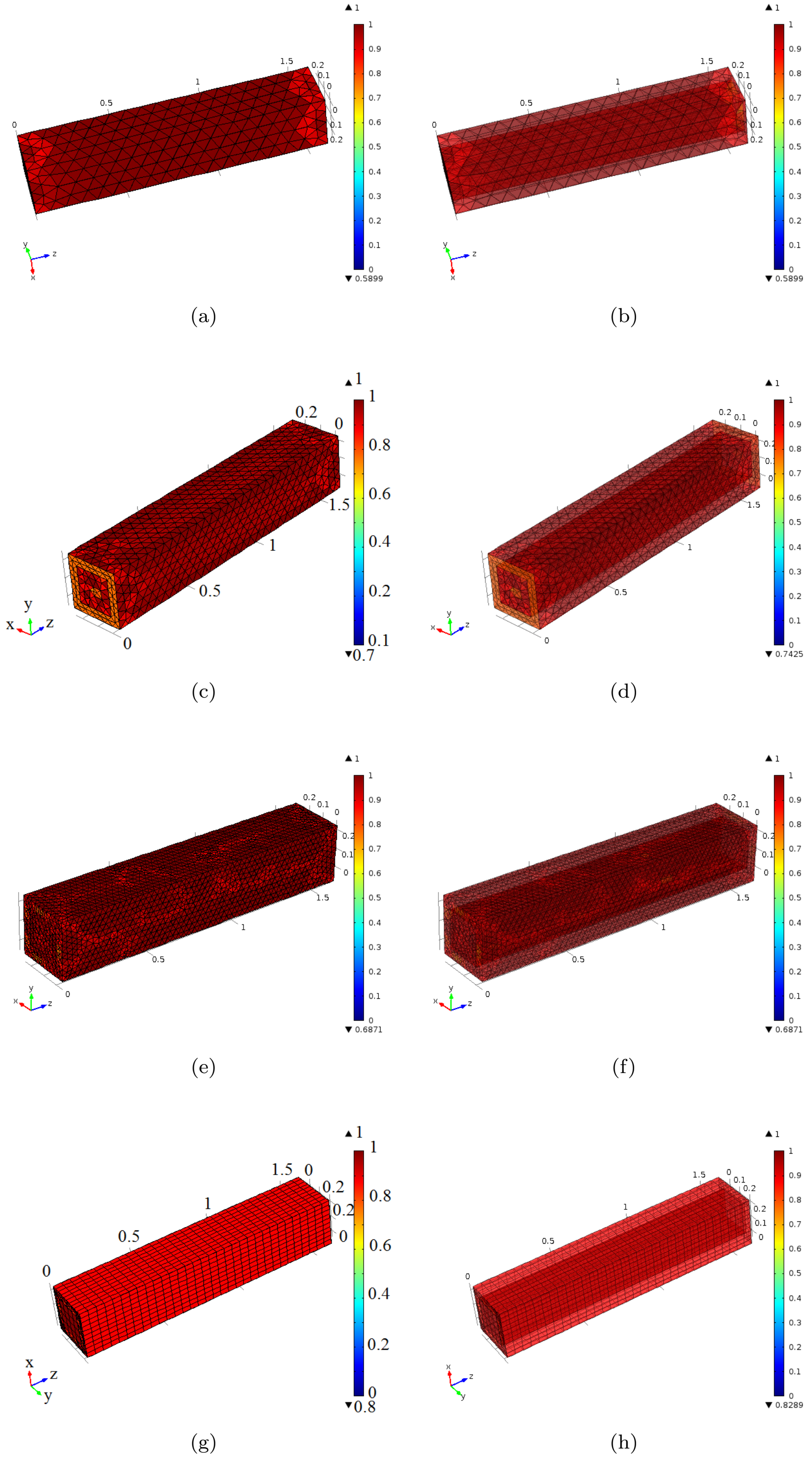

(a) (b)

(c) (d)

(e) (f)

(g) (h)

FIGURE C.7: Comparison of different size *free-tetrahedral* node meshed element (a to f) with *swept-and-mapped* node meshed method (g and h). (a, c, e and g) show external mesh size (*left-side figures*). (b, d f and h) show internal mesh size (*right-side figures*).

C.3 Estimation of Absorption Coefficients Using Flow-Resistivity Data

C.3.1 Improving Flow-Resistivity Value

Figure C.8 shows the comparison between the absorption coefficient and magnitude of reflection coefficient for a sample of porous plastic open-cell foam $RX33/160$ with its improved version, where the flow-resistivity value has been calibrated. The impedance-tube measurement has been compared with measured flow-resistivity value in conjunction with the empirical absorption coefficients and magnitude of refection coefficient from *Wu Qunli.*

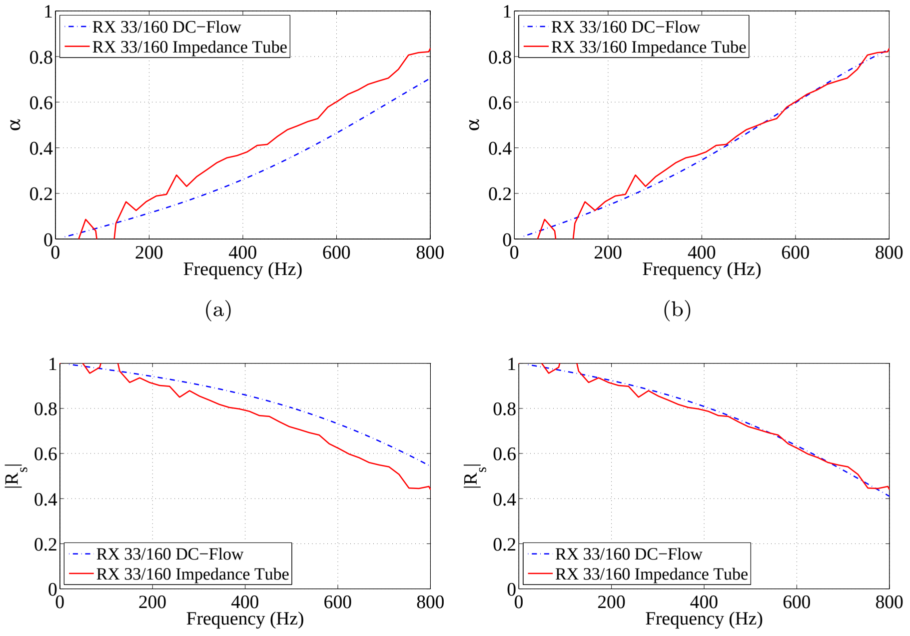

(a) (b)

(c) (d)

Figure C.8: Comparison of α and $|r|$ for a sample $RX33/160$ with its improved version, where the flow-resistivity value has been calibrated. The impedance-tube measurement has been compared with measured flow-resistivity value in conjunction with the empirical absorption coefficients and magnitude of refection coefficient from *Wu Qunli.* (a) Measured comparison of α, (b) comparison of α for improved σ, (c) measured comparison of $|r|$ and (d) comparison of $|r|$ for improved σ. Impedance-tube results (*solid line*) and empirical results (*dot dashed line*)

The flow-resistivity values were measured using the *Aermacchi* DC-flow test rig. These values were then compared with the impedance-tube measurements conducted in the *ISVR* which shows some discrepancy between the two measurements. Therefore the attempt was made to correct the flow-resistivity values by calibrating the flow-resistivity values based on the impedance-tube measurements. Figure C.9 shows the comparison between the in-situ measurement and the numerical prediction with the improved flow-resistivity value and pistonic excitation for straight-duct treated duct for sample of porous plastic open-cell foam $RX33/160$ (green foam).

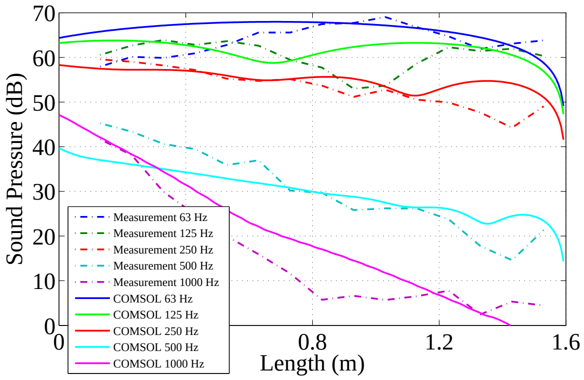

FIGURE C.9: Comparison of direct measurement and numerical prediction of sound pressure along the straight duct with improved σ value treated with sample $RX33/160$ for frequencies 63, 125, 250, 500 and 1000 Hz. *COMSOL* results (*solid lines*) and measurement results (*dot dashed lines*).

As can be seen in Fig. C.9, the improvement of flow-resistivity value in the numerical model with respect to impedance-tube measurement does not improve the overall prediction and the lack of accuracy in the mid and high frequency at 500 and 1000 Hz still can be observed. Other than that the measurement and prediction has close similarity as explained for Fig. 4.17. The effect of pressure-release boundary at the open end of the duct can be observed for the frequencies of 500 and 1000 Hz which is due to the sudden expansion in the acoustic boundary at the open end of the waveguide. The direct measurements for the frequencies of $63, 125$ and 250 Hz exhibit close similarity in their trend with the numerical prediction, with the comparison of 250 Hz being almost the same apart from the prediction at the opening-end of the duct, which was due to choosing the pressure-release boundary condition for the opening-end of the duct, to keep the numerical models as robust as possible. The measurements at 500 and 1000 Hz show far less similarity in their comparison of magnitude of the sound pressure with the predicted values.

C.3.2 Improving Excitation Source in Numerical Prediction

Figure C.10 illustrates the comparison between the results of the numerical prediction for the straight duct with non-uniform excitation, loaded with a sample of porous sound absorbing liner $RX33/160$ (green foam) with the direct measurements on the corresponding treated duct.

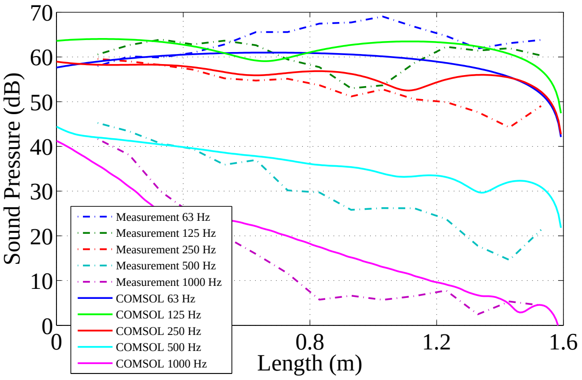

FIGURE C.10: Comparison of in-situ measurement results of sound pressure along the straight duct, non-uniform excitation treated with sample $RX33/160$ (green foam) for the frequencies 63, 125, 250, 500 and 1000 Hz. *COMSOL* results (*solid lines*) and measurement results (*dot dashed lines*).

The assumption has been made that the loudspeaker driver motion at low-frequency can be modelled as a uniform pistonic movement. Therefore, a pistonic excitation is considered as the excitation source for the driver of the *TLL*. The advanced numerical model, however, should consider a lumped parameter model of the driver as an excitation source in the numerical model to accurately predict the frequency dependent behaviour of the driver at the frequency range of interest. Using the mathematical model developed in Chapter 2 Section 2.4.3, a special case of non-uniform excitation source such as a rolling piston has been chosen to excite a large number of modes in the numerical model, as described in Eq. (2.18) and shown in Fig. 2.13, where the square cross-sectional area of transmission-line duct has been divided into two isosceles triangles separated by the diagonal line of the cross-section. One triangle is pulsating inwards and outwards and another one has been clamped into the duct-body to be fixed.

As can be seen in Fig. C.10, the improvement of excitation source in the numerical model does not improve the overall prediction and the lack of accuracy in the mid and high frequencies at 500 and 1000 Hz still can be observed. Other than that the measurements and predictions have close similarity as explained for Fig. 4.17. The effect of a pressure-release boundary at the open end of the duct can be observed for the frequencies of 500 and 1000 Hz which is due to the sudden expansion in the acoustic boundary at the open end of the waveguide. At frequencies of 63, 125 and 250 Hz the direct measurements exhibit close similarity in their trend with the numerical prediction, with the comparison of 250 Hz being almost the same apart from the prediction at the opening-end of the duct, which was due to choosing the pressure-release boundary condition for the opening-end of the duct, to keep the numerical models as robust as possible. The measurements at 500 and 1000 Hz show far less similarity in their comparison of magnitude of the sound pressure with the predicted values.

Appendix D

Manuals and Data-Sheets

The data-sheets and manuals of the *Microflown* Pressure/Velocity *PU-Match* probe as shown in Fig. 4.11, and the *Microflown* signal conditioner *MFSC-2* are given in Appendix D Section D.1.1, D.1.2, D.1.3 and D.1.4. The calibration report of the *PU-match* used in the measurements has also been supplied by *Microflown Technologies* and is been reprinted in Appendix D Section D.1.5.

Next, the data-sheets and manuals of the *Microflown* Ultimate Sound Probe *USP-Regular* as shown in Fig. **??**, and the *Microflown* signal conditioner *MFSC-4* are given in Appendix D Section D.2.1, D.2.2, D.2.3 and D.2.4.[1].

---

[1] Materials presented here are courtesy of *Microflown Technologies*. $http://www.microflown.com$

D.1 *PU-Match* Sensor

D.1.1 *Microflown PU-Match* Data-Sheet

[2]

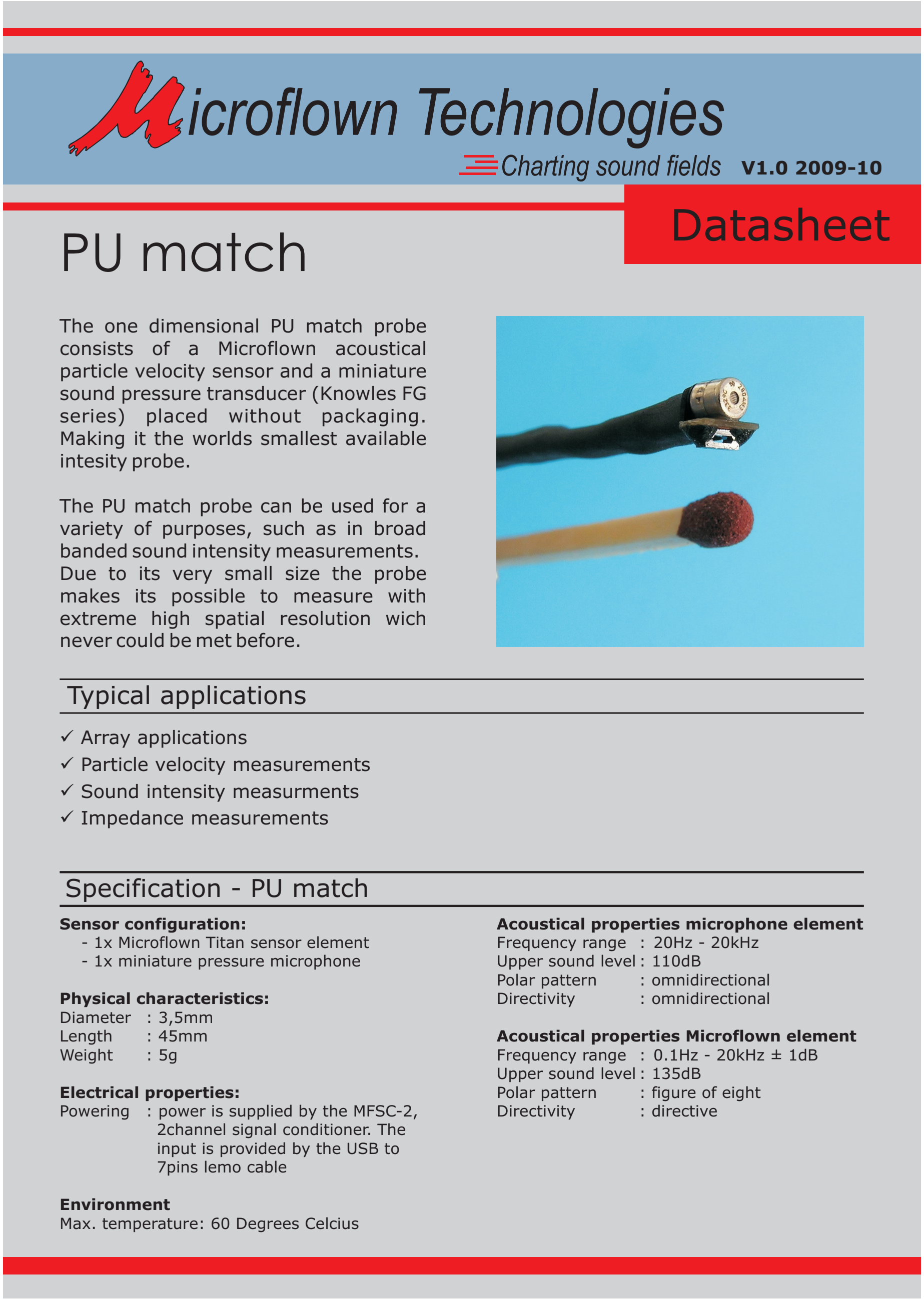

Microflown Technologies

Charting sound fields **V1.0 2009-10**

Datasheet

PU match

The one dimensional PU match probe consists of a Microflown acoustical particle velocity sensor and a miniature sound pressure transducer (Knowles FG series) placed without packaging. Making it the worlds smallest available intesity probe.

The PU match probe can be used for a variety of purposes, such as in broad banded sound intensity measurements. Due to its very small size the probe makes its possible to measure with extreme high spatial resolution wich never could be met before.

Typical applications

- ✓ Array applications
- ✓ Particle velocity measurements
- ✓ Sound intensity measurments
- ✓ Impedance measurements

Specification - PU match

Sensor configuration:
- 1x Microflown Titan sensor element
- 1x miniature pressure microphone

Physical characteristics:
Diameter : 3,5mm
Length : 45mm
Weight : 5g

Electrical properties:
Powering : power is supplied by the MFSC-2, 2channel signal conditioner. The input is provided by the USB to 7pins lemo cable

Environment
Max. temperature: 60 Degrees Celcius

Acoustical properties microphone element
Frequency range : 20Hz - 20kHz
Upper sound level : 110dB
Polar pattern : omnidirectional
Directivity : omnidirectional

Acoustical properties Microflown element
Frequency range : 0.1Hz - 20kHz ± 1dB
Upper sound level : 135dB
Polar pattern : figure of eight
Directivity : directive

---

[2] Materials presented here are courtesy of *Microflown Technologies*. *http://www.microflown.com*

Model sound pressure microphone

The sensitivity of the pressure microphone (independent of high/low gain or corrected/uncorrectede mode):

$$S_p[mV/Pa] = S_p @1kHz \frac{\sqrt{1+\frac{f^2}{f_{c3p}^2}}}{\sqrt{1+\frac{f_{c1p}^2}{f^2}}\sqrt{1+\frac{f_{c2p}^2}{f^2}}}$$

The phase of the pressure microphone (independent of high/low gain or corrected/uncorrectede mode):

$$\varphi_p[\deg] = \arctan\frac{C_{1p}}{f} + \arctan\frac{C_{2p}}{f} + \arctan\frac{f}{C_{3p}}$$

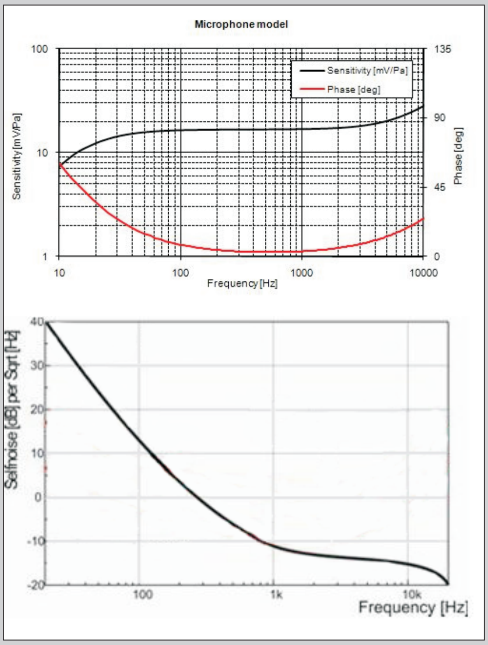

Parameters pressure equations		
Sensititivity:		
S_p @1kHz=	*55,0*	*[mV/Pa]*
Sensitivity cornerfrequencies		
fc1p=	*30*	*[Hz]*
fc2p=	*15*	*[Hz]*
fc3p=	*10000*	*[Hz]*
Phase cornerfrequencies		
C1p=	*30*	*[Hz]*
C2p=	*15*	*[Hz]*
C3p=	*10000*	*[Hz]*

Model Microflown sensor

The sensitivity in uncorrected mode:

$$S_u\left[mV/Pa^*\right]=\frac{S_u @250Hz}{\sqrt{1+\frac{f_{c1u}^2}{f^2}}\sqrt{1+\frac{f^2}{f_{c2u}^2}}\sqrt{1+\frac{f^2}{f_{c3u}^2}}\sqrt{1+\frac{f_{c4u}^2}{f^2}}\sqrt{1+\frac{f_{c5u}^2}{f^2}}}$$

The phase in uncorrected mode:

$$\varphi_u\left[\deg\right]=\arctan\frac{C_{1u}}{f}-\arctan\frac{f}{C_{2u}}-\arctan\frac{f}{C_{3u}}-\arctan\frac{C_{4u}}{f}+\arctan\frac{C_{5u}}{f}$$

The sensitivity in corrected mode:

$$S_u\left[mV/Pa^*\right]=\frac{S_u @250Hz}{\sqrt{1+\frac{f_{c1u}^2}{f^2}}\sqrt{1+\frac{f_{c4u}^2}{f^2}}\sqrt{1+\frac{f_{c5u}^2}{f^2}}}$$

The phase in corrected mode:

$$\varphi_u\left[\deg\right]=\arctan\frac{C_{1u}}{f}+\arctan\frac{C_{4u}}{f}+\arctan\frac{C_{5u}}{f}$$

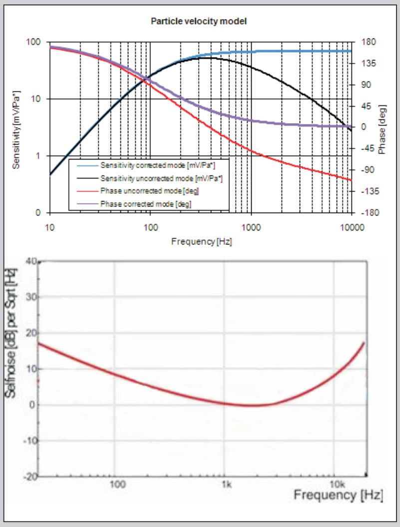

Parameters velocity equations		
Sensititivity in high gain:		
Su @250Hz=	25	[mV/Pa*]
Su @250Hz=	10	[V/(m/s)]
Sensititivity in low gain:		
Su @250Hz=	0,25	[mV/Pa*]
Su @250Hz=	0,1	[V/(m/s)]
Sensitivity cornerfrequencies		
fc1u=	150	[Hz]
fc2u=	600	[Hz]
fc3u=	10000	[Hz]
fc4u=	77	[Hz]
Phase cornerfrequencies		
C1u=	180	[Hz]
C2u=	700	[Hz]
C3u=	20000	[Hz]
C4u	77	[Hz]

D.1.2 ***Microflown PU-Match*** Manual

[3]

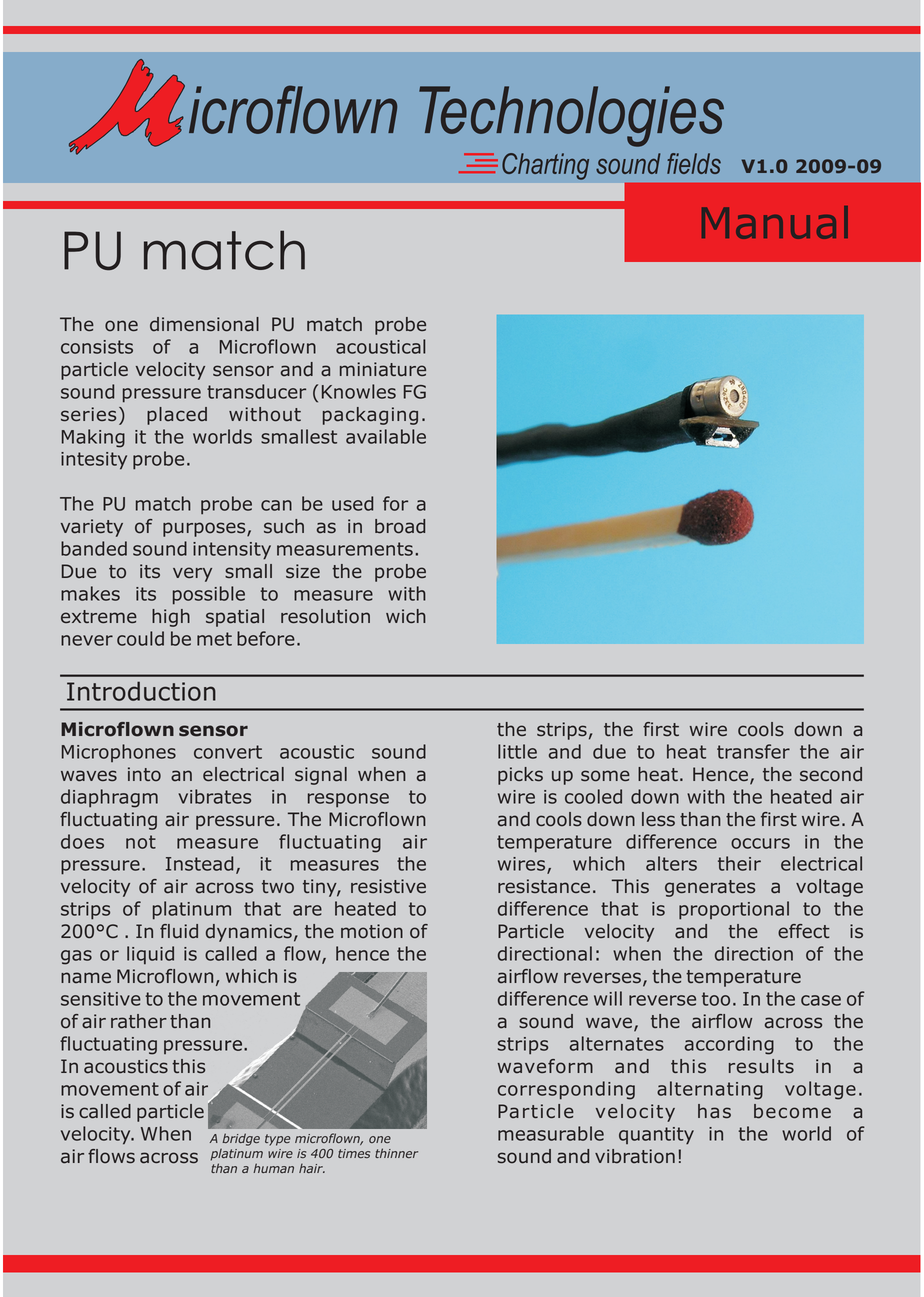

Microflown Technologies

Charting sound fields **V1.0 2009-09**

Manual

PU match

The one dimensional PU match probe consists of a Microflown acoustical particle velocity sensor and a miniature sound pressure transducer (Knowles FG series) placed without packaging. Making it the worlds smallest available intesity probe.

The PU match probe can be used for a variety of purposes, such as in broad banded sound intensity measurements. Due to its very small size the probe makes its possible to measure with extreme high spatial resolution wich never could be met before.

Introduction

Microflown sensor

Microphones convert acoustic sound waves into an electrical signal when a diaphragm vibrates in response to fluctuating air pressure. The Microflown does not measure fluctuating air pressure. Instead, it measures the velocity of air across two tiny, resistive strips of platinum that are heated to 200°C . In fluid dynamics, the motion of gas or liquid is called a flow, hence the name Microflown, which is sensitive to the movement of air rather than fluctuating pressure. In acoustics this movement of air is called particle velocity. When air flows across the strips, the first wire cools down a little and due to heat transfer the air picks up some heat. Hence, the second wire is cooled down with the heated air and cools down less than the first wire. A temperature difference occurs in the wires, which alters their electrical resistance. This generates a voltage difference that is proportional to the Particle velocity and the effect is directional: when the direction of the airflow reverses, the temperature difference will reverse too. In the case of a sound wave, the airflow across the strips alternates according to the waveform and this results in a corresponding alternating voltage. Particle velocity has become a measurable quantity in the world of sound and vibration!

A bridge type microflown, one platinum wire is 400 times thinner than a human hair.

---

[3] Materials presented here are courtesy of *Microflown Technologies*. *http://www.microflown.com*

Directivity

If you measure with a standard microphone you will not only measure the source but also all the background noises and reflections. The microflown does only measure the source and not the background noises and reflections. This is because of the difference in polar response of sound pressure and particle velocity. The two quantities in acoustic, sound pressure and particle velocity, have both a different kind of polar response. If you look at sound pressure, it has an omnidirectional reponse. Sound, and also vibrations, are only measured from one side.

Particle velocity is an vector and so is directional. This directivity effect makes the microflown extremly suitable to measure in real operating situations with background noise and reflections. An omni pattern picks up sound equally from all directions. Particle Velocity has a directional, figure of eight, response.

Figure of eight response of the Microflown

List of equipment

The Microflown PU match comes with:

- ✓ 1x PU match in protective box
- ✓ 1x MFSC-2 (2 channel signal conditioner)
- ✓ 1x Power supply
- ✓ 1x cable
- ✓ 1x Protective case

How to connect the PU match

The power supply can be connected with the signal conditioner using the Power Input 18VDC connection on the backside of the signal conditioner. See right sided picture.

At the frontside of the signal conditioner there is 7 pins female lemo connector called Probe input. See right sided picture. The with the probe integrated lemo cable connects the signal conditioner with the probe.

More info on the MFSC-2, 2 channel signal conditioner, can be found in the datasheet and manual of the MFSC-2

Manual - PU match **Page 2** Microflown Technologies

How to read the calibration report

The natural response of the Microflown is not flat, and thus needs to be calibrated. The goal of calibration is to find out how much the voltage output is when a certain acoustic signal is applied to a Microflown or microphone. In other words: it has to be determined what the amplitude response, or the frequency dependent sensitivity is. In case of a Microflown this means how many volts output per meter per second particle velocity input and in case of a microphone it means how many volts output per Pascal input.

To calibrate a PU probe, white Gaussian noise from a point source is radiated and measured at a known distance. Also, for a point source at any location on the axis in front of this source the ratio of pressure to velocity is known. It is via this property that both sensors are calibrated, referenced to a known (calibrated) G.R.A.S microphone.

The results of the calibration measurements are used to fit a mathematical model over. This model describes the response of the sensors as a function of frequency. A model makes it also easier to implement it and apply it as a software correction.

In the calibration report all relevant calibrated quantities can be found. For pressure as well as for velocity it's sensitivity and phase (relative to the reference microphone) are shown. Since the signal conditioner has a corrected and uncorrected mode, these quantities are plotted twice.

Last graphs in the calibration report is the phase response between pressure and velocity. This phase is necessary when one needs to determine from which half of the figure of eight sound approaches the PU-probe. Again, for both corrected and uncorrected mode the graphs are shown.

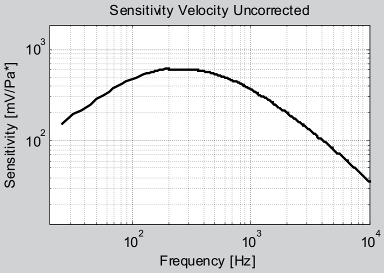

Example of the frequency dependent sensitivity of the particle velocity sensor, measured in uncorrected mode.

Below each graph is the mathematical model stated together with it's coefficients which approximates the shown behavior. To apply this model, divide the measurement's results (transformed to frequency domain) by this curve to obtain a calibrated response (also in frequency domain):

$$\frac{\text{Output Data Acquisition (V)}}{\text{Calibration model }\left(\frac{v}{m/s}\right)} = \text{Calibrated response }\left(\frac{m}{s}\right)$$

D.1.3 *Microflown MFSC-2* Data-Sheet

[4]

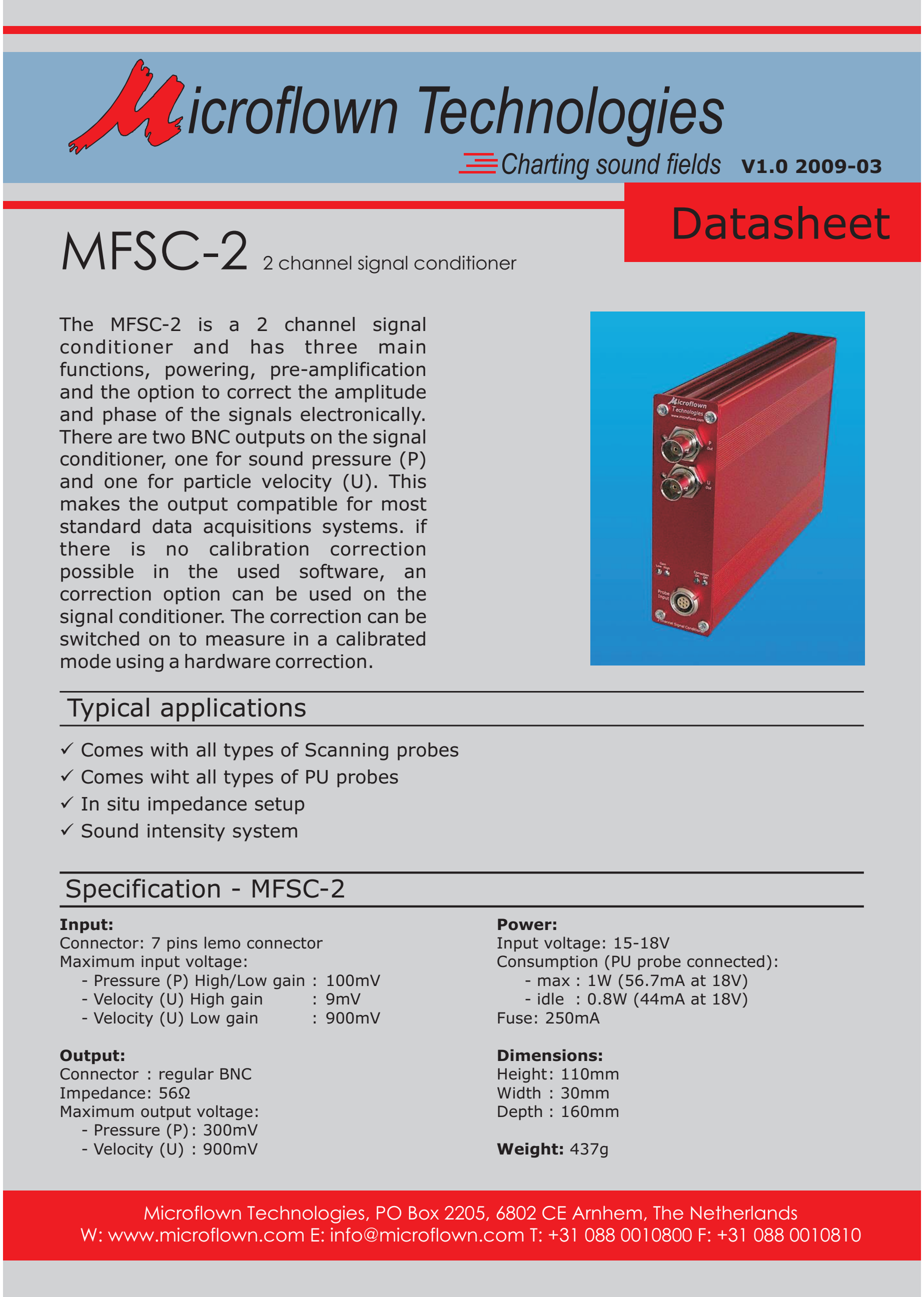

Microflown Technologies

Charting sound fields **V1.0 2009-03**

Datasheet

MFSC-2

2 channel signal conditioner

The MFSC-2 is a 2 channel signal conditioner and has three main functions, powering, pre-amplification and the option to correct the amplitude and phase of the signals electronically. There are two BNC outputs on the signal conditioner, one for sound pressure (P) and one for particle velocity (U). This makes the output compatible for most standard data acquisitions systems. if there is no calibration correction possible in the used software, an correction option can be used on the signal conditioner. The correction can be switched on to measure in a calibrated mode using a hardware correction.

Typical applications

✓ Comes with all types of Scanning probes
✓ Comes wiht all types of PU probes
✓ In situ impedance setup
✓ Sound intensity system

Specification - MFSC-2

Input:
Connector: 7 pins lemo connector
Maximum input voltage:
- Pressure (P) High/Low gain : 100mV
- Velocity (U) High gain : 9mV
- Velocity (U) Low gain : 900mV

Output:
Connector : regular BNC
Impedance: 56Ω
Maximum output voltage:
- Pressure (P): 300mV
- Velocity (U) : 900mV

Power:
Input voltage: 15-18V
Consumption (PU probe connected):
- max : 1W (56.7mA at 18V)
- idle : 0.8W (44mA at 18V)

Fuse: 250mA

Dimensions:
Height: 110mm
Width : 30mm
Depth : 160mm

Weight: 437g

Microflown Technologies, PO Box 2205, 6802 CE Arnhem, The Netherlands
W: www.microflown.com E: info@microflown.com T: +31 088 0010800 F: +31 088 0010810

---

[4] Materials presented here are courtesy of *Microflown Technologies*. *http://www.microflown.com*

D.1.4 *Microflown MFSC-2* Manual

[5]

Microflown Technologies

Charting sound fields **V1.0 2009-03**

Manual

MFSC-2 2 channel signal conditioner

The MFSC-2 is a 2 channel signal conditioner and has three main functions, powering, pre-amplification and the option to correct the amplitude and phase of the signals electronically. There are two BNC outputs on the signal conditioner, one for sound pressure (P) and one for particle velocity (U). This makes the output compatible for most standard data acquisitions systems. If there is no calibration correction possible in the used software, an correction option can be used on the signal conditioner. The correction can be switched on to measure in a calibrated mode using a hardware correction. The MFSC-2 is designed as signal conditioner for all type of Scanning propes (0, 45 & 90 degrees) and all type of PU probes (Regular, Mini & Match). This type of signal conditioner is standard included in a kit with one of these type of probes.

1: BNC output sound pressure (P)
2: BNC output particle velocity (U)
3: LED indication if the signal
conditioner is in high or low gain
4: LED indication if the corection mode
is on or off
5: 7 pins lemo connector that is
connected with the probe
6: Power switch
7: Gain switch
8: Correction switch
9: Power input

---

[5] Materials presented here are courtesy of *Microflown Technologies*. *http://www.microflown.com*

Probe input

At the front cover of the signal conditioner there is an 7 pins lemo connector. This conector connects the probe with the signal conditioner using a lemo cable. The lemo cable is used as data cable as it gives power input from the signal conditioner to the probe and the probe signals are read in by the signal conditioner.

Correction switch

The lowest switch on the backside of the signal conditioner is the Correction switch. The response of the microflown is not flat. Preferable is to the correction for this in the software. If there is no calibration correction possible in the used software, the correction option can be used on the signal conditioner. When the corrected mode is on the signal conditioner will equalize the microflown signal to give it a flat amplitude and phase response. When the correction is done in the software the correction mode should be switched off. At the front side of the signal conditioner there is an LED wich also indicates if the signal conditioner is corrected or uncorrected mode.

BNC ouput

There are two BNC outputs on the frontsdide of the signal conditioner, one for sound pressure (P) and one for particle velocity (U). This makes the output compatible for most standard data acquisitions systems. Left, next to the BNC output conectors there is an indication LED. When the LED is green the output channel works correct, when the LED is red than this indicates a possible overload. If the signal conditioner is in high gain mode and the LED is red than it overload can (mostly) be solved by putting the signal conditioner in low gain.

Gain switch

The middle of the three swithes on the back of the signal conditioner is the Gain switch. The high gain setting is used for low Microflown signals. The low gain setting is used for high Microflown signals. Usually the high gain setting is used.
The high gain mode increases the sensitivity of the Microflown with approx 40 dB. The Gain switch is only for the particle velocity (U) channel, switching does not influence the sound pressure channel. At the front side of the signal conditioner there is an LED wich also indicates if the signal conditioner is high or low gain mode.

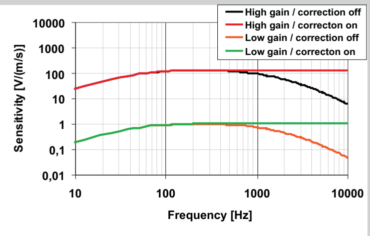

Sensitivity in for the particle velocity (U) signal in different signal conditioner settings

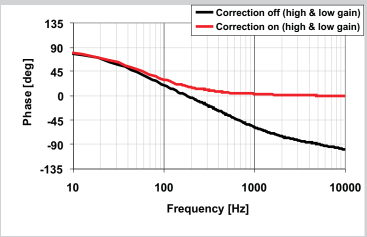

Phase of the particle velocity (U) signal if correction mode is on or off

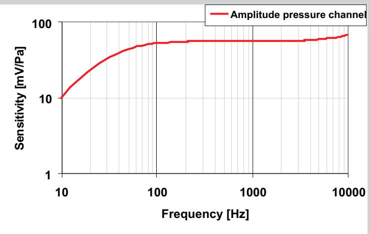

Sensitivity of the sound pressure signal wich is not influenced by different signal conditioner settings

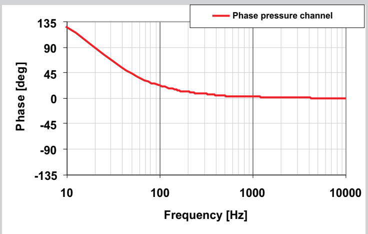

Phase response of the sound pressure signal wich is not influenced by different signal conditioner settings

D.1.5 *Microflown PU-Match* Calibration Report

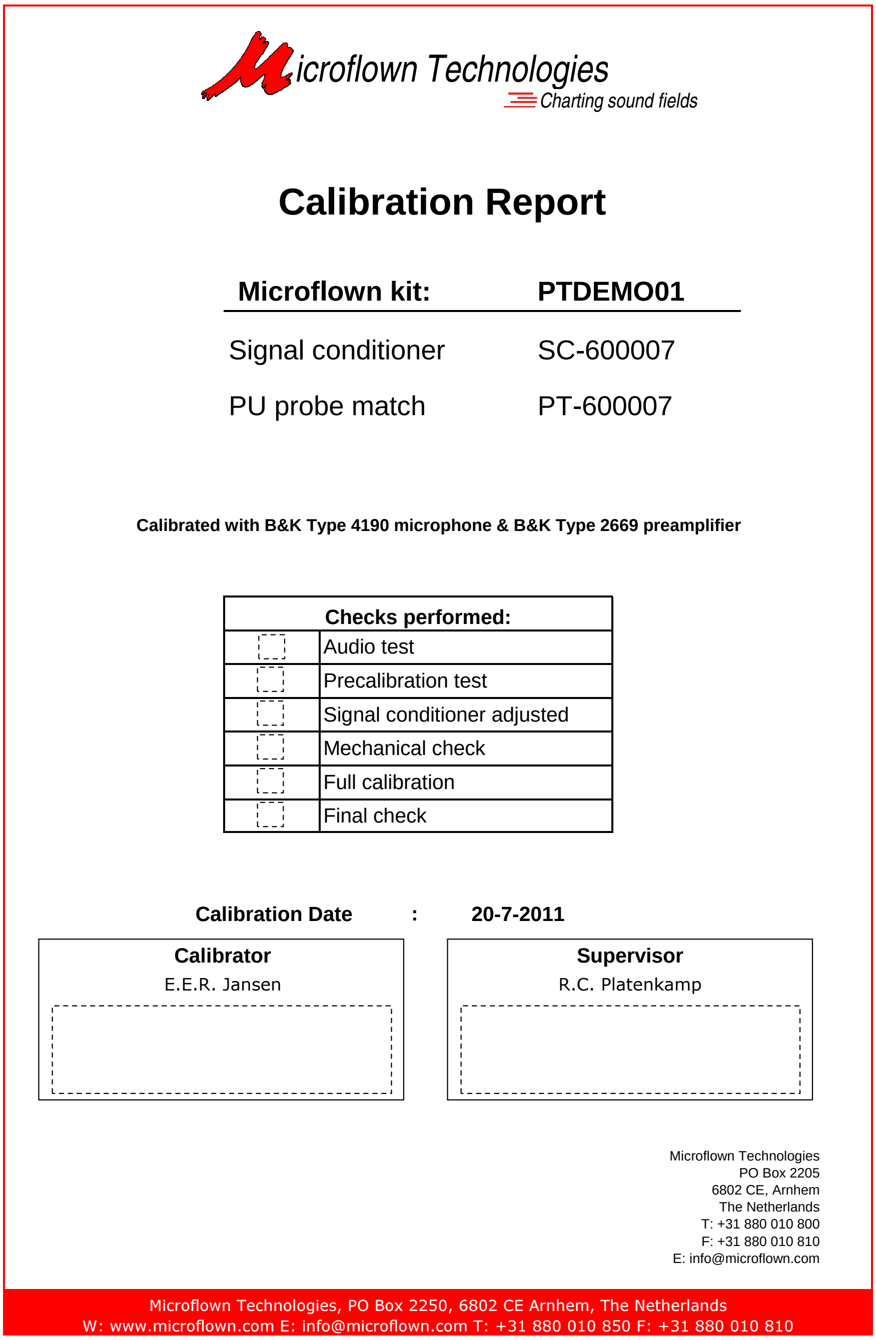

Microflown Technologies
Charting sound fields

Calibration Report

Microflown kit:	**PTDEMO01**
Signal conditioner	SC-600007
PU probe match	PT-600007

Calibrated with B&K Type 4190 microphone & B&K Type 2669 preamplifier

Checks performed:	
☐	Audio test
☐	Precalibration test
☐	Signal conditioner adjusted
☐	Mechanical check
☐	Full calibration
☐	Final check

Calibration Date : 20-7-2011

Calibrator	**Supervisor**
E.E.R. Jansen	R.C. Platenkamp

Microflown Technologies
PO Box 2205
6802 CE, Arnhem
The Netherlands
T: +31 880 010 800
F: +31 880 010 810
E: info@microflown.com

Microflown Technologies, PO Box 2250, 6802 CE Arnhem, The Netherlands
W: www.microflown.com E: info@microflown.com T: +31 880 010 850 F: +31 880 010 810

Microflown Technologies

Additional information

What does high and low gain mean?

The high/low gain and equaliser switches only affect the particle velocity output of the signal conditioner. The pressure output of the signal conditioner is unaffected!

When the signal conditioner switch is in lower position the low gain option is selected. Then particle velocity output of the signal conditioner (in Volts) is the same as the output of the Microflown (in Volts).

When the signal conditioner switch is in upper position the high gain option is selected. The particle velocity output of the signal conditioner is then amplified with 42 dB.

What does the equaliser option mean?

The equaliser option equalises the amplitude and phase response of the particle velocity signal.

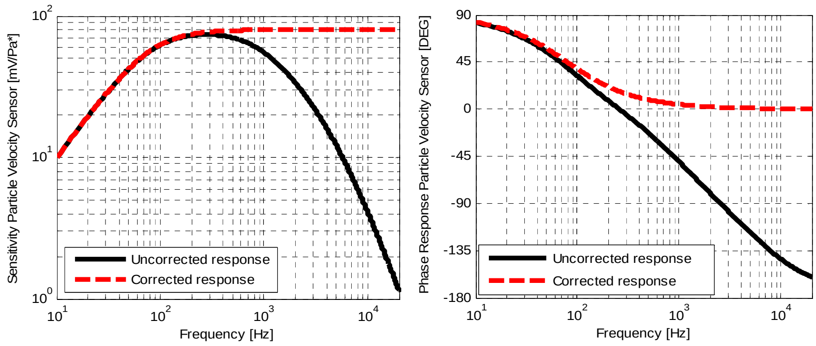

The left figure shows the amplitude response in uncorrected and corrected mode, the right figure shows the phase response.

Selfnoise

Typical selfnoise boundries of the pressure and the particle velocity sensor:

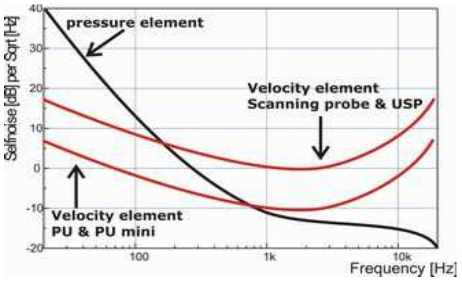

This probe is calibrated with MetalMesh. This means that the hardware correction is optimized for the probe using a metal mesh.

If you have any questions email: platenkamp@microflown.com

Microflown Technologies, PO Box 2250, 6802 CE Arnhem, The Netherlands
W: www.microflown.com E: info@microflown.com T: +31 880 010 850 F: +31 880 010 810

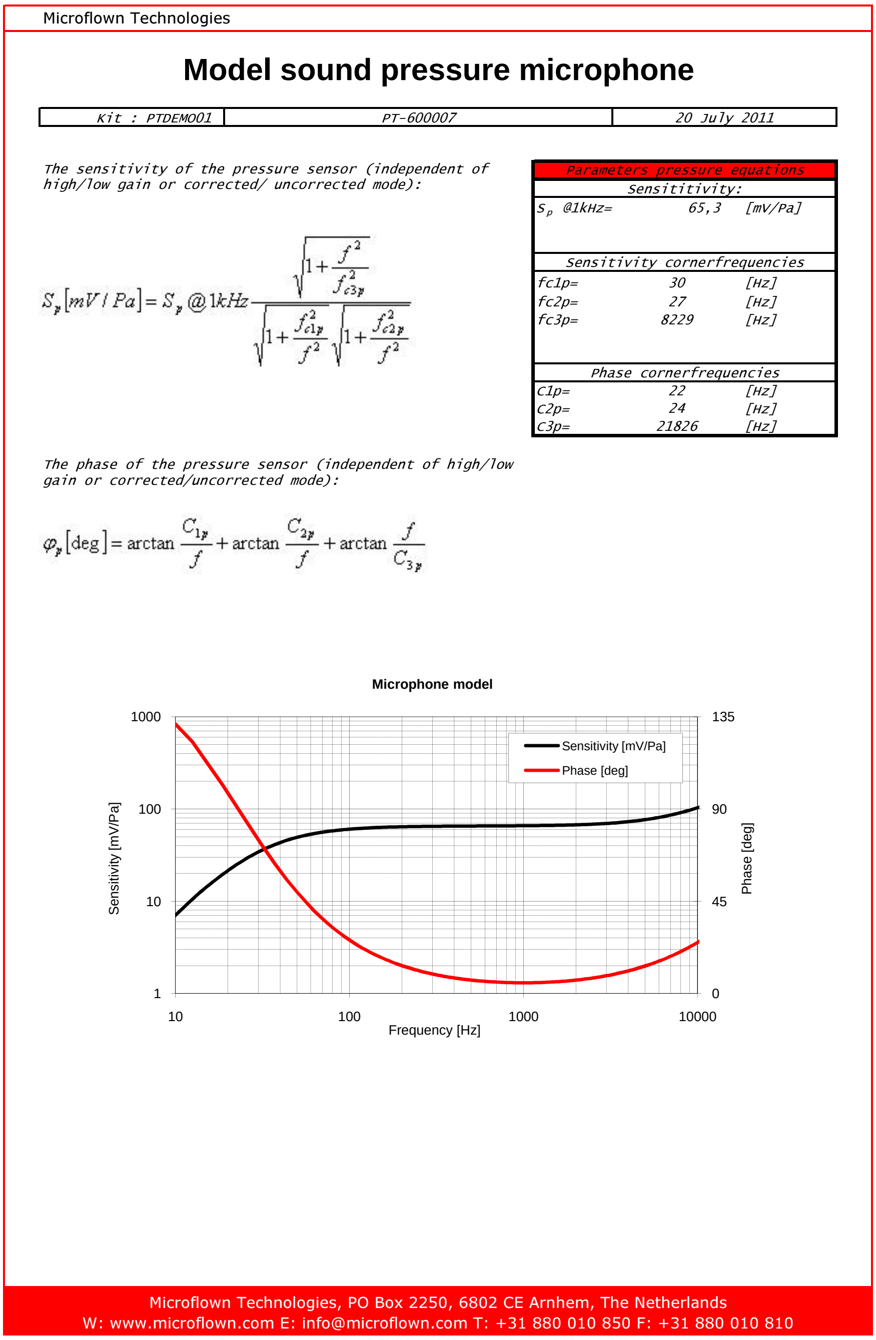

Microflown Technologies

Model sound pressure microphone

Kit : PTDEMO01	*PT-600007*	*20 July 2011*

The sensitivity of the pressure sensor (independent of high/low gain or corrected/ uncorrected mode):

$$S_p[mV/Pa] = S_p@1kHz\frac{\sqrt{1+\frac{f^2}{f_{c3p}^2}}}{\sqrt{1+\frac{f_{c1p}^2}{f^2}}\sqrt{1+\frac{f_{c2p}^2}{f^2}}}$$

Parameters pressure equations		
Sensititivity:		
S_p *@1kHz=*	*65,3*	*[mV/Pa]*
Sensitivity cornerfrequencies		
fc1p=	*30*	*[Hz]*
fc2p=	*27*	*[Hz]*
fc3p=	*8229*	*[Hz]*
Phase cornerfrequencies		
C1p=	*22*	*[Hz]*
C2p=	*24*	*[Hz]*
C3p=	*21826*	*[Hz]*

The phase of the pressure sensor (independent of high/low gain or corrected/uncorrected mode):

$$\varphi_p[\deg] = \arctan\frac{C_{1p}}{f} + \arctan\frac{C_{2p}}{f} + \arctan\frac{f}{C_{3p}}$$

Microphone model

Microflown Technologies, PO Box 2250, 6802 CE Arnhem, The Netherlands
W: www.microflown.com E: info@microflown.com T: +31 880 010 850 F: +31 880 010 810

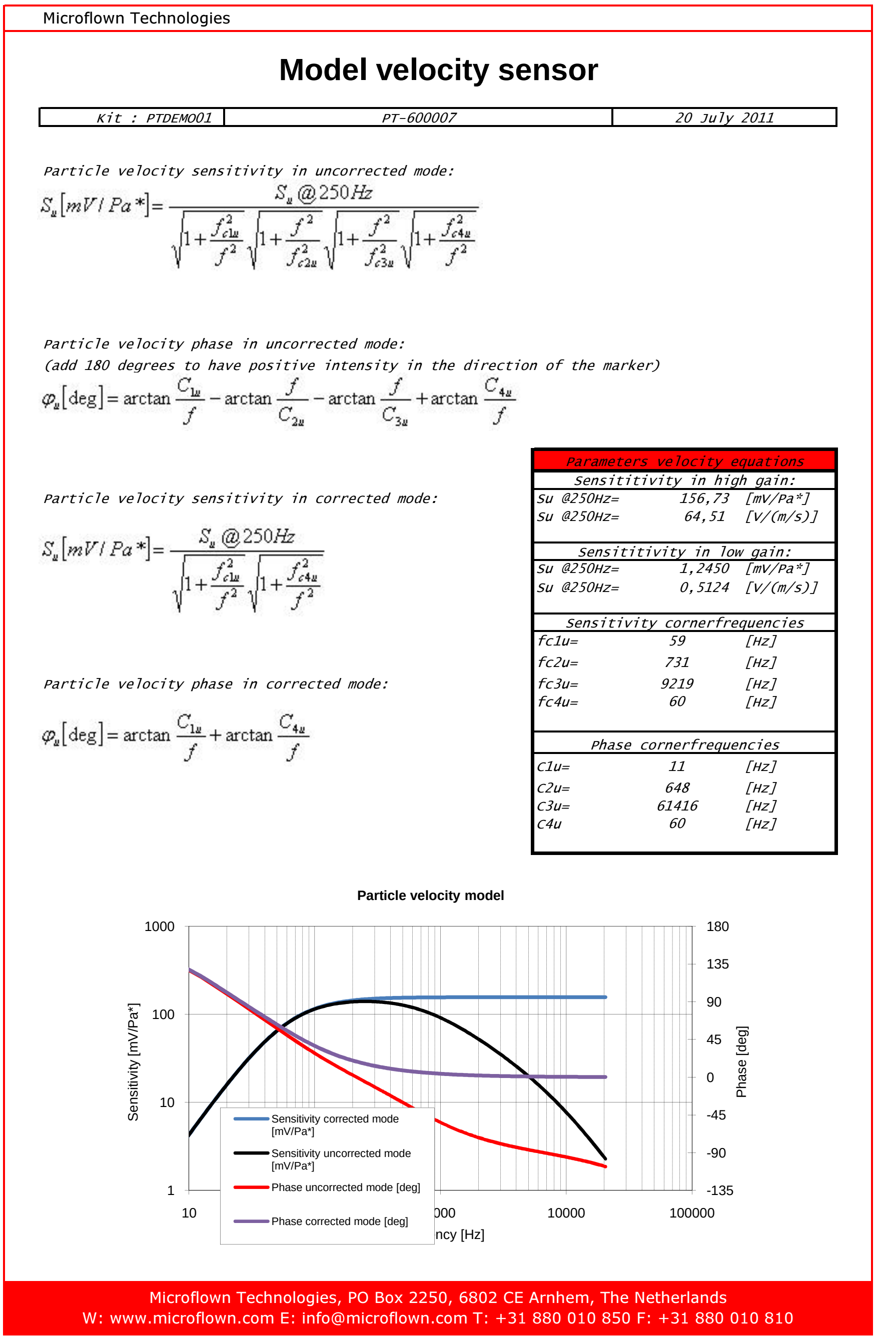

Model velocity sensor

Kit : PTDEMO01	PT-600007	20 July 2011

Particle velocity sensitivity in uncorrected mode:

$$S_u[mV/Pa^*]=\frac{S_u@250Hz}{\sqrt{1+\frac{f_{c1u}^2}{f^2}}\sqrt{1+\frac{f^2}{f_{c2u}^2}}\sqrt{1+\frac{f^2}{f_{c3u}^2}}\sqrt{1+\frac{f_{c4u}^2}{f^2}}}$$

Particle velocity phase in uncorrected mode:
(add 180 degrees to have positive intensity in the direction of the marker)

$$\varphi_u[\deg]=\arctan\frac{C_{1u}}{f}-\arctan\frac{f}{C_{2u}}-\arctan\frac{f}{C_{3u}}+\arctan\frac{C_{4u}}{f}$$

Particle velocity sensitivity in corrected mode:

$$S_u[mV/Pa^*]=\frac{S_u@250Hz}{\sqrt{1+\frac{f_{c1u}^2}{f^2}}\sqrt{1+\frac{f_{c4u}^2}{f^2}}}$$

Particle velocity phase in corrected mode:

$$\varphi_u[\deg]=\arctan\frac{C_{1u}}{f}+\arctan\frac{C_{4u}}{f}$$

Parameters velocity equations		
Sensititivity in high gain:		
Su @250Hz=	156,73	[mV/Pa*]
Su @250Hz=	64,51	[V/(m/s)]
Sensititivity in low gain:		
Su @250Hz=	1,2450	[mV/Pa*]
Su @250Hz=	0,5124	[V/(m/s)]
Sensitivity cornerfrequencies		
fc1u=	59	[Hz]
fc2u=	731	[Hz]
fc3u=	9219	[Hz]
fc4u=	60	[Hz]
Phase cornerfrequencies		
C1u=	11	[Hz]
C2u=	648	[Hz]
C3u=	61416	[Hz]
C4u	60	[Hz]

Particle velocity model

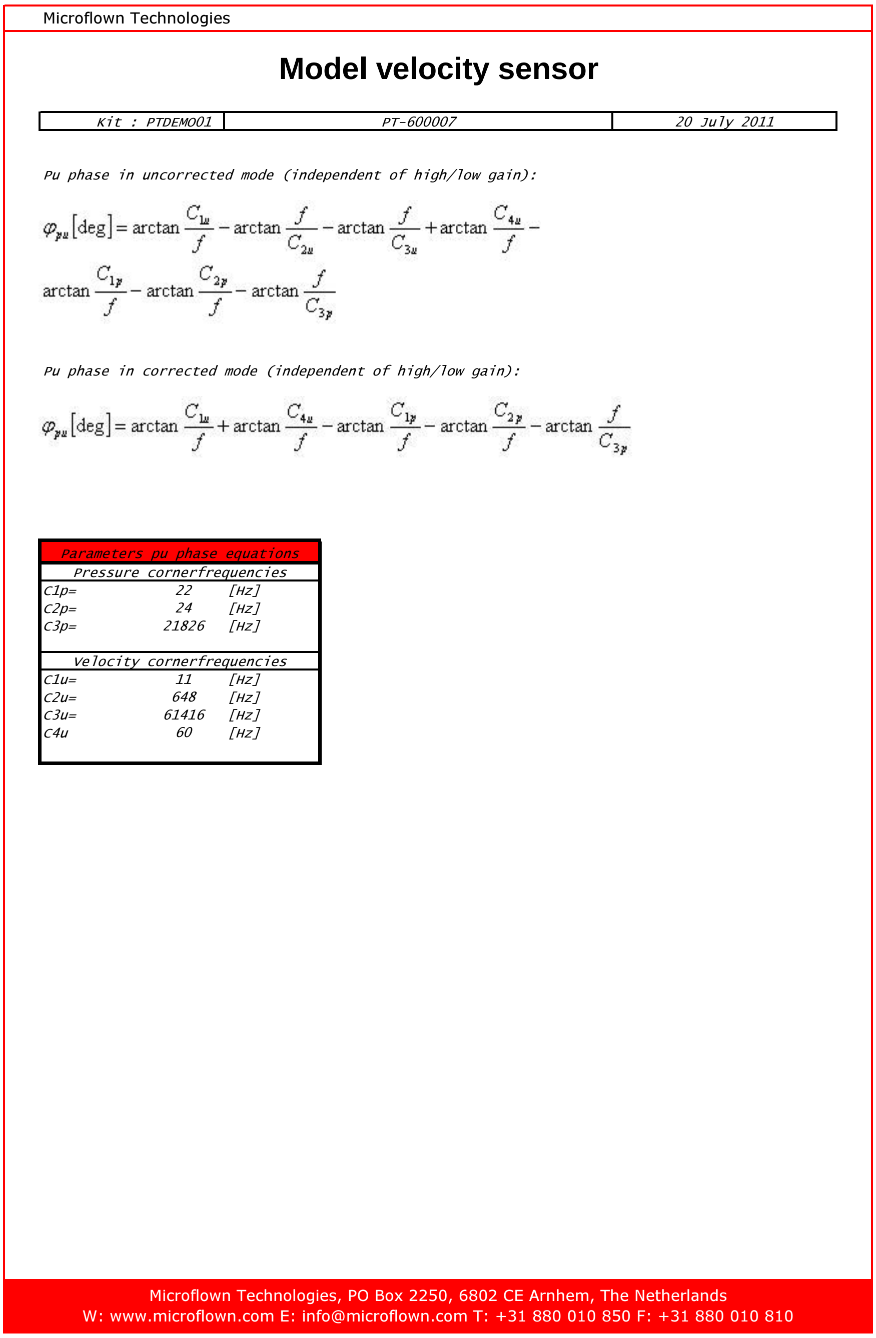

Microflown Technologies

Model velocity sensor

Kit : PTDEMO01	PT-600007	20 July 2011

Pu phase in uncorrected mode (independent of high/low gain):

$$\varphi_{pu}\left[\deg\right] = \arctan\frac{C_{1u}}{f} - \arctan\frac{f}{C_{2u}} - \arctan\frac{f}{C_{3u}} + \arctan\frac{C_{4u}}{f} - \arctan\frac{C_{1p}}{f} - \arctan\frac{C_{2p}}{f} - \arctan\frac{f}{C_{3p}}$$

Pu phase in corrected mode (independent of high/low gain):

$$\varphi_{pu}\left[\deg\right] = \arctan\frac{C_{1u}}{f} + \arctan\frac{C_{4u}}{f} - \arctan\frac{C_{1p}}{f} - \arctan\frac{C_{2p}}{f} - \arctan\frac{f}{C_{3p}}$$

Parameters pu phase equations		
Pressure cornerfrequencies		
C1p=	22	[Hz]
C2p=	24	[Hz]
C3p=	21826	[Hz]
Velocity cornerfrequencies		
C1u=	11	[Hz]
C2u=	648	[Hz]
C3u=	61416	[Hz]
C4u	60	[Hz]

Microflown Technologies, PO Box 2250, 6802 CE Arnhem, The Netherlands
W: www.microflown.com E: info@microflown.com T: +31 880 010 850 F: +31 880 010 810

D.2 *USP-Regular* Sensor

D.2.1 *Microflown USP-Regular* Data-Sheet

[6]

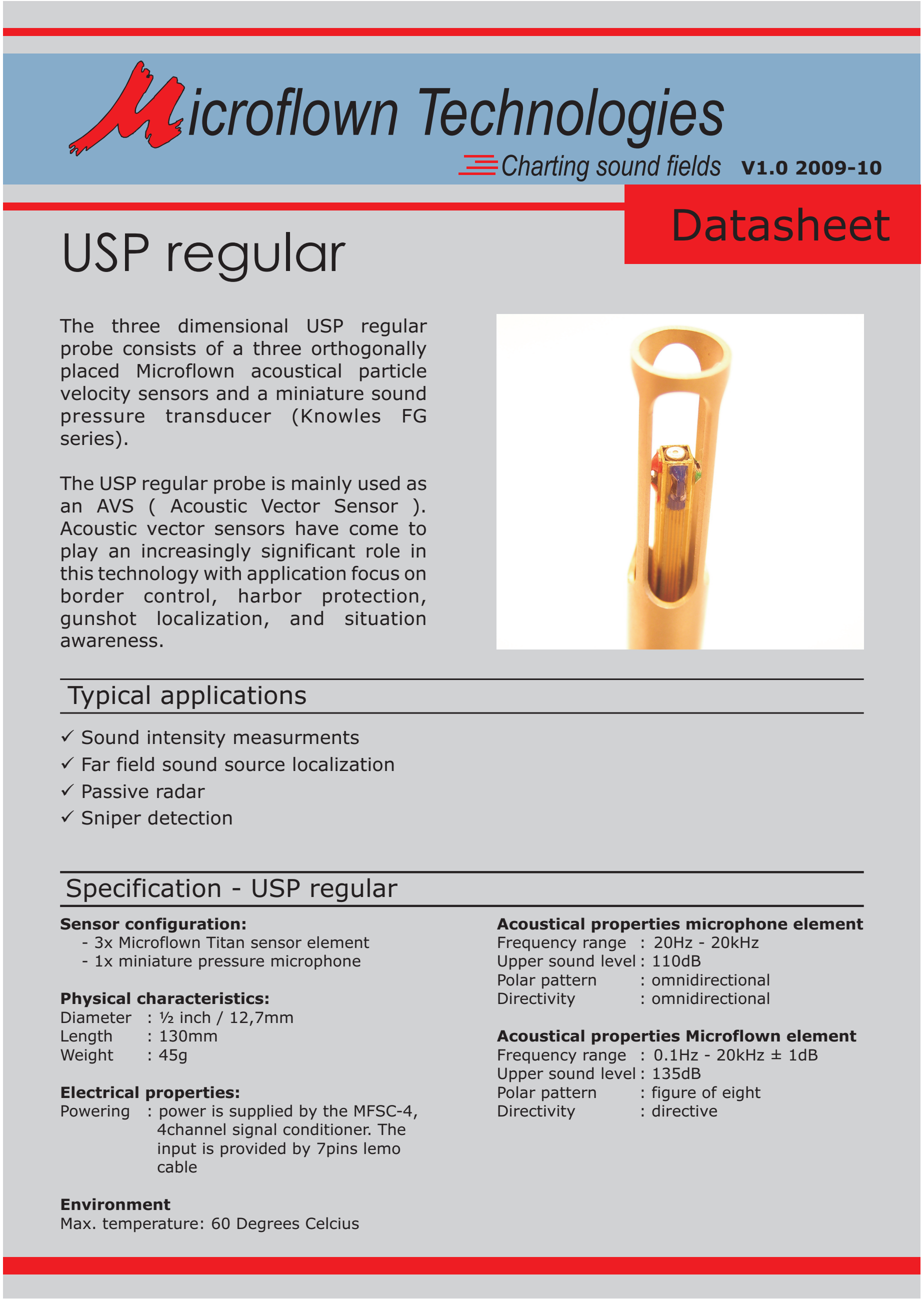

Microflown Technologies

Charting sound fields **V1.0 2009-10**

Datasheet

USP regular

The three dimensional USP regular probe consists of a three orthogonally placed Microflown acoustical particle velocity sensors and a miniature sound pressure transducer (Knowles FG series).

The USP regular probe is mainly used as an AVS (Acoustic Vector Sensor). Acoustic vector sensors have come to play an increasingly significant role in this technology with application focus on border control, harbor protection, gunshot localization, and situation awareness.

Typical applications

✓ Sound intensity measurments
✓ Far field sound source localization
✓ Passive radar
✓ Sniper detection

Specification - USP regular

Sensor configuration:
- 3x Microflown Titan sensor element
- 1x miniature pressure microphone

Physical characteristics:
Diameter : ½ inch / 12,7mm
Length : 130mm
Weight : 45g

Electrical properties:
Powering : power is supplied by the MFSC-4, 4channel signal conditioner. The input is provided by 7pins lemo cable

Environment
Max. temperature: 60 Degrees Celcius

Acoustical properties microphone element
Frequency range : 20Hz - 20kHz
Upper sound level : 110dB
Polar pattern : omnidirectional
Directivity : omnidirectional

Acoustical properties Microflown element
Frequency range : 0.1Hz - 20kHz ± 1dB
Upper sound level : 135dB
Polar pattern : figure of eight
Directivity : directive

---

[6] Materials presented here are courtesy of *Microflown Technologies*. *http://www.microflown.com*

Model sound pressure microphone

The sensitivity of the pressure microphone (independent of high/low gain or corrected/uncorrectede mode):

$$S_p[mV/Pa] = S_p@1kHz\frac{\sqrt{1+\frac{f^2}{f_{c3p}^2}}}{\sqrt{1+\frac{f_{c1p}^2}{f^2}}\sqrt{1+\frac{f_{c2p}^2}{f^2}}}$$

The phase of the pressure microphone (independent of high/low gain or corrected/uncorrectede mode):

$$\varphi_p[\deg] = \arctan\frac{C_{1p}}{f} + \arctan\frac{C_{2p}}{f} + \arctan\frac{f}{C_{3p}}$$

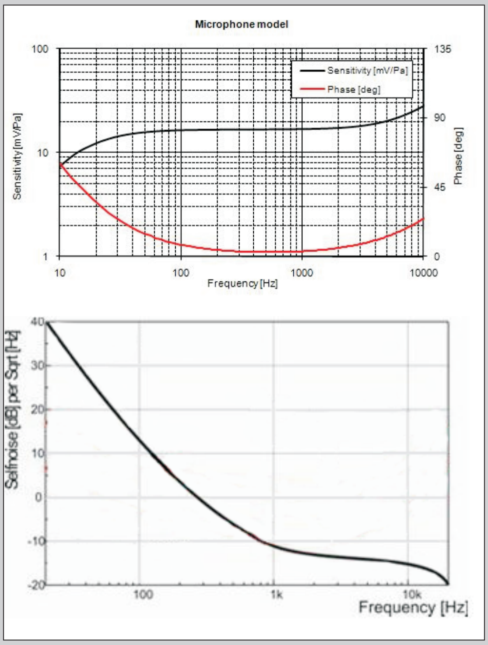

Parameters pressure equations		
Sensititivity:		
S_p @1kHz=	*55,0*	*[mV/Pa]*
Sensitivity cornerfrequencies		
fc1p=	*30*	*[Hz]*
fc2p=	*15*	*[Hz]*
fc3p=	*10000*	*[Hz]*
Phase cornerfrequencies		
C1p=	*30*	*[Hz]*
C2p=	*15*	*[Hz]*
C3p=	*10000*	*[Hz]*

Model Microflown sensor

The sensitivity in uncorrected mode:

$$S_u\left[mV/Pa^*\right]=\frac{S_u@250Hz}{\sqrt{1+\frac{f_{c1u}^2}{f^2}}\sqrt{1+\frac{f^2}{f_{c2u}^2}}\sqrt{1+\frac{f^2}{f_{c3u}^2}}\sqrt{1+\frac{f_{c4u}^2}{f^2}}\sqrt{1+\frac{f_{c5u}^2}{f^2}}}$$

The phase in uncorrected mode:

$$\varphi_u\left[\deg\right]=\arctan\frac{C_{1u}}{f}-\arctan\frac{f}{C_{2u}}-\arctan\frac{f}{C_{3u}}-\arctan\frac{C_{4u}}{f}+\arctan\frac{C_{5u}}{f}$$

The sensitivity in corrected mode:

$$S_u\left[mV/Pa^*\right]=\frac{S_u@250Hz}{\sqrt{1+\frac{f_{c1u}^2}{f^2}}\sqrt{1+\frac{f_{c4u}^2}{f^2}}\sqrt{1+\frac{f_{c5u}^2}{f^2}}}$$

The phase in corrected mode:

$$\varphi_u\left[\deg\right]=\arctan\frac{C_{1u}}{f}+\arctan\frac{C_{4u}}{f}+\arctan\frac{C_{5u}}{f}$$

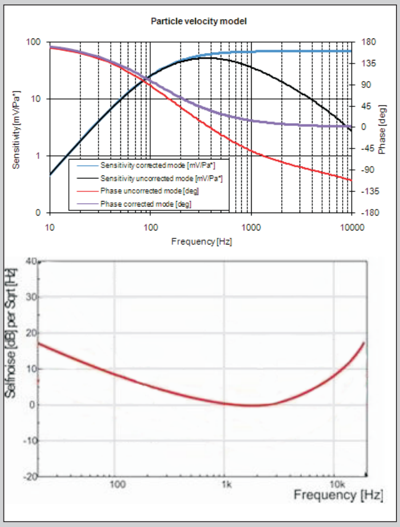

Parameters velocity equations		
Sensititivity in high gain:		
Su @250Hz=	25	[mV/Pa*]
Su @250Hz=	10	[V/(m/s)]
Sensititivity in low gain:		
Su @250Hz=	0,25	[mV/Pa*]
Su @250Hz=	0,1	[V/(m/s)]
Sensitivity cornerfrequencies		
fc1u=	150	[Hz]
fc2u=	600	[Hz]
fc3u=	10000	[Hz]
fc4u=	77	[Hz]
Phase cornerfrequencies		
C1u=	180	[Hz]
C2u=	700	[Hz]
C3u=	20000	[Hz]
C4u	77	[Hz]

D.2.2 *Microflown USP-Regular* Manual

[7]

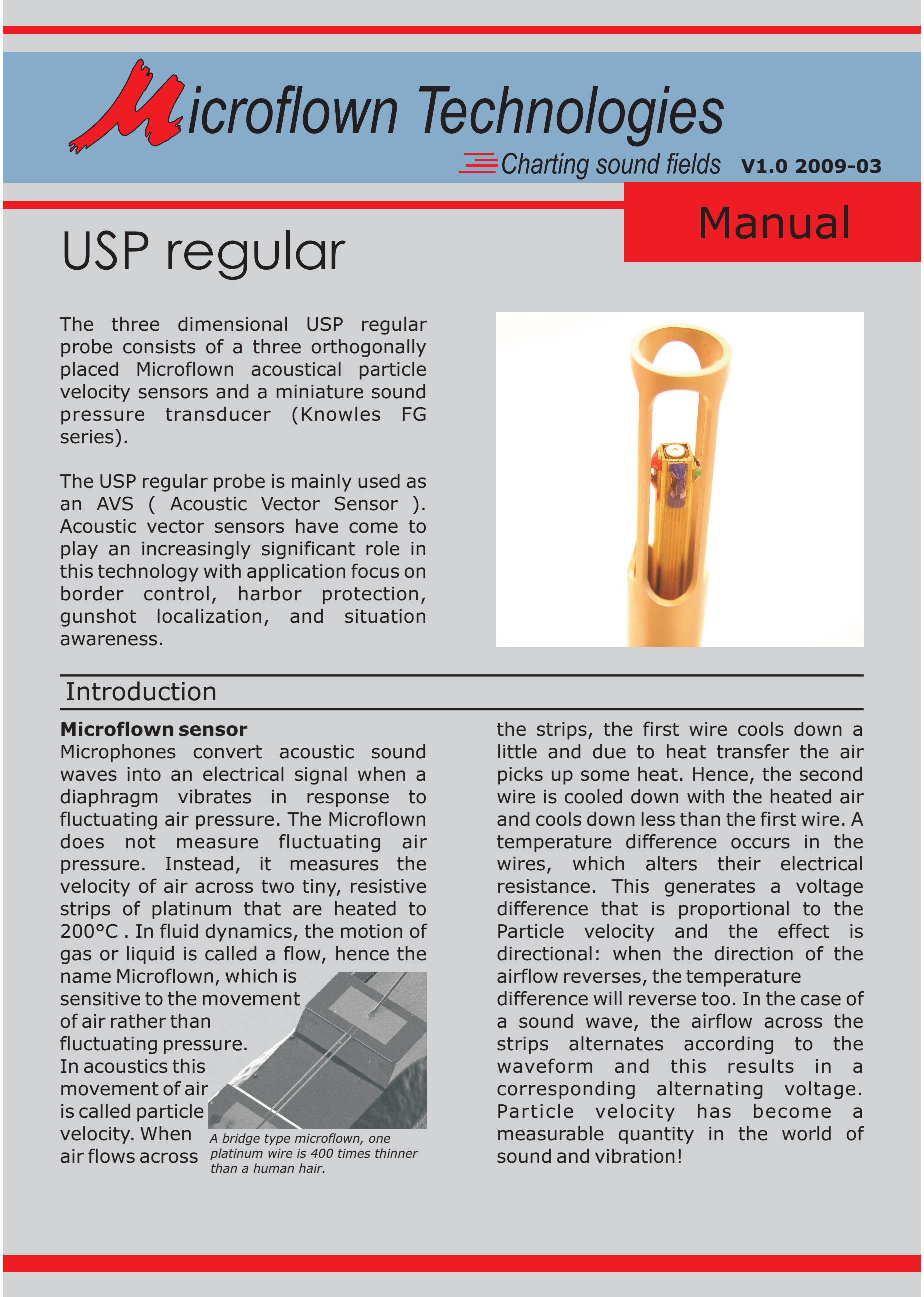

Microflown Technologies

Charting sound fields **V1.0 2009-03**

Manual

USP regular

The three dimensional USP regular probe consists of a three orthogonally placed Microflown acoustical particle velocity sensors and a miniature sound pressure transducer (Knowles FG series).

The USP regular probe is mainly used as an AVS (Acoustic Vector Sensor). Acoustic vector sensors have come to play an increasingly significant role in this technology with application focus on border control, harbor protection, gunshot localization, and situation awareness.

Introduction

Microflown sensor

Microphones convert acoustic sound waves into an electrical signal when a diaphragm vibrates in response to fluctuating air pressure. The Microflown does not measure fluctuating air pressure. Instead, it measures the velocity of air across two tiny, resistive strips of platinum that are heated to 200°C . In fluid dynamics, the motion of gas or liquid is called a flow, hence the name Microflown, which is sensitive to the movement of air rather than fluctuating pressure. In acoustics this movement of air is called particle velocity. When air flows across the strips, the first wire cools down a little and due to heat transfer the air picks up some heat. Hence, the second wire is cooled down with the heated air and cools down less than the first wire. A temperature difference occurs in the wires, which alters their electrical resistance. This generates a voltage difference that is proportional to the Particle velocity and the effect is directional: when the direction of the airflow reverses, the temperature difference will reverse too. In the case of a sound wave, the airflow across the strips alternates according to the waveform and this results in a corresponding alternating voltage. Particle velocity has become a measurable quantity in the world of sound and vibration!

A bridge type microflown, one platinum wire is 400 times thinner than a human hair.

---

[7] Materials presented here are courtesy of *Microflown Technologies*. *http://www.microflown.com*

Directivity

If you measure with a standard microphone you will not only measure the source but also all the background noises and reflections. The microflown does only measure the source and not the background noises and reflections. This is because of the difference in polar response of sound pressure and particle velocity. The two quantities in acoustic, sound pressure and particle velocity, have both a different kind of polar response. If you look at sound pressure, it has an omnidirectional reponse. Sound, and also vibrations, are only measured from one side.

Particle velocity is an vector and so is directional. This directivity effect makes the microflown extremly suitable to measure in real operating situations with background noise and reflections. An omni pattern picks up sound equally from all directions. Particle Velocity has a directional, figure of eight, response.

Figure of eight response of the Microflown

List of equipment

The Microflown USP regular comes with:

- ✓ 1x USP regular in protective box
- ✓ 1x MFSC-4 (4 channel signal conditioner)
- ✓ 1x LEMO cable with 7pins male connector on both ends
- ✓ 1x Power supply
- ✓ 1x Protective case

How to connect the USP regular

The power supply can be connected with the signal conditioner using the Power Input 18VDC connection on the backside of the signal conditioner. See right sided picture.

At the frontside of the signal conditioner there is 7 pins female lemo connector called Probe input. See right sided picture. The connector can be found on the downside of the probe. The 7 pins male lemo cable connects the signal conditioner with the probe.

More info on the MFSC-4, 4 channel signal conditioner, can be found in the datasheet and manual of the MFSC-4

Manual - USP regular **Page 2** Microflown Technologies

USP directivity

Axis	Colour
X	**Blue**
Y	**Red**
Z	**Green**

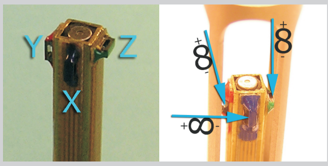

How to read the calibration report

The natural response of the Microflown is not flat, and thus needs to be calibrated. The goal of calibration is to find out how much the voltage output is when a certain acoustic signal is applied to a Microflown or microphone. In other words: it has to be determined what the amplitude response, or the frequency dependent sensitivity is. In case of a Microflown this means how many volts output per meter per second particle velocity input and in case of a microphone it means how many volts output per Pascal input.

To calibrate a PU probe, white Gaussian noise from a point source is radiated and measured at a known distance. Also, for a point source at any location on the axis in front of this source the ratio of pressure to velocity is known. It is via this property that both sensors are calibrated, referenced to a known (calibrated) G.R.A.S microphone.

The results of the calibration measurements are used to fit a mathematical model over. This model describes the response of the sensors as a function of frequency. A model makes it also easier to implement it and apply it as a software correction.

In the calibration report all relevant calibrated quantities can be found. For pressure as well as for velocity it's sensitivity and phase (relative to the reference microphone) are shown. Since the signal conditioner has a corrected and uncorrected mode, these quantities are plotted twice.

Last graphs in the calibration report is the phase response between pressure and velocity. This phase is necessary when one needs to determine from which half of the figure of eight sound approaches the PU-probe. Again, for both corrected and uncorrected mode the graphs are shown.

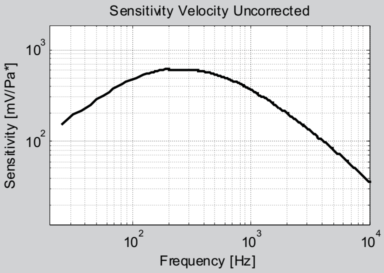

Example of the frequency dependent sensitivity of the particle velocity sensor, measured in uncorrected mode.

Below each graph is the mathematical model stated together with it's coefficients which approximates the shown behavior. To apply this model, divide the measurement's results (transformed to frequency domain) by this curve to obtain a calibrated response (also in frequency domain):

$$\frac{\textit{Output Data Acquisition}\ (\ \mathrm{V}\ )}{\textit{Calibration model}\ (\frac{\mathrm{v}}{\mathrm{m/s}})} = \textit{Calibrated response}\ (\frac{\mathrm{m}}{\mathrm{s}})$$

D.2.3 *Microflown MFSC-4* Data-Sheet

[8]

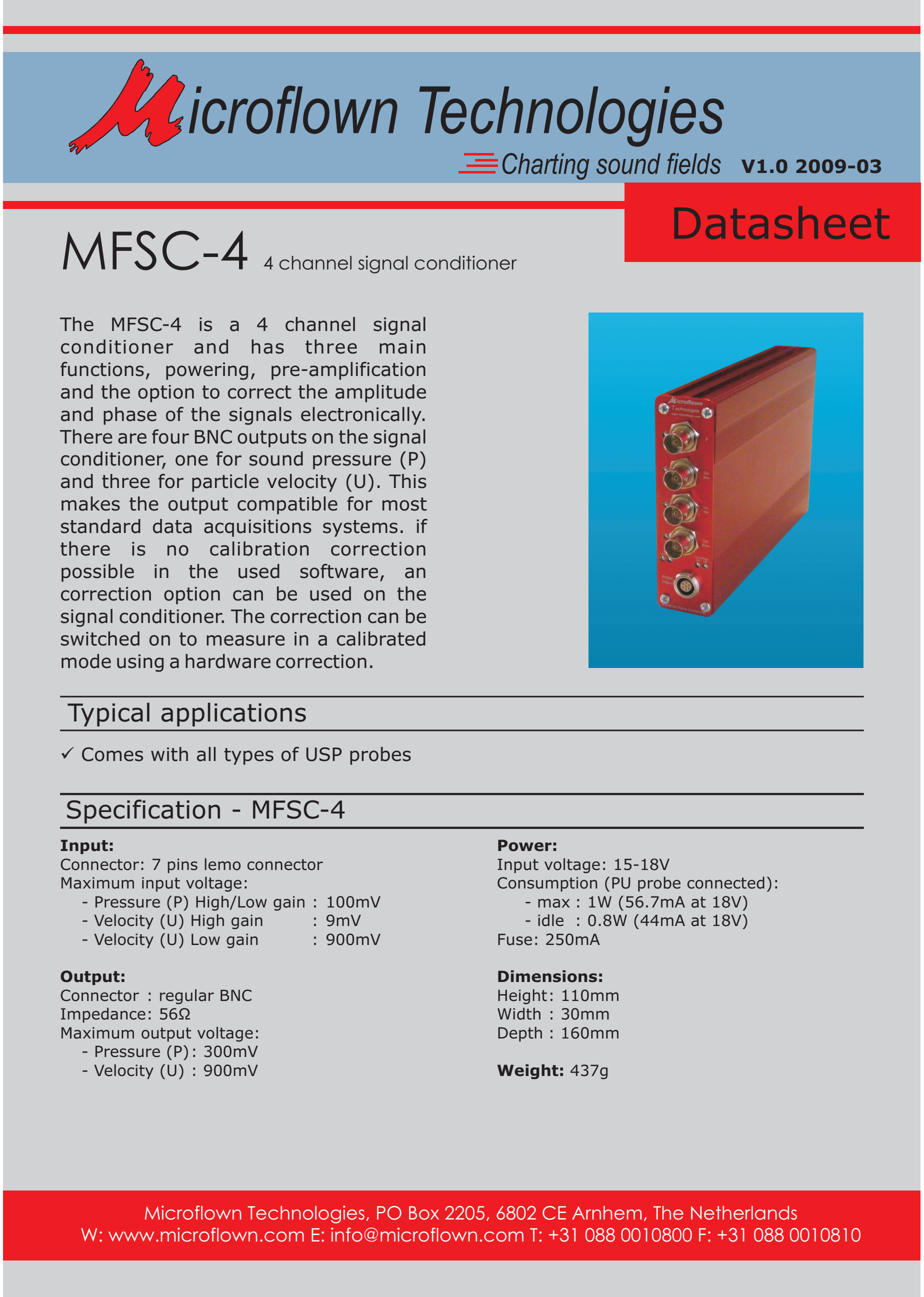

Microflown Technologies

Charting sound fields **V1.0 2009-03**

Datasheet

MFSC-4 4 channel signal conditioner

The MFSC-4 is a 4 channel signal conditioner and has three main functions, powering, pre-amplification and the option to correct the amplitude and phase of the signals electronically. There are four BNC outputs on the signal conditioner, one for sound pressure (P) and three for particle velocity (U). This makes the output compatible for most standard data acquisitions systems. if there is no calibration correction possible in the used software, an correction option can be used on the signal conditioner. The correction can be switched on to measure in a calibrated mode using a hardware correction.

Typical applications

✓ Comes with all types of USP probes

Specification - MFSC-4

Input:
Connector: 7 pins lemo connector
Maximum input voltage:
  - Pressure (P) High/Low gain : 100mV
  - Velocity (U) High gain : 9mV
  - Velocity (U) Low gain : 900mV

Output:
Connector : regular BNC
Impedance: 56Ω
Maximum output voltage:
  - Pressure (P): 300mV
  - Velocity (U) : 900mV

Power:
Input voltage: 15-18V
Consumption (PU probe connected):
  - max : 1W (56.7mA at 18V)
  - idle : 0.8W (44mA at 18V)
Fuse: 250mA

Dimensions:
Height: 110mm
Width : 30mm
Depth : 160mm

Weight: 437g

Microflown Technologies, PO Box 2205, 6802 CE Arnhem, The Netherlands
W: www.microflown.com E: info@microflown.com T: +31 088 0010800 F: +31 088 0010810

---

[8] Materials presented here are courtesy of *Microflown Technologies*. *http : //www.microflown.com*

D.2.4 *Microflown MFSC-4* Manual

[9]

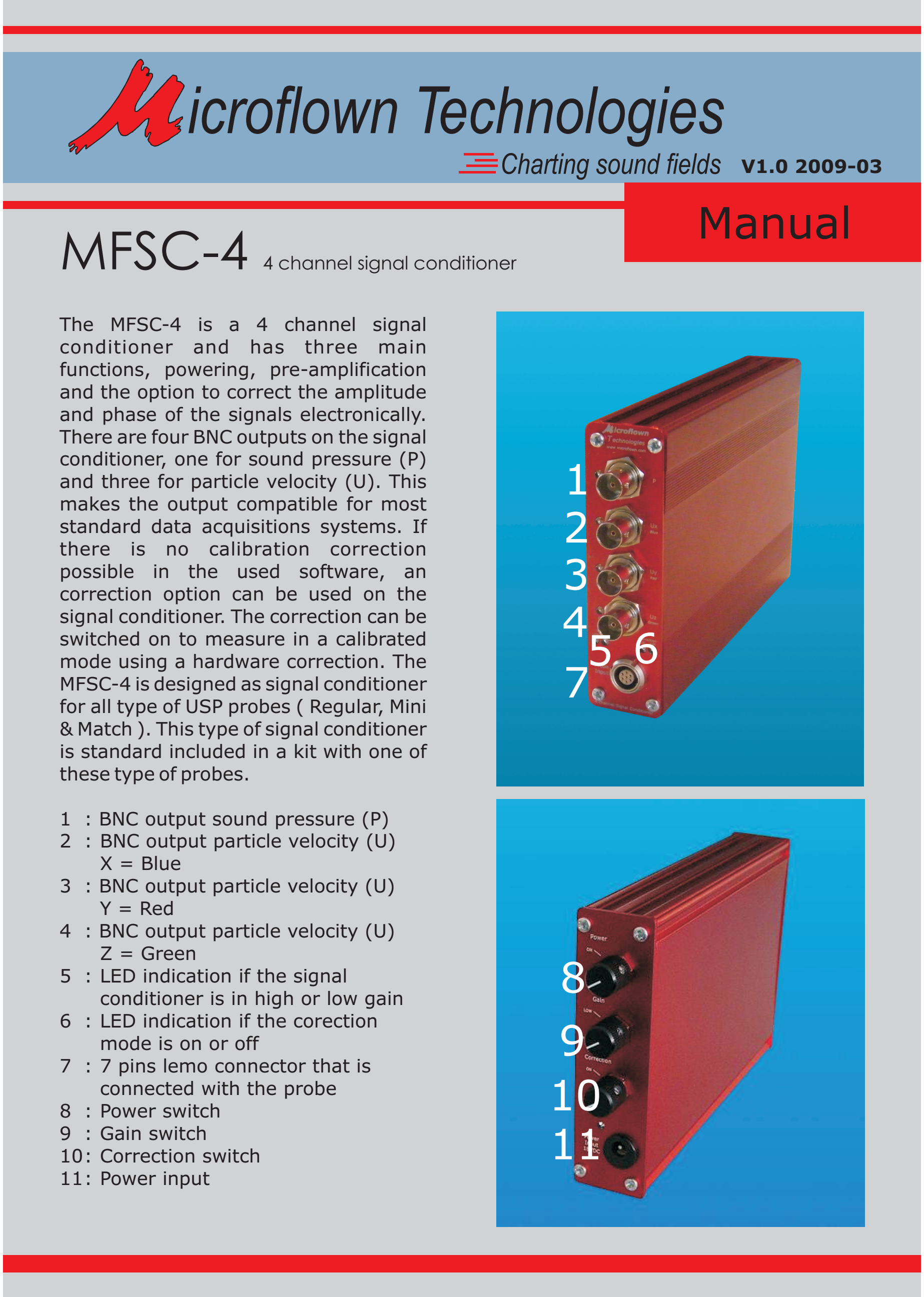

Microflown Technologies

Charting sound fields **V1.0 2009-03**

Manual

MFSC-4 4 channel signal conditioner

The MFSC-4 is a 4 channel signal conditioner and has three main functions, powering, pre-amplification and the option to correct the amplitude and phase of the signals electronically. There are four BNC outputs on the signal conditioner, one for sound pressure (P) and three for particle velocity (U). This makes the output compatible for most standard data acquisitions systems. If there is no calibration correction possible in the used software, an correction option can be used on the signal conditioner. The correction can be switched on to measure in a calibrated mode using a hardware correction. The MFSC-4 is designed as signal conditioner for all type of USP probes (Regular, Mini & Match). This type of signal conditioner is standard included in a kit with one of these type of probes.

1 : BNC output sound pressure (P)
2 : BNC output particle velocity (U)
X = Blue
3 : BNC output particle velocity (U)
Y = Red
4 : BNC output particle velocity (U)
Z = Green
5 : LED indication if the signal conditioner is in high or low gain
6 : LED indication if the corection mode is on or off
7 : 7 pins lemo connector that is connected with the probe
8 : Power switch
9 : Gain switch
10: Correction switch
11: Power input

---

[9] Materials presented here are courtesy of *Microflown Technologies*. *http://www.microflown.com*

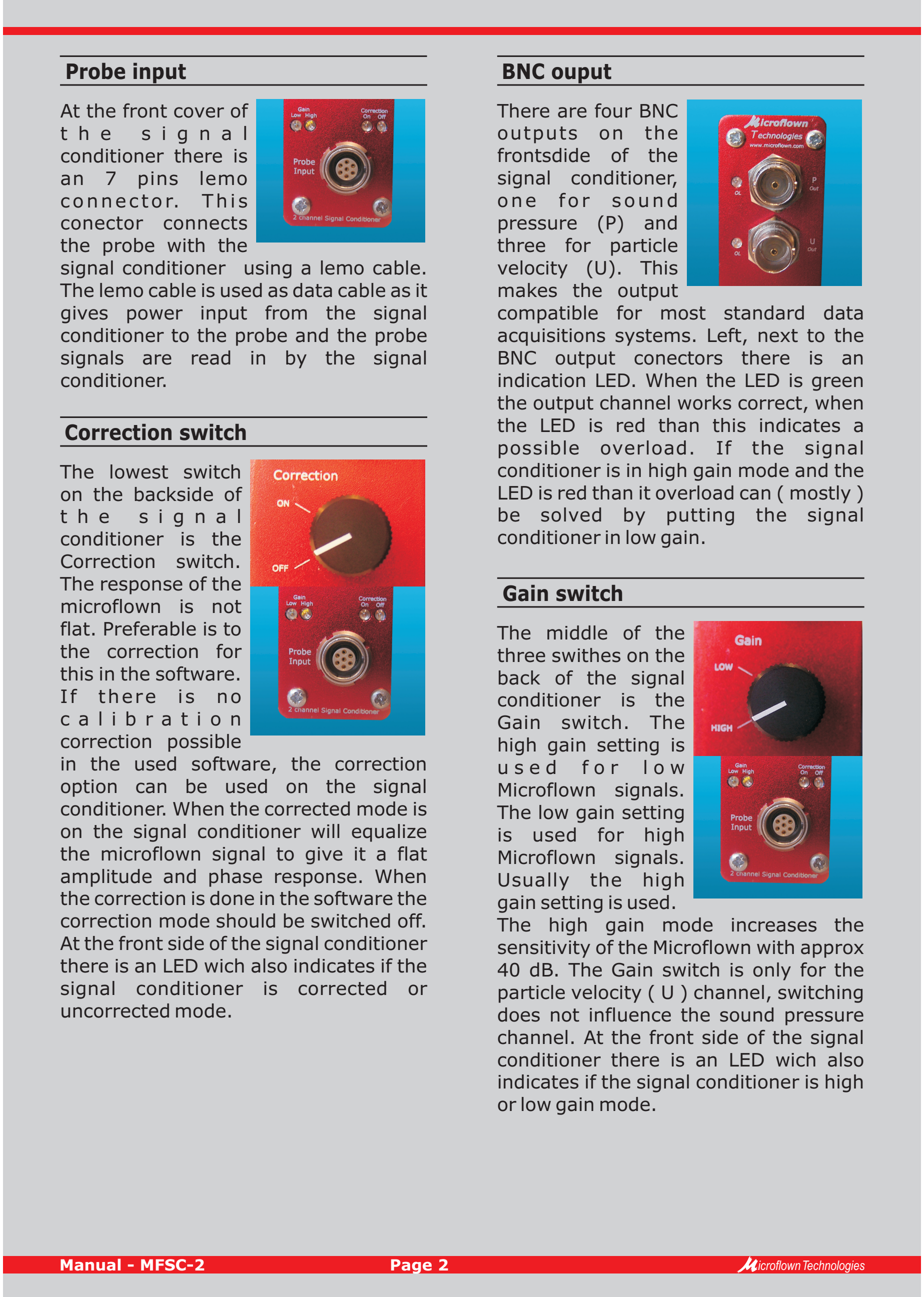

Probe input

At the front cover of the signal conditioner there is an 7 pins lemo connector. This conector connects the probe with the signal conditioner using a lemo cable. The lemo cable is used as data cable as it gives power input from the signal conditioner to the probe and the probe signals are read in by the signal conditioner.

Correction switch

The lowest switch on the backside of the signal conditioner is the Correction switch. The response of the microflown is not flat. Preferable is to the correction for this in the software. If there is no calibration correction possible in the used software, the correction option can be used on the signal conditioner. When the corrected mode is on the signal conditioner will equalize the microflown signal to give it a flat amplitude and phase response. When the correction is done in the software the correction mode should be switched off. At the front side of the signal conditioner there is an LED wich also indicates if the signal conditioner is corrected or uncorrected mode.

BNC ouput

There are four BNC outputs on the frontsdide of the signal conditioner, one for sound pressure (P) and three for particle velocity (U). This makes the output compatible for most standard data acquisitions systems. Left, next to the BNC output conectors there is an indication LED. When the LED is green the output channel works correct, when the LED is red than this indicates a possible overload. If the signal conditioner is in high gain mode and the LED is red than it overload can (mostly) be solved by putting the signal conditioner in low gain.

Gain switch

The middle of the three swithes on the back of the signal conditioner is the Gain switch. The high gain setting is used for low Microflown signals. The low gain setting is used for high Microflown signals. Usually the high gain setting is used. The high gain mode increases the sensitivity of the Microflown with approx 40 dB. The Gain switch is only for the particle velocity (U) channel, switching does not influence the sound pressure channel. At the front side of the signal conditioner there is an LED wich also indicates if the signal conditioner is high or low gain mode.

Manual - MFSC-2 **Page 2** Microflown Technologies

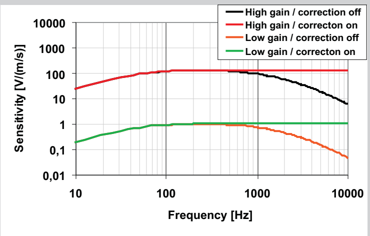

Sensitivity in for the particle velocity (U) signal in different signal conditioner settings

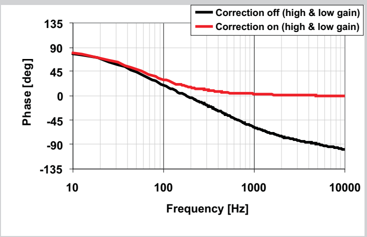

Phase of the particle velocity (U) signal if correction mode is on or off

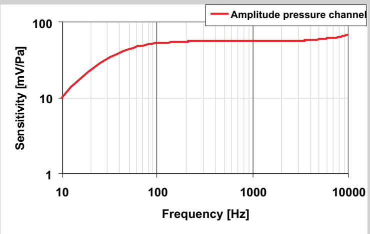

Sensitivity of the sound pressure signal wich is not influenced by different signal conditioner settings

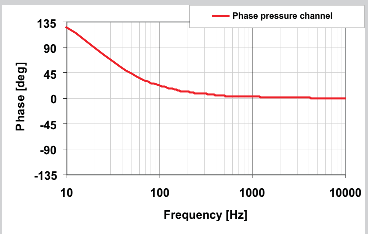

Phase response of the sound pressure signal wich is not influenced by different signal conditioner settings

Bibliography

[1] K. R. Holland. *Loudspeaker and headphone handbook*, chapter 1, Principles of sound radiation, pages 1–40. Focal Press, Oxford, 3rd edition, 2001.

[2] P. Newell; K. R. Holland. *Audio engineering explained*, chapter 11, What is a loudspeaker?, pages 331–349. Elsevier Ltd, Focal Press, 2010.

[3] P. Newell; K. R. Holland. *Loudspeakers for music recording and reproduction*. Elsevier Ltd, Focal Press, 2007.

[4] P. Newell; K. R. Holland. *Audio engineering explained*, chapter 13, Loudspeaker cabinets, pages 381–403. Elsevier Ltd, Focal Press, 2010.

[5] D. Davis; E. Patronis. *Sound system engineering*. Elsevier Ltd, Focal Press, 3rd edition, 1928.

[6] M. Colloms; P. Darlington. *High performance loudspeakers*. John Wiley & Sons Ltd, 6th edition, 2005.

[7] I. Johnston. *Measured tones*. IOP Publishing Ltd, 1997.

[8] F. E. Toole. Audio engineering, science in the service of art. *The Audio Critic*, 28:5–15, 2002.

[9] A. R. Bailey. A non-resonant loudspeaker enclosure design. *Wireless World*, October 1965.

[10] M. Roberts. An acoustical model for transmission-line woofer systems. *Proceedings of the Institute of Acoustics*, 12(8):111–119, 1990.

[11] A. R. Bailey. The transmission-line loudspeaker enclosure. *Wireless World*, May 1972.

[12] L. J. S. Bradbury. The use of fibrous materials in loudspeaker enclosure. *Journal of Audio Engineering Society*, 24(3):162–170, April 1976.

[13] R. M. Bullock; P. E. Hillman. A transmission-line woofer model. *Journal of Audio Engineering Society*, page Preprint No.2384, November 1986.

[14] J. Backman. A computational model of transmission-line loudspeakers. *Proceeding of Audio Engineering Society*, 92nd Convention, 1992.

[15] B. Olney. A method of eliminating cavity resonance, extending low frequency response and increasing acoustic damping in cabinet type loudspeakers. *Journal of Acoustical Society of America*, 8(2):104–111, 1936.

[16] G. Bank; J. Wright. *Loudspeaker and headphone handbook*, chapter 7, Loudspeaker enclosures, pages 297–325. Focal Press, Oxford, 3rd edition, 2001.

[17] L. Cremer; H. A. Muller. *Principles and applications of room acoustics.* Applied Science Publisher, London, 1982.

[18] *Introduction to COMSOL Multiphysics documentation.* COMSOL Multiphysics, 4.2a edition, October 2011.

[19] C. L. Morfey. *Dictionary of acoustics.* Academic Press, 2001.

[20] J. Eargle. *Loudspeaker handbook.* Kluwer Academic Publishers, 2nd edition, 2003.

[21] G. James; D. Burley; D. Clements; P. Dyke; J. Searl; J. Wright. *Modern engineering mathematics.* Pearson Education, Prentice Hall, 3rd edition, 2001.

[22] A. D. Pierce. *Acoustics an introduction to its physical principles and applications*, chapter 7, Low-frequency models of sound transmission, pages 313–370. McGraw-Hill, 1981.

[23] H. F. Olson. *Acoustical engineering.* D. Van Nostrand company, Inc., 1957.

[24] F. Jacobsen; P. Møller Juhl. *Fundamentals of general linear acoustics.* John Wiley & Sons Ltd, 2013.

[25] L. E. Kinsler; A. R. Frey; A. B. Coppens; J. V. Sanders. *Fundamentals of acoustics.* John Wiley & Sons Inc, 4th edition, 2000.

[26] P. M. Morse; K. U. Ingard. *Theoretical acoustics.* McGraw-Hill, Inc., 1968.

[27] Wu Qunli. Empirical relations between acoustical properties and flow resistivity of porous plastic open-cell foam. *Applied Acoustics*, 25:141–148, 1988.

[28] F. J. Fahy. *Foundations of engineering acoustics.* Elsevier Academic Press, 2007.

[29] F. J. Fahy; J. G. Walker, editor. *Advanced applications in acoustics, noise and vibration.* Spon Press, 2004.

[30] F. J. Fahy; J. G. Walker, editor. *Fundamentals of noise and vibration.* Spon Press, 1998.

[31] B. Massey. *Mechanics of Fluids*, chapter 8, Boundary layers, wakes and other shear layers, pages 298–361. Taylor & Francis, 2006.

[32] M. A. Biot. Theory of propagation of elastic wave in a fluid saturated porous solid. *Journal of Acoustical Society of America*, 28:168–178, 1958.

[33] D. J. Sides; K. Attenborough and K. A. Mulholland. Application of a generalized acoustic propagation theory to fibrous absorbants. *Journal of Sound and Vibration*, 19:49–64, 1971.

[34] C. C. Bissell. *Control engineering.* Chapman & Hall, 1991.

[35] N. W. McLachlan. *Bessel function for engineers.* Clarendon press, Oxford, 1955.

[36] M. L. Munjal. *Acoustics of ducts and mufflers with application to exhaust and ventilation system design.* Wiley-Interscience, John Wiley & Sons, 1986.

[37] A. Ishimaru. *Electromagnetic wave propagation, radiation, and scattering*, chapter 3, Waves in inhomogeneous and layered media, pages 31–76. Prentice-Hall International, Inc., 1991.

[38] B. D. Hahn; D. T. Valentine. *Essential MATLAB for engineers and scientists.* Elsevier, Butterworth-Heinemann, 3rd edition, 2002.

[39] K. Shin; J. K. Hammond. *Fundamentals of signal processing for sound and vibration engineers.* John Wiley & Sons Ltd, 2008.

[40] M. E. Goldstein. *Aeroacoustics.* McGraw-Hill, 1976.

[41] B. Massey. *Mechanics of fluids*, chapter 7, Flow and losses in pipes and fittings, pages 245–289. Taylor & Francis, 2006.

[42] M. C. M. Wright, editor. *Lecture notes on the mathematics of acoustics.* Imperial College Press, 2005.

[43] E. Kreyszig. *Advanced engineering mathematics.* John Wiley & Sons, Inc., 2006.

[44] A. Ishimaru. *Electromagnetic wave propagation, radiation, and scattering*, chapter 4, Waveguides and cavities, pages 76–121. Prentice-Hall International, Inc., 1991.

[45] R. F. Lambert. Surface acoustic admittance of highly porous open-cell foams. *Journal of Acoustical Society of America*, 73:1139–1146, 1982.

[46] A. Ishimaru. *Electromagnetic wave propagation, radiation, and scattering.* Prentice-Hall International, Inc., 1991.

[47] K. Weltner; J. Grosjean; P. Schuster; W. J. Weber. *Mathematics for engineers and scientists.* Stanley Thornes Ltd, 1986.

[48] P. A. Nelson. *Advanced applications in acoustics, noise and vibration*, chapter 2, Acoustic modelling, Source identification and location, pages 100–154. Spon Press, 2004.

[49] M. Petyt; C. J. C. Jones. *Advanced applications in acoustics, noise and vibration*, chapter 2, Acoustic modelling, numerical methods in acoustics, pages 51–100. Spon Press, 2004.

[50] L. L. Beranek. Acoustic impedance of porous materials. *Journal of Acoustical Society of America*, 13:248, 1943.

[51] R. F. Lambert. The acoustical structure of highly porous open-cell foams. *Journal of Acoustical Society of America*, 72:879–887, 1982.

[52] D. A. Nelsen. Propagation of finite-amplitude sound in air-field porous materials. *Journal of Acoustical Society of America*, 79:2095–2105, 1986.

[53] P. B. Murray; P. Ferrante; A. Scofano. Manufacturing process and boundary layer influences on perforate liner impedance. *American Institute of Aeronautics and Astronautics*, 2849 (2005):1–17, 2005.

[54] M. E. Delany; E. N. Bazley. Acoustical properties of fibrous absorbent materials. *Applied Acoustics*, 3:105–116, 1970.

[55] R. F. Lambert. Propagation of sound in highly porous open-cell foams. *Journal of Acoustical Society of America*, 73:1131–1138, 1982.

[56] P. Brunet; Z. Rimkunas; S. Temme. Evaluation of time-frequency analysis methods and their practical applications. *Journal of Audio Engineering Society*, 123rd Convention, 2007.

[57] F. P. Mechel. Absorption cross section of absorber cylinders. *Journal of Sound and Vibration*, 107:131–148, 1986.

[58] C. Zwikker; C. W. Kosten. *Sound absorbing materials.* Elsevier, New York, 1949.

[59] BS EN ISO 10534-1:2001. Acoustics - determination of sound absorption coefficient and impedance in impedances tubes - part 1 method using standing wave ratio, November 2001.

[60] M. R. Schroeder. New method of measuring reverberation time. *Journal of Acoustical Society of America*, pages 409–412, 1965.

[61] M. E. Delany; E. N. Bazley. Uncertainties in realizing the standard of sound pressure by the close-coupler reciprocity technique. *Metrologia*, 18:117–132, 1982.

[62] M. Vorländer; H. Bietz. Comparison of methods for measuring reverberation time. *Acoustica*, 80:205–215, 1994.

[63] I. P. Dunn; W. A. Davern. Calculation of acoustic impedance of multi-layer absorbers. *Applied Acoustics*, 19:321–334, 1986.

[64] BS EN ISO 354: 2003. Acoustics - measurement of sound absorption in a reverberation room., June 2003.

[65] J. F. Allard; A. Aknine; C. Depollier. Acoustical properties of partially reticulated foams with high and medium flow resistance. *Journal of Acoustical Society of America*, 79:1734–1740, 1986.

[66] Wu Qunli. The relationship between acoustical and physical properties of highly porous foams. *Inter-Noise*, 87:447–450, 1987.

[67] M. Barron. Impulse testing techniques for auditoria. *Applied Acoustics*, 17:165–181, 1984.

[68] F. Kawakami; T. Sakai. Deep-well approach for canceling the edge effect in random incident absorption measurement. *Journal of Acoustical Society of Japan*, (E) 19, 5:327–338, 1998.

[69] V. Rok; A. Druzhinin; J. R. Evans; X-Y. Li. Frequency-power-law attenuation scattering by fractal inclusions. In *EAGE 65th Conference & Exhibition*, Stavanger, Norway, 2003.

[70] D. Fernández Comesaña; E. Tijs; H. E. de Bree. Exploring the properties of acoustic particle velocity sensors for near-field noise source localisation applications. Kraków, 7-12Spetember 2014. Forum Acusticum 2014.

[71] D. B. Weems. *Designing, building and testing your own speaker system with projects,*. McGraw-Hill, 4th edition, 1997.

[72] B. Gibson. *Instrument & vocal recording.* Hal Leonard, 2007.

[73] F. E. Toole. The measurement and calibration of sound reproducing systems. *Journal of Audio Engineering Society*, 63, No. 7/8:512–541, July/August 2015.

[74] B. Gibson. *Microphones & mixers.* Hal Leonard, 2007.

[75] BS EN 61094-2:2009. Electroacoustics - measurement microphones - part 2: Primary method for pressure calibration of laboratory standard microphones by the reciprocity technique, June 2009.

[76] D. Fernández Comesaña; E. Tijs; H. E. de Bree. Sound visualisation tools for investigating acoustic fiels based on scanning measurements. Kraków, 7-12Spetember 2014. Forum Acusticum 2014.

[77] D. Fernández Comesaña; S. Steltenpool; G. Carrillo Pousa; H. E. de Bree; K. R. Holland. Scan and paint: Theory and practice of a sound field visualization method. *ISRN Mechanical Engineering*, 2013, Article ID 241958, 2013.

[78] D. Fernández Comesaña; B. O. Peksel; H. E. de Bree. Expanding the sound power measurement criteria for sound intensity p-u probes. In *ICSV 21*, Beijing, China, 13-17July 2014. The 21st International Congress on Sound and Vibration.

[79] Brüel & Kjær. Fundamentals of measuring sound, 2010.

[80] M. Lavandier; P. Herzog; S. Meunier. Comparative measurements of loudspeakers in a listening situation. *Journal of Acoustical Society of America*, 123 (1):77–87, 2008.

[81] D. Fernández Comesaña; S. Steltenpool; M. Korbasiewicz; E. Tijs. Direct acoustic vector field mapping: new scanning tools for measuring 3d sound intensity in 3d space. pages 891–895, Maastricht, 31 May-3June 2015. EuroNoise 2015.

[82] J. R. Bareham. Introduction to electroacoustic measurement on telephones, 2010.

[83] P. Newell; K. R.Holland. *Audio engineering explained*, chapter 12, Diversity of design, pages 349–381. Elsevier Ltd, Focal Press, 2010.

[84] F. P. Toole. *Sound reproduction, the acoustics and psychoacoustics of loudspeakers and rooms.* Elsevier Ltd, Focal Press, 2008.

[85] M. Lavandier; P. Herzog; S. Meunier. Physical and perceptual estimation of differences between loudspeakers. *Elsevire, Masson SAS, C. R. Mecanique*, 334:732–736, 2006.

[86] M. Lavandier; S. Meunier; P. Herzog. Identification of some perceptual dimensions underlying loudspeaker dissimilarities. *Journal of Acoustical Society of America*, 123 (6):4186–4198, 2008.

[87] P. E. Gill; W. Murray; M. H. Wright. *Practical optimization.* Academic Press, 1993.

[88] F. J. Fahy. *Sound intensity.* Chapman & Hall, E & FN Spon, 2nd edition, 1995.